High-performance adaptive optics control for the Gran Telescopio Canarias

Lucas Marquis

THESE DE DOCTORAT

NNT : 2023UPAST087

Commande haute performance de l'optique adaptative du Gran Telescopio Canarias

High-performance adaptive optics control for the Gran Telescopio Canarias

Thèse de doctorat de l'université Paris-Saclay et de l'université de La Laguna

École doctorale n°575 : electrical, optical, bio: physics and engineering (EOBE)
Spécialité de doctorat: Physique
Graduate School : Sciences de l'ingénierie et des systèmes. Référent : Institut d'Optique

Thèse préparée dans les unités de recherche **Laboratoire Charles Fabry (Université Paris-Saclay, Institut d'Optique Graduate School, CNRS)** et **Instituto de Astrofísica de Canarias (Université de La Laguna, Gobierno de Canarias, Ministerio de Ciencia e Innovación, CSIC)**,
sous la direction de **Caroline KULCSÁR**, professeure des universités,
la co-direction de **Icíar MONTILLA**, ingénieure de recherche,
le co-encadrement de **Henri-François RAYNAUD**, maître de conférences

Thèse soutenue à Paris-Saclay, le 23 juin 2023, par

Lucas MARQUIS

Composition du jury

Membres du jury avec voix délibérative

Sihem TEBBANI Professeure, Université Paris-Saclay	Présidente
Jean-Pierre VÉRAN Professeur adjoint (eq. HDR), University of Victoria	Rapporteur & Examinateur
Tim MORRIS Professeur associé (eq. HDR), Durham University	Rapporteur & Examinateur
Olivier GUYON Professeur, Arizona University	Examinateur
Michel TALLON Chargé de recherche, CRAL, Université de Lyon	Examinateur
Maud LANGLOIS Directrice de recherche, CRAL, Université de Lyon	Examinatrice

université PARIS-SACLAY

ÉCOLE DOCTORALE
Physique et ingénierie : Electrons, Photons, Sciences du vivant (EOBE)

Titre: Commande haute performance de l'optique adaptative du Gran Telescopio Canarias
Mots clés: Modélisation et commande des systèmes, Optique adaptative, Filtrage de Kalman, Astronomie

Résumé: La turbulence atmosphérique dégrade la qualité des images acquises par les télescopes terrestres. L'optique adaptative (OA) permet de compenser en temps réel ces dégradations à l'aide d'un miroir déformable. Le Gran Telescopio Canarias (GTC, La Palma, Îles Canaries) de 10 m de diamètre va se doter d'un tel système, GTCAO, conçu par l'Instituto de Astrofísica de Canarias (IAC). Dans ma thèse, je conçois et mets en œuvre un asservissement très performant pour GTCAO : des modèles mathématiques prédisent la turbulence pour mieux la compenser. C'est une première pour un système dédié à un télescope de cette taille et en conditions expérimentales. J'ai développé les stratégies d'identification et de mise à jour des modèles (car la turbulence évolue), et les résultats sont au rendez-vous. La qualité des images a été améliorée de façon spectaculaire dans un grand nombre de cas. Cette thèse, en cotutelle internationale avec l'université de La Laguna, a été menée en collaboration avec l'IAC.

Title: High-performance adaptive optics control for the Gran Telescopio Canarias
Keywords: System modeling and control, Adaptive optics, Kalman filtering, Astronomy

Abstract: Atmospheric turbulence degrades the quality of images acquired by terrestrial telescopes. Adaptive optics (AO) makes it possible to compensate for these degradations in real time using a deformable mirror. The 10 m diameter Gran Telescopio Canarias (GTC, La Palma, Canary Islands) will be equipped with such a system, GTCAO, designed by the Instituto de Astrofísica de Canarias (IAC). In my thesis, I design and implement a very efficient servo-control for GTCAO: mathematical models predict turbulence to better compensate for it. This is a first for a system dedicated to a telescope of this size and under experimental conditions. I developed the strategies for identifying and updating the models (because turbulence evolves rapidly), and the results are there! Image quality has improved dramatically in a large number of cases. This thesis, in international cotutelle with the University of La Laguna, was carried out in collaboration with the IAC.

Acknowledgements – Remerciements

Il ne me reste plus qu'à m'affranchir des remerciements. Alors c'est parti.

Merci à mon triptyque de direction, Caroline, Icíar et Henri-François. Avec notamment toi au centre Caroline. Bravo d'avoir monté et dégoté ce projet comme tu sais si bien le faire, en en faisant le sujet de thèse le plus intéressant parmi les centaines que j'ai lues. Ton instinct professionnel t'a de plus fait savoir que j'étais la bonne personne. Nos réunions, bien que spatio-temporellement éparses, m'ont toujours apporté motivation et bonne humeur. Nos passions pour notre travail se sont très bien retrouvées, parfois même jusqu'à pas d'heure et jusqu'à pas de jour. J'ai adoré la circonspection constructive qu'est la recherche appliquée.

Gracias a ti Icíar, para tu interés en ese proyecto para GTCAO, incluso luchando con las pesadillas administrativas. Al final, lo pudimos convertir en realidad en el AIV del IAC. Con tu defensa, seguida por la confianza de Marcos quien agradezco también, realizamos un montón de pruebas. Esas fueron posibles gracias a ti Jose. Tu conocimiento en el software me fue imprescindible para desembarazarme de los «coñazos », si recuerdo la palabra. Nos has hecho una multitud de herramientas, mis salvadores. Gracias a ti también Óscar para las salidas en Tenerife, entre otros. Por fin, agradezco Jesús Patrón por manejar mis estancias, cuando sé que no es mi especialidad organizar los viajes con anticipación.

Merci également au jury pour leurs intéressantes attention, questions et remarques. Cela commença par les rapports gracieusement rédigés par Tim MORRIS et Jean-Pierre VERAN ; le jour de la soutenance ensuite, avec la présidente Sihem TEBBANI, les examinateurs Olivier GUYON et Michel TALLON et l'examinatrice Maud LANGLOIS alors toutes et tous remerciées.

A large thank you to Peter WIZINOWICH and Sam RAGLAND for your share of tons of on-sky data from the Keck observatory. You transmitted us some key parameters too for our work, this with a very motivating kindness. Let us hope this PhD thesis work extends throughout Pacific Ocean.

Je donne maintenant mes félicitations et remerciements à Nicolas. On était très complémentaires au boulot. Félicitation entre autres pour ton talent caché de développeur avec lequel j'aurais aimé jouer davantage, jusqu'au CBLAS effrayant. J'espère qu'on se reverra aux [Ca, na, ries] par exemple ! Merci à Baptiste, pour tes codes et ton aide prolongée, de même qu'à Léonard pour mon initialisation extrovertie à OOMAO.

Viennent alors mes proches et mes lointains, qui ont participé au bien-être de ma sérénité. Ma compagne Yangji, merci beaucoup. Tu m'as tellement aidé et tellement ludiquement pour la rédaction... Sans toi comme coach, je n'aurais peut-être pas réussi et pour sûr pas aussi bien. 생각보니까 우리 행복했어요. 같이 리스트 만들고, 커피 마시고, 미암탱 셰프 부라따 먹고, 드라마 보고 트립 가고 웃었어요. 우리 공부하는 팀예요. 이제 너도 화이팅. Merci à ma famille, aux drogués font du ski,

Aitor para tu ayuda en La Laguna, Kevin pour l'hébergement hippique, Benjamin pour les cadeaux de soutenance, Viviane pour mes invités, ...

Aller, un peu de pub pour finir, en signalant qu'au bar-restaurant Celestino, à La Laguna, ils sont super sympas avec de la bonne nourriture maison locale et un excellent vin rouge de Tenerife à prix dérisoire.

Contents

List of Figures

List of Tables

Table of Notations

ρ	Polar coordinate
h	Altitude
ν	Spatial frequency
$I(\cdot)$	Image
$O(\cdot)$	Object
J_1	Bessel function of the first kind
ρ^{air}	Air density
G^{air}	Gladstone-Dale constant
PSF	Point spread function
OTF	Optical transfer function
r_0	Fried parameter
C_n^2	Refractive index structure
V_0	Wind speed
L_0	Outer scale
r_0^{LQG}	LQG AR2 coherence length
V_0^{LQG}	LQG AR2 modal speed
L_0^{LQG}	LQG AR2 outer scale
T_{s}	Sampling period
F_{s}	Sampling frequency
D_{pup}	Telescope primary mirror diameter
λ_{sci}	Scientific wavelength
M_{ngs}	Natural guide star magnitude
λ_{wfs}	Natural guide star observation wavelength
μ_{wfs}	WFS CCD pixel size
μ_{sci}	Scientific camera CCD pixel size
n_y	Size of measurement vector y
d_{SA}	Size of subapertures
n_{px}	Number of pixels per subaperture
Nyq	WFS CCD sampling ratio wrt the Shannon-Nyquist limit
n_{SA}	WFS Number of subapertures linear
y	Measurement vector
D	WFS measurement matrix
σ_{RON}	WFS read-out noise
σ_{photon}	WFS photon noise
G	WFS CCD gain
σ_w	WFS measurement noise RMS
n_{act}	Number of actuators linear
u	Command vector
n_u	Command vector size

u_{clip}	Command clipping value
C_{DM}	DM coupling
IF	DM influence function
N	DM influence functions matrix
θ_{DM}	DM-to-WFS spin angle
σ_{fit}	DM fitting error RMS
σ_{tempo}	Temporal error RMS
R_{MAP}	Maximum *a posteriori* reconstructor
α_{MAP}	Maximum *a posteriori* reconstructor regularization parameter
δ^{OP}	Optical path
ϕ	Disturbed phase
ϕ^{tur}	Turbulence related phase disturbance
ϕ^{cor}	DM phase correction
ϕ^{res}	Residual phase
$\overline{\phi}^{\text{res}}$	DM-synchronized residual phase average
$\overline{\phi}^{\delta}$	WFS-synchronized residual phase average
f_{vib}	Vibration natural frequency
σ_{vib}	Vibration STD
n_{iter}	Number of iterations
M_{com}	Command matrix
M_{int}	Interaction matrix
n_{filt}	Number of SVD filtered modes
g	Integrator loop gain
g^{TT}	Integrator tip-tilt loop gain
g^{HO}	Integrator high orders loop gain
α_{leak}	Leaky factor
α_{FF}	Fudge factor
Σ_v	Process noise covariance matrix
Σ_ϕ	Phase disturbance covariance matrix
Σ_w	Measurement noise covariance matrix
Σ_∞	Asymptotic state prediction error covariance matrix
L_∞	Prediction Kalman gain
H_∞	Estimation Kalman gain
A, Γ, C_y	Disturbance state-space matrices
X	State vector
P_u	Phase-to-command projector
Δ	Loop delay (exposure time excluded)
δ	Decimal part of loop delay
TF	Transfer function
i_{rad}	Zernike radial order
i_{azi}	Zernike azimuthal order
η_{a}	Parallactic angle
γ	Elevation angle

Table of Notations

Z_{a}	Zenith angle
Φ_{a}	Latitude angle
h_{a}	Hour angle
δ_{a}	Declination angle
A_{a}	Azimuth angle
$C^{\mathrm{ZernToZon}}$	Zernike-to-zonal phase projector
i^{dead}	Dead actuator
$\mathcal{F}$	Fourier transform
$\mathcal{P}$	Pupil function
S_{pup}	Pupil surface
$\mathcal{I}$	Interspectrum
F_{cut}	Cut-off frequency
F_{noise}	Noise plateau starting frequency
X_R	Regulator state vector
X_R^{switch}	Switching state vector
A_R, B_R, C_R	Regulator state-space matrices
q	Intersampling factor
$\mu_{\mathrm{sci}}^{\mathrm{ov}}$	Scientific camera oversampling
SR	Strehl ratio
$n_{\mathrm{px}}^{\mathrm{SR}}$	Number of pixels for SR estimation

Acronyms

AO	Adaptive optics
ARn	Autoregressive of order n
CL	Closed-loop
DM	Deformable mirror
FPS	Frames per second
FWHM	Full width at half maximum
GPI	Gemini planet imager
GTC	Gran Telescopio Canarias
GTCAO	Gran Telescopio Canarias adaptive optics
HO	High order
IAC	Instituto de Astrofísica de Canarias
LO	Low order
LQG	Linear Quadratic Gaussian
LS	Least squares
M1	Primary mirror
M2	Secondary mirror
MAP	Maximum *a posteriori*
MMSE	Minimum mean square error
NCPA	Non-common path aberrations
NGS	Natural guide star
OL	Open-loop
OOMAO	Object-oriented Matlab adaptive optics
OTF	Optical transfer function
POL	Pseudo-open-loop
PSD	Power spectral density
PSF	Point spread function
RTC	Real-time computer
RTF	Rejection transfer function
SCAO	Single conjugated adaptive optics
SCExAO	Subaru Coronagraphic Extreme Adaptive Optics
SPHERE	Spectro-Polarimetry High-contrast Exoplanet REsearch
SR	Strehl ratio
SVD	Singular values decomposition
TT	Tip-tilt
WFS	Wavefront sensor
WHT	William Herschel Telescope
XAO	Extreme adaptive optics
ZOH	Zero-order hold

Résumé en français

Les systèmes d'optique adaptative astronomiques permettent de compenser les dégradations induites par la turbulence atmosphérique sur les images acquises par les télescopes terrestres. D'autres sources d'aberrations dégradent également les images, comme de petites erreurs de pointage du télescope, des vibrations de sa structure dues au vent ou des vibrations générées par des composants tels que des pompes, des ventilateurs, etc. Ces dégradations se traduisent par une déformation du front d'onde incident, qui devrait être plan en l'absence d'aberrations. En OA dite classique, un miroir déformable compense ces déformations en temps-réel à partir de mesures fournies par un analyseur de surface d'onde. Un calculateur temps-réel calcule la commande à partir des mesures. L'algorithme de commande le plus largement utilisé est une commande à action intégrale. Cependant, les boucles d'asservissement des systèmes d'OA comportent des retards que l'intégrateur ne peut compenser. Afin d'améliorer les performances, des commandes prédictives à base de modèle ont donc été proposées pour prédire la perturbation et ainsi compenser le retard global du système.

Le but de ce travail de recherche doctorale est la conception et la validation d'un régulateur optimal prédictif linéaire quadratique gaussien (LQG) pour GTCAO, le système d'optique adaptative qui équipera bientôt le Gran Telescopio Canarias (GTC) et qui a été intégré par l'Instituto de Astrofísica de Canarias (IAC). GTC est un télescope de classe 10 m de l'Observatoire Roque de los Muchachos situé sur l'île de La Palma aux Îles Canaries. Ce travail a été mené dans le cadre d'une cotutelle internationale entre l'Université Paris Saclay-Institut d'Optique (Palaiseau, France) et l'Université de la Laguna-IAC (La Laguna, Tenerife, Espagne), et soutenue principalement par le programme Actions Doctorales Internationales (ADI) apportées par l'IDEX Paris-Saclay. La pandémie a limité (voire arrêté) l'accès à Tenerife et donc à GTCAO pendant une assez longue période et a aussi provoqué des changements dans la réalisation du projet GTCAO. Néanmoins, j'ai eu la chance d'obtenir une prolongation de 7 mois qui m'a permis de poursuivre mes tests à l'IAC.

Le manuscrit est composé de 8 chapitres : une introduction générale (chapitre 1), une partie sur la formation d'image en présence de turbulence (chapitre 2) et une description de l'optique adaptative classique (un seul miroir et un seul analyseur, analyse et correction se faisant dans la même direction) avec ses composants et régulateurs standards que sont la commande à action intégrale et le régulateur LQG sous forme générale (chapitre 3).

Comme détaillé dans le chapitre 3, les régulateurs LQG sont construits sur une représentation d'état de la boucle d'optique adaptative avec des *a priori* spatiaux et temporels. La commande LQG est une approche basée sur un modèle d'état linéaire, où le régulateur comprend un filtre de Kalman qui calcule de manière récursive une prédiction à court terme optimale (à variance minimale) des perturbations à

compenser.

Le chapitre 4 est composé d'un article en voie de soumisson. Cet article revient sur le problème de la commande optimale (à variance minimale) pour les systèmes d'optique adaptative dont les mesures et les commandes sont asynchrones, ce qui se traduit par un retard non entier de la boucle d'asservissement. Lorsqu'ils ne sont pas correctement pris en compte, ces retards fractionnaires peuvent significativement dégrader les performances de l'optique adaptative, en particulier en présence de vibrations à haute fréquence. Ceci est démontré grâce à des mesures expérimentales en laboratoire sur le système GTCAO. Une méthode LQG constructive et facile à mettre en œuvre est proposée et validée en simulation pour les vibrations affectant les modes de basculement. En particulier, notre méthodologie permet la construction d'un modèle de perturbation à temps continu à partir d'un modèle d'état à temps discret identifié sur les mesures.

Dans le chapitre 5 de ce manuscrit est présentée la première exploration des méthodes de modélisation et des procédures d'étalonnage pour la commande LQG d'un système d'OA dédié à un très grand télescope, avec une pupille segmentée non circulaire. Ceci est proposé comme une alternative performante à la commande par action intégrale standard. Pour construire certains des modèles et également faire des simulations, le simulateur OOMAO (*Object-oriented Matlab adaptive optics*, codé en Matlab© orienté objet par R. Conan et C. Correia) et ses nombreux modules sont utilisés. Nous développons en particulier dans ce chapitre 5 certains aspects liés au télescope lui-même, comme la façon dont les miroirs primaire et secondaire sont structurés, ainsi que la description de la rotation/dérotation nécessaire de la pupille pour les observations astronomiques. En outre, la façon dont le vent peut faire trembler le miroir secondaire est modélisée. Cela met en évidence le risque potentiel de présence d'une vibration de fréquence propre 12 Hz et d'amplitude significative. Or, ce type de perturbations que sont les vibrations ne peuvent pas être corrigées par un intégrateur lorsque le système d'optique adaptative tourne à une cadence inférieure à 200 Hz.

Ensuite, parmi les paramètres clés d'un banc d'optique adaptative, nous proposons une méthode simple pour estimer le retard fractionnaire de la boucle. Ce retard doit être connu non seulement pour simuler correctement la boucle d'optique adaptative mais aussi pour concevoir le contrôleur LQG. Nous proposons une méthode basée sur les estimations moindres carrés combinant robustesse et précision. Des simulations et des tests de mesures de retard sur banc permettent cette mise en évidence des qualités de notre estimateur. Cela passe par la comparaison de la méthode avec une autre méthode basée sur l'analyse spectrale (utilisant la transformée de Fourier), pour laquelle nous proposons également des pistes d'amélioration.

De surcroît, un important travail est dédié à la modélisation pseudo-synthétique de la matrice dite d'interaction (matrice reliant les commandes envoyées au miroir déformable et les mesures du déphasage résultant fournies par l'analyseur de surface d'onde). Cette matrice est cruciale notamment pour l'étude des conditions

atmosphériques. La modélisation pseudo-synthétique (plutôt qu'une version expérimentale mesurée sur le banc d'optique adaptative) permet d'abord de caractériser le miroir déformable. De sa caractérisation s'ensuit la possibilité de définir une matrice de projection efficace permettant de convertir les phases prédites par le filtre de Kalman en des commandes à envoyer au miroir pour corriger ces phases. Les avantages apparus sont notamment la bonne prise en compte des éventuels actionneurs morts du miroir et de la géométrie de ce dernier. Outre le miroir déformable, l'analyseur de surface d'onde doit également être modélisé. C'est fait *via* sa matrice de mesure, de façon à pouvoir modéliser les mesures correspondant à une phase de perturbation donnée. Nous détaillons donc un protocole nécessaire à la bonne prise en compte à la fois de la géométrie du système optique et de la taille des pixels des images de la caméra de l'analyseur.

Un dernier point appréciable de ce chapitre 5 est la proposition d'une méthode pour modéliser la variance du bruit de mesure de l'analyseur de surface d'onde, basée sur l'étude spectrale des mesures et la prise en compte du flux sous forme de carte d'intensité. Cela consiste à disqualifier les zones de l'analyseur de surface d'onde qui n'ont pas ou très peu reçu de flux de la part de l'étoile guide. Une extension de la méthode est également présentée. Celle-ci consiste à non plus simplement disqualifier les zones invalides de manière statique, mais plutôt d'analyser en temps réel les zones qui semblent manquer de flux, et remplacer les mesures correspondantes par une estimation que fournit le filtre de Kalman.

Toutes les méthodes de ce chapitre sont appliquées au système GTCAO.

Dans le chapitre 6, nous nous dirigeons vers la modélisation non plus du système d'optique adaptative mais vers celle des perturbations. Un critère attendu est la possibilité de mise à jour régulière du régulateur, en fonction de l'évolution des statistiques de perturbation.

Nous prenons comme base les méthodes de modélisation et d'identification de modèles récemment confirmées par des tests sur le ciel. La phase est représentée dans la base de Zernike. Ces méthodes consistent à établir deux modèles dynamiques stochastiques de perturbation complémentaires :

- Un premier modèle non paramétrique consiste en une identification dite par sous-espaces (méthode N4SID). Elle permet de modéliser tout type de perturbation (vibrations incluses). Notre travail a permis la mise en lumière de certains avantages ou désavantages possibles de cette méthode de modélisation dans notre cas d'étude GTCAO.

- Un deuxième modèle plus simple et paramétrique consiste en une prise en compte de certaines caractéristiques statistiques globales des perturbations. Nous avons proposé des méthodes d'estimation n'utilisant que les mesures de l'analyseur de surfce d'onde pour ces paramètres, notamment des vitesses de vent dites modales qui fixent les vitesses de décorrélation des modes de Zernike. Le fonctionnement non-supervisé de l'estimation est également abordé.

Un résultat intéressant a permis d'axer l'optimisation d'un paramètre clé du réglage du régulateur LQG, le fudge factor, qui permet d'obtenir un bon compromis entre performance et stabilité, ce qui sera illustré dans les résultats expérimentaux du chapitre 7.

Outre l'identification des modèles, nous étudions en simulation dans ce chapitre 7 la façon dont on peut mettre à jour le régulateur en temps réel afin d'éviter un ressaut trop important des mesures et des commandes lors de la transition. Des simulations montrent que le changement de régulateur peut se faire en douceur. Ces méthodes doivent être développées plus en profondeur pour une utilisation sur le ciel. Enfin, le chapitre 7 aborde la mise en œuvre expérimentale de notre régulateur LQG sur GTCAO (dont le calculateur temps-réel DARC a été développé par l'Université de Durham) et sur des données ciel du système d'OA du télescope Keck (Hawaii).

Ce chapitre commence par une présentation d'outils utiles pour l'analyse des performances, dans l'objectif notamment d'analyser spatio-temporellement les qualités et défauts du régulateur LQG et de l'intégrateur. Cela inclut en particulier l'étude des algorithmes standards d'évaluation de la qualité des images scientifiques prises sur le banc : le rapport de Strehl, compris entre 0% (image catastrophique) et 100% (image parfaite sans aucune perturbation optique).

Les résultats des tests expérimentaux sur GTCAO révèlent que :

- Pour une perturbation liée à la turbulence atmosphérique pure, l'écart de performance entre le LQG et l'intégrateur est plus important pour une forte turbulence. Le LQG améliore alors le rapport de Strehl de 5 à 10 points. Les avantages en cas de turbulence atmosphérique faible apparaissent pour des cas d'étoile guide de flux moyen, avec jusqu'à 10 points de Strehl d'amélioration lorsque le flux est faible.

- Dans le cas où le miroir secondaire vibrerait à 12 Hz (en présence de *windshake*), l'intégrateur est plus pénalisé que le LQG, ce qui conduit à une augmentation des écarts indiqués ci-dessus.

- Quand des perturbations plus complexes apparaissent, telles que celles que l'on peut voir dans les données sur le ciel de l'optique adaptative du télescope Keck, le LQG permet un gain de 10 points par rapport à l'intégrateur pour une étoile guide de flux moyen. Nous avons également pu montrer expérimentalement que même des vibrations à très haute fréquence (typiquement 315 Hz pour une fréquence d'échantillonnage de $F_\mathrm{s} = 1$ kHz) pouvaient être compensées par le régulateur LQG sur le système GTCAO.

Dans tous ces tests, les marges de stabilité du LQG sont très confortables, de l'ordre de 9 dB pour le gain et 40° pour la phase. La figure 1 illustre un cas emblématique de vibrations générées sur le banc GTCAO suivant des données enregistrées sur le ciel issues du système d'OA de Keck. Les vibrations affectent les premiers 9 modes de Zernike, le système fonctionne à 200 Hz sur une étoile modérément brillante. Les

images scientifiques montrent le gain spectaculaire de l'OA d'une façon générale, mais aussi l'amélioration impressionnante de 11 points du rapport de Strehl, qui passe de 38% pour l'intégrateur à 49% pour la commande LQG.

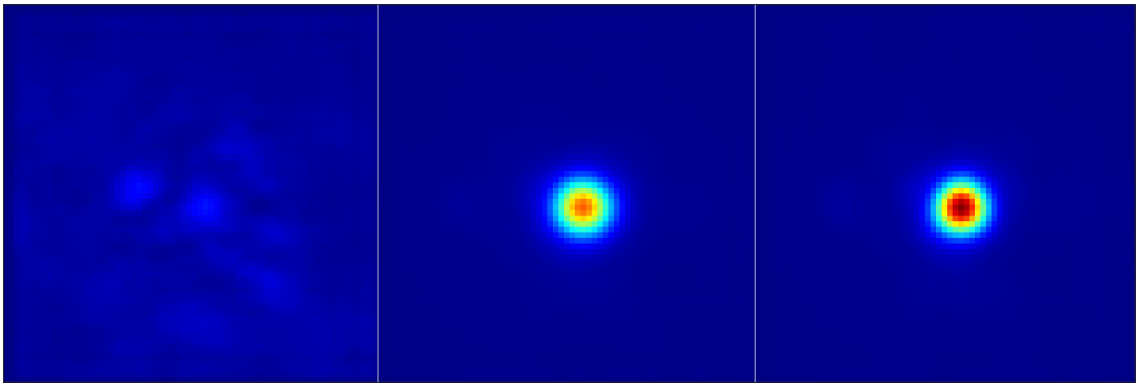

FIGURE 1 : (banc avec vibrations, 8 novembre 2022) Images scientifiques en présence de vibrations sur 9 modes générées à partir d'un jeu de données ciel de l'OA de Keck et injectées *via* le miroir déformable. Gauche : boucle ouverte (pas de correction par OA). Milieu : integrateur (rapport de Strehl 38%). Droite : régulateur LQG (rapport de Strehl 49%).

Enfin, de nombreuses simulations en rejeu sont effectuées grâce à l'utilisation de données ciel de l'optique adaptative du télescope de l'observatoire de Keck. Les mêmes procédures de calcul (modélisation – partielle ici – du système d'optique adaptative et identification des modèles de perturbation) pour la conception des régulateurs LQG ont permis de confirmer en simulation notre stratégie d'autotuning telle que développée dans les précédents chapitres. L'ordre de grandeur du gain de performance en moyenne pour ces jeux de données Keck est estimé à environ 100 nm RMS. Cela a de plus confirmé que notre stratégie de conception du régulateur LQG pouvait rapidement être adaptée à un autre système d'optique adaptative – à condition que le calculateur temps-réel dispose de l'algorithme de commande adéquat, un régulateur sous forme d'état linéaire étant suffisant.

Pour conclure, la maturité de la méthodologie permettrait de procéder maintenant à des essais de régulateur non supervisé sur le ciel. Ceux-ci seraient d'un grand intérêt pour confronter les résultats à ceux obtenus sur banc et en rejeu, et pour confronter la modélisation à des perturbations réelles qui ne seraient plus vraiment stationnaires. Il faut également tester la performance sur des intervalles de temps suffisamment longs, et ainsi pouvoir éprouver la stabilité du régulateur.

Je remets mon grand remerciement à l'équipe de GTCAO pour leur accueil dans l'équipe et leur aide sur leur système d'optique adaptative. La formation offerte pour la manipulation du banc, mêlée à la prise de confiance à l'AIV, ont permis un long et plaisant travail pour le développement de cette régulation à haute performance.

Un grand merci également à Peter Wizinowich et Sam Ragland pour le partage

de nombreuses données ciel de l'observatoire de Keck, accompagnées de paramètres clés tels que la matrice d'interaction. La gentillesse avec laquelle furent remis les jeux de données rendit leur exploitation très motivante, vers l'aboutissement de mon travail de thèse.

Chapter 1
Introduction

1.1 A short history of high angular resolution and its path towards adaptive optics

For millennia (Rappenglück, 1997), the humankind has been developing a fascination for its host Universe. It was mainly in the seek of its interpretation first, followed by its practical usage (e.g. orientation). In the past centuries, the field of astrophysical targets have been continuously backed away from the Earth, always expecting both a clearer and stronger light signal.

This has come synergistically with the dedication of more observation sites (e.g., Cheomseongdae, figure 1.1) and more instruments. The key one was the telescope, starting in the 17th century. It was an instrumental tool to turn the sky interpretations into a scientific research, with the growing principle that the laws of nature apply everywhere equally in our solar system and everywhere in the universe (Van Helden, 1974).

Figure 1.1: Left: 첨성대 , among the oldest surviving astronomical observatories, constructed in the 7th century on demand of Queen Seondeok (South Korea, credit Lucas Marquis).
Right: the Gran Telescopio Canarias (Spain, credit University of Florida).

In 1609, Galileo Galilei perfected a refraction telescope with several lenses and pointed it at the night sky, enabling him to discover the satellites around Jupiter (Rose, 1964). The German astronomer Johannes Kepler – before his heliocentric model of the Solar System – published the theoretical foundation for the study of such lens systems (Helden, 1974). In the same century, another Italian astronomer, Giovanni

Cassini, designed a telescope with increased focal length, which allowed him to observe the moons of Saturn and to make the first accurate measurement of the distance between the Earth and the Sun, our modern astronomical unit (Augusto, Difa, and Rossi, 2021). In the meantime, Isaac Newton invented the reflector, a reflecting telescope, using a concave mirror to reflect and focus light until the eyepiece without chromatic aberrations (Augusto, Difa, and Rossi, 2021). In 1789, the astronomer William Herschel built such a reflecting telescope, with sufficient resolution to discover Uranus (Augusto, Difa, and Rossi, 2021). Neptune and its 6 times fainter brightness was first observed again a few decades later by the German astronomer Galle, with a 10-cm refractive telescope (made of achromatic lenses thanks to the English optician John Dollond), by conducting the predictive localisation calculated by the French mathematician Le Verrier: given a bright guide star to track, Galle could see alongside the blue spot of the 8th solar system planet (Krajnovic, 2016). In the early 20th century, the application of interferometry allowed for even higher angular resolution with telescopes. The angular resolution is the smallest allowed distance between two close objects to keep them distinguishable. Combining simultaneously the light from multiple telescopes, interferometry creates images with greater details than what could be achieved with one single telescope. In 1920, the American astronomer Albert Michelson used an interferometer to measure the diameter of Betelgeuse star (higher than one astronomical unit, roughly equal to the distance between the Sun and the Earth, that is about 150 million kilometers!). Those results were published by Pease in (Pease, 1921), in which is repeatedly mentioned one difficulty: the seeing.

For a single-mirror telescope, the best achievable theoretical resolution (that is, at the diffraction limit) is inversely proportional to its diameter. For an interferometer, it is inversely proportional to the maximum distance between the individual telescopes which are used in combination. In astronomy, seeing refers to the effect of atmospheric turbulence on the sharpness of astronomical images. Because of the seeing, a telescope or interferometer of size 10 meters will have as poor resolution as one of size 10 centimeters. Good seeing conditions were then of utmost importance for high-resolution observations. To address this issue, Babcock first suggested in 1953 (Babcock, 1953) a disturbance correction principle which was the basis of adaptive optics (AO). The AO systems aim at compensating the image deformations induced by the atmospheric turbulence on ground-based telescopes. To do so, a deformable mirror (DM) is inserted on the optical path and is controlled in real time using measurements of the deformations delivered by a wavefront sensor (WFS).

In 1989, an astronomical AO system is finally successfully operational, the COME-ON AO prototype, tackling the atmospheric turbulence related optical effects (Rousset et al., 1990). The global interest in AO immediately soared, making it since then a staple in the ground-based astronomy, an integral part of new telescopes design. Around 10 years after COME-ON, the 10-m Keck telescope started its observations (Wizinowich et al., 2000). It has been followed for instance by the Very Large

Telescope (Hubin et al., 1994), the Large Binocular Telescope (Esposito et al., 2010), the Subaru Telescope (Guyon, Hayano, et al., 2014). The largest telescope today is the 10.4-m Gran Telescopio Canarias (GTC), not yet but soon to be equipped with GTCAO, a Single Conjugated AO (SCAO) system, that is, a DM and a WFS, with analysis and correction performed in the same direction. GTCAO has been integrated by the Instituto de Astrofísica de Canarias (IAC) for infrared observations. It is in the final stages of testing at the IAC laboratory on the island of Tenerife (La Laguna town). As for most of the operational AO systems, the baseline for the controller of the GTCAO is an integral action controller, or in short, an integrator. An integrator is easy to implement (already used for the first AO system COME-ON) and in most cases it has a very good performance. In addition, it requires only a modest amount of knowledge about the AO system.

1.2 Advanced controllers to cope with vibrations (and other adverse situations)

However, poor signal-to-noise ratios or non-atmospheric disturbances such as vibration may severely affect integral control performance, see e.g. (Kulcsár, Sivo, et al., 2012). Combining good performance in these unfavorable situations with robustness and ease of implementation is not straightforward and very few operational AO systems have more advanced controllers able to efficiently adapt to these types of cases. Most, if not all, of these systems are dedicated to exoplanet detection: SPHERE (Beuzit et al., 2005) at the Very Large Telescope, GPI (B. Macintosh et al., 2007) at Geminy South and SCExAO (Guyon, Martinache, et al., 2010) at Subaru telescope. The latter is based on multivariable linear regression (Guyon, Lozi, et al., 2020) while the first two use Linear Quadratic Gaussian (LQG) regulators on tip and tilt for SPHERE (Petit et al., 2014) and on tip, tilt and focus for GPI (L. Poyneer, Rosa, et al., 2014), higher orders being controlled with an integrator. These regulators aim at predicting the upcoming disturbance in order to address the temporal delays that AO systems inherently suffer from. They are all eXtreme AO (XAO) systems, with very strong performance requirements. Apart from these operational systems, very few on-sky experiments have been carried out. Using a similar scheme, that is a limited number of low-order modes with an advanced controller capable of vibration mitigation, the higher orders with an integrator, there is, to the best of our knowledge, only a few examples: tip/tilt control for a 1.5 meter solar telescope (Doelman, Fraanje, and Breeje, 2011), 20 modes for a 5 meter astronomical telescope (Tesch et al., 2015), tip/tilt control for another solar telescope of 1.8 meter (Guo et al., 2021). As for the control of all modes in SCAO, full LQG control has been demonstrated on sky only twice: in 2012 by Sivo (Sivo et al., 2014) and in 2019 by Sinquin (Sinquin et al., 2020), both on the CANARY (Myers et al., 2008) demonstrator at the 4.2 meter William Herschel telescope in La Palma (Canary Islands).

So what is an LQG regulator? It has been proposed for the first time in AO in

1991 (Paschall, Von Bokern, and Welsh, 1991). It consists in using a linear stochastic state-space model to predict the disturbances from noisy and delayed WFS measurements thanks to a Kalman filter. It can be designed in discrete time in an optimal way in the sense of the minimal variance of the residual phase (Le Roux et al., 2004; Kulcsár, H.-F. Raynaud, et al., 2006; Looze, 2009; Kulcsár, H. F. Raynaud, et al., 2012). Of course, the state-space model should describe well enough the spatio-temporal statistics of the disturbances. With GTCAO, the objective is to bring to a SCAO system the main advantages of these types of regulators, that is efficiency and robustness, and to ease their implementation thanks to well-defined procedures.

1.3 The Gran Telescopio Canarias and adaptive optics LQG control: context and objectives

The GTC is a world-class optical and infrared telescope. It has a primary mirror diameter of 10.4 meters, making it the largest single-aperture telescope in the world. This primary mirror is a segmented mirror, composed of 36 hexagonal mirrors (GTC, 2023), as illustrated in figure 1.2.

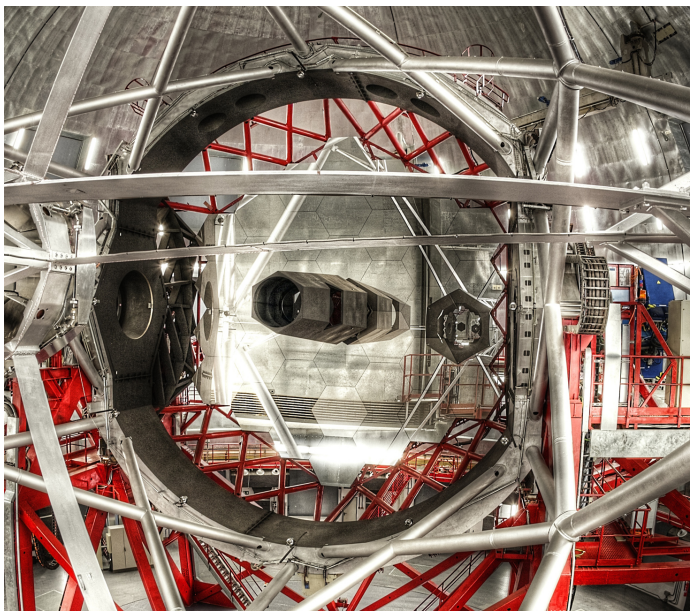

Figure 1.2: Photograph (credit GTC) of the GTC primary mirror M1. We can distinguish some of the 36 grey-appearing hexagonal segments. The red beams are carrying the M1 rotation platform. The grey ones are carrying the secondary mirror M2, visible by reflection on the right side of the primary mirror (M2 has the same shape as M1 but is about 10 times smaller). The black pipe in the center of the primary mirror is the final entrance of the light once successively reflected by M1 and M2.

1.3. The Gran Telescopio Canarias and adaptive optics LQG control: context and objectives

It was in the late 1980s that the idea of building a large telescope at the Spanish Observatory of Roque de los Muchachos was suggested. The trigger was pulled in 1995 when the Spanish authorities secured granting funds. One appealing criteria was the quest for an unprecedented optical quality, notably highlighted by the design of an AO system (Rodriguez-Espinosa and Alvarez, 1997). The site of el Roque de los Muchachos appeared as a promising place in terms of sky conditions to erect a 10-m telescope (Varela, Muñoz-Tuñón, and Gurtubai, 2001). It is located on the island of La Palma, part of the Canary Islands (Spain), at the top of mountains reaching over 2.3 kilometers of height. There, thanks to climate cells, the atmosphere is of excellent quality for astro-observations.

Figure 1.3: Map of Canary Islands location (Credit (Blázquez-Bermejo et al., 2020)). The island of La Palma (GTC host) is the most north-west. The island of Tenerife (where are the premises of the IAC) is the fourth from the left or from the right.

In 2004, the 36 segments of the primary mirror are received and three years later is happening the first light at the GTC (Sánchez-Martínez and F., 2008). Although the AO implementation was delayed, GTC found a large success with cutting edge scientific instruments such as OSIRIS (first scientific instrument, for high sensitivity spectroscopic observations, allowing for instance the study of exoplanets (Murgas et al., 2019), which is a hot topic nowadays), or HiPERCAM (high-speed optical imager (Dhillon et al., 2021)). For the last few years, the AO installation program has been reactivated, with the aim of extending the GTC high-technology instruments and high light flux towards a higher spatial resolution, as initially planned. The corresponding high-resolution new instrument is FRIDA, a diffraction-limited imager and integral-field spectrograph for the adaptive-optics focus (Watson et al., 2022).

The AO system for GTC, GTCAO, is now in the end of its test phase and will

Figure 1.4: Comparison of images taken by GTC (left, credit GTC) and by Hubble Space Telescope (right, credit HST) of the center of a galactic cluster. GTC discovers more new galaxies (bigger photon collection surface) but with poorer resolution (atmospheric turbulence does not affect space telescopes).

be soon shipped to La Palma and integrated on one of the GTC Nasmyth platforms.

My PhD targets the full design and test of an optimal LQG controller for the GTCAO system. Nowadays, an LQG regulator is not straightforward to set up. Some underlying modeling difficulties certainly play a major role in its underutilization on sky, while the recent hardware evolution facilitates its real-time implementation and is thus nowadays not the main obstacle. Besides the fact that it can significantly improve the performance with respect to an integrator, LQG control for GTCAO benefits from an existing module on the real-time computer DARC (A. Basden et al., 2010) (used for the full LQG on-sky experiments mentioned above) which happened to be the real-time computer chosen for GTCAO.

This manuscript presents the first exploration of modeling methods and calibration procedures for the LQG control of an AO system on a very large telescope, the latter having moreover a non-circular segmented pupil. Our work aim at providing well defined methodologies to model the disturbances and the AO system, including protocols that should ease the calibration of the system components. The whole methodology is validated on the GTCAO bench. The objective is to go towards an unsupervised LQG regulator that adapts to turbulence conditions evolution and that should work without the help of a control specialist, delivering therefore accessible high performance.

The PhD takes place in the frame of an international joint supervision between the Université Paris-Saclay and the Universidad de La Laguna in collaboration with the IAC, with main support of the Actions Doctorales Internationales (ADI) program funded by IDEX Paris-Saclay. Of course, the pandemic limited (or even stopped) access to Tenerife for quite a long period and caused changes in the realization of the GTCAO project. Nevertheless, I was lucky enough to be granted a 7-month extension that allowed me to continue my tests at IAC.

1.4 Manuscript organization

This PhD thesis manuscript is composed of eight chapters, starting with this introduction as chapter 1, ending with the Conclusion and perspectives in chapter 8.

The chapter 2 is dedicated to the description of astronomy pictures from the ground. An accent is set on the turbulence disturbance with its main statistic properties that we need in our work.

In chapter 3, we explain the principle of adaptive optics systems. These explanations go with the introduction of linear systems modeling which is necessary for the control. We focus on the description of some regulators used nowadays on operational telescopes, including the LQG controller.

The chapter 4 aims at giving a description of the impact of the AO systems delay and of the modeling thereof in high-performance control. The highlighted issue is tackled by defining an optimal controller thanks to exact temporal modeling of the DM and the WFS for the definition of LQG regulator. It is the occasion for showing the main drawback of the integrator and the strength of LQG control: the vibration mitigation.

In chapter 5, we describe the GTCAO system. We detail for each of its components a simple method to calibrate it, the fundamental parameters being supposedly known (e.g. interaction matrix, WFS pixel size...). The simple methods are thus applied to GTCAO, with in mind their applicability to other SCAO systems. This calibration is oriented towards the LQG control, which involves the linear modeling of the AO components presented in chapter 3.

Then, in chapter 6, the described modeling protocols are targeting the disturbances. It mainly consists in defining simple procedures to estimate the spatio-temporal disturbance priors we invoke in the LQG regulator definition. This chapter also aims at clarifying the state-space modeling of the complete disturbance. Some comments are made about the validity of the models when the disturbance statistics have evolved and about the switching aspects between two consecutive models.

Eventually, we show in chapter 7 the global performance reached with the LQG regulator implemented as proposed in the previous chapters. This chapter consists in describing first our performance criteria. Those criteria are used to study the respective GTCAO on-bench performance of the integrator and LQG controllers, in terms of scientific image quality and system behaviour. A short experimental comparison is also done with the widely used MMSE (Minimum Mean-Square Error) reconstructor. In the same chapter, a part of my PhD work is applied to data from the Keck telescope. Once the system is modeled following chapters 5 and 6, the performance is validated throughout replay tests with on-sky data of Keck's AO system.

Chapter 2
Image formation for ground-based telescopes

2.1 Introduction

This starting chapter explains the fundamental optical concepts and some characteristics of the turbulence and other disturbances such as windshake and vibration, helping for the understanding of the upcoming work of this manuscript. For a large part of the material presented here, details can be found in (Roddier, 1999).

The mirror diameters of the latest high-tech telescopes are hundreds of times larger than those of our amateur binoculars. The principles of image formation in section 2.2 allow us to understand why the resolution of the images becomes hundreds of times better. However, as mentioned in the introductory chapter, when observing the universe from the Earth's surface, our images are degraded by atmospheric turbulence, whose main parameters are described in section 2.3. These disturbances are often represented by the so-called Zernike basis described in section 2.4. This basis will be used throughout the manuscript to represent the disturbances. We will go on highlighting the other critical perturbations generated by the wind, which makes the telescope structures shake, or by the mechanical vibrations induced by some components. Finally, in section 2.6, we present the Strehl ratio (SR), the common metric that we have used to evaluate astronomical image quality.

2.2 Principle of image formation – Fourier optics

Point spread function

An optical system is in a standard way described by its point spread function (PSF). It is the impulse response of that system, or in other words the image obtained when observing a point-like object. For any object O (not necessarily point-like), the image I at the focus of the telescope can be described, for translation invariant optical systems, by a convolution: for each coordinate $x^{\text{im}}, y^{\text{im}}$ in the focal plane,

$$I\left(x^{\text{im}}, y^{\text{im}}\right) = \left(O * PSF\right)\left(x^{\text{im}}, y^{\text{im}}\right) . \tag{2.1}$$

With the acceptable hypothesis that the astrophysics objects are infinitely far (relatively to the size of the telescope pupil), the Fourier optics formula gives the PSF as the square modulus of the inverse Fourier transform $\mathcal{F}^{-1}$ of the telescope pupil:

$$PSF(x^{\text{im}}, y^{\text{im}}) = \left|\mathcal{F}^{-1}(\mathcal{P})(x^{\text{im}}, y^{\text{im}})\right|^2 , \tag{2.2}$$

with $(x^{\text{im}}, y^{\text{im}})$ the Cartesian coordinates in the image plane. Here $\mathcal{P}$ is the aperture function: the Fourier transform allows to switch between the image plane

and the pupil plane. For instance, in the classical case of a circular pupil (like a circular primary mirror without central obstruction) of diameter D_{pup}, noting $\rho^{\text{pup}} = \sqrt{x^{\text{pup}^2} + y^{\text{pup}^2}}$ (polar coordinates with $(x^{\text{pup}}, y^{\text{pup}})$ being the Cartesian coordinates in the pupil plane), we have

$$\mathcal{P}(\rho^{\text{pup}}) = \begin{cases} 1, & \text{if } \rho^{\text{pup}} \leq D_{\text{pup}}/2 \\ 0, & \text{else} \end{cases} , \tag{2.3}$$

and the PSF is the Airy disk with analytical expression

$$\text{Airy}(\theta) = \frac{\pi D_{\text{pup}}^2}{4\lambda^2} \left| \frac{2J_1\left(\pi D_{\text{pup}}\theta/\lambda\right)}{\pi D_{\text{pup}}\theta/\lambda} \right|^2 , \tag{2.4}$$

which depends on the wavelength λ. For the PSF, we often use as above the angle θ as coordinate rather than the position $\rho^{\text{im}} = \sqrt{x^{\text{im}^2} + y^{\text{im}^2}} = f\theta$, with f the focal distance of the optical system under consideration. The term J_1 is the Bessel function of the first kind, and this diffraction-limited PSF has a full width at half maximum (FWHM) of λ/D_{pup} radian.

Optical transfer function

The optical transfer function (OTF) of the optical system is defined as the Fourier transform of the PSF for each spatial frequency $\nu \triangleq \rho^{\text{pup}}/\lambda$:

$$OTF(\nu) = \mathcal{F}\left(PSF\right)(\nu) . \tag{2.5}$$

The PSF and the OTF are thus bijectively equivalent. The particularity is that the PSF gives directly the point image obtained with the optical system, while the OTF is detailing the spatial spectrum also called spectral transmissivity. We can then "close the loop" with the telescope pupil, stating the Wiener–Khintchine theorem: the OTF is the autocorrelation of the pupil function. Denoting the normalized spatial frequency by $\nu' = \nu/\nu_c = \nu\lambda/D_{\text{pup}}$, the calculation gives:

$$OTF(\nu') = \begin{cases} \frac{2}{\pi}\left(\arccos(\nu') - \nu'\sqrt{1-\nu'^2}\right), & \text{if } \nu \leq \nu_c \\ 0, & \text{else.} \end{cases} \tag{2.6}$$

This defines the so-called cut-off frequency ν_c of the optical system. The diffraction phenomenon written in equation (2.1) corresponds then, in terms of spectral content, to

$$\mathcal{F}(I)\left(\nu'\right) = \mathcal{F}(O)\left(\nu'\right) OTF(\nu') . \tag{2.7}$$

Object frequencies higher than ν_c are therefore cancelled out, meaning that the pupil is a low-pass filter. We retrieve a definition of the diffraction-limited resolution of the telescope $1/\nu_c = \lambda/D_{\text{pup}}$, that is to say the FWHM.

2.3 Atmospheric turbulence problem and parameters

In our study, we are in the case of disturbed images when the incident wavefront undergoes more perturbations than the inevitable pupil diffraction previously described.

2.3.1 Loss of coherence when crossing the atmosphere

Our atmosphere is not homogeneous. It is composed of multiple gas bubbles, moved by the wind, each having a different temperature and humidity. As a consequence, each has its own optical index $n(t, x^{\text{pup}}, y^{\text{pup}}, z)$ if located at $(x^{\text{pup}}, y^{\text{pup}}, z)$ at the instant t. This index can be linearly evaluated as done in the empirical law of Gladstone-Dale (Barrell and Sears, 1939):

$$n(t, x^{\text{pup}}, y^{\text{pup}}, z) = 1 + G^{\text{air}} \rho^{\text{air}}(t^{\text{pup}}, x^{\text{pup}}, y^{\text{pup}}, z)\,, \tag{2.8}$$

where ρ^{air} stands for the density and $G^{\text{air}} = 2.26 \times 10^{-4} \text{m}^3/\text{kg}$ denotes the Gladstone-Dale constant, almost independent from the wavelength. In this way, the light rays emitted from one same point in the space will be more or less slowed down depending on the atmospheric cells they go through before reaching the pupil. Their optical path is expressed with

$$\delta^{\text{OP}}(t, x^{\text{pup}}, y^{\text{pup}}) \triangleq \int_{h^{\text{tur}}}^{0} n(t, x^{\text{pup}}, y^{\text{pup}}, z) dz\,, \tag{2.9}$$

where h^{tur} is the altitude of the highest turbulence layer. The optical path when reaching the telescope pupil at $z = z^{\text{pup}} = 0$ depends on spatio-temporal coordinates $(t, x^{\text{pup}}, y^{\text{pup}})$. In other words, the temperature-dependent refraction index of the air will lead to different Descartes-described angle variations.

In our case of wave optics, we describe the full wavefront above the telescope pupil as the resulting dephasing

$$\phi(t, x^{\text{pup}}, y^{\text{pup}}) \triangleq \frac{2\pi}{\lambda}\, \delta^{\text{OP}}(t, x^{\text{pup}}, y^{\text{pup}}, z^{\text{pup}})\,, \tag{2.10}$$

so as to take into account the wavelength influence on the distorted images. This loss of coherence will deteriorate image formation (at pupil level $z = 0$). In Fourier optics with j the complex number, equation (2.2) is then replaced by

$$PSF(t, x^{\text{im}}, y^{\text{im}}) = \left| \mathcal{F}^{-1} \left(\exp\left(j\phi(t)\right) \mathcal{P} \right) (x^{\text{im}}, y^{\text{im}}) \right|^2\,, \tag{2.11}$$

computed from the pupil space 2-D function

$$(x^{\text{pup}}, y^{\text{pup}}) \mapsto \exp\left(j\phi(t, x^{\text{pup}}, y^{\text{pup}})\right) \mathcal{P}(x^{\text{pup}}, y^{\text{pup}})\,. \tag{2.12}$$

The two basic examples of distortion are:

- The 1-D case ($y^{\text{pup}} = 0$), where the deformed wavefront is still plane but simply inclined by an angle $\alpha(t)$. We have then

$$\phi^{\text{incl}}(t, x^{\text{pup}}) = \frac{2\pi}{\lambda} x^{\text{pup}}\, \alpha(t)\,, \tag{2.13}$$

  and the Fourier transform property tells us that the PSF we get with $\phi^{\text{incl}}(t)$ in equation (2.11) is therefore the same as the diffraction-limited one but shifted with an angle $\alpha(t)$ in the image plane (or with a distance $\alpha(t)f$). Since $\exp(a+b) = \exp(a)\exp(b)$, the same reasoning is applicable to a wavefront that is not plane anymore but whose spatial first order approximation is (2.13):

$$\phi(t, x^{\text{pup}}) = \phi^{\text{incl}}(t, x^{\text{pup}}) + \mathcal{O}(x^{\text{pup}^2})\,. \tag{2.14}$$

  The final image we get is the image distorted by the dephasing $\mathcal{O}(x^{\text{pup}^2})$ but shifted with an angle $\alpha(t)$.

- The piston case, defined as

$$\phi(t, x^{\text{pup}}, y^{\text{pup}}, z^{\text{pup}}) = \phi^{\text{pist}}(t)\,, \tag{2.15}$$

  the same over the full pupil. The value $\exp(j\phi(t))$, which is now scalar, can then get out of the Fourier transform in equation (2.11), and its unitary modulus has no impact on the PSF value.

2.3.2 Definition of the main turbulence characteristics

The spatial and temporal characteristics of the turbulence are described through its spatio-temporal statistics. These are essential part of the construction of our stochastic models for control.

Fried parameter r_0

The Fried parameter r_0 (Fried, 1966) represents the characteristic coherence size of the wavefront: the bigger r_0, the better the image quality. It can also be interpreted as the maximal length which limits the dephasing to a pure tip-tilt, as in equation (2.13). The parameter r_0 is typically of 10 cm at the default wavelength of 500 nm (T. Fusco et al., 2004; Osborn et al., 2018). It depends notably on the wavelength at power $6/5 = 1.2$ in its analytical formula

$$r_0 = \left[0.42 \left(\frac{2\pi}{\lambda}\right)^2 \sin(\gamma)^{-1} \int_0^\infty C_n^2(z')dz'\right]^{-\frac{3}{5}}\,, \tag{2.16}$$

where γ is the elevation angle. This gives the relation between the r_0 values at two different wavelengths λ_1 and λ_2:

$$r_0(\lambda_1) = r_0(\lambda_2) \left(\frac{\lambda_1}{\lambda_2}\right)^{6/5}\,. \tag{2.17}$$

From equation (2.16), we can see that $r_0 \propto \sin(\gamma)^{\frac{3}{5}}$, so that the best elevation for observations is at the zenith ($\gamma = 90\,\text{deg}$). The integrated term $C_n^2(z)$ is the refractive index structure parameter, or simply the turbulence strength parameter. It provides a statistical measure of the strength of atmospheric turbulence, representing the spatial variations of the refractive index in the atmosphere as a function of altitude z. A usual approximation is to partition the atmosphere into several discrete layers ($\int_0^\infty C_n^2(z')dz' = \sum_{i=1}^{N_{\text{layer}}} C_n^2(i)$, Taylor hypothesis (Taylor, 1938)) and estimate their respective energy (with dedicated instrument e.g. (Vernin and Munoz-Tunon, 1992)). Indeed the atmospheric temperature mixing occurs mainly:

- close to the ground (0 to 40 m)
- at the inversion layer (1 to 2 km)
- at the jet-stream level (8 to 12 km)

with the main part for the ground layer.

Wind speed V_0

A second key variable to describe the atmosphere is the wind speed average V_0. With the well accepted Taylor approximation, each layer k of the atmosphere is animated by its proper wind speed V_k into a translation motion. It corresponds to a horizontal translation of its proper air cells. In the end, the value of V_0 is obtained as the energy-weighted average of the wind speed of all layers:

$$V_0 = \left(\frac{\sum_{i=1}^{N_{\text{layer}}} C_n^2(i) V_i^{5/3}}{\sum_{i=1}^{N_{\text{layer}}} C_n^2(i)} \right)^{\frac{3}{5}} . \tag{2.18}$$

A typical value is of $10\,\text{m}\,\text{s}^{-1}$ (T. Fusco et al., 2004; J. Osborn et al., 2016).

Temporal coherence τ_0

The third variable to describe the atmosphere, based on the two previous ones, is the resulting characteristic coherence time of the wavefront,

$$\tau_0 = 0.31 \frac{r_0}{V_0} . \tag{2.19}$$

For the previous numerical values ($r_0 = 10\,\text{cm}$ and $V_0 = 10\,\text{m}\,\text{s}^{-1}$), this gives a value of 3 ms similar to on-sky measures (Osborn et al., 2018). Thus, the atmospheric optics is a severely non-stationary phenomenon. When taking images through the atmosphere, the distortion will affect the PSF differently according to the exposure time T_{exp} of the camera:

- If $T_{\text{exp}} < \tau_0$, the PSF will consist of several randomly distributed speckles of characteristic size λ / D_{pup} radians (diffraction limited) spreading with a characteristic size of λ / r_0 radians.

- If $T_{\text{exp}} >> \tau_0$, the PSF will be the sum of many independent spreads of the speckles described above, whose accumulation will lead to a 2-D Gaussian image of FWHM close to λ/r_0 radians.

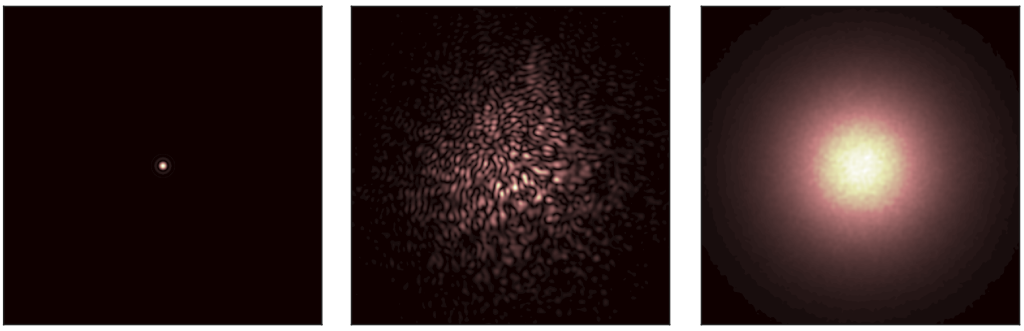

Figure 2.1: (simulation) PSF obtained in diffraction limited case (left), in presence of turbulence with a short exposure time $T_{\text{exp}} < \tau_0$ (middle), and in presence of turbulence with a long exposure time $T_{\text{exp}} \simeq 500\tau_0$). Fried parameter at $r_0(\lambda = 500\,\text{nm}) = 10\,\text{cm}$, telescope diameter 11.35 m (as is GTC), imaging camera in H-band 1600 nm.

In the end, the resolution boundary in turbulent conditions, called seeing, is evaluated with the formula (Tatarski, Silverman, and Chako, 1961):

$$\alpha^{\text{tur}} = 0.975\lambda/r0\,, \tag{2.20}$$

and with equation (2.17), we see that $\alpha^{\text{tur}} \propto \lambda^{\frac{-1}{5}}$. It is a big issue in visible-infrared spectrum (reaching one arcsecond), but negligible for radio waves telescope.

Outer scale parameter L_0

The outer scale parameter L_0 refers to the characteristic length scale over which the refractive index fluctuations are uncorrelated. As a consequence, the low spatial orders of the turbulence will have less energy when L_0 decreases.

Power spectral density

Kolmogorov formalized a model to describe spectrally the atmospheric turbulence energy (Kolmogorov, 1941). It is involved in our work since describing the power spectral density (PSD) $W(k,i)$ (k in m^{-1}, i-th layer of atmosphere) of the phase disturbance:

$$W_\phi^{\text{Kol}}(k,i)\,(f_s,h) \simeq 0.033\,(2\pi)^{-\frac{2}{3}} C_n^2(i) k^{-\frac{11}{3}}\,. \tag{2.21}$$

Von Kármán extended this model to take notably the outer scale L_0 into account (Kármán, 1948):

$$W_\phi^{\text{Kar}}\,(k,i) \simeq 0.033\,(2\pi)^{-\frac{2}{3}} C_n^2(i) \left(\frac{1}{L_0^2} + k^2\right)^{-\frac{11}{6}}\,, \tag{2.22}$$

which is the model used in our work for all theoretical PSD calculations. When L_0 tends to infinity, we retrieve the Kolmogorov model.

2.4 Wavefront description: the Zernike base

In this section, we define the Zernike modes (Zernike, 1934) and their usage in the description of atmospheric disturbance statistics.

2.4.1 Zernike polynomials

The Zernike basis is an orthonormal basis of polynomials defined on a circular support in polar coordinates. The j-th polynomial is defined, $\forall \rho \in [0,1]$ and $\forall \theta \in [0, 2\pi]$, by:

$$Z_j(\rho,\theta) = \begin{cases} \sqrt{j_{\text{rad}}+1} R_{j_{\text{rad}}}^{j_{\text{azi}}}(\rho)\sqrt{2}\cos(j_{\text{azi}}\theta) & \text{for } j_{\text{azi}} \neq 0 \text{ and } j \text{ even} , \\ \sqrt{j_{\text{rad}}+1} R_{j_{\text{rad}}}^{j_{\text{azi}}}(\rho)\sqrt{2}\sin(j_{\text{azi}}\theta) & \text{for } j_{\text{azi}} \neq 0 \text{ and } j \text{ odd} , \\ \sqrt{j_{\text{rad}}+1} R_{j_{\text{rad}}}^{j_{\text{azi}}}(\rho)\sqrt{2} & \text{for } j_{\text{azi}} = 0 , \end{cases} \tag{2.23}$$

j_{rad} being the radial order and j_{azi} the azimuthal order. The indexes j, j_{rad} and j_{azi} are defined by Noll (Noll, 1976), and the function $R_{j_{\text{rad}}}^{j_{\text{azi}}}$ is expressed by:

$$R_{j_{\text{rad}}}^{j_{\text{azi}}}(\rho) = \sum_{k=0}^{j_{\text{rad}}-j_{\text{azi}}+2} \frac{(-1)^k (j_{\text{rad}}-k)!}{k!(\frac{j_{\text{rad}}+j_{\text{azi}}}{2}-k)!(\frac{j_{\text{rad}}+j_{\text{azi}}}{2}+k)!} \rho^{j_{\text{rad}}-2k} . \tag{2.24}$$

The first polynomials are shown in figure 2.2. A phase defined on a Zernike basis is decomposed in the form

$$\phi(\rho,\theta) = \sum_{j=0}^{+\infty} a_j Z_j(\frac{2\rho}{D},\theta) , \tag{2.25}$$

with $\rho \in [0, D/2]$. In this equation, a_j is the coefficient of the j-th Zernike polynomial Z_j.

The turbulence energy is concentrated in the first Zernike modes. For the models, this motivates the use of a phase vector on a limited basis, of dimension n_{modes}, where the piston is removed since not sensed by the WFS and without impact on the PSF:

$$\phi^{\text{Zer}} = \begin{pmatrix} a_1 \\ a_2 \\ \vdots \\ a_{n_{\text{modes}}} \end{pmatrix} . \tag{2.26}$$

The phase variance (in rad^2) is the norm of this vector:

$$\sigma_\phi^2(t) = \sum_{j=1}^{\infty} a_j(t)^2 . \tag{2.27}$$

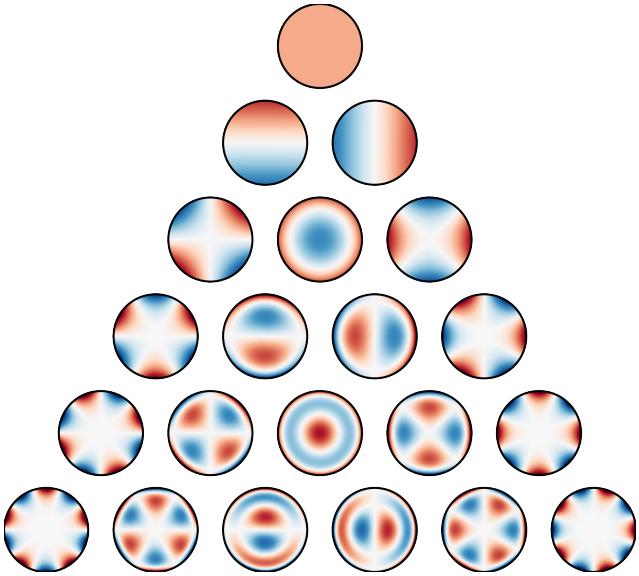

Figure 2.2: 2-D representation of the first 9 Zernike modes. Top to bottom: radial order i_{rad} 0 to 5. Left to right: the $(i_{\text{rad}}+1)$ azimuthal orders. Credit: Nschloe.

If the radial order is n_{rad}, the total number of Zernike modes is given by:

$$n_{\text{modes}} = \frac{n_{\text{rad}}(n_{\text{rad}}+3)}{2}\,. \tag{2.28}$$

The total number of modes considered for the phase decomposition depends on the spatial resolution we want to achieve.

2.4.2 Spatio-temporal statistics of atmospheric disturbances in Zernike base

2.4.2.1 Modal energy distribution

Once expressed in the Zernike base, we can compute the covariance matrix Σ_ϕ of atmospheric phase disturbance (Noll, 1976) for each couple of mode (i,j) whose radial order are $(i_{\text{rad}}, j_{\text{rad}})$ and azimuthal order are $(i_{\text{azi}}, j_{\text{azi}})$:

$$\begin{aligned}\Sigma_\phi(i,j) &\triangleq \text{Cov}\left(a_i, a_j\right)\\ &= 3.90\sqrt{(i_{\text{rad}}+1)\left(j_{\text{rad}}+1\right)}(-1)^{(i_{\text{rad}}+j_{\text{rad}}-2i_{\text{azi}})/2}\delta_{i_{\text{azi}},j_{\text{azi}}}\left(\frac{D_{\text{pup}}}{r_0}\right)^{5/3}\\ &\times \frac{2^{-14/3}\Gamma\left(\frac{i_{\text{rad}}+j_{\text{rad}}-5/3}{2}\right)}{\Gamma\left(\frac{-i_{\text{rad}}+j_{\text{rad}}+17/3}{2}\right)\Gamma\left(\frac{i_{\text{rad}}-j_{\text{rad}}+17/3}{2}\right)\Gamma\left(\frac{i_{\text{rad}}+j_{\text{rad}}+23/3}{2}\right)}\,.\end{aligned} \tag{2.29}$$

This is derived from the Kolmogorov statistical description of the turbulence (Kolmogorov, 1941). The non-diagonal shape of this matrix means that modes are correlated. The diagonal term $\Sigma_\phi(i,i)$ gives access to the expected energy as the spatial variance stemming from the mode i. It corresponds to the temporal variance of the i-th Zernike coefficient:

$$\Sigma_\phi(i,i) =< a_i^2 >= \lim_{T\to\infty} \frac{1}{T}\int_0^T a_i(t)^2 dt\,, \tag{2.30}$$

and thus the trace of Σ_ϕ is giving the global wavefront expected variance (Noll, 1976)

$$\sigma_\phi^2 = \frac{1}{S_{\text{pup}}}\int_{S_{\text{pup}}} \left\langle \phi^2(\rho)\right\rangle \mathrm{d}\rho = \sum_{i=1}^{\infty} < a_i^2 > \ . \tag{2.31}$$

To account for the outer scale L_0, an adjustment based on Von Kármán spatial statistics (2.22) is made (Chassat, 1992) by applying a coefficient $\eta(i)\eta(j)$ to each $\Sigma_\phi(i,j)$, where η is defined by:

$$\begin{cases} \eta(i) \approx 1 - 0.77\left(\frac{2\pi D_{\text{pup}}}{L_0}\right)^{1/3} + 0.09\left(\frac{2\pi D_{\text{pup}}}{L_0}\right)^{2} - 0.054\left(\frac{2\pi D_{\text{pup}}}{L_0}\right)^{7/3} & \text{if } i_{\text{rad}} = 1, \\ \eta(i) \approx 1 - 0.039\left(\frac{2\pi D_{\text{pup}}}{L_0}\right)^{2} + 0.027\left(\frac{2\pi D_{\text{pup}}}{L_0}\right)^{7/3} & \text{if } i_{\text{rad}} = 2, \\ \eta(i) \approx 1 - \frac{1}{(i_{\text{rad}}-11/6)(i_{\text{rad}}+23/6)}\left(\frac{2\pi D_{\text{pup}}}{L_0}\right)^{2} & \text{if } i_{\text{rad}} \geq 3\,. \end{cases} \tag{2.32}$$

It was also shown that the variances are well approximated by an asymptotic dependence on the radial order when the latter is large enough (R. Conan, 2008):

$$\sigma^2_{i_{\text{rad}}} \approx 0.7632\,(i_{\text{rad}}+1)^{-11/3}\left(\frac{D_{\text{pup}}}{r_0}\right)^{5/3}\ . \tag{2.33}$$

If n_{rad} Zernike modes are corrected, the atmospheric turbulence energy left over is then equal to (R. Conan, 2008):

$$\sigma^2_{\text{left}} = 0.458\,(n_{\text{rad}}+1)^{-5/3}\left(\frac{D_{\text{pup}}}{r_0}\right)^{5/3}\ . \tag{2.34}$$

2.4.2.2 Temporal spectral distribution

With the Taylor hypothesis where each discrete turbulence layer is supposed to evolve as a frozen screen that translates at the wind speed, the previous spatial study can be converted into temporal spectrum with the basic fact that the changes between two Δx-separated points will be the same as the changes between two $\Delta t = \Delta x/V_0$-separated instants (J.-M. Conan, Gérard Rousset, and Madec, 1995; Le Roux et al., 2004). The PSDs of Zernike coefficients (example in figure 2.4) exhibit the two following noteworthy properties:

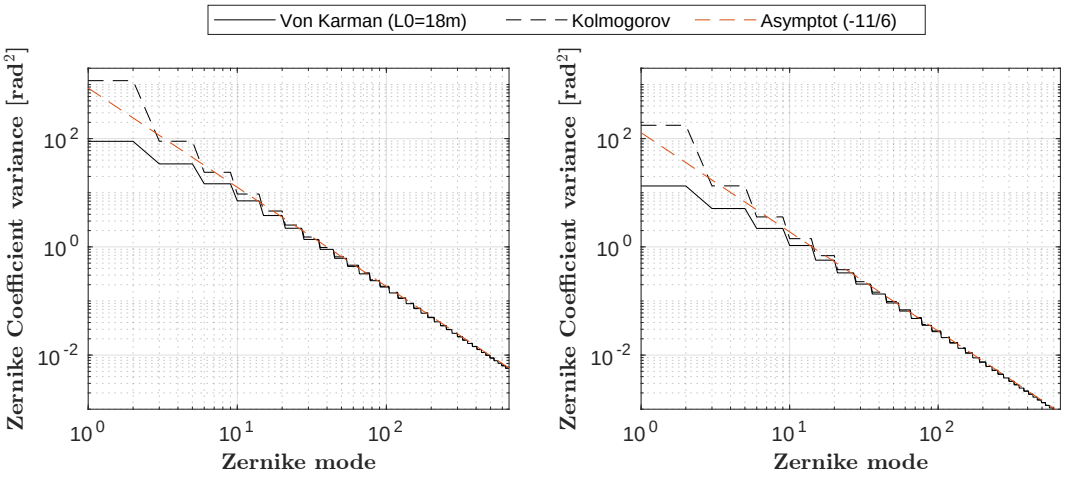

Figure 2.3: Theoretical modal energy with respect to the Zernike mode number for a telescope diameter of 11.35 m (as is GTC). Left: $r_0 = 8$ cm. Right: $r_0 = 25$ cm. The modes of a same radial order have the same energy (steps). Von Kármán statistics are limiting the low orders energy according to L_0/D_{pup} ratio. A factor α applied to r_0 leads to a vertical shift of $\alpha^{5/3}$ (close to ~ 15 on this graph).

- Cut-off frequencies located at $F_{\text{cut}} = 0.3\,(n_{\text{rad}}+1)(V_0/D_{\text{pup}})$ (frequency at the break of slope of the curves)
- Beyond the cut-off frequency, an exponential decrease with a logarithmic slope of $-17/3$

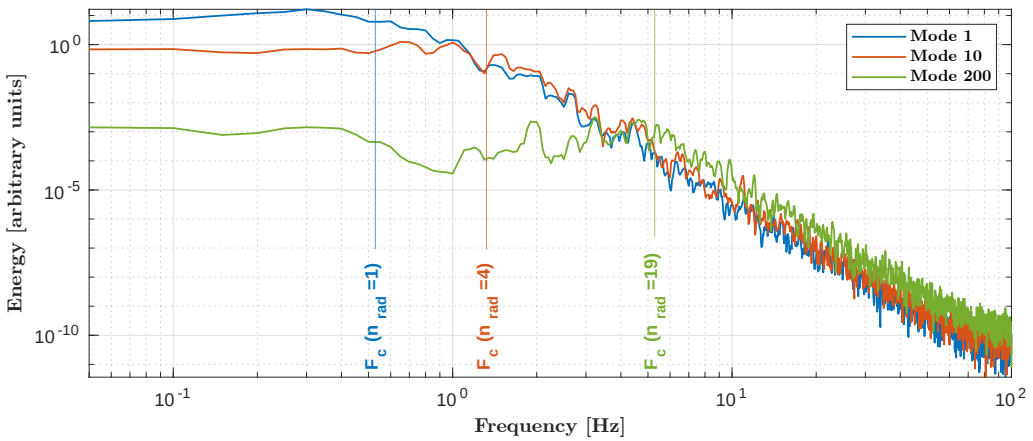

Figure 2.4: PSD of the turbulence of three Zernike modes (OOMAO simulation with $L_0 = 20$ m and $V_0 = 10\,\text{m}\,\text{s}^{-1}$).

Eigenmode description	Eigenfrequency [Hz]
Lateral mount bending	5.14
Front bending of the tube around its axis	9.33
Front bending of the mount	12.26
Torque of the mount	13.23
Vertical bending of the rotating floor	14.88
Local torque of the Nasmyth platforms	15.94

Table 2.1: List of some of the GTC mechanical eigenmodes. Credit: extracted from a table of (Pan et al., 2000).

2.5 Windshake and vibration

Windshake and vibration can originate from various sources, such as wind blowing on the structure of the telescope or components like fans, cooling pumps... The resulting mechanical displacements have a direct repercussion on the wavefront distortion and are likely to significantly impact the quality of the scientific images (Kulcsár, H. F. Raynaud, et al., 2012).

The Zernike modes are a good support to describe the effects of these non-atmospheric disturbances on the wavefront. With the growth in complexity of large telescopes architectures, the number of modes to be affected is likely to go beyond the three standard modes of tip, tilt and defocus. However, mechanical vibration affecting the telescope structure will probably concern the low temporal frequencies. An example of some of the GTC mechanical eigenmodes together with their resonance frequency are given in table 2.1. With the induced motions, the same frequencies will appear in the PSDs of the first optical modes. A typical root-mean-square (RMS) of the tip and tilt vibrations for instance is $\sigma_{\text{vib}} = 5$ to 100 mas (Kulcsár, Sivo, et al., 2012), which is the same order of magnitude as the Airy disk of telescopes observing in the visible-infrared wavelengths. Some disturbances other than those structure-induced can reach similar energies, with potentially much higher temporal frequencies (e.g figure 7.21 in chapter 7). Vibration mitigation on telescopes is therefore crucial for obtaining the diffraction-limited astronomical images.

2.6 Image quality evaluation – Strehl ratio

When developing a high-resolution optical system it is of utmost importance to set a quality criterion. In the case of scientific images, the standard one is the Strehl ratio. It is defined as the ratio of the intensity peak of the actual PSF over the intensity peak of an ideal diffraction-limited PSF, reaching the best possible value of 1 in case

of an indeed diffraction-limited PSF. For a centered PSF, it is written as:

$$SR \triangleq \frac{\max(PSF)}{\max(PSF_{\text{diffr}})} = \frac{\sum OTF}{\sum OTF\text{diffr}}\,, \tag{2.35}$$

with thus the possibility of using the OTF instead of the PSF. The Strehl ratio can be approximated from the phase variance σ_ϕ^2, so without the need of a scientific image, using the approximation proposed in (Mahajan, 1983) as:

$$SR \approx \exp(-\sigma_\phi^2)\,, \tag{2.36}$$

valid for SR values typically higher than 0.3. Using this formula, the SR scales from one wavelength λ_1 to another one λ_2 by the simple rule

$$SR_{\lambda_2} \approx SR_{\lambda_1}^{(\lambda_1/\lambda_2)^2}\,.$$

We saw in figure 2.3 that the simple tip and tilt turbulence-induced dephasing modes could easily reach $20\,\text{rad}^2$ in visible wavelength, a regime where equation (2.36) is not valid.

2.7 Conclusion

We have seen the dramatic impact the atmosphere has on image resolution for the ground-based telescopes. With a very short overview, we have described the disturbances with some spatial and temporal parameters. These are well described in the Zernike basis, which will be also used to express the mechanical-related vibration perturbations. Performance assessment through image quality will be evaluated in a standard way with the Strehl ratio, and the Mahajan approximation (Mahajan, 1983) will also be used when appropriate.

Adaptive optics systems are used to achieve the full resolution possible in the diffraction limit. Their principle and operation, together with their main components and their standard servoing, are discussed in the following chapter.

Chapter 3
Adaptive optics principle and standard controllers

3.1 Introduction

We have seen in chapter 2 how the atmospheric turbulence and some mechanical motions affect the visible/infrared wavefronts and the impact on images. This is well described in the Zernike base, including some spatio-temporal behaviors. We are extremely far from achieving the full possible resolution without the use of an adaptive optics system. The principle of adaptive optics, along with its key components, will be detailed in the following sections. The components will be modeled linearly, and the delays of the different stages of the servo loop will be specified. Some standard regulators will also be presented in the last section.

3.2 Adaptive optics principle and system modeling

Adaptive optics (AO) systems aim at restoring the wavefront to its aberration-free pre-atmospheric shape, in real time, by interposing a deformable mirror (DM) on the optical path. The DM shape correction is managed with a servo control. We will focus in this manuscript on single conjugated AO (SCAO) systems, featuring a single DM and a single wavefront sensor (WFS), the latter measuring the residual wavefront deformation after correction by the DM.

3.2.1 Components

3.2.1.1 Wavefront sensor

With our current technologies, it is impossible to detect the temporal oscillations of the electromagnetic fields in the infrared ($\nu > c/\lambda_{\mathrm{IR}} > 10^{-14}\,\mathrm{Hz}$), making their dephasing not directly measurable. We are thus exploiting their energy variations, encoding the dephasing into an intensity modulation. The WFS used in GTCAO system is a Shack-Hartmann wavefront sensor. Its principle is represented in figure 3.2. It is made of a 2-D grid of $n_{\mathrm{SA}} \times n_{\mathrm{SA}}$ micro-lenses. Each micro-lense focuses the beam corresponding to its surface on the CCD plane of the WFS camera, producing a spot corresponding to the PSF. The position of the center of the spot is in the first approximation linearly related to the local slope of the wavefront as detailed below. A Shack-Hartmann with n_{SA} linear subapertures must have a maximum subaperture size $d_{\mathrm{SA}} = D_{\mathrm{pup}}/n_{\mathrm{SA}}$ of around r_0 –at scientific wavelength– to be able to measure the wavefront with limited error in the first order approximation. This is why many AO systems feature a subaperture size of around $d_{\mathrm{SA}} = 50\,\mathrm{cm}$ (GTC, Keck, William Herschel...).

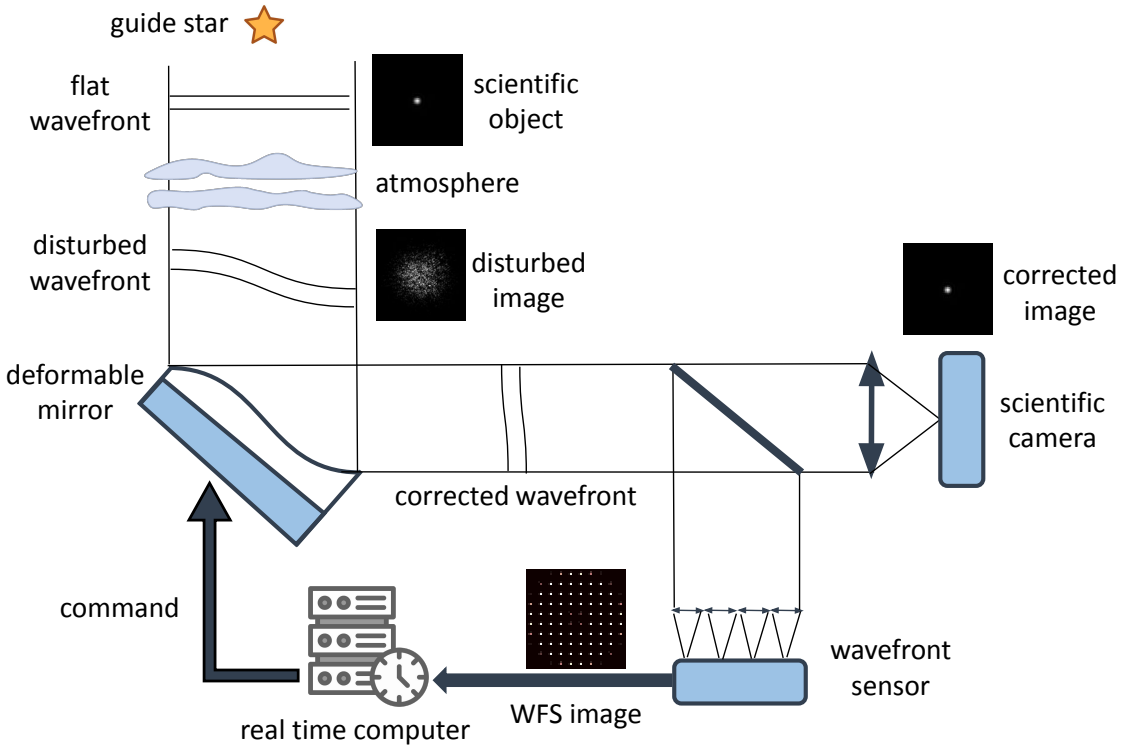

Figure 3.1: Adaptive optics principle for a SCAO system. The illustrated WFS is of Shack-Hartmann type. A bright enough guide star is needed to allow for measurements.

The WFS camera integrates images over each sampling period T_s with values typically ranging from 1 ms to 10 ms. It defines the sampling frequency of the AO loop, $F_\mathrm{s} = 1/T_\mathrm{s}$. If I is the 2-D intensity map of one sub-aperture, the center of gravity $(c_\mathrm{horiz}, c_\mathrm{verti})$, or centroid of the spot, is estimated by:

$$c_\mathrm{horiz} = \frac{\sum\limits_{\substack{1\leq i\leq n_\mathrm{px}\\1\leq j\leq n_\mathrm{px}}} I(i,j)i}{\sum\limits_{\substack{1\leq i\leq n_\mathrm{px}\\1\leq j\leq n_\mathrm{px}}} I(i,j)}, \qquad c_\mathrm{verti} = \frac{\sum\limits_{\substack{1\leq i\leq n_\mathrm{px}\\1\leq j\leq n_\mathrm{px}}} I(i,j)j}{\sum\limits_{\substack{1\leq i\leq n_\mathrm{px}\\1\leq j\leq n_\mathrm{px}}} I(i,j)}, \tag{3.1}$$

where n_px is the number of linear pixels in each subaperture. Some algorithms are better at estimating the centroids positions (A. G. Basden et al., 2016), notably by relying on a fixed number of the most illuminated pixels (instead of a threshold leading to a variable number of selected pixels). The local slope of the incident wavefront is deduced from the Gauss optics geometrical formula $\alpha = (c_\mathrm{horiz}, c_\mathrm{verti})/f$,

assuming that the spots stay close to their optical axis, f being the focal length of the WFS microlenses. Once we have α, the corresponding dephasing ϕ can be computed using the basic formula (2.13). Note that the piston is not sensed by the Shack-Hartmann WFS since it induces no displacement of the spot.

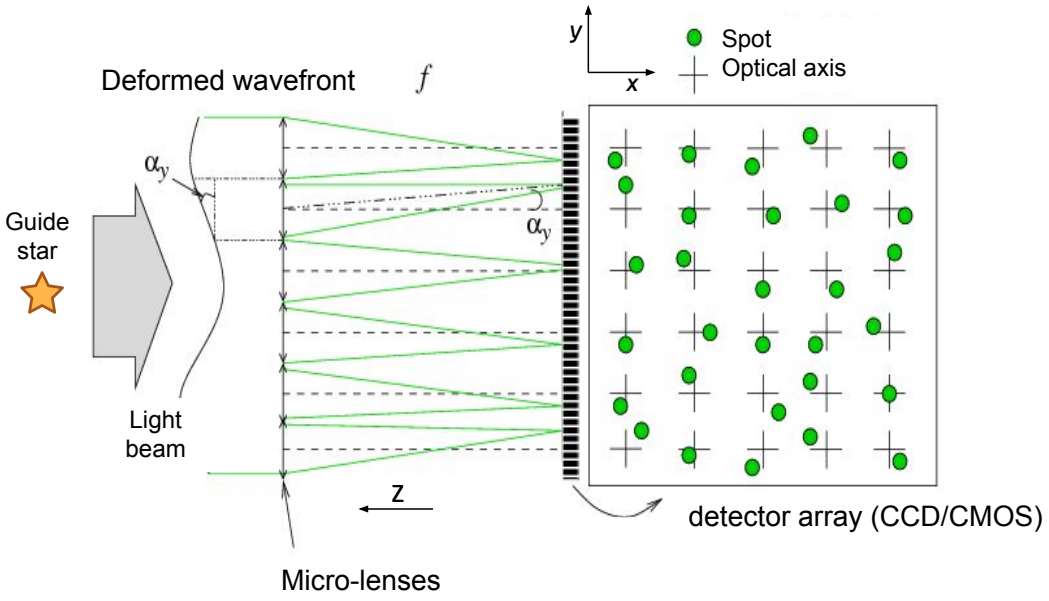

Figure 3.2: Shack-Hartmann wavefront sensor principle. The flux comes from a bright enough guide star (along the z axis). The distorted wavefront above one of the WFS subapertures has a slope α_y. The vertical displacement of the image spot on the CCD camera will then be $\alpha_y f$.

The vector gathering all the measurement is noted y, containing $n_y \approx 2 \times n_{\text{SA}}^2$ values. Some unilluminated subapertures are discarded, notably those in the four corners and those in the telescope pupil obscuration. The unit of y is generally the pixel (WFS CCD pixel). The WFS linear measurement operator is denoted by D, which is a gradient matrix that computes the slope between the opposite sides of the subapertures as shown in figure 3.3. It depends on the WFS CCD pixel size and on the wavelength at which ϕ is given. With D, the measurement can be written

$$y = D\overline{\phi} + w\,. \tag{3.2}$$

The measurement noise w is assumed to be white, zero-mean and Gaussian. The delay of one frame due to the integration time of the WFS camera (see chronogram in figure 3.5) allows us to complete equation (2.24) by taking into account the temporal occurrences to obtain

$$y_k = D\overline{\phi}_{k-1} + w_k\,, \tag{3.3}$$

where

$$\overline{\phi}_k \triangleq \frac{1}{T_{\text{s}}} \int_{(k-1)T_{\text{s}}}^{kT_{\text{s}}} \phi(t)dt\,. \tag{3.4}$$

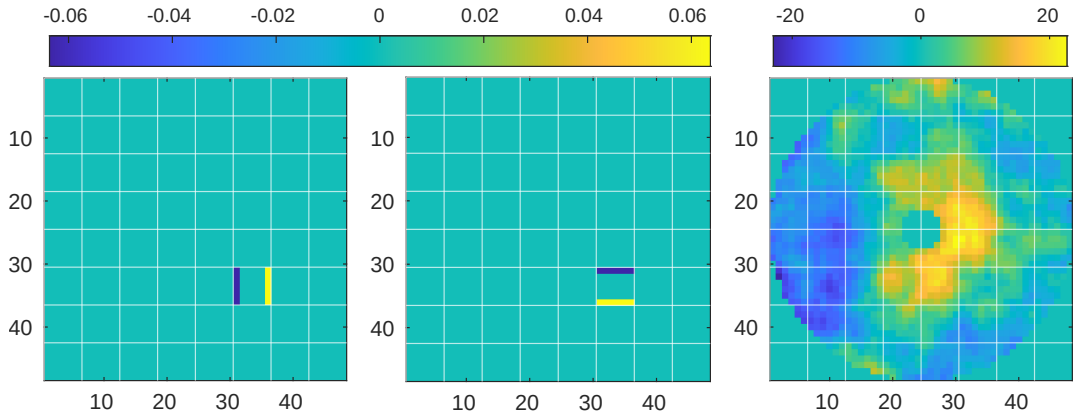

Figure 3.3: Representation in pupil plane of the measurement matrix D of one subaperture. Left and middle: horizontal and vertical gradient vectors (each reshaped in the 2D pupil plane, unit px/rad). Right: wavefront, unit rad (OOMAO simulation). The white grid represents the microlenses grid of the WFS. The three subapertures in each corner are invalid (illumination surface lower than 50% due to pupil obscuration).

The measurement noise w has two main sources. Denoting by $n_{\text{pixel}} \leq n_{\text{px}}^2$ the number of pixels actually used to estimate each centroid in equation (3.1), the sources are:

- The photon noise, whose repercussion on the WFS slopes error variance is given by (G. Rousset, Primot, and Fontanella, 1987):

$$\sigma^2_{\text{photon}} = \frac{\pi^2}{2n_{\text{photon}}} \left(\frac{X_T}{X_D}\right)^2 \tag{3.5}$$

  in rad^2, defined as the variance of the phase difference between the subaperture edges, where n_{photon} is the total number of photons received by the n_{pixel} involved pixels during one frame. The FWHM of the subaperture image is $X_T \approx \lambda/r_0$ while $X_D \approx \lambda/d_{\text{SA}}$ is its size in diffraction-limited case.

- The read-out noise, depending on the electronic noise of the CCD σ_e (in electrons per pixel per frame), whose repercussion on the WFS slopes error variance is given by (G. Rousset, Primot, and Fontanella, 1987; Roddier, 1999):

$$\sigma^2_{\text{RON}} = \frac{\pi^2}{3} \left(\frac{\frac{\sigma_e}{G} n_{\text{pixel}}}{n_{\text{photon}} X_D}\right)^2, \tag{3.6}$$

  again defined as the variance (in rad^2) of phase difference between two subaperture edges. Here G is the gain in CCD electron per photoelectron (generally around 10^3).

As the two noise sources are independent, we conclude that

$$\sigma_w^2 = \sigma_{\text{photon}}^2 + \sigma_{\text{RON}}^2 \,.$$

The photon quantity represents a limitation for the Shack-Hartmann WFS when we know that many astrophysical targets are not located right next to a bright enough guide star. To remedy these too low signal-to-noise ratio situations, it is then necessary to increase the WFS integration time T_s. This increase has an impact on the temporal delay, which is usually in the order of $\tau \sim 2T_\text{s}$. It has a cost in the temporal error variance. An evaluation of this temporal error, induced by a pure delay of τ, is given in (Roddier, 1999) and depends on τ_0:

$$\sigma_{\text{tempo}}^2 = (\tau/\tau_0)^{5/3} \,. \tag{3.7}$$

It corresponds to the residual wavefront phase variance left when applying a perfect correction $\phi^{\text{cor}}(t)$ at delayed time $\phi^{\text{cor}}(t+\tau)$. The decorrelation time τ_0 was defined by equation (2.19) in chapter 2. Another source of error in the measurement is the spatial sampling set by the WFS subapertures, which prevents from measuring all the wavefront distortions. Notably, the spatial frequencies higher than the Shannon limit $\frac{1}{2d_{\text{SA}}}$ are not measured. The impact on the final residual dephasing variance of the AO system is approximated by the aliasing term (E. Gendron and G. Rousset, 2012):

$$\sigma_{\text{alias}}^2 = 0.07 \left(\frac{d_{\text{SA}}}{r_0} \right)^{5/3} \,. \tag{3.8}$$

The propagation of aliasing in the loop depends on the controller, as shown in (Juvénal et al., 2018).

3.2.1.2 Deformable mirror

A deformable mirror is typically made of a thin, flat reflective surface that is coated with a layer of reflective material such as aluminum (Madec, 2012). The mirror's surface is then divided into a grid of actuators. Actuators are located under the surface and can push or pull on the mirror membrane, to modify the mirror's surface shape. We assume here that the DM has a linear response. For each actuator, the influence function IF is defined as the continuous profile taken by the membrane when a unitary command is applied. The coupling C_{DM} is then the DM surface deformation above the nearest neighbour actuator. The dephasing (or phase) ϕ^{cor} generated by the DM when a control vector u is applied to the n_u actuators is thus:

$$\phi^{\text{cor}} = \sum_{i=1}^{n_u} u(i) IF(i) \,. \tag{3.9}$$

When the influence functions are concatenated as column vectors in a matrix denoted here by N and called influence functions matrix, the correction phase can be expressed as

$$\phi^{\text{cor}} = Nu \tag{3.10}$$

for any vector u. Typical units are volts for u, and thus radians per volt for N, but any other unit is possible if consistent with the unit of the dephasing.

This equation (3.10) assumes that u remains in the linearity range of the actuators, which is generally considered to be the case in astronomy. However, there is always a clipping (saturation) value u_{clip} such that $|u| < u_{\text{clip}}$, imposed by the electronics stage. Generally, the actuators are located at each corner of the WFS microlenses grid. It is the Fried geometry, in which case the linear number of actuators is $n_{\text{act}} = n_{\text{SA}} + 1$. It is the place where their effect on the DM membrane is the most visible by the WFS, as illustrated in figure 3.4. Had an actuator been in the center of a subaperture, the gradient would have been close to zero regardless of the voltage applied to that actuator: seen from the WFS, the wavefront would appear flat in that subaperture.

The finite number of actuators and their coupling set a limit to the spatial frequencies the DM can generate, producing a fitting error. Its variance is approximated by (Roddier, 1999; Hardy and Thompson, 1998)

$$\sigma^2_{\text{fit}} \simeq 0.2 \left(\frac{\text{pitch}}{r_0} \right)^{5/3}, \tag{3.11}$$

where the pitch corresponds to the distance between two actuators in the telescope pupil. The coefficient of 0.2 depends on the DM influence functions (chapter 9 of (Hardy and Thompson, 1998), table 9.3).

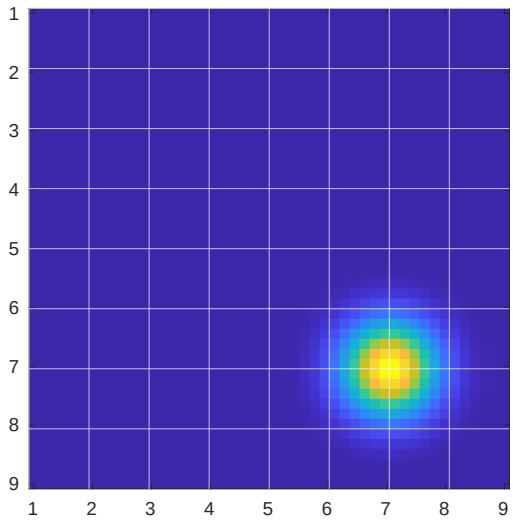

Figure 3.4: (OOMAO simulation) Representation in the pupil plane of an influence function of one actuator with a coupling factor of $C_{\text{DM}} = 0.18$. White lines represent the microlenses grid of the WFS. This actuator is in Fried geometry at a corner of the WFS subaperture grid.

3.3 Adaptive optics standard regulators

3.3.1 Chronogram and AO loop block-diagram

The chronogram of the AO loop with a delay of 2 frames ($2T_s$) is given in figure 3.5, where the measurement delay corresponds to the integration of the phase over one frame T_s (equation (3.3)). All the other operations (WFS camera read-out, slopes and commands computations, data transfers, DM membrane reshaping) are supposed to take one additional frame. The case of a non-integer loop delay will be detailed later in chapter 4. The block diagram corresponding to the chronogram of figure 3.5

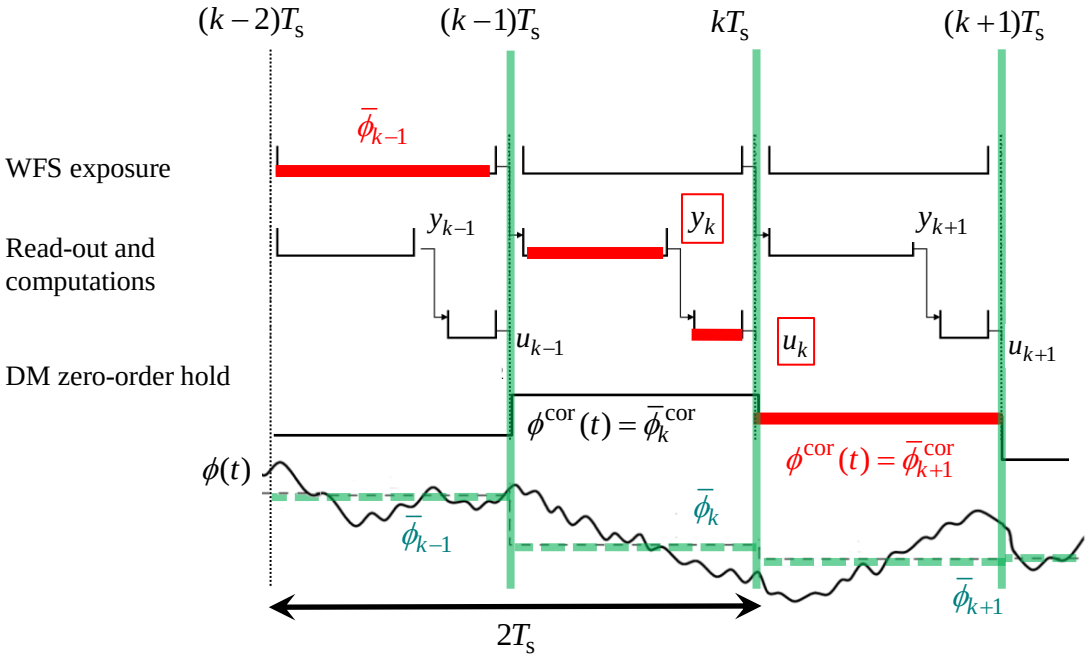

Figure 3.5: Chronogram of the AO loop with a total loop delay of 2 frames.

is given in figure 3.6. Each component is represented by its matrix operator as we supposed that all subsystems were linear. The regulator or controller is also linear, with transfer function denoted by $G(z)$.

3.3.2 Interaction and control matrices

3.3.2.1 Interaction matrix

The interaction matrix (sometimes called poking matrix) is the basis of AO systems calibration. It describes how a control vector u sent to the DM will be registered by the WFS which returns a measurement vector y:

$$y = M_{\text{int}}\, u\,. \tag{3.12}$$

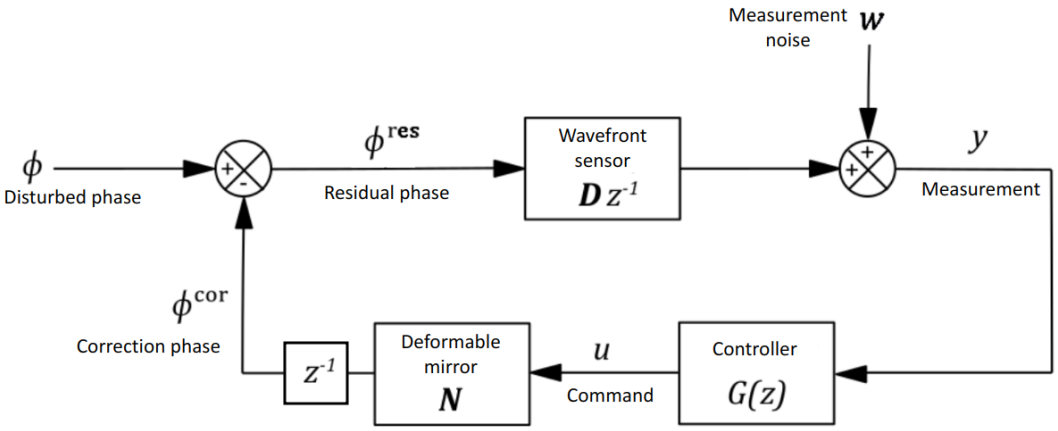

Figure 3.6: Block diagram of a closed-loop AO system in the usual 2-frame loop delay case. One frame is due to WFS integration time, and the correction phase is delayed by another frame.

The interaction matrix model is immediately deduced from D (WFS measurement matrix) and N (DM influence functions matrix) as

$$M_{\text{int}} = DN\,. \tag{3.13}$$

To be measured on a bench by the use of an internal light source (so without turbulence), a calibration process is performed: the DM is actuated with a variety of chosen commands, and the resulting changes in the incoming wavefront are measured by the WFS. See (Currie et al., 2020) about interaction matrix calibration. When only one actuator at a time is poked, the process has to be repeated for each of the n_u actuators. An illustration of the WFS measurement obtained with one single poked actuator is given in figure 3.7.

3.3.2.2 Command matrix

The command matrix M_{com} (sometimes called reconstruction matrix) relates the measurements to the commands through $u = M_{\text{com}} y$. This relationship is obtained by the least square minimization

$$\arg\min_{u} ||M_{\text{int}} u - y||^2\,, \tag{3.14}$$

leading to

$$M_{\text{com}} \triangleq M_{\text{int}}^{\dagger} = \left({M_{\text{int}}}^{\text{T}} M_{\text{int}}\right)^{-1} M_{\text{int}}^{\text{T}}\,. \tag{3.15}$$

When ${M_{\text{int}}}^{\text{T}} M_{\text{int}}$ is poorly conditioned, which is often the case, the calculation (3.15) requires a singular value decomposition and a filtering of the smallest eigenvalues, thus filtering out the associated DM modes. This allows to avoid some strong DM loads that are harmful for the hardware. It also allows to remove some DM modes

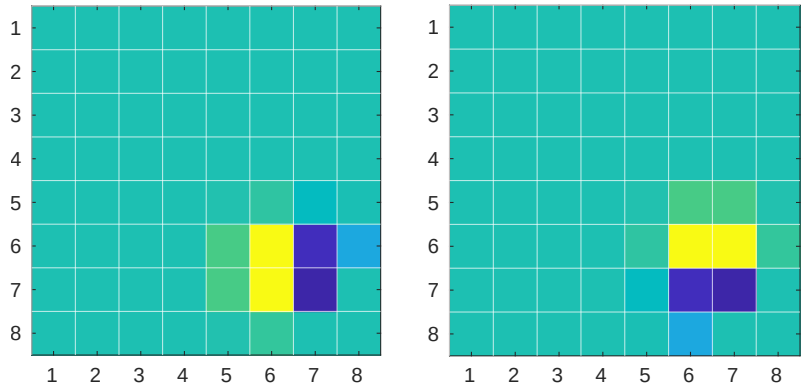

Figure 3.7: (OOMAO simulation) Representation in pupil plane of the interaction matrix M_{int} of the actuator poked in figure 3.4. This corresponds to one column of the interaction matrix M_{int}.

that degrade the residual phase while leading to almost zero WFS measurements. Those two aspects are illustrated in figure 3.8.

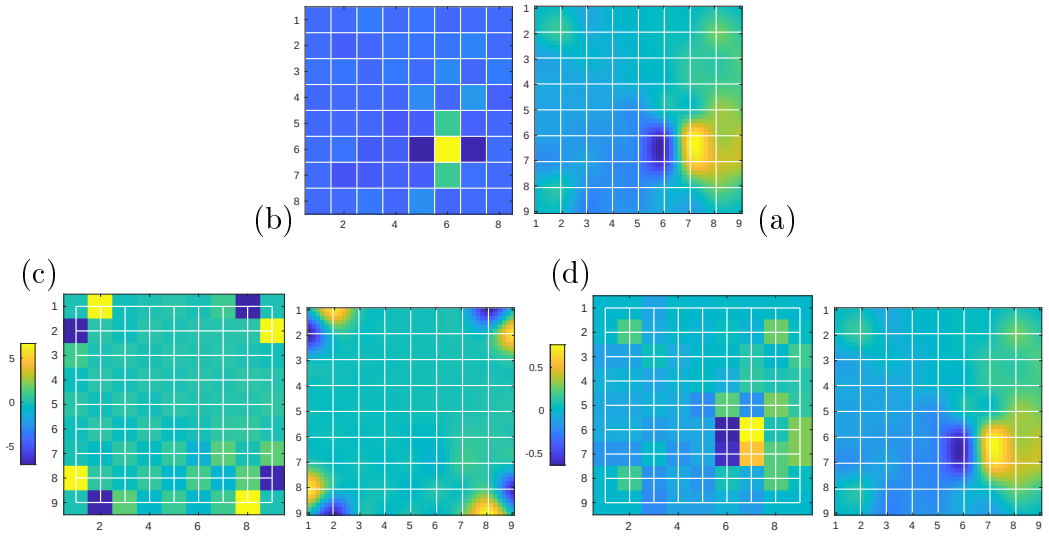

Figure 3.8: (OOMAO simulation) Example of command computation based on $u = M_{\text{com}}y$ with two command matrices differently filtered. Up: the desired phase on the right (a) and corresponding measurement y by the WFS on the left (b). Down (c): obtained command u with 5 filtered modes (left) and corresponding correction phase (right). Down (d): obtained command u with 21 filtered modes (left) and corresponding correction phase (right). The 5-filtered-mode command matrix produces 10 times higher commands, with high spatial frequencies, for a wrong resulting correction phase. The 21-filtered-mode command matrix gives a correction corresponding to the desired phase: (d)-right is similar to (a).

3.3.3 Integral action controller

The standard integral action controller, or integrator, is the most commonly used regulator on the AO systems and is based on the knowledge of the command matrix. It was the one used for the first AO system COME-ON (Rousset et al., 1990), and its simplicity has kept it on first place.

The calculation of a leaky integrator command at time kT_s using the residual wavefront slopes measurement y_k is given by

$$u_k^{\mathrm{int}} = \alpha_{\mathrm{leak}} u_{k-1}^{\mathrm{int}} - g M_{\mathrm{com}} y_k \,. \tag{3.16}$$

The leaky factor $\alpha_{\mathrm{leak}} < 1$ aims at preventing integrator wind-up in case of frequent actuator saturation. Typical values range from $\alpha_{\mathrm{leak}} = 0.99$ to 0.999 (Van Dam, Le Mignant, and B. A. Macintosh, 2004). When $\alpha_{\mathrm{leak}} = 1$, we recover an integrator. The loop gain g is a scalar parameter that is to be tuned according to the disturbance strength, the measurement noise variance, and the sampling frequency F_s. Generally, as tip and tilt (TT) modes have dynamics and energy very different from high order (HO) modes, it is advantageous to attribute different loop gains g^{TT} and g^{HO} for respectively the TT and HO modes. For the 2-frame delay case, the stability condition is given by $g < 1$ (the smaller the loop gain g, the larger the stability margins).

3.3.4 Linear Quadratic Gaussian regulator

For a linear system with Gaussian statistics, the optimal minimum variance control is known to be a Linear Quadratic Gaussian regulator (Anderson and Moore, 1990). In AO, when a linear stochastic dynamical model is used for the disturbance, it has been shown that the optimal control problem (minimizing the residual phase variance) could be equivalently solved in discrete time (Le Roux et al., 2004; Kulcsár, H.-F. Raynaud, et al., 2006). Indeed, the residual phase variance $\sigma^2_{\overline{\phi}^{\mathrm{res}}}$ can be decomposed into two terms:

$$\sigma^2_{\overline{\phi}^{\mathrm{res}}} = \lim_{K\to+\infty} \frac{1}{K} \sum_{k=1}^{K} ||\overline{\phi}_k^{\mathrm{res}}||^2 + \sigma^2_{\mathrm{inter}} \,, \tag{3.17}$$

where $\sigma^2_{\mathrm{inter}}$ is the so-called intersampling variance. The latter does not depend on the control u and can be for instance computed from the disturbance PSD (Kulcsár, H. F. Raynaud, et al., 2012). When the loop delay is non-integer, the problem is more complicated and will be addressed in chapter 4. Therefore, in the 2-frame delay case, the optimal control is obtained by minimizing the term in (3.17) that does depend on u, that is

$$J(u) = \lim_{K\to+\infty} \frac{1}{K} \sum_{k=1}^{K} ||\overline{\phi}_k^{\mathrm{res}}||^2 = \lim_{K\to+\infty} \frac{1}{K} \sum_{k=1}^{K} \left\| \overline{\phi}_{k+1} - N u_k \right\|^2 \,. \tag{3.18}$$

Assuming that $\overline{\phi}$ is a stationary and ergodic zero-mean stochastic process, the optimal control is then simply

$$u_k^{\text{opt}} = P_u \mathrm{E}[\overline{\phi}_{k+1}|\mathcal{I}_k]\,, \tag{3.19}$$

where $P_u \triangleq N^\dagger$ is the pseudo-inverse of N and $\mathrm{E}[\bullet|\mathcal{I}_k]$ is the conditional expectation with respect to the past information $\mathcal{I}_k$ from which u_k is computed. With a state space representation of the AO system (including wavefront perturbations) in the form

$$\begin{cases} X_{k+1} = AX_k + \Gamma v_k \\ y_k = C_y X_k - DNu_{k-2} + w_k \\ \overline{\phi}_k = C_{\overline{\phi}} X_k \end{cases}, \tag{3.20}$$

where noises $\{v\}$ and $\{w\}$ are zero-mean, Gaussian and white with covariance matrices Σ_v and Σ_w respectively, the optimal prediction $\mathrm{E}[\overline{\phi}_{k+1}|\mathcal{I}_k]$ is obtained as the output of a Kalman filter. In open-loop, the term $-DNu_{k-2}$ disappears. The vector X_k is the state vector for the disturbance model at time k. It can contain for instance several temporal occurrences of the perturbation when the model is autoregressive. The matrix A is the state matrix containing the poles of the dynamical disturbance model, Γ ensures consistency of process noise v_k injection with the dimensions of the state vector X_k, and C_y is the observation matrix. The state model (3.20) should be efficient to represent the disturbance spatio-temporal statistics and the AO system. The optimal control (3.19) then takes the form

$$u_k = C_u \hat{X}_{k+1|k}\,, \tag{3.21}$$

where $C_u = P_u C_{\overline{\phi}}$ is the projector of the state vector on the deformable mirror actuators and $\hat{X}_{k+1|k} = \mathrm{E}[X_{k+1}|\mathcal{I}_k]$ is obtained as the output of the asymptotic Kalman filter built from (3.20). As it may be difficult on a real system to ensure that N has the right bench geometry with respect to D, P_u can be modified as $P_u = M_{\text{com}} D$ (Sivo et al., 2014).

Kalman filter equations

The asymptotic Kalman filter can be used without loss of optimality in infinite horizon control problems (Kucera, 1991). It gives the solution to the minimum prediction error variance problem. It is a recursive filter, and its steps are defined below:

1. Update of the state estimation $\widehat{X}_{k|k}$:

$$\widehat{X}_{k|k} = \widehat{X}_{k|k-1} + H_\infty \left(y_k - \widehat{y}_{k|k-1}\right)\,, \tag{3.22}$$

with $\widehat{y}_{k|k-1} = C_y \widehat{X}_{k|k-1} - DNu_{k-2}$ is the prediction of the closed-loop slopes and H_∞ the estimation Kalman gain:

$$H_\infty = \Sigma_\infty C_y^{\mathrm{T}} \left(C_y \Sigma_\infty C_y^{\mathrm{T}} + \alpha_{\mathrm{FF}} \Sigma_w\right)^{-1}. \tag{3.23}$$

The so-called fudge factor α_{FF} is not present in a standard Kalman filter. It aims at absorbing unmodeled dynamics or inaccurate values of the matrices in (3.20). It is to be tuned around its default value $\alpha_{\mathrm{FF}} = 1$, increasing notably for very low measurement noise variance cases (high flux NGS). The asymptotic state prediction error covariance matrix Σ_∞ is the solution of the discrete algebraic Riccati equation:

$$\Sigma_\infty = A\Sigma_\infty A^{\mathrm{T}} + \Gamma\Sigma_v\Gamma^{\mathrm{T}} - A\Sigma_\infty C_y^{\mathrm{T}}\left(C_y\Sigma_\infty C_y^{\mathrm{T}} + \alpha_{\mathrm{FF}}\Sigma_w\right)^{-1} C_y\Sigma_\infty A^{\mathrm{T}}\,. \quad (3.24)$$

To solve numerically the Riccati equation (3.24), we use the doubling algorithm (Lainiotis, Assimakis, and Katsikas, 1994). It has repeatedly shown its high stability and most of all its remarkable speed of convergence. The matrix Σ_∞ is computed off-line.

2. State prediction $\widehat{X}_{k+1|k}$:

$$\widehat{X}_{k+1|k} = A\widehat{X}_{k|k}\,. \quad (3.25)$$

By combining equations (3.22) and (3.25), one obtains a single prediction equation:

$$\widehat{X}_{k+1|k} = A\widehat{X}_{k|k-1} + L_\infty\left(y_k - \widehat{y}_{k|k-1}\right) \quad (3.26)$$

$$= \left(A - L_\infty C_y\right)\widehat{X}_{k|k-1} + L_\infty\left(y_k + M_{\mathrm{int}}u_{k-2}\right)\,, \quad (3.27)$$

where $L_\infty \triangleq AH_\infty$ is the prediction Kalman gain, computed offline. Equation (3.27) is the one that is in practice implemented in real time (with of course an adapted real-time formulation).

In our upcoming cases, we set for the doubling algorithm the following solving parameters: residual error 10^{-9}, resolution method "normAlpha". The latter method did not appear to give different results from the other method "traceGamma". A change in the residual error (tested from 10^{-2} to 10^{-20}) neither modified the obtained Σ_∞ nor its computation time (typically around 20 iterations involved, carried out in around 10 seconds with an Intel® Xeon(R) E-2276M CPU @ 2.80GHz×12 computer for a 1500×1500-size Σ_∞). When increasing the residual error to 10^0, it leads to a state prediction error covariance matrix faster computed (only two iterations) but with very poor closed-loop results.

3.3.5 Minimum Mean Square Error reconstructor

The MMSE has been widely employed in AO, in particular in wide-field AO, e.g. (B. Ellerbroek, 2002; B. L. Ellerbroek and Vogel, 2009; Neichel et al., 2010; Vidal et al., 2011). The MMSE reconstructor is a minimum variance reconstruction method that relies solely on the last pseudo-open loop measurement, corresponding to

$$\hat{\overline{\phi}}_{k-1|k} = \mathrm{E}[\overline{\phi}_{k-1}|y_k^{\mathrm{POL}}]\,. \quad (3.28)$$

At each time k, we thus have:

$$u_k = N^\dagger \hat{\overline{\phi}}_{k-1|k} \tag{3.29}$$

$$= N^\dagger R_{\text{MAP}} y_k^{\text{POL}} . \tag{3.30}$$

The pseudo-open loop slopes y^{POL} are computed from the actual closed-loop ones y and using the interaction matrix to cancel the effect of the DM correction (taking the loop delays into account):

$$y_k^{\text{POL}} = y_k + M_{\text{int}} u_{k-2} . \tag{3.31}$$

The index $k-1|k$ in the MMSE equation means that we make an estimation of the past disturbance $\overline{\phi}_{k-1}$ based on its measurement y_k. It does not use any temporal statistics. That is why it is sometimes called a static reconstructor. The reconstruction matrix is obtained as

$$R_{\text{MAP}} = \Sigma_\phi D^T \left(D \Sigma_\phi D^T + \alpha_{\text{MAP}} \Sigma_w \right)^{-1} , \tag{3.32}$$

where Σ_ϕ stands for the theoretical Von Kármán covariance matrix. As is the fudge factor α_{FF} in the LQG case, α_{MAP} is to be tuned according to the signal-to-noise ratio.

We recognize in (3.32) the same structure as for the Kalman gain H_∞ in equation (3.23) but without temporal evolution. In this case, when the model is close to a random walk (A close to I), the resulting Kalman gain H_∞ tends towards R_{MAP}, as shown in figure 3.9 for the defocus mode.

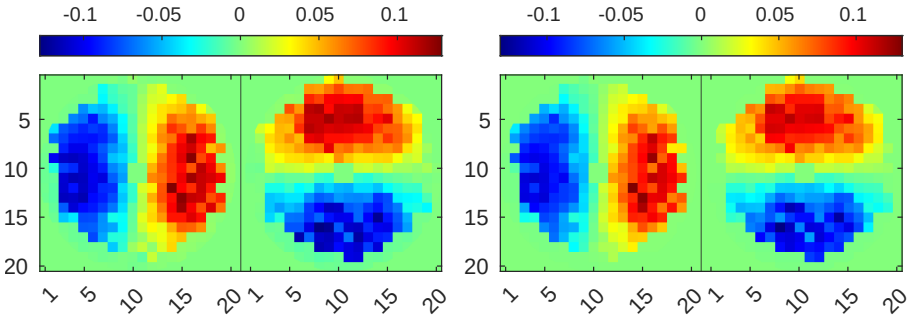

Figure 3.9: Comparison between the Kalman gain matrix H_∞ (left, AR1 model with A close to I) and the MAP reconstructor R_{MAP} (right). The line corresponding to the defocus mode is displayed in 2-D (WFS measurement space).

3.3.6 Real-time computer

The real-time computer (RTC) is at the heart of the AO system servoing. An RTC requires precise timing and synchronization to ensure that tasks are completed within

the required time frame T_s. In the case of a generic linear regulator, the RTC should compute the commands as fast as possible to limit the loop delay. For example, for LQG control, the commands are calculated using an equation that has the same complexity as the integrator, albeit some remaining update calculations are done in idle time. For example in the 2-frame delay case, this efficient implementation takes the following form:

$$\begin{cases} u_k &= u_{k-1}^- + M_1 y_k \\ \hat{X}_{k+1|k} &= \hat{X}^+ + M_2 y_k \\ \hat{X}^+ &= M_3 \hat{X}_{k+1|k} + M_4 u_{k-1} \\ u_k^- &= M_5 \hat{X}^+ \end{cases} \tag{3.33}$$

where matrices M_1 to M_5 are derived from (3.21) and (3.27). Those matrices are defined offline and loaded on the RTC. All the calculations depending on y_k can be done sequentially with the arrival of data. In particular, the multiplication by $M_1 = N^\dagger C_{\bar{\phi}} L_\infty$ for the LQG is of same size as $M_1 = g M_\mathrm{com}$ for the integrator. Once the command u_k (first line of equation (3.33)) is sent to the DM, and while waiting for the end of next WFS image integration (so as to compute the next measurement y_{k+1}), the RTC computes the more time-consuming lines 2 to 4 among the LQG equations (3.33) (for instance, $M_2 = L_\infty$ is of bigger size than M_1).

3.4 Conclusion

We have seen the main components of an AO system and what are their respective roles. It is generally possible to fully model it with linear equations, allowing the definition of an optimal high-performance controller: the LQG regulator. Its construction has been recalled in the case where the AO system has a 2-frame loop delay, the extension to any integer loop delay being straightforward. In the next chapter, we extend this construction to the case when the total loop delay takes non-integer values.

We have seen that the complexity degree for the integral control was lower than the MMSE one, the latter itself lower than the LQG. Both MMSE and LQG need the knowledge of some system characteristics: WFS matrix D, measurement noise covariance matrix Σ_w, interaction matrix M_int and influence matrix N. We will see in chapter 5, what simple procedures can solve these system modeling issues.

Chapter 4
Fractional loop delay in adaptive optics modeling and control

Summary content

This chapter features a forthcoming paper that focuses on fractional delays in adaptive optics. The paper introduces specific notations that facilitate a comprehensive explanation of the modeling and control design aspects when fractional delays are present.

We tackle the following issues:

- The derivation of the optimal (minimum-variance) LQG controller for AO systems with integer delays is recalled to show that in the absence of actuator dynamics the optimal LQG control in presence of a fractional delay retains the same general structure, albeit with a Kalman filter based on a model of asynchronous WFS measurements.

- Suboptimal LQG controllers used in the literature and based on approximations of the fractional delay for discrete-time models are introduced. The Kalman filter is synchronized either with the DM as in (L. Poyneer and Véran, 2008; L. A. Poyneer, D. W. Palmer, et al., 2016; L. A. Poyneer, Ammons, et al., 2023), or with the WFS as in (Sivo et al., 2014; Sinquin et al., 2020; Marquis et al., 2022).

- We present simulations and GTCAO bench tip-tilt performance evaluations of integral and suboptimal LQG controllers in presence of fractional delay, together with simulation results for the optimal LQG regulator. We show that problems arise when vibrations are present.

- We detail the construction of the asynchronous optimal LQG control based on a continuous-time stochastic disturbance model, similarly to (Looze, 2009; H.-F. Raynaud, Correia, et al., 2011). However, we present a solution to build this continuous-time model from a standard non-fractional discrete-time one and we use calculations that involve only simple ingredients like matrix exponentials and solving Lyapunov equations (no numerical integrations are needed, contrarily to (Looze, 2009)).

- We develop tools for theoretical performance assessment in presence of fractional delay for any linear regulator. This includes temporal spectral study and robustness analysis. These tools are applied to GTCAO tip-tilt simulations.

Fractional loop delays in adaptive optics modeling and control

LUCAS MARQUIS[1*], HENRI-FRANÇOIS RAYNAUD[1], NICOLAS GALLAND[1], JOSE MARCO DE LA ROSA[2], ICÍAR MONTILLA[2], OSCAR TUBÍO ARAÚJO[2], MARCOS REYES GARCÍA-TALAVERA[2], AND CAROLINE KULCSÁR[1]

[1] *Institut d'Optique Graduate School, Laboratoire Charles Fabry - CNRS, Université Paris-Saclay, Palaiseau, France*
[2] *Instituto de Astrofísica de Canarias, La Laguna, Spain*
[*] *lucas.marquis@institutoptique.fr*

This paper revisits the problem of optimal (minimum-variance) control for Adaptive Optics (AO) systems when measurements and commands application are asynchronous, resulting in a non-integer servo-loop delay. When not properly accounted for, such fractional delays may severely degrade AO performance, especially in presence of high-frequency vibrations. We present evidence of this performance degradation thanks to in-lab experimental measurements on the Gran Telescopio Canarias Adaptive Optics (GTCAO) system controlled with standard suboptimal LQG controllers. A constructive, easy to implement Linear Quadratic Gaussian (LQG) control design is then proposed and validated in simulation for vibrations affecting the tip-tilt modes. Our methodology is very interesting as it allows performance assessment for any linear controller in terms of variance, rejection transfer functions, power spectral densities and stability margins. We also show how the continuous-time disturbance model can be derived from standard discrete-time disturbance data-based modeling.

http://dx.doi.org/10.1364/ao.XX.XXXXXX

1. INTRODUCTION

Adaptive optics (AO) systems aim to compensate in real-time for optical aberrations which degrade image quality. They operate via a deformable mirror (DM) that compensates for the optical path distortions estimated from wavefront sensor (WFS) measurements. The increasing size of the large telescopes' primary mirror renders the use of AO systems mandatory in order to approach the diffraction limit. This also requires efficient compensation of the disturbances generated by wind and vibrations, see, e.g., [1]. This leads to a gain of interest in high-performance predictive AO control [2–6], especially LQG control based on a Kalman filter constructed from a stochastic disturbance model. However, efficient predictive compensation of high-frequency disturbances requires taking accurately into account the servo-loop delay.

In AO systems, as in many feedback systems, control design is generally based on the simplifying assumption that the real time computer provides measurements and sends commands at successive sampling instants, so that the total servo-loop delay is an integral multiple of the control sampling period. However, in many AO systems WFS measurements and DM commands are actually de-synchronized, resulting in a fractional loop delay.

Modeling such asynchronous AO systems cannot be achieved using standard discretization techniques. It requires a lifting procedure, see,, e.g., [7], which essentially boils down to building an augmented state-space representation in order to account for the sequence of non-evenly spaced events occurring during each sampling interval (see, e.g., [7]). Lifting techniques were indeed applied to AO control with non-integer measurement delays in [8, 9], allowing the derivation of an optimal LQG controller and the computation of the theoretical optimal performance also in presence of DM dynamics. The constructions proposed required as a starting point a continuous-time state-space stochastic disturbance model, and the optimal control design procedure involved the computation of several integrals of matrix-valued functions, resulting in tedious numerical computations.

In recent years, simpler suboptimal alternatives were proposed and implemented. In [10], Poyneer and Véran developed a closed-loop state space model where predicted phases at non-integer time indexes are approximated by weighted averages of phases estimated at integer time indexes. Such approximations were repeatedly validated with on-bench [6] and on-sky experiments [11]. The same principle of weighted averages has been used for a full LQG control with vibration mitigation carried out on sky by Sivo [12] and Sinquin [3].

A question nevertheless arises: are these approximations still acceptable when the disturbance contains oscillations at high temporal frequencies? In this paper, we present experimental results obtained on the AO test-bench currently under develop-

ment for the 10-meter class Gran Telescopio Canarias (GTC). In these on-bench tests, two suboptimal LQG controllers based on different ways to take fractional delays into account were tested and compared to standard integral action control. These results showed that the performance of the two suboptimal LQG were markedly different and were sensitive to variation/uncertainties in the actual value of the fractional delay.

These on-bench results suggested that implementing instead an optimal LQG control could yield significantly improved and more robust performance. This provided the motivation to revisit the construction of the lifted model of an asynchronous AO system and of the resulting optimal minimum-variance LQG control. This paper presents the resulting procedure, where all calculations are performed using two standard and computationally stable routines – computing matrix exponentials and solving Lyapunov equations. In addition, we show how to construct the key necessary ingredient – the underlying continuous-time disturbance model – from discrete-time models built from statistical priors and/or identified from WFS measurements. We also provide constructive procedures enabling to compute theoretical performance assessments for the optimal LQG regulator or any other linear controller, in terms of variance, but also and for the first time, in terms of rejection transfer functions, power spectral densities and stability margins.

The paper is organized as follows. Section 2 recalls the derivation of the optimal (minimum-variance) LQG controller for AO systems with integer delays, and shows that in the absence of actuator dynamics the optimal LQG retains the same general structure whatever the delay, albeit with a Kalman filter based on a model of asynchronous WFS measurements. Section 3 introduces the suboptimal LQG controllers based on approximations of the fractional delay for discrete-time models synchronized either with the DM or with the WFS. Sections 4 and 5 present simulation and test-bench tip-tilt performance evaluations of integral and suboptimal LQG controllers in presence of fractional delay, together with simulation results for the optimal LQG regulator. Section 6 details the construction of the asynchronous optimal LQG control based on a continuous-time stochastic disturbance model, and shows how to build this model from a standard (non-fractional) discrete-time one. Tools for theoretical performance and robustness evaluation are presented in section 7. In section 8, those evaluation tools are applied to GTCAO tip-tilt simulations. Conclusions are presented in section 9.

2. OPTIMAL PREDICTION FOR OPTIMAL CONTROL

In the basic case where WFS and DM are synchronized and when DM dynamics can be neglected, the optimal control solution to AO disturbance rejection is known to be obtained as a discrete-time LQG regulator [13–16]. We briefly recall here how this solution is obtained, in order to specify clearly what must be modified in presence of a fractional delay.

Consider an AO system operating in closed-loop with a sampling frequency of F_s (sampling time $T_\mathrm{s} = 1/F_\mathrm{s}$). Since the actual performance of the AO correction is obtained by integrating the light flux over very long exposure times (with respect to the AO sampling rate), the performance cost function J to be minimized is the residual phase variance defined as the average power of the residual phase aberration ϕ^{res} over an infinite time horizon:

$$J(u) \triangleq \lim_{T\to+\infty} \frac{1}{T}\int_0^T \left\|\phi^{\mathrm{res}}(t)\right\|^2 dt. \tag{1}$$

The command is applied via a zero-order hold (ZOH), and therefore is piecewise constant over successive sampling intervals:

$$\forall t \in [kT_\mathrm{s}, (k+1)T_\mathrm{s}[, \qquad u(t) = u(kT_\mathrm{s}) \triangleq u_k\,. \tag{2}$$

The control applied at time kT_s is thus u_k, and the correction phase is also piecewise constant, with

$$\forall t \in [kT_\mathrm{s}, (k+1)T_\mathrm{s}[, \qquad \phi^{\mathrm{cor}}(t) = Nu(t) = Nu_k\,. \tag{3}$$

As done in [13, 14, 16], let us define time average values over one frame for any continuous-time variable $x(t)$ as

$$\bar{x}_k \triangleq \frac{1}{T_\mathrm{s}}\int_{(k-1)T_\mathrm{s}}^{kT_\mathrm{s}} x(t)dt. \tag{4}$$

From Eq. (3), the correction phase equation is simply

$$\overline{\phi}^{\mathrm{cor}}_{k+1} = Nu_k\,. \tag{5}$$

By slicing the integral in Eq. (1) on DM ZOH intervals, the optimal control that minimizes $J(u)$ can be equivalently obtained by minimizing the discrete-time cost function

$$J^{\mathrm{d}}(u) \triangleq \lim_{K\to+\infty} \frac{1}{K}\sum_{k=0}^{K-1} J_k(u_k) \tag{6}$$

with the incremental cost J_k defined as

$$J_k(u_k) \triangleq \|\overline{\phi}^{\mathrm{res}}_{k+1}\|^2 \tag{7}$$

$$= \left\|\overline{\phi}_{k+1} - Nu_k\right\|^2, \tag{8}$$

where $\overline{\phi}^{\mathrm{res}}_{k+1}$ and $\overline{\phi}_{k+1}$ are defined similarly to Eq. (4).

The intersampling variance, denoted by $\sigma^2_{\phi,\mathrm{is}}$, is then the cost associated with the part of the continuous-time disturbance that cannot be corrected by the AO system and therefore does not depend on the regulator:

$$\sigma^2_{\phi,\mathrm{is}} \triangleq \lim_{N\to+\infty} \frac{1}{N}\sum_{k=0}^{N-1}\frac{1}{T_\mathrm{s}}\int_{kT_\mathrm{s}}^{(k+1)T_\mathrm{s}} \left\|\phi(t) - \overline{\phi}_{k+1}\right\|^2 dt\,, \tag{9}$$

so that

$$J(u) = J^{\mathrm{d}}(u) + \sigma^2_{\phi,\mathrm{is}}. \tag{10}$$

The intersampling variance $\sigma^2_{\phi,\mathrm{is}}$ represents the variance of the continuous-time disturbance variation around its temporal averages $\overline{\phi}_k$, and can be explicitly calculated from the disturbance power spectral density [16].

Assume that the phase trajectory is known in advance (complete information hypothesis). In this unrealistic ideal case, the optimal control u^{ci} would be obtained at each step by minimizing $J_k(u_k)$ in Eq. (8), which yields

$$u^{\mathrm{ci}}_k \triangleq P_u\overline{\phi}_{k+1}\,, \tag{11}$$

where P_u is the pseudo-inverse of the influence matrix N:

$$P_u \triangleq (N^{\mathrm{T}}N)^{-1}N^{\mathrm{T}}\,. \tag{12}$$

In the real world (incomplete information hypothesis), the phase trajectory is not known and the control needs to be computed from available WFS measurements. The stochastic separation theorem applies here: the optimal control u^* is obtained by replacing the unknown value of $\overline{\phi}_{k+1}$ in Eq. (11) by its optimal

estimate in the sense of the minimum variance of the estimation error. This optimal prediction is the conditional expectation with respect to the set of past information (controls and measurements) $\mathcal{I}_k = \{u_0, \ldots, u_{k-1}, y_0, y_1, \ldots, y_k\}$, where y_k is defined as the latest measurement used to compute the control applied at time kT_s. The optimal control at each frame k is thus obtained as:

$$u_k^* \triangleq \arg\min_{u_k} \mathrm{E}[J_k(u_k)|\mathcal{I}_k] \tag{13}$$

$$= P_u\, \mathrm{E}[\bar{\phi}_{k+1}|\mathcal{I}_k]. \tag{14}$$

At this point, it is worth noting that in all cases (integer or fractional loop delays), the optimal control expression in Eq. (14) does not change. However, the calculation of the conditional expectation itself will depend on the measurement model, and thus on the loop delay.

Let us suppose that the total loop delay is $(d+\delta)T_\mathrm{s}$, with $d \in \mathbb{N}$ and $0 < \delta \leq 1$. This total loop delay is the time lag from the beginning of WFS exposure to the beginning of DM commands application by the ZOH. This includes readout of the WFS camera CCD, slopes and commands computation, data transfers, *etc*. The measurement equation can then be defined as

$$y_k \triangleq \frac{1}{T_\mathrm{s}} \int_{(k-d-\delta)T_\mathrm{s}}^{(k+1-d-\delta)T_\mathrm{s}} D\phi^{\mathrm{res}}(t)\, dt + w_k\,, \tag{15}$$

where D is the WFS measurement matrix and w the measurement noise, which as usual is assumed to be a zero-mean Gaussian white noise. For the sake of simplicity, we will assume throughout this paper that the total loop delay is $1+\delta$, so that $d = 1$. It means that the WFS exposure frame is bigger than the sum of the AO computational delays – see the chronogram in figure 1. (Larger values of d can then be handled by adding additional delayed states in the models.) When $d = 1$, the last measurement available to compute u_k is thus

$$y_k = D\bar{\phi}_k^{\mathrm{res},\delta} + w_k\,, \tag{16}$$

where

$$\bar{\phi}_k^{\mathrm{res},\delta} \triangleq \frac{1}{T_\mathrm{s}} \int_{(k-1-\delta)T_\mathrm{s}}^{(k-\delta)T_\mathrm{s}} \phi^{\mathrm{res}}(t)\, dt\,. \tag{17}$$

Using Eq. (3), the measurement equation becomes

$$y_k = D\bar{\phi}_k^{\delta} - DN\left((1-\delta)\, u_{k-1} + \delta u_{k-2}\right) + w_k\,, \tag{18}$$

where

$$\bar{\phi}_k^{\delta} \triangleq \frac{1}{T_\mathrm{s}} \int_{(k-1-\delta)T_\mathrm{s}}^{(k-\delta)T_\mathrm{s}} \phi(t)\, dt\,. \tag{19}$$

All is needed to constructively solve the incomplete information optimal control problem, that is to compute the conditional expectation in Eq. (14), is a linear time-invariant stochastic model that outputs the discrete-time variables $\bar{\phi}$ and $\bar{\phi}^{\delta}$. This model can be put in standard state-space form as

$$\begin{cases} x_{k+1} = Ax_k + \Gamma v_k & (20)\\ \bar{\phi}_k = C_{\bar{\phi}} x_k & (21)\\ \bar{\phi}_k^{\delta} = C_{\bar{\phi}^{\delta}} x_k\,, & (22) \end{cases}$$

where v is a zero-mean Gaussian white noise with covariance matrix Σ_v and independent of the measurement noise w. The measurement model then translates into

$$y_k = C_y x_k - DN\Big((1-\delta)u_{k-1} + \delta u_{k-2}\Big) + w_k\,, \tag{23}$$

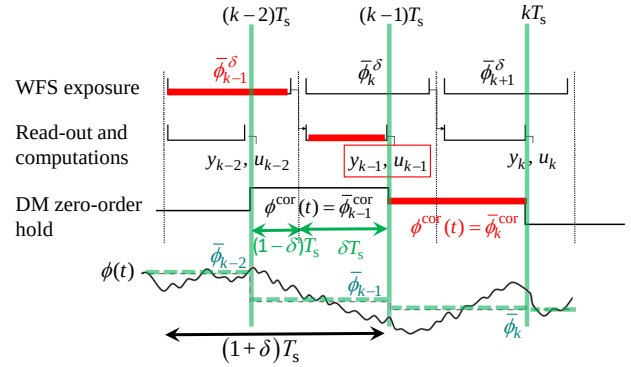

Fig. 1. Chronogram of the AO loop with a total loop delay of $d+\delta$ with $d = 1$. The discrete-time phase $\bar{\phi}$ is the time-average of the continuous-time phase $\phi(t)$ on DM-related intervals, as defined in Eq. (4) with $\phi(t)$ in place of $x(t)$, and $\bar{\phi}^{\delta}$ is the discrete-time variable averaged on WFS-related intervals, as defined in Eq. (19). The computational delays (middle red line) are here smaller than one frame.

where $C_y = DC_{\bar{\phi}^{\delta}}$. The optimal control in Eq. (14) can be rewritten as

$$u_k^* = P_u C_{\bar{\phi}} \widehat{x}_{k+1|k}\,, \tag{24}$$

where the minimum-variance prediction $\widehat{x}_{k+1|k} = \mathrm{E}[x_{k+1}|\mathcal{I}_k]$ is the output of a Kalman filter built on Eq. (20)-(23). We briefly recall below the Kalman filter equations.

The real-time part of the asymptotic Kalman filter corresponds to

$$\widehat{x}_{k+1|k} = A\widehat{x}_{k|k-1} + L_\infty(y_k - \widehat{y}_{k|k-1})\,, \tag{25}$$

involving the prediction of the closed-loop residual slopes based on Eq. (23):

$$\widehat{y}_{k|k-1} = C_y\widehat{x}_{k|k-1} - DN\left((1-\delta^{\mathrm{ctrl}})u_{k-1} + \delta^{\mathrm{ctrl}}u_{k-2}\right). \tag{26}$$

We distinguish here on purpose the loop delay value δ^{ctrl} used to define the LQG regulator matrices from the true system loop delay δ. The prediction Kalman gain L_∞ is computed off-line as

$$L_\infty = A\Sigma_\infty C_y^{\mathrm{T}}\left(C_y\Sigma_\infty C_y^{\mathrm{T}} + \alpha_{\mathrm{FF}}\Sigma_w\right)^{-1}, \tag{27}$$

where Σ_∞ is the asymptotic estimation error covariance matrix and the constant $\alpha_{\mathrm{FF}} > 0$ is a fudge factor which enables to tune the global signal-to-noise ratio in order to account for modeling errors. The matrix Σ_∞ is obtained as the unique solution – which is guaranteed to exist when the model Eq. (20)-(22) is stable – of the following discrete algebraic Riccati equation (DARE):

$$\Sigma_\infty = A\Sigma_\infty A^{\mathrm{T}} + \Gamma\Sigma_v\Gamma^{\mathrm{T}} - A\Sigma_\infty C_y^{\mathrm{T}}\left(C_y\Sigma_\infty C_y^{\mathrm{T}} + \alpha_{\mathrm{ff}}\Sigma_w\right)^{-1} C_y\Sigma_\infty A^{\mathrm{T}}. \tag{28}$$

Details on the Kalman filter and conditions to obtain a unique solution of the DARE can be found, e.g., in [17, 18].

The usual 2-frame delay case will correspond to $\delta = 1$, so that $\bar{\phi} = \bar{\phi}^{\delta}$ leading to the measurement equation

$$y_k = D\bar{\phi}_{k-1} - DNu_{k-2} + w_k\,. \tag{29}$$

In this case, the optimal control is based on the discrete state-space model (20)-(21), which only needs to output $\bar{\phi}$.

3. SUBOPTIMAL DISCRETE-TIME LQG CONTROL WITH FRACTIONAL DELAY

When $0 < \delta < 1$, optimal control design requires a model capable of producing as outputs both discrete-time variables $\overline{\phi}$ and $\overline{\phi}^{\delta}$ – that is, averages of ϕ over overlapping time intervals. As it will be show in section 6, such a model can be constructed from a continuous-time stochastic disturbance model, which can itself be derived from a simpler to construct model of $\overline{\phi}$.

A simple suboptimal way to cope with fractional delays is to keep using a model of the disturbance averaged on a sampling period T_s and synchronized on either the DM, as in [6, 10, 11], or on the WFS, as in [3, 12, 19].

In the DM-synchronized case, the Kalman filter is built on a state-space model of $\overline{\phi}$ with internal state $x_k = x_{\overline{\phi},k}$, in the form

$$\begin{cases} x_{\overline{\phi},k+1} = A_{\overline{\phi}} x_{\overline{\phi},k} + \Gamma_{\overline{\phi}} v_{\overline{\phi},k} & \textbf{(30)} \\ \overline{\phi}_k = C_{\overline{\phi}} x_{\overline{\phi},k} & \textbf{(31)} \\ \overline{\phi}_{k-1} = C_{\overline{\phi},1} x_{\overline{\phi},k}\,. & \textbf{(32)} \end{cases}$$

Since $\overline{\phi}^{\delta}$ is not an output of this model, the measurement equation can no longer be rewritten in the form of Eq. (18). It is replaced by the approximation

$$\begin{aligned} y_k &= D\big((1-\delta^{\text{ctrl}})\overline{\phi}_k + \delta^{\text{ctrl}}\overline{\phi}_{k-1}\big) - \\ &\qquad DN\Big((1-\delta^{\text{ctrl}})u_{k-1} + \delta^{\text{ctrl}}u_{k-2}\Big) + w_k \qquad \textbf{(33)} \\ &= D\big((1-\delta^{\text{ctrl}})C_{\overline{\phi}} + \delta^{\text{ctrl}}C_{\overline{\phi},1}\big)x_{\overline{\phi},k} - \\ &\qquad DN\Big((1-\delta^{\text{ctrl}})u_{k-1} + \delta^{\text{ctrl}}u_{k-2}\Big) + w_k\,. \qquad \textbf{(34)} \end{aligned}$$

The Kalman filter then produces the non-optimal prediction $\widehat{\overline{\phi}}_{k+1|k} = C_{\overline{\phi}}\widehat{x}_{\overline{\phi},k+1|k}$, yielding a suboptimal control that retains the same expression as in Eq. (24):

$$u_k = P_u C_{\overline{\phi}} \widehat{x}_{\overline{\phi},k+1|k}\,. \qquad \textbf{(35)}$$

Conversely, in the WFS-synchronized case, the Kalman filter is built on a state-space model of $\overline{\phi}^{\delta}$. But since the underlying continuous-time process ϕ is always assumed to be stationary, averaging it over WFS intervals will result in exactly the same discrete-time stochastic model as in the DM-synchronized case, namely:

$$\begin{cases} x_{\overline{\phi},k+1} = A_{\overline{\phi}} x_{\overline{\phi},k} + \Gamma_{\overline{\phi}} v_{\overline{\phi},k} & \textbf{(36)} \\ \overline{\phi}^{\delta}_k = C_{\overline{\phi}} x_{\overline{\phi},k} & \textbf{(37)} \\ \overline{\phi}^{\delta}_{k-1} = C_{\overline{\phi},1} x_{\overline{\phi},k}\,. & \textbf{(38)} \end{cases}$$

One can put the measurement equation in the form of Eq. (23) by taking $C_y = C_{\overline{\phi}}$. However, since $\phi(t)$ is not constant over WFS sampling intervals, the optimal prediction $\mathrm{E}[\overline{\phi}_{k+1}|\mathcal{I}_k]$ can no longer be computed from $\widehat{x}_{\overline{\phi},k+1|k}$. Approximating it by a weighted average of the predictions of $\overline{\phi}^{\delta}_{k+1}$ and $\overline{\phi}^{\delta}_k$ leads to the suboptimal control

$$\begin{aligned} u_k &= P_u\Big(\delta^{\text{ctrl}}\mathrm{E}[\overline{\phi}^{\delta}_{k+1}|\mathcal{I}_k] + (1-\delta^{\text{ctrl}})\mathrm{E}[\overline{\phi}^{\delta}_k|\mathcal{I}_k]\Big) \\ &= P_u\big(\delta^{\text{ctrl}}C_{\overline{\phi}} + (1-\delta^{\text{ctrl}})C_{\overline{\phi},1}\big)\widehat{x}_{\overline{\phi},k+1|k} \\ &= P_u C_{\overline{\phi},2}\widehat{x}_{\overline{\phi},k+1|k}\,, \qquad \textbf{(39)} \end{aligned}$$

with $C_{\overline{\phi},2} \triangleq \delta^{\text{ctrl}}C_{\overline{\phi}} + (1-\delta^{\text{ctrl}})C_{\overline{\phi},1}$. As noted in [10, 20], Eq. (33) would be valid only if $\phi(t)$ remained constant over successive DM intervals. Also, while both simplifications result in non optimal controllers, this will not matter much as long as the PSD of ϕ is mainly concentrated on low temporal frequencies so that the intersampling variance remains small. Conversely, one should expect problems when the controller has to compensate for high-frequency vibration peaks. These aspects are investigated by means of simulation examples in Section 4 and through experimental results on the GTCAO bench in Section 5.

4. EFFECT OF FRACTIONAL DELAY ON TIP-TILT CONTROL SIMULATION

The impact on performance of the two modelings, which are

1. the DM-synchronized model based on $\overline{\phi}$ that gives an LQG controller denoted by LQG-DM,
2. the WFS-synchronized model based on $\overline{\phi}^{\delta}$ that gives an LQG controller denoted by LQG-WFS,

depends of course on the values taken by the actual loop delay δ, on the loop delay value δ^{ctrl} used for controller design, and on the disturbance. We consider here a scalar model, namely a tip-tilt control. This is relevant since the tip and tilt modes are the two optical modes for which the impact of vibrations is the most significant, and thus the ones for which fractional delay most strongly impacts performance.

The performance of these two suboptimal LQG controllers are compared with a standard leaky integrator:

$$u_k = \alpha_{\text{leak}}u_{k-1} + gM_{\text{com}}y_k\,, \qquad \textbf{(40)}$$

where $0 < g < 1$ is the integrator gain, $\alpha_{\text{leak}} \leq 1$ is the leakage factor and M_{com} is a pseudo-inverse of the interaction matrix $M_{\text{int}} \triangleq DN$.

A. Simulation set-up

In these simulations, atmospheric turbulence is generated as the output of a continuous-time second order low-pass shaping filter with transfer function $\omega_{0_{\text{tur}}}^2 F_0/(\omega_{0_{\text{tur}}}^2 + 2\xi_{\text{tur}}\omega_{0_{\text{tur}}}s + s^2)$, where s is the Laplace variable. The cut-off frequency is set to $f_{\text{tur}} = \omega_{0_{\text{tur}}}/2\pi = 1\,\text{Hz}$ (equivalent to a wind speed of $10\,\text{m}\,\text{s}^{-1}$), the damping coefficient to $\xi_{\text{tur}} = 0.9$, and the DC gain F_0 is adjusted so as to set the total disturbance variance to $e_{\text{tur}} = 20\,\text{rad}^2$ at the WFS wavelength ($500\,\text{nm}$).

The vibration-like disturbances are generated also using this type of model, albeit with a value of the frequency $f_{\text{vib}} = \omega_{0_{\text{vib}}}/2\pi$ that will take different values throughout the spectrum, a damping coefficient set to $\xi_{\text{vib}} = 10^{-3}$ and an energy $e_{\text{vib}} = 2\,\text{rad}^2$ (corresponding to 110 nm RMS, or an angle of arrival of 9 mas RMS for a 10-m diameter pupil).

In this scalar set-up, the matrices N and D are set to 1, so that the commands u_k and the measurements y_k can be considered to be both in radians. The variance of the tip-tilt measurement noise w is taken as $\sigma_w^2 = 0.1\,\text{rad}^2$, a typical value for a 10-meter diameter telescope with a 20x20-subaperture Shack-Hartmann WFS [21]. Two sampling frequencies will be considered in the simulations: $F_s = 200\,\text{Hz}$ and $F_s = 500\,\text{Hz}$.

The discrete-time disturbance state-space model used to compute the LQG controllers was identified using the N4SID subspace algorithm [3, 22] from a 20 s-long batch of open-loop WFS data. The order of the model is set to 10 for all disturbance cases.

The closed-loop system is simulated at a fine rate of 40 times the sampling frequency of the AO system, allowing to generate the desired spectra for both turbulence and vibrations. The WFS measurements are obtained every $T_s = 1/F_s$ by averaging the fast rate samples, and the DM commands are applied through a ZOH of sampling period T_s that respects the chosen loop delay $1 + \delta$, so as to match the chronogram in Figure 1.

B. Case with turbulence only

Performance results in terms of residual disturbance RMS in nm are shown in figure 2 for the integrator, LQG-DM and LQG-WFS regulators, and with disturbance generated exclusively by the turbulence model. Two scenarios are considered for the LQG controllers: in solid line, the actual loop delay of the system and of the model used for control design are equal ($\delta = \delta^{\text{ctrl}}$). In dashed line, the system loop delay is set at $\delta = 0.5$, whereas δ^{ctrl} varies from 0 to 1. Both LQG regulators give similar results, as expected in presence of atmospheric turbulence only. Also, their performance evolves smoothly for δ varying from 0 to 1; for the middle value $\delta = 0.5$, taking a wrong value for δ^{ctrl} does not impact much performance, showing that all controllers are essentially insensitive to an error on the loop delay.

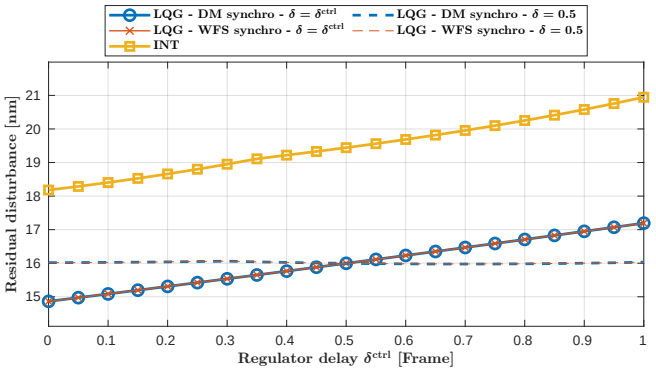

Fig. 2. (simulation, $\delta = \delta^{\text{ctrl}}$ or $\delta = 0.5 \neq \delta^{\text{ctrl}}$) Residual phase RMS (nm) in a pure turbulence case for integrator ($\square-$), and with $\delta = \delta^{\text{ctrl}}$ (solid lines) for LQG-DM ($\circ-$) and LQG-WFS ($\times-$), or with a fixed value of $\delta = 0.5$ and δ^{ctrl} in $[0, 1]$ (dashed lines).

C. Case with turbulence and vibration

One knows that a key factor for the predictive control advantages is the presence of high-frequency disturbances, typically vibrations. In this subsection, we will highlight the delay modeling issue when the vibration frequencies are approaching the AO system Shannon-Nyquist frequency $F_s/2$. Simulations results are displayed in figure 3.

We notice that whatever the sampling frequency (200 Hz or 500 Hz here), once the vibration frequency exceeds $F_s/4$ its rejection gets critical if the system delay is around $\delta = 0.5$ frame. In the case of $f_{\text{vib}} = F_s/4$, the situation starts being complicated, with a residual disturbance RMS 50% higher than if $f_{\text{vib}} = F_s/10$. When increasing even more the vibration peak frequency ($f_{\text{vib}} = F_s/3$), the rejection is poor especially at $\delta = 0.5$ frame where about 50% of the 110 nm-RMS vibration is rejected when using the WFS-synchronised modeling, dropping to about 40% with the DM-synchronised modeling.

The simulations have also shown that in addition the DM-synchronised LQG requires a strong increase in the fudge factor α_{FF} to around ten times its pure-turbulence value. In the case of multi-modal LQG control (not developed in this article), despite a gain in stability margin (increasing from 40 degrees to 60 degrees), this high fudge factor has a deleterious effect on higher spatial orders correction.

In this case of high-frequency vibrations and using the WFS-synchronised modeling, a solution is to take F_s higher than around $5f_{\text{vib}}$ – if the sampling frequency F_s can be increased without degrading the SNR (left graphs in figure 3); meanwhile, the value of $1/F_s$ must be closer to a multiple of δ (to be at the bottom of the bells in figure 3).

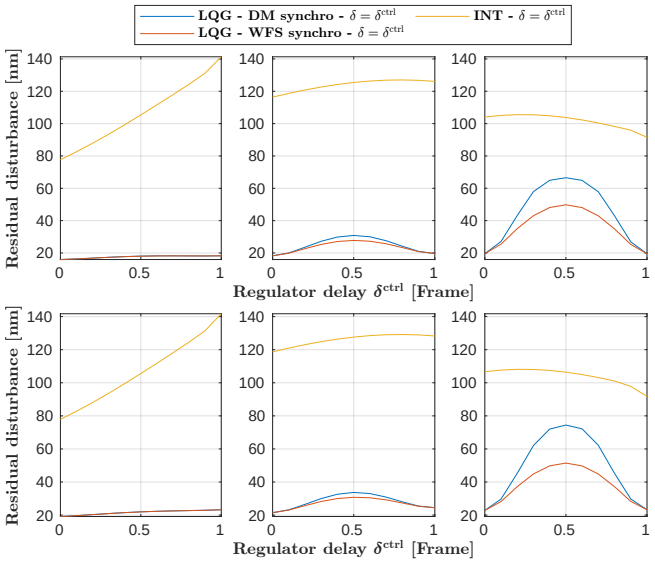

Fig. 3. (simulation, $\delta = \delta^{\text{ctrl}}$) Residual phase RMS in a case of turbulence (single tip mode) with added vibration (total RMS of 370 nm) with respect to the regulator's delay value δ^{ctrl}. Sampling frequency, top: $F_s = 200$ Hz, bottom: $F_s = 500$ Hz. Vibration frequency f_{vib} value, left to right: $F_s/10, F_s/4, F_s/3$.

5. GTCAO ON-BENCH PERFORMANCE

The AO bench GTCAO [23] is in commissioning phase at the Nasmyth platform of the 10.4 m Gran Telescopio Canarias at La Palma (Canary Islands, Spain). Its SCAO mode features an on-axis Shack-Hartmann sensor with 20 × 20 lenslets, for which the image scale is 0.35 arcsecond per pixel. There are 312 active lenslets leading to 624 measurements. A Cilas© deformable mirror with 373 active actuators is used to correct the incoming wavefront disturbance. The performance is evaluated with:

- a near-IR camera and its corresponding internal light source (central wavelength of 1.6 µm)
- the residual WFS slopes average (allowing for residual tip/tilt estimation)

The real-time computer is DARC [24], allowing for LQG controller implementation in both a WFS-synchro setting and a DM-synchro setting.

A. Tests description

During those runs, the control frequency was set to $F_s = 500$ Hz, with a loop delay of $\delta = 0.8$ (1.6 ms). A shifted phase screen simulates an atmosphere of $r_0 = 23$ cm with a speed of 10 m s^{-1}.

A tip-tilt vibration signal is simulated on the bench by sending in real time the corresponding tip-tilt commands sequences to the deformable mirror. This is of the outmost importance to stipulate in this paper, since it turns the vibrations into a both discrete and DM-synchronised perturbation. In this way, the regulator with a DM-synchro setting should here allow for a perfect "vibration" rejection. Indeed, what used to be an approximation in the slope projector C_y becomes exact (cf. section B). We can however evaluate with the WFS-synchronised regulator cases whether an error in the projectors is indeed detrimental to the final AO system performance.

The spectra of the tip and tilt disturbances are displayed in figure 4. The vibrations generated by the DM consists in four peaks, each of energy 2 rad^2, located at respective frequencies $f_{\text{vib}} = [30, 60, 100, 150]$ Hz.

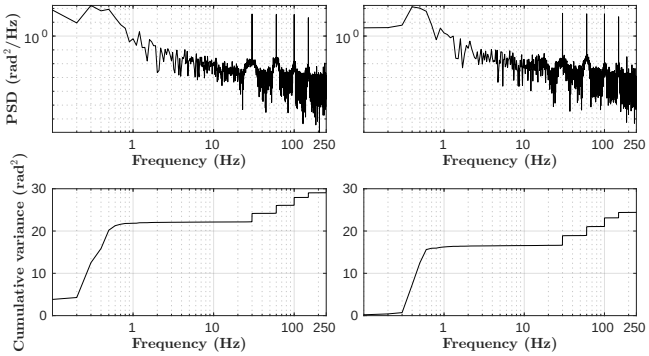

Fig. 4. (bench) PSD of the open-loop tip and tilt, with the cumulative energy on the bottom. The phase reconstruction is based on the WFS slopes. Case with DM-introduced vibrations and turbulence phase-screen related disturbance.

B. Tests results

The experimental results are compared with a simulation performed as described in section 4, taking care of simulating constant disturbances on DM time intervals .

The performances obtained on bench and in simulation are shown in figure 5. For the WFS-synchronized LQG, the on-bench performance curve features the "bell shaped" experienced in simulation (cf. section 4). For this controller (red curve and markers), the Strehl ratio is 6 points better when the delay is slightly over-estimated ($\delta^{\text{ctrl}} = \delta + 0.2$) and one point better when it is severely under-estimated ($\delta^{\text{ctrl}} = \delta - 0.7$). The DM-synchronised controller (blue curve and markers) shows the concurrence between the optimal δ^{ctrl} value and the system one, leading to choose $\delta^{\text{ctrl}} = \delta$. The values at $\delta^{\text{ctrl}} = 0.1$ shows a close-to-unstable AO loop with poor stability margins.

Finally, the congruence between bench results and simulations validates those described in section 4. Noting that the two TT curves (o) are a translation downwards of the two SR bench curves (+), we confirm that the correction of turbulence-only disturbance for higher-order Zernike modes is not affected by the modeling error on δ^{ctrl}. As seen in figure 2, the pure turbulence distortion correction is not deteriorated.

C. Optimal asynchronous LQG

In figure 6, we compare in simulation the performance (residual variance) obtained with the suboptimal DM- or WFS-synchronized LQGs and with the optimal LQG based on the

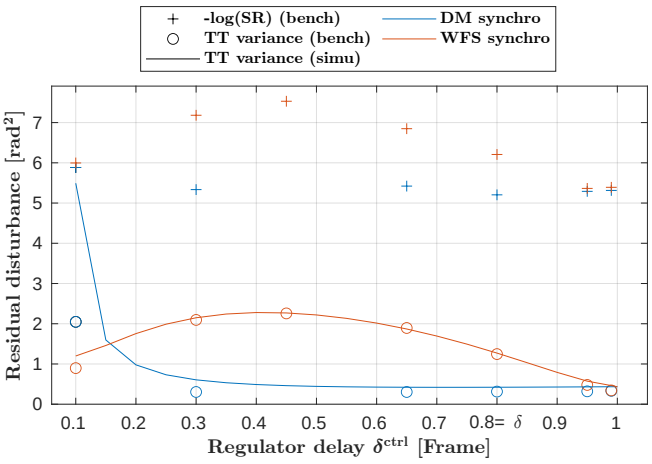

Fig. 5. (bench and simulation, $\delta = 0.8$) Residual disturbance energy evaluated from bench scientific images (crosses), bench residual slopes (circles) and simulations (solid line). The DM-synchronised and WFS-synchronised LQG regulators are build and tested for different value given to δ^{ctrl}. Case with DM-introduced vibrations. On bench as on simulations, the integrator residual TT overcrosses 8 rad^2 (with $-\log(\text{SR}) = 13$ rad^2).

asynchronous model presented in section 6. Note that this optimal LQG was not designed from the continuous-time model corresponding to shaping filters used to generate the perturbation, but from a continuous state-space model computed by de-discretizing (using results of section C) the same disturbance model identified from simulated WFS measurements as in section 4. All LQG controllers were designed using values of δ^{ctrl} ranging from zero to one, while the actual system delay was set to $\delta = 0.8$.

As expected, the optimal LQG gives the best performance for $\delta^{\text{ctrl}} = \delta$. This performance level corresponds to what could be achieved for the best tuning of the DM-synchronized LQG on the bench, as shown in figure 5. Interestingly, the optimal LQG regulator also outperforms the two suboptimal controllers even when $\delta^{\text{ctrl}} \neq \delta$, and its performance is robust to even a large mismatch between the two values.

We also notice, as in figure 5, that it is still advantageous to take a value of δ^{ctrl} slightly larger than δ for the WFS-synchronised LQG (optimal value $\delta^{\text{ctrl}} = 0.9$ in this test).

6. ASYNCHRONOUS DISCRETE-TIME MODEL AND OPTIMAL CONTROL

As noted in Section 2, when the measurement delay δ takes non-integer values, solving the optimal control problem requires a disturbance model able to produce as outputs successive temporal occurrences of both $\overline{\phi}$ and $\overline{\phi}^{\delta}$, *i.e.*, averages of ϕ over asynchronous time intervals. This model should take the standard state-space form of Eq. (20)-(22).

In this section, we show how to construct this discrete-time model from a continuous-time stochastic model of ϕ by applying the lifting procedure. Lifting essentially involves discretizing the continuous-time model over control (DM) intervals and augmenting this discrete model with appropriate additional states corresponding to all events occurring between two successive sampling times – in our case, the asynchronous measurement

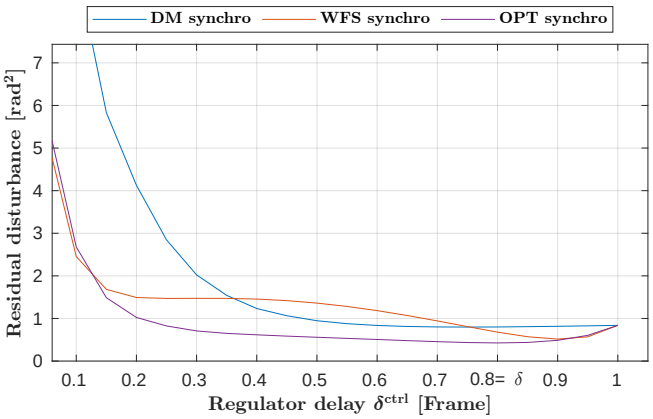

Fig. 6. (simulation, $\delta = 0.8$) Residual disturbance energy evaluated from simulations with *continuous-time* vibrations. The DM-synchronised, WFS-synchronised and optimal LQG regulators are built and tested for several values of δ^{ctrl}.

process (see, e.g., [7]).

As noted previously, the lifting technique was applied to optimal AO control with fractional delays in [8, 9]. The streamlined construction presented here develops simpler constructive procedures to compute the matrices $A, \Gamma, C_{\overline{\phi}}, C_{\overline{\phi}^\delta}, \Sigma_v$ with fully analytical tools that involve only matrix exponentials and Lyapunov equations resolution.

A. Disturbance evolution over arbitrary time intervals

We now proceed to build a model describing the evolution of the phase and of its integral over arbitrary time intervals. The starting point of this construction will a be a continuous stochastic model in standard state-space form:

$$\begin{cases} dx_\phi(t) = A_\phi x_\phi(t)\,dt + v_c(t)\,dv_c\,, & \textbf{(41)} \\ \phi(t) = C_\phi x_\phi(t)\,, & \textbf{(42)} \end{cases}$$

where the model input v_c is a (vector-valued) continuous Gaussian white noise with variance $Q_\phi \geq 0$. This model is required to be stable. This means that the matrix A_ϕ is Hurwitz, *i.e.* has all its eigenvalues values with strictly negative real parts. Discretizing Eq. (41) on any time interval $[t_1, t_2]$ yields:

$$x_\phi(t_2) = e^{A_\phi(t_2-t_1)} x_\phi(t_1) + v_1(t_1,t_2)\,, \qquad \textbf{(43)}$$

with

$$v_1(t_1,t_2) = \int_{t_1}^{t_2} e^{A_\phi s} v_c(t_2-s)\,ds\,. \qquad \textbf{(44)}$$

From the definition of a continuous-time white noise, this random vector is zero-mean and Gaussian, with covariance matrix

$$\Sigma_{v_1}(t_2-t_1) = \int_0^{t_2-t_1} e^{A_\phi s} Q_\phi e^{A_\phi s^{\mathrm{T}}}\,ds\,. \qquad \textbf{(45)}$$

Also from the definition of a continuous-time white noise, $v_1(t_1,t_2)$ and $v_1(t_3,t_4)$ are independent when the two intervals do not overlap, *i.e.* when $t_3 \geq t_2$. The continuous variable allowing the computation of both $\overline{\phi}_k^\delta$ and $\overline{\phi}_k$ is the rescaled integral $\psi(t)$ of the phase:

$$\psi(t) \triangleq \frac{1}{T_\mathrm{s}} \int_0^t \phi(s)\,ds\,. \qquad \textbf{(46)}$$

The next step is to augment the state by setting

$$\eta(t) \triangleq \begin{pmatrix} x_\phi(t) \\ \psi(t) \end{pmatrix}. \qquad \textbf{(47)}$$

Since $d\psi/dt = \phi/T_\mathrm{s} = C_\phi x_\phi/T_\mathrm{s}$, the differential equation governing the stochastic process η is

$$d\eta(t) = A_\eta \eta(t)dt + \Gamma_\eta v_c(t) dv_c\,, \qquad \textbf{(48)}$$

with

$$A_\eta \triangleq \begin{pmatrix} A_\phi & 0 \\ \frac{1}{T_\mathrm{s}} C_\phi & 0 \end{pmatrix} \quad \Gamma_\eta \triangleq \begin{pmatrix} I \\ 0 \end{pmatrix}. \qquad \textbf{(49)}$$

Discretizing Eq. (48) over the time interval $[t_1, t_2]$ yields:

$$\eta(t_2) = e^{A_\eta(t_2-t_1)} \eta(t_1) + v_\eta(t_1,t_2)\,, \qquad \textbf{(50)}$$

where

$$v_\eta(t_1,t_2) \triangleq \begin{pmatrix} v_1(t_1,t_2) \\ v_2(t_1,t_2) \end{pmatrix} = \int_{t_1}^{t_2} e^{A_\eta s} \Gamma_\eta v_c(t_2-s)\,ds\,. \qquad \textbf{(51)}$$

The vector-valued random variable $v_\eta(t_1,t_2)$ is zero-mean and Gaussian, with covariance matrix

$$\Sigma_{v_\eta}(t_2-t_1) = \int_0^{t_2-t_1} e^{A_\eta s} \Gamma_\eta \Gamma_\eta^{\mathrm{T}} e^{A_\eta s^{\mathrm{T}}}\,ds\,. \qquad \textbf{(52)}$$

As shown in Appendix A, the matrix exponential of A_η is given by

$$e^{A_\eta s} = \begin{pmatrix} e^{A_\phi s} & 0 \\ C_\psi(s) & I \end{pmatrix}, \qquad \textbf{(53)}$$

with

$$C_\psi(s) = \frac{1}{T_\mathrm{s}} C_\phi A_\phi^{-1} (e^{A_\phi s} - I)\,. \qquad \textbf{(54)}$$

As for the covariance matrix function $\Sigma_{v_\eta}(s)$, it can be partitioned as

$$\Sigma_{v_\eta}(s) \triangleq \begin{pmatrix} \Sigma_{v_1}(s) & \Sigma_{v_1 v_2}(s) \\ \Sigma_{v_1 v_2}(s)^{\mathrm{T}} & \Sigma_{v_2}(s) \end{pmatrix}, \qquad \textbf{(55)}$$

where Σ_{v_1}, Σ_{v_2} and $\Sigma_{v_1 v_2}$ are matrix-valued functions which can be evaluated using formulas in Appendix A.

B. Discrete-time model

The phase averages over the DM and WFS intervals can now be retrieved from the corresponding increments of the integral ψ:

$$\overline{\phi}_k = \psi(kT_\mathrm{s}) - \psi((k-1)T_\mathrm{s}) \qquad \textbf{(56)}$$

$$\overline{\phi}_k^\delta = \psi((k-\delta)T_\mathrm{s}) - \psi((k-1-\delta)T_\mathrm{s})\,. \qquad \textbf{(57)}$$

A convenient choice of augmented state vector is then:

$$z_k \triangleq \begin{pmatrix} x_\phi(kT_\mathrm{s}) \\ \psi(kT_\mathrm{s}) - \psi((k-\delta)T_\mathrm{s}) \\ \psi((k-\delta)T_\mathrm{s}) - \psi((k-1)T_\mathrm{s}) \\ \psi((k-1)T_\mathrm{s}) - \psi((k-1-\delta)T_\mathrm{s}) \end{pmatrix}. \qquad \textbf{(58)}$$

The process noise corresponding to this augmented state will be similarly constructed from the values of $v_\eta(t_1,t_2)$ computed over the intervals $[kT_\mathrm{s},(k+1-\delta)T_\mathrm{s}]$ and $[(k+1-\delta)T_\mathrm{s},(k+1)T_\mathrm{s}]$:

$$v_k \triangleq \begin{pmatrix} v_\eta((k+1-\delta)T_\mathrm{s},(k+1)T_\mathrm{s}) \\ v_\eta(kT_\mathrm{s},(k+1-\delta)T_\mathrm{s}) \end{pmatrix} \tag{59}$$

$$= \begin{pmatrix} v_{k,1} \\ v_{k,2} \\ v_{k,3} \\ v_{k,4} \end{pmatrix} = \begin{pmatrix} v_1\left((k+(1-\delta))T_\mathrm{s},(k+1)T_\mathrm{s}\right) \\ v_2\left((k+(1-\delta))T_\mathrm{s},(k+1)T_\mathrm{s}\right) \\ v_1\left(kT_\mathrm{s},k+(1-\delta)T_\mathrm{s}\right) \\ v_2\left(kT_\mathrm{s},k+(1-\delta)T_\mathrm{s}\right) \end{pmatrix}. \tag{60}$$

Because occurrences of v_η taken over non-overlapping intervals are independent zero-mean Gaussian vectors, the random process v is a discrete zero-mean Gaussian white noise with block-diagonal covariance matrix

$$\Sigma_v = \begin{pmatrix} \Sigma_{v_\eta}(\delta T_\mathrm{s}) & 0 \\ 0 & \Sigma_{v_\eta}((1-\delta)T_\mathrm{s}) \end{pmatrix}. \tag{61}$$

The evolution of this augmented state between two successive DM sampling instants is obtained by successively applying Eq. (50) for the intervals $[kT_\mathrm{s},(k+1-\delta)T_\mathrm{s}]$ and $[(k+1-\delta)T_\mathrm{s},(k+1)T_\mathrm{s}]$. This yields:

$$x_\phi((k+1)T_\mathrm{s}) = e^{A_\phi \delta T_\mathrm{s}} x_\phi((k-\delta+1)T_\mathrm{s}) + v_{k,1}\,, \tag{62}$$

$$x_\phi((k-\delta+1)\,T_\mathrm{s}) = e^{A_\phi(1-\delta)T_\mathrm{s}} x_\phi(kT_\mathrm{s}) + v_{k,3}\,, \tag{63}$$

$$\psi((k+1)T_\mathrm{s}) - \psi((k-\delta+1)T_\mathrm{s} = C_\psi(\delta T_\mathrm{s}) x_\phi((k-\delta+1)\,T_\mathrm{s}) + v_{k,2}\,, \tag{64}$$

$$\psi((k-\delta+1)T_\mathrm{s}) - \psi(kT_\mathrm{s}) = C_\psi((1-\delta)T_\mathrm{s}) x_\phi(kT_\mathrm{s}) + v_{k,4}\,. \tag{65}$$

Rearranging these terms leads to a discrete-time state equation in the desired form

$$z_{k+1} = Az_k + \Gamma v_k\,, \tag{66}$$

with

$$A = \begin{pmatrix} e^{A_\phi T_\mathrm{s}} & 0 & 0 & 0 \\ C_\psi(\delta T_\mathrm{s}) e^{A_\phi(1-\delta)T_\mathrm{s}} & 0 & 0 & 0 \\ C_\psi((1-\delta)T_\mathrm{s}) & 0 & 0 & 0 \\ 0 & I & 0 & 0 \end{pmatrix}, \tag{67}$$

$$\Gamma = \begin{pmatrix} I & 0 & e^{A_\phi \delta T_\mathrm{s}} & 0 \\ 0 & I & C_\psi(\delta T_\mathrm{s}) & 0 \\ 0 & 0 & 0 & I \\ 0 & 0 & 0 & 0 \end{pmatrix}. \tag{68}$$

The two desired averaged phases $\overline{\phi}_k$ and $\overline{\phi}^\delta_k$ are then obtained as

$$\overline{\phi}_k = C_{\overline{\phi}} z_k\,, \tag{69}$$

$$\overline{\phi}^\delta_k = C_{\overline{\phi}^\delta} z_k\,, \tag{70}$$

with:

$$C_{\overline{\phi}} = \begin{pmatrix} 0 & I & I & 0 \end{pmatrix}, \tag{71}$$

$$C_{\overline{\phi}^\delta} = \begin{pmatrix} 0 & 0 & I & I \end{pmatrix}, \tag{72}$$

giving thereupon access to the measurement as

$$y_k = C_y z_k - DN\left((1-\delta)\,u_{k-1} + \delta u_{k-2}\right) + w_k\,, \tag{73}$$

where

$$C_y = DC_{\overline{\phi}^\delta} = \begin{pmatrix} 0 & 0 & D & D \end{pmatrix}. \tag{74}$$

Setting $x_k = z_k$, the optimal LQG then retains the same form as in Section 2:

$$u^*_k = P_u C_{\overline{\phi}} \widehat{x}_{k+1|k}\,, \tag{75}$$

where the minimum-variance prediction $\widehat{x}_{k+1|k} = \mathrm{E}[x_{k+1}|\mathcal{I}_k]$ is the output of a Kalman filter built on Eq. (20)-(21):

$$\widehat{x}_{k+1|k} = A\widehat{x}_{k|k-1} + L_\infty(y_k - \widehat{y}_{k|k-1})\,, \tag{76}$$

$$\widehat{y}_{k|k-1} = C_y \widehat{x}_{k|k-1} - DN\left((1-\delta)u_{k-1} + \delta u_{k-2}\right). \tag{77}$$

C. Building the continuous disturbance model

A key ingredient to construct lifted asynchronous disturbance model is a continuous-time stochastic disturbance model in the form of Eq. (41)-(42), and more precisely the three matrices A_ϕ, C_ϕ and Q_ϕ.

We show here how these matrices can be retrieved from a state-space model of the averaged disturbance $\overline{\phi}$, which in turn can be built either from statistical priors or identified from WFS recorded data. Such a model would correspond to the state-space representation (30)-(31) in the synchronous case $\delta = 1$. For the sake of clarity, we recall here this state-space representation:

$$\begin{cases} x_{\overline{\phi},k+1} = A_{\overline{\phi}} x_{\overline{\phi},k} + \Gamma_{\overline{\phi}} v_{\overline{\phi},k}\,, & (78) \\ \overline{\phi}_k = C_{\overline{\phi}} x_{\overline{\phi},k}\,. & (79) \end{cases}$$

We will make the additional assumption that the disturbance covariance matrix $\mathrm{Var}(\overline{\phi}) = \Sigma_{\overline{\phi}}$ is known.

Let us now suppose that ϕ has been generated by a continuous model in the form (41)-(42). Applying the results in the previous subsection in the special case $\delta = 1$, we get

$$x_\phi(kT_\mathrm{s}) = e^{A_\phi T_\mathrm{s}} x_\phi((k-1)T_\mathrm{s}) + v_1((k-1)T_\mathrm{s},kT_\mathrm{s})\,, \tag{80}$$

$$\overline{\phi}_k = C_\psi(T_\mathrm{s}) x_\phi(k-1) + v_2((k-1)T_\mathrm{s},kT_\mathrm{s})\,. \tag{81}$$

The first equation can be made to match Eq. (78) by setting $x_{\overline{\phi},k} = x_\phi((k-1)T_\mathrm{s})$ and $\Gamma_{\overline{\phi}} v_{\overline{\phi},k} = v_1((k-1)T_\mathrm{s},kT_\mathrm{s})$. The second one needs to be slightly modified by noting that when (78)-(79) is a model identified from WFS measurements, its output corresponds to the predictable part of $\overline{\phi}_k$, in other words to the conditional expectation

$$\mathrm{E}(\overline{\phi}_k|x_{\overline{\phi},k}) = \mathrm{E}(\overline{\phi}_k|x_\phi((k-1)T_\mathrm{s})) = C_\psi(T_\mathrm{s}) x_\phi((k-1)T_\mathrm{s}) = \frac{1}{T_\mathrm{s}} C_\phi A_\phi^{-1}(e^{A_\phi T_\mathrm{s}} - I) x_{\overline{\phi},k}\,. \tag{82}$$

Equating Eq. (78) with Eq. (80) and Eq. (79) with Eq. (82) leads to:

$$A_\phi = \frac{1}{T_\mathrm{s}} \log(A_{\overline{\phi}})\,, \tag{83}$$

$$C_\phi = C_{\overline{\phi}}(A_{\overline{\phi}} - I)^{-1} \log(A_{\overline{\phi}})\,. \tag{84}$$

Note that $\log(A_{\overline{\phi}})$ is well defined and computable as long as $A_{\overline{\phi}}$ has no eigenvalue on the negative real axis. This condition can always be enforced by computing a modal realization of (78)-(79) and removing the offending states.

To compute Q_ϕ, we use the fact that $\mathrm{Var}(\phi) \approx \mathrm{Var}(\overline{\phi})$, since the difference between the two is the intersampling variance. Thus, $\mathrm{Var}(\overline{\phi}) = \Sigma_{\overline{\phi}}$ should be approximately equal to $\Sigma_\phi = C_\phi P_\phi C_\phi^{\mathrm{T}}$, where P_ϕ is the solution of the continuous Lyapunov equation

$$A_\phi P_\phi + P_\phi A_\phi^{\mathrm{T}} + Q_\phi = 0\,. \tag{85}$$

To select the appropriate value of Q_ϕ, we first note that the mapping from Q_ϕ to Σ_ϕ is obviously linear. Consider first the case where the shaping filter transfer function $F(z) = C_{\overline{\phi}}(zI - A_{\overline{\phi}})^{-1}\Gamma_{\overline{\phi}}$ is diagonal. Under this assumption, it is immediately shown that this mapping is a pointwise matrix multiplication, in other words that for every couple of coordinates (i,j), $\Sigma_\phi(i,j) = Q_\phi(i,j)G(i,j)$, where G is a square symmetric matrix.

Thus, a simple procedure to ensure that $\Sigma_\phi = \Sigma_{\overline{\phi}}$ is:

1. select $Q_\phi = Q_{\phi,0}$, where $Q_{\phi,0}$ is any positive definite matrix with all its element non-zero (for example, $Q_{\phi,0} = I + \varepsilon$);
2. compute the corresponding solution $P_{\phi,0}$ of Eq. (85);
3. compute $\Sigma_{\phi,0} = C_\phi P_{\phi,0} C_\phi^{\mathrm{T}}$;
4. for all couples of coordinates (i,j), take

$$Q_\phi(i,j) = \frac{Q_{\phi,0}(i,j)\Sigma_{\overline{\phi}}(i,j)}{\Sigma_{\phi,0}(i,j)}\,. \tag{86}$$

When $F(z)$ is non diagonal, the linear mapping between the coordinates of Q_ϕ and those of Σ_ϕ needs to be identified using a sequence of semi-positive definite test matrices $Q_{\phi,1}, \ldots, Q_{\phi,n(n+1)/2}$, where $n = \dim(\phi)$ is the number of disturbance modes. Inverting this linear transformation then enables to compute the appropriate value of Q_ϕ.

7. THEORETICAL PERFORMANCE AND ROBUSTNESS

The discrete-time disturbance model (20)-(22) constructed in the previous section can be used to compute the expected performance of the asynchronous AO system for any optimal or suboptimal linear controller. As we shall see, it is possible to compute not only the theoretical value of the residual phase variance (including the intersampling variance), but also the residual phase PSD, thus enabling a detailed performance assessment in the form of a frequency-dependent rejection gain. The asynchronous model also enables to evaluate the AO loop's modal stability margins (gain, phase and delay).

These performance calculations rely on the key property that *both* the continuous-time model (41)-(42) and the discrete-time model (66)-(73) define stationary and ergodic zero-mean Gaussian processes. In particular, the solution z of Eq. (66) is a stationary ergodic zero-mean Gaussian vector-valued process, the covariance matrix of which is the unique solution $\Sigma_z = \mathrm{Var}(z_k)$ of the discrete Lyapunov equation

$$A\Sigma_z A^{\mathrm{T}} + \Gamma\Sigma_v\Gamma^{\mathrm{T}} = \Sigma_z\,. \tag{87}$$

A. Intersampling variance and disturbance PSD

As shown in Section 2, in the absence of actuator dynamics the overall performance of the AO system, measured by the averaged residual phase variance $J(u)$ of the AO system, is the sum of a control-dependent discrete criterion $J^{\mathrm{d}}(u)$ and of a control-independent intersampling variance:

$$J(u) = J^{\mathrm{d}}(u) + \sigma^2_{\phi,\mathrm{is}}\,. \tag{88}$$

Because $\phi(t)$ and $\overline{\phi}_k$ are both ergodic, for $u = 0$ the almost-sure identities hold:

$$\begin{aligned} J(0) &= \mathrm{trace}(\mathrm{Var}(\phi(t))) \\ &= J^{\mathrm{d}}(0) + \sigma^2_{\phi,\mathrm{is}} \\ &= \mathrm{trace}(\mathrm{Var}(\overline{\phi}_k)) + \sigma^2_{\phi,\mathrm{is}}\,, \end{aligned} \tag{89}$$

where $\mathrm{trace}(\Sigma)$ denotes the trace of Σ. But since $\overline{\phi}_k = C_{\overline{\phi}} z_k$, we get

$$\mathrm{Var}(\overline{\phi}_k) = C_{\overline{\phi}}\Sigma_z C_{\overline{\phi}}^{\mathrm{T}}\,. \tag{90}$$

Because the augmented state x_k contains an occurrence of $x_\phi(t)$ at sampling time $t = kT_\mathrm{s}$, the corresponding value of $\phi(kT_\mathrm{s})$ can be generated as $\phi(kT_\mathrm{s}) = C_{\phi,z} z_k$, with

$$C_{\phi,z} = \begin{pmatrix} C_\phi & 0 & 0 & 0 \end{pmatrix}. \tag{91}$$

Thus, the following almost-sure identities hold:

$$\mathrm{Var}(\phi(t)) = \mathrm{Var}(\phi(kT_\mathrm{s})) = C_{\phi,z}\Sigma_z C_{\phi,z}^{\mathrm{T}}\,, \tag{92}$$

$$\begin{aligned} \sigma^2_{\phi,\mathrm{is}} &= \mathrm{trace}(\mathrm{Var}(\phi(t))) - \mathrm{trace}(\mathrm{Var}(\overline{\phi}_k)) \\ &= \mathrm{trace}(C_{\phi,z}\Sigma_z C_{\phi,z}^{\mathrm{T}}) - \mathrm{trace}(C_{\overline{\phi}}\Sigma_z C_{\overline{\phi}}^{\mathrm{T}})\,. \end{aligned} \tag{93}$$

The discrete-time stochastic model (20)-(22) also enables to evaluate the PSD of (for example) ϕ. This stems from the fact that the z-transforms of v and ϕ are related through $\Phi(z) = H_{v,\phi}(z)V(z)$, where $H_{v,\phi}(z)$ is the transfer function of the corresponding shaping filter:

$$H_{v,\phi}(z) = C_{\phi,z}(zI - A)^{-1}\Gamma\,. \tag{94}$$

Since v is a white noise, for any frequency f the PSD Φ_ϕ of ϕ can be evaluated by setting $z = 2i\pi f/F_\mathrm{s}$ and computing

$$\Phi_\phi(z) = H_{v,\phi}(z)\Phi_v(z)H_{v,\phi}(z)^* = H_{v,\phi}(z)\Sigma_v H_{v,\phi}(z)^* \tag{95}$$

(where M^* denotes the conjugate transpose of M). One can similarly evaluate the PSD of $\overline{\phi}$, or for that matter any possible linear combination of the coordinates of x.

B. Closed-loop state-space representation

In order to apply the same procedures to evaluate control performance, one needs to construct a stochastic state-space model of the closed-loop AO system with inputs v and w and output $\overline{\phi}^{\mathrm{res}}$. The first step is to put the AO controller itself in the general state-space form

$$\begin{cases} x_{u,k+1} = A_u x_{u,k} + B_u y_k\,, & (96) \\ u_k = C_u x_{u,k+1}\,. & (97) \end{cases}$$

For an integrator, this is achieved by setting $x_{u,k} = u_{k-1}$, so that $A_u = \alpha_{\mathrm{leak}} I$, $C_u = I$ and $B_u = gM_{\mathrm{com}}$. For LQG AO controllers, an appropriate choice of x_u and B_u is

$$x_{u,k} = \begin{pmatrix} \widehat{x}_{k|k-1} \\ u_{k-2} \end{pmatrix}, \quad B_u = \begin{pmatrix} L_\infty \\ 0 \end{pmatrix}. \tag{98}$$

The construction of A_u and C_u for the optimal and suboptimal LQG controllers in Sections 3 and 6 is detailed in Appendix B.

A convenient choice of internal state for the closed-loop AO system model is then:

$$x_{\text{perf},k} \triangleq \begin{pmatrix} z_k \\ x_{u,k} \\ u_{k-2} \end{pmatrix} . \tag{99}$$

Combining Eq. (66), Eq. (69), Eq. (73), Eq. (96) and Eq. (97), we get the stochastic state-space "performance model"

$$x_{\text{perf},k+1} = A_{\text{perf}} x_{\text{perf},k} + \Gamma_{\text{perf},v} v_k + \Gamma_{\text{perf},w} w_k , \tag{100}$$

$$\overline{\phi}^{\text{res}}_k = C_{\text{perf}} x_{\text{perf},k} , \tag{101}$$

where

$$A_{\text{perf}} = \begin{pmatrix} A & 0 & 0 \\ B_u C_y & A_u - (1-\delta) B_u M_{\text{int}} C_u & -\delta B_u M_{\text{int}} \\ 0 & C_u & 0 \end{pmatrix} , \tag{102}$$

$$\Gamma_{\text{perf},v} = \begin{pmatrix} \Gamma \\ 0 \\ 0 \end{pmatrix} , \qquad \Gamma_{\text{perf},w} = \begin{pmatrix} 0 \\ B_u \\ 0 \end{pmatrix} , \tag{103}$$

$$C_{\text{perf}} = \begin{pmatrix} C_{\overline{\phi}} & -NC_u & 0 \end{pmatrix} . \tag{104}$$

C. Performance evaluation: residual phase variance and PSD

Using the performance model following the same approach as in the previous subsection, we can evaluate the theoretical values of J^d and also the spatial covariance matrix of $\overline{\phi}^{\text{res}}$. First, we compute the unique solution $\Sigma_{\text{perf}} = \text{Var}(x_{\text{perf},k})$ of the discrete Lyapunov equation

$$A_{\text{perf}} \Sigma_{\text{perf}} A_{\text{perf}}^{\text{T}} + \Gamma_{\text{perf},v} \Sigma_v \Gamma_{\text{perf},v}^{\text{T}} + \Gamma_{\text{perf},w} \Sigma_w \Gamma_{\text{perf},w}^{\text{T}} = \Sigma_{\text{perf}} . \tag{105}$$

From this, we get

$$J^d(u) = \text{trace}(\text{Var}(\overline{\phi}^{\text{res}}_k)) = \text{trace}(C_{\text{perf}} \Sigma_{\text{perf}} C_{\text{perf}}^{\text{T}}) . \tag{106}$$

To evaluate $\Phi_{\overline{\phi}^{\text{res}}}$, the PSD of $\overline{\phi}^{\text{res}}$, we first compute the closed-loop transfer functions between v and $\overline{\phi}^{\text{res}}$ and between w and $\overline{\phi}^{\text{res}}$:

$$H_{v,\overline{\phi}^{\text{res}}}(z) = C_{\text{perf}} (zI - A_{\text{perf}})^{-1} \Gamma_{\text{perf},v} , \tag{107}$$

$$H_{w,\overline{\phi}^{\text{res}}}(z) = C_{\text{perf}} (zI - A_{\text{perf}})^{-1} \Gamma_{\text{perf},w} . \tag{108}$$

Since v and w are mutually independent white noises, we get:

$$\Phi_{\overline{\phi}^{\text{res}}}(z) = H_{v,\overline{\phi}^{\text{res}}}(z) \Sigma_v H_{v,\overline{\phi}^{\text{res}}}(z)^* + H_{w,\overline{\phi}^{\text{res}}}(z) \Sigma_w H_{w,\overline{\phi}^{\text{res}}}(z)^* . \tag{109}$$

An example of application is presented in figure 7, allowing for a mutual validation of this method and of the simulations performed in section 4.

D. Performance evaluation: rejection and noise propagation gains

In the non-asynchronous case, the PSD of the residual phase $\overline{\phi}^{\text{res}}$ can also be computed from the PSD of $\overline{\phi}$, using AO loop rejection transfer function $T_{\text{rej}}(z)$:

$$\Phi_{\overline{\phi}^{\text{res}}}(z) = T_{\text{rej}}(z) \Phi_{\overline{\phi}}(z) T_{\text{rej}}(z)^* . \tag{110}$$

This calculation is no longer possible in the asynchronous case, since the trajectories of $\overline{\phi}^{\text{res}}$ cannot be computed from those of $\overline{\phi}$. However, it is possible to evaluate for all turbulence modes a "rejection gain" by setting $\Sigma_w = 0$ and taking the ratios of the corresponding diagonal terms of $\Phi_{\overline{\phi}^{\text{res}}}(z)$ and $\Phi_{\overline{\phi}}(z)$. Likewise, a noise propagation gain can be evaluated by following the same procedure with $\Sigma_v = 0$ and taking the ratios of the diagonal terms of $\Phi_{\overline{\phi}^{\text{res}}}(z)$ and Σ_w. The theoretical evaluation procedure is implemented in the next section, with a display of the rejection gains $\Phi_{\overline{\phi}^{\text{res}}} / \Phi_{\overline{\phi}}$ in figure 12.

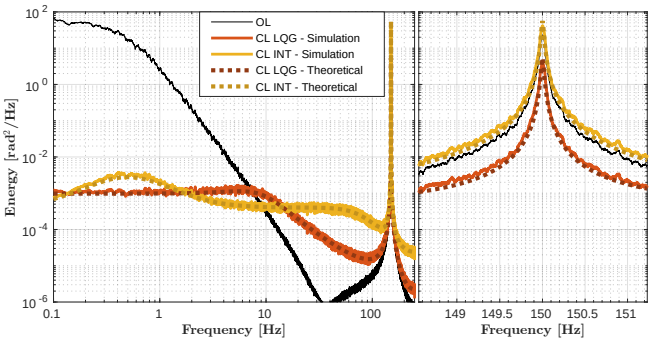

Fig. 7. (simulation and theoretical, $\delta = 0.5$) PSD of the DM-synchronized phase, disturbed $\overline{\phi}$ (OL, black curve) and residual $\overline{\phi}^{\text{res}}$ (yellowish: integrator; reddish: WFS-synchronized LQG controller with $\delta^{\text{ctrl}} = 0.5$). Comparison of simulation-based (solid lines) and state-space-based (dashed lines, from Eq. (109)) computations. On the right is a zoom on the vibration peak. Sampling frequency $F_s = 500\,\text{Hz}$.

E. Stability margins

An important issue in control design is whether the closed-loop system remains stable in presence of modeling errors. In the case of asynchronous measurements, it is of course critical to take into account discrepancies between the actual system delay δ and the value δ^{ctrl} used to design the LQG controller. In the non-asynchronous case, a relevant way to assess robust stability is to evaluate the phase, gain and delay margins corresponding to the turbulence modes. This is achieved by taking the diagonal terms of the rejection transfer function and computing the corresponding equivalent open-loop transfer function (OLTF).

This procedure can be adapted to the asynchronous case by noting that the incoming continuous-time disturbance $\phi(t)$ can be decomposed as $\phi = \overline{\phi}^{\delta} + \widetilde{\phi}^{\delta}$, where the WFS-synchronized intersampling signal $\widetilde{\phi}^{\delta}(t)$ is not measured by the WFS. As a consequence, the stability of the asynchronous loop is equivalent to the stability of the closed-loop system with input $\overline{\phi}^{\delta}$ and output y.

This closed-loop transfer function can itself be computed from the regulateur transfer function, namely:

$$TF_{\text{regul}}(z) = zC_u (zI - A_u)^{-1} B_u . \tag{111}$$

Taking the fractional delay into account, the corresponding open-loop transfer function is

$$TF_{\mathrm{OL}}(z) = N\left(\delta z^{-1} + (1-\delta)\right) TF_{\mathrm{regul}}(z) D z^{-1} \qquad \textbf{(112)}$$

In the single-mode case, D and N become scalar numbers. This enables to draw a Nyquist plot and to evaluate the stability margins.

8. PERFORMANCE EVALUATION FOR TIP-TILT SIMULATIONS

We come back to the LQG-DM and LQG-WFS regulators performance compared now with the third one which is the optimal LQG, LQG-OPT, in Figure 8. The performance results show that the optimal LQG allows to correct the wavefront independently from the presence of a fractional delay in the system.

We show in Figure 9 the effect of a calibration error of ± 0.1 between δ^{ctrl} and the true value δ (0.2 ms), where the worst residual disturbance RMS is retained in each case. All controllers show a robust behavior, the optimal one keeping its advantage over almost the whole range of delays. Our experience on the processed examples made us realize that it was possible to slightly improve the performance of LQG-WFS by tuning δ^{ctrl} away from δ, as done in Figure 8. The best tuned value of δ^{ctrl} for the LQG-DM controller stays equal to δ. This is visible in a detailed example of the error impact, shown in Figure 11 for the case where $\delta = 0.5$ frame.

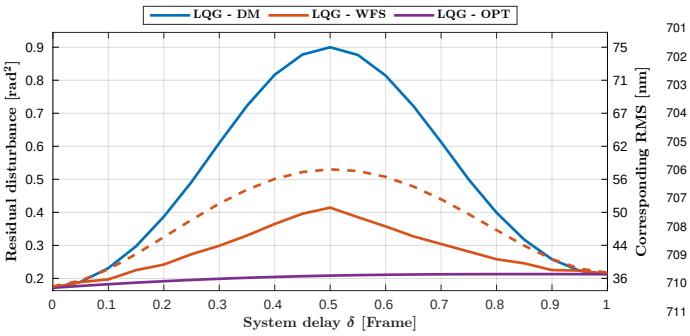

Fig. 8. (theoretical, tuned δ^{ctrl}) Residual phase variance in rad^2 (left scale) and corresponding residual phase RMS (right nonlinear scale) in case of turbulence with added vibrations (total RMS of 370 nm) as a function of the system delay δ. Sampling frequency $F_{\mathrm{s}} = 500$ Hz. Vibration frequencies $f_{\mathrm{vib}} = 30, 60, 100$ and 150 Hz. Suboptimal regulators are defined with their best-tuned δ^{ctrl}. The dashed red curve corresponds to $\delta^{\mathrm{ctrl}} = \delta$, different from the best-tuned values.

A. Stability margins and robustness

We can calculate and compare the stability margins displayed in figure 10. It can be seen that the gain margins are roughly the same whatever the LQG design, with the usual possibility to increase them by tuning upwards the fudge factor. However, the delay margins are interestingly showing that:

- Contrarily to LQG-WFS and LQG-OPT, LQG-DM cannot gain much in delay stability margin by tuning the fudge factor. It is way easier for LQG-WFS. This is understandable from the fact that the Kalman filter in the LQG-WFS case is not making approximations while LQG-DM does.

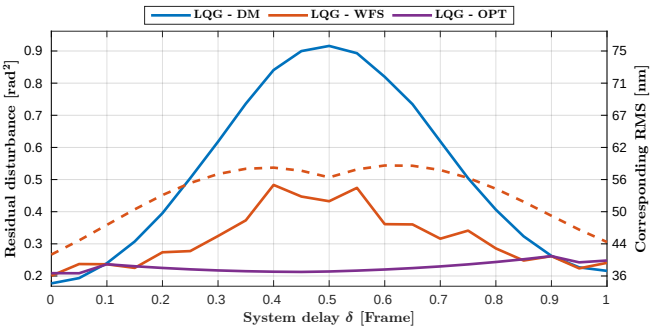

Fig. 9. (theoretical, mistuned δ^{ctrl}) Residual phase variance in rad^2 (left scale) and corresponding residual phase RMS (right nonlinear scale) in case of turbulence with added vibrations (total RMS of 370 nm) as a function of the system delay δ. Sampling frequency $F_{\mathrm{s}} = 500$ Hz. Vibration frequencies $f_{\mathrm{vib}} = 30, 60, 100$ and 150 Hz. Suboptimal regulators are defined by taking the best-tuned δ^{ctrl} of Figure 8 ± 0.1 frame. The dashed red curve corresponds to $\delta^{\mathrm{ctrl}} = \delta \pm 0.1$.

- The change in stability margin, by playing with the fudge factor, is mainly possible for delay values δ nearby 0.5 frame. It is the location where the vibration rejection is compromised by the modeling error in the LQG-WFS regulator case. Moreover, the margin value itself is almost doubled for $\delta = 0.5$ frame with respect to the integer delay case.

- Despite an approximation in the delay modeling, LQG-WFS shows the best delay margins. For instance, for $\delta = 0.8$ frame, it benefits from a 1.3-frame delay margin, while limited to respectively 1 frame and 0.8 frame for LQG-OPT and LQG-DM. This was actually predictable looking at figure 6 where the bench tests and simulations revealed greater forbearance of LQG-WFS compared to the other two regulators when δ^{ctrl} deviated from the actual δ. In that same figure 6, we can even notice an improvement of the performance of LQG-WFS for greater values of $\delta^{\mathrm{ctrl}} = \delta + 0.1$.

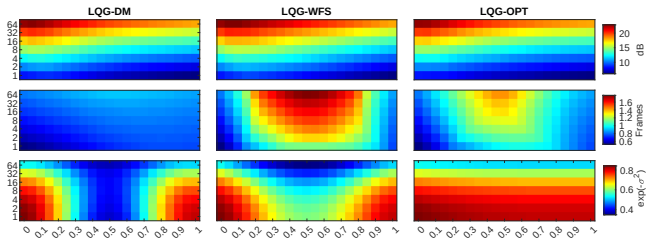

Fig. 10. (theoretical, $\delta^{\mathrm{ctrl}} = \delta$) Stability margins and corresponding performance as a function of the fudge factor (y-axis) and the delay δ (x-axis). Left to right: LQG with phase model synchronized with DM (LQG-DM), with WFS (LQG-WFS), and optimal controller (LQG-OPT). Top to bottom: gain [dB], delay [frames] margins and performance expressed as $[\exp(-\sigma^2_{\lambda=500\mathrm{nm}})]$.

This comment of the last item is confirmed and detailed in figure 11, representing the same variables as figure 10 but with a fixed value of $\delta = 0.5$ and making δ^{ctrl} deviating on both sides. We notice that the gain margins stay unchanged while delay

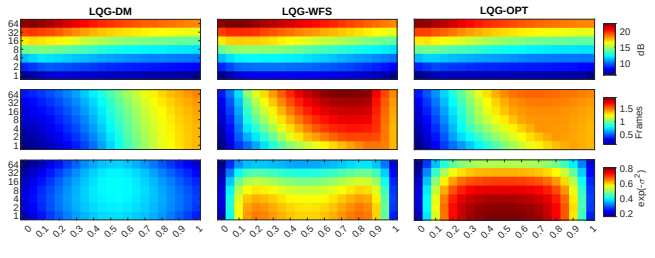

Fig. 11. (theoretical, $\delta = 0.5$) Stability margins and corresponding performance as a function of the fudge factor (y-axis) and the regulator delay δ^{ctrl} (x-axis). Left to right: LQG with phase model synchronized with DM (LQG-DM), with WFS (LQG-WFS), and optimal controller (LQG-OPT). Top to bottom: gain [dB], delay [frames] margins and performance expressed as $[\exp(-\sigma^2_{\lambda=500\text{nm}})]$.

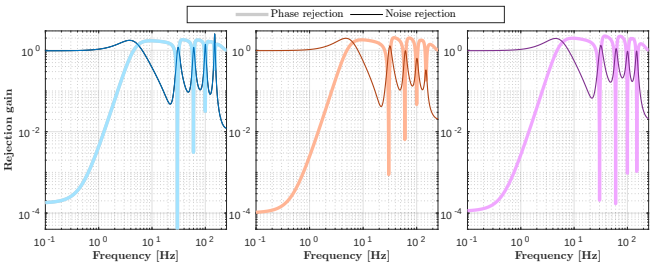

Fig. 12. (theoretical, $\delta = 0.5$) Phase rejection and noise propagation gains. Left to right: LQG-DM, LQG-WFS and LQG-OPT controllers. Sampling frequency $F_s = 500\,\text{Hz}$. Vibration frequencies $f_{\text{vib}} = 30, 60, 100$ and $150\,\text{Hz}$. Best-tuned δ^{ctrl}.

margins are logically impacted. They are interestingly degraded when underestimating $\delta^{\text{ctrl}} < \delta$ but improved when making an overestimation $\delta^{\text{ctrl}} > \delta$. We see on the performance maps (bottom) that LQG-WFS is surprisingly not convex, with best results for $\delta^{\text{ctrl}} = \delta + 0.3$ while having great stability margins. In the end, one should better overset the delay value δ^{ctrl} a little: the performance is almost unchanged – or even improved if using LQG-WFS –, the delay margins are improved, and the gain margins are almost not degraded.

However, whatever the tuning, the image quality criteria $\exp(-\sigma^2_{\lambda=500\text{nm}})$ (visible wavelength) in figure 10 and for delays from 0.4 to 0.6, is dramatically jumping from 40% with LQG-DM to 60% for LQG-WFS and to 80% for the optimal LQG regulator.

B. Rejection gains

In figure 12, we present the frequency-dependent rejection and noise propagation gains of the three LQG regulators. These gains are evaluated by computing the ratios $\Phi_{\overline{\phi}^{\text{res}}}(z)/\Phi_{\overline{\phi}}(z)$ (light thick lines) and $\Phi_{\overline{\phi}^{\text{res}}}(z)/\sigma^2_w$ (dark thin lines). The results on the graphs enable us to highlight the potential loss of vibration rejection with respect to the vibration frequency. Indeed, we notice that LQG-WFS (middle graph) loses efficiency when the signal frequency increases, with a rejection gain limited to 0.2 at 150 Hz. The same phenomenon is visible for LQG-DM (left graph), the latter having moreover a more critical noise propagation, notably at 150 Hz (gain superior to 2). This is related to the delay margins observed in figure 10, in which the values are significantly lower for the LQG-DM case. On the other hand, LQG-OPT (right graph) remains effective in completely rejecting the four vibration peaks. This is made possible without overshooting the noise at high frequencies, again in accordance with the good stability margins described in the previous section.

9. CONCLUSION

This paper revisits the optimal (minimum-variance) AO control design in presence of fractional delay. This problem has been tackled (using the lifting technique) in [8, 9] in the case of a DM with temporal dynamics. Based on the same lifting technique, we present here a constructive and new procedure to design the optimal controller under the hypothesis of DM with instantaneous response. Our constructive procedure is easy to implement and can be readily extended to solve the optimal control problem in presence of (linear) actuator dynamics.

It is first shown that the optimal control problem with fractional delay keeps the same simple structure than in the case of integer delay. However, the disturbance prediction is then obtained by a Kalman filter based on a lifted disturbance model that outputs two averaged values: the disturbance averaged over the DM sampling period and over the WFS sampling period. We propose in this paper to directly construct this lifted state-space representation, starting from a standard discrete-time disturbance model derived from statistical priors and/or identified from WFS measurements. This construction procedure is markedly different from the ones proposed in [8, 9], which required computationally involved numerical integrations in particular for the state noise covariance matrix. Our streamlined optimal control design relies on calculation procedures involving only matrix exponentials and Lyapunov equations. It is applied in simulation to optimize tip-tilt vibrations rejection on the GTCAO case (the AO system dedicated to GTC, see [23]). It yields significant improvement in performance and robustness compared with simpler but suboptimal LQG controllers.

The two suboptimal LQG controllers that are used for comparison are adapted to the presence of a fractional delay. One, denoted by LQG-DM, uses a disturbance model synchronised with the DM intervals, as in [6, 10, 11]. The other one, denoted by LQG-WFS, is based on a disturbance model synchronized with the WFS, as in [3, 12]. We show that in presence of atmospheric turbulence only, all three controllers (LQG-DM, LQG-WFS and optimal) behave the same way, and far better than the integrator. However, in presence of vibrations, both LQG-DM and LQG-WFS see their performance degrading all the more the vibration's natural frequency increases. This expected behavior is evidenced thanks to on-bench experiments on GTCAO. We also show that injecting piecewise constant vibrations on a bench *via* the DM favors LQG-DM over LQG-WFS. When the vibration is acting as a continuous-time signal, LQG-WFS generally outperforms LQG-DM and exhibits stronger stability margins.

The design of the optimal controller relies on a continuous-time model of the disturbances, which is in practice not available. We propose in this paper to build the continuous-time model by "dediscretizing" the discrete-time model identified from the telemetry data. This provides a Kalman filter which delivers minimum variance estimates of phase temporal averages over past and future WFS and DM intervals, and hence optimal commands. This makes it possible to have for the first time a complete control design procedure that starts from the standard discrete-time models to the optimal discrete-time controller that takes fractional delays into account.

This is used to derive theoretical performance evaluations in

terms of residual phase variance, but also to propose for the first time, thanks to our constructive method, the calculation of the phases and residual phases PSD, rejection and noise propagation transfer functions or gains, plus all stability margins.

While the applications presented above are scalar, the proposed method is applicable to multi-modal AO control with large dimensions.

A. INTEGRALS OF MATRIX EXPONENTIALS

The integrals of matrix exponentials used throughout this paper can all be computed using two basic matrix algebra routines, namely computing matrix exponentials and solving continuous Lyapunov functions, which are available in many software packages (in MATLAB, the functions `expm` and `lyap`).

Start with the integral of the exponential of an invertible matrix A_ϕ. It can be evaluated over any time interval as

$$\int_0^t e^{A_\phi s} ds = A_\phi^{-1}(e^{A_\phi t} - I) = (e^{A_\phi t} - I)A_\phi^{-1}\,. \tag{113}$$

This formula enables to compute the integral of the non-invertible block-triangular matrix

$$A_\eta = \begin{pmatrix} A_\phi & 0 \\ \frac{1}{T_s}C_\phi & 0 \end{pmatrix}. \tag{114}$$

To achieve this, it suffices to note that the solution of the deterministic autonomous equation $\dot\eta(t) = A_\eta \eta(t)$, where $\eta = (x_\phi^{\mathrm{T}} \;\; \psi^{\mathrm{T}})^{\mathrm{T}}$, is

$$x_\phi(t) = e^{A_\phi t} x_\phi(0)\,, \tag{115}$$

$$\begin{aligned}\psi(t) &= \int_0^t \frac{1}{T_s} C_\phi x_\phi(s)\, ds + \psi(0) \\ &= \frac{1}{T_s} C_\phi \left(\int_0^t e^{A_\phi s} ds\right) x_\phi(0) + \psi(0)\,.\end{aligned} \tag{116}$$

Since this should be equal to $e^{A_\eta t}\eta(0)$ for all $t \geq 0$ and any possible choice of $x_\phi(0)$, this matrix exponential is

$$e^{A_\eta s} = \begin{pmatrix} e^{A_\phi s} & 0 \\ C_\Phi(s) & I \end{pmatrix}, \tag{117}$$

with

$$C_\Phi(s) = \frac{1}{T_s} C_\phi \left(\int_0^t e^{A_\phi s} ds\right) = \frac{1}{T_s} C_\phi A_\phi^{-1}\left(e^{A_\phi s} - I\right). \tag{118}$$

A second standard result from control theory is that when A_ϕ is a Hurwitz square matrix (all eigenvalues with strictly negative real parts) and $Q_\phi = Q_\phi^{\mathrm{T}} \geq 0$ (all eigenvalues positive), the following identity holds:

$$\int_0^\infty e^{A_\phi s} Q_\phi e^{A_\phi^{\mathrm{T}} s} ds = P_\phi\,, \tag{119}$$

where $P_\phi \geq 0$ is the unique solution of the continuous-time Lyapunov equation

$$A_\phi P_\phi + P_\phi A_\phi^{\mathrm{T}} + Q_\phi = 0\,. \tag{120}$$

As an immediate corollary, the corresponding integral over a finite interval is given by

$$\int_0^t e^{A_\phi s} Q_\phi e^{A_\phi^{\mathrm{T}} s} ds = P_\phi - e^{A_\phi t} P_\phi e^{A_\phi^{\mathrm{T}} t}\,. \tag{121}$$

As it turns out, $P_\phi = \Sigma_{x_\phi}$, where Σ_{x_ϕ} is the covariance matrix of the stationary solution of Eq. (48).

We now proceed to evaluate the noise covariance matrix

$$\Sigma_{v_\eta}(t) = \int_0^t e^{A_\eta s} Q\, e^{A_\eta s^{\mathrm{T}}} ds\,, \tag{122}$$

where $Q = \begin{pmatrix} Q_\phi & 0 \\ 0 & 0 \end{pmatrix}$. It is immediately checked that the integrand in Eq. (122) is

$$e^{A_\eta s} Q e^{A_\eta s^{\mathrm{T}}} = \begin{pmatrix} e^{A_\phi s} Q_\phi\, e^{A_\phi s^{\mathrm{T}}} & e^{A_\phi s} Q_\phi C_\Phi(s)^{\mathrm{T}} \\ C_\Phi(s) Q_\phi\, e^{A_\phi s^{\mathrm{T}}} & C_\Phi(s) Q_\phi C_\Phi(s)^{\mathrm{T}} \end{pmatrix}. \tag{123}$$

Applying Eq. (113) and Eq. (121) leads to:

$$\Sigma_{v_\eta}(t) \triangleq \begin{pmatrix} \Sigma_{v_1}(t) & \Sigma_{v_1 v_2}(t) \\ \Sigma_{v_1 v_2}(t)^{\mathrm{T}} & \Sigma_{v_2}(t) \end{pmatrix}, \tag{124}$$

where

$$\Sigma_{v_1}(t) = P_\phi - e^{A_\phi t} P_\phi e^{A_\phi^{\mathrm{T}} t} \tag{125}$$

$$\Sigma_{v_1 v_2}(t) = \Sigma_{v_1}(t) - \frac{1}{T_s} A_\phi^{-1}(e^{A_\phi t} - I) Q_\phi A_\phi^{-\mathrm{T}} C_\phi^{\mathrm{T}} \tag{126}$$

$$\begin{aligned}\Sigma_{v_2}(t) = \frac{1}{T_s^2} C_\phi A_\phi^{-1} \times \big(&\Sigma_{v_1}(t) + t Q_\phi \\ &- A_\phi^{-1}(e^{A_\phi t} - I) Q_\phi - Q_\phi (e^{A_\phi^{\mathrm{T}} t} - I) A_\phi^{-\mathrm{T}}\big) \\ &\times A_\phi^{-\mathrm{T}} C_\phi^{\mathrm{T}}\,.\end{aligned} \tag{127, 128}$$

B. LQG REGULATORS IN STATE-SPACE FORM

We detail here the construction of matrices A_u and C_u for the LQG controllers in Sections 3 and 6. Recall that this state representation is in the form

$$\begin{cases} x_{u,k+1} = A_u x_{u,k} + B_u y_k\,, & (129) \\ u_k = C_u x_{u,k+1}\,. & (130) \end{cases}$$

With

$$x_{u,k} = \begin{pmatrix} \widehat{x}_{k|k-1} \\ u_{k-2} \end{pmatrix}, \quad B_u = \begin{pmatrix} L_\infty \\ 0 \end{pmatrix}. \tag{131}$$

A. Optimal LQG

For the optimal LQG regulator in Section 2, we take $x_k = z_k$, the augmented state vector is defined by equation Eq. (58). Combining Eq. (24), Eq. (25) and Eq. (26) then yields

$$A_u = \begin{pmatrix} A - L_\infty C_y + (1-\delta^{\mathrm{ctrl}}) DNP_u C_{\bar\phi} & \delta^{\mathrm{ctrl}} L_\infty DN \\ P_u C_{\bar\phi} & 0 \end{pmatrix}, \tag{132}$$

$$C_u = \begin{pmatrix} P_u C_{\bar\phi} & 0 \end{pmatrix}. \tag{133}$$

B. DM-synchronized LQG

In this case, $x_k = \widehat{x}_{\overline{\phi},k|k-1}$. From Eq. (33), we get

$$\widehat{y}_{\overline{\phi},k|k-1} = D\big((1-\delta^{\text{ctrl}})C_{\overline{\phi}} + \delta^{\text{ctrl}}C_{\overline{\phi},1}\big)\widehat{x}_{\overline{\phi},k|k-1} - DNu_{k-2}\,, \tag{134}$$

The control being given by Eq. (35), this results in

$$A_u = \begin{pmatrix} A_{\overline{\phi}} - L_\infty D\big((1-\delta^{\text{ctrl}})C_{\overline{\phi}} + \delta^{\text{ctrl}}C_{\overline{\phi},1}\big) & L_\infty DN \\ P_u C_{\overline{\phi}} & 0 \end{pmatrix}, \tag{135}$$

$$C_u = \begin{pmatrix} P_u C_{\overline{\phi}} & 0 \end{pmatrix}. \tag{136}$$

C. WFS-synchronized LQG

As in the DM-synchronized case, we take $x_k = \widehat{x}_{\overline{\phi},k|k-1}$. Combining Eq. (23) and Eq. (39) yields:

$$\widehat{y}_{\overline{\phi},k|k-1} = D\big(C_{\overline{\phi}} - (1-\delta^{\text{ctrl}})NP_u C_{\overline{\phi},2}\big)\widehat{x}_{\overline{\phi},k|k-1} - \delta^{\text{ctrl}}DNu_{k-2}\,. \tag{137}$$

Thus:

$$A_u = \begin{pmatrix} A_{\overline{\phi}} - L_\infty DC_{\overline{\phi}} + (1-\delta^{\text{ctrl}})L_\infty DNP_u C_{\overline{\phi},2} & \delta^{\text{ctrl}}L_\infty DN \\ P_u C_{\overline{\phi},2} & 0 \end{pmatrix}, \tag{138}$$

$$C_u = \begin{pmatrix} P_u C_{\overline{\phi},2} & 0 \end{pmatrix}. \tag{139}$$

Funding. This work is supported by the "Investissements d'Avenir" project funded by the IDEX Paris-Saclay, ANR-11-IDEX-0003-02. This project has received funding from the European Union's Horizon 2020 research and innovation programme under grant agreement No 101004719.

Disclosures. The authors declare no conflicts of interest.

REFERENCES

1. C. Kulcsár, G. Sivo, H.-F. Raynaud, B. Neichel, F. Rigaut, J. Christou, A. Guesalaga, C. Correia, J.-P. Véran, E. Gendron, F. Vidal, G. Rousset, T. Morris, S. Esposito, F. Quiros-Pacheco, G. Agapito, E. Fedrigo, L. Pettazzi, R. Clare, R. Muradore, O. Guyon, F. Martinache, S. Meimon, and J.-M. Conan, "Vibrations in AO control: a short analysis of on-sky data around the world," Adapt. Opt. Syst. III **8447**, 84471C–84471C–14 (2012).
2. O. Guyon and J. Males, "Adaptive optics predictive control with empirical orthogonal functions (EOFs)," arXiv preprint arXiv:1707.00570 (2017).
3. B. Sinquin, L. Prengère, C. Kulcsár, H. F. Raynaud, E. Gendron, J. Osborn, A. Basden, J. M. Conan, N. Bharmal, L. Bardou, L. Staykov, T. Morris, T. Buey, F. Chemla, and M. Cohen, "On-sky results for adaptive optics control with data-driven models on low-order modes," Mon. Notices Royal Astron. Soc. **498**, 3228–3240 (2020).
4. S. Y. Haffert, J. R. Males, L. M. Close, K. van Gorkom, J. D. Long, A. D. Hedglen, L. Schatz, J. Lumbres, A. Rodack, J. M. Knight, H. Sun, K. Fogarty, and L. Pearce, "Data-driven subspace predictive control: lab demonstration and future outlook," https://doi.org/10.1117/12.2594910 **11823**, 413–419 (2021).
5. A. Zidi, H.-F. Raynaud, C. Kulcsár, F. Vidal, E. Gendron, Y. Clénet, and R. Davies, "The MICADO first light imager for the ELT: SCAO LQG control performance with windshake, vibrations, and mirror dynamics," https://doi.org/10.1117/12.2629863 **12185**, 892–897 (2022).
6. L. A. Poyneer, S. M. Ammons, M. K. Kim, B. Bauman, J. Terrel-Perez, A. J. Lemmer, and J. Nguyen, "Laboratory demonstration of the prediction of wind-blown turbulence by adaptive optics at 8 kHz with use of LQG control," Appl. Opt. **62**, 1871–1885 (2023).
7. T. Chen and B. A. Francis, *Optimal Sampled-Data Control Systems* (Springer-Verlag, London, 1995).
8. D. P. Looze, "Discrete-time model for an adaptive optics system with input delay," https://doi.org/10.1080/00207171003664836 **83**, 1217–1231 (2010).
9. H.-F. Raynaud, C. Correia, C. Kulcsár, and J.-M. Conan, "Minimum-variance control of astronomical adaptive optics systems with actuator dynamics under synchronous and asynchronous sampling," Int. J. Robust Nonlinear Control. **21**, 768–789 (2011).
10. L. Poyneer and J.-P. Véran, "Predictive wavefront control for adaptive optics with arbitrary control loop delays," JOSA A, Vol. 25, Issue 7, pp. 1486-1496 **25**, 1486–1496 (2008).
11. L. A. Poyneer, D. W. Palmer, B. Macintosh, D. Savransky, N. Sadakuni, S. Thomas, J.-P. Véran, K. B. Follette, A. Z. Greenbaum, S. M. Ammons *et al.*, "Performance of the gemini planet imager's adaptive optics system," Appl. Opt. **55**, 323–340 (2016).
12. G. Sivo, C. Kulcsár, J.-M. Conan, H.-F. Raynaud, É. Gendron, A. Basden, F. Vidal, T. Morris, S. Meimon, C. Petit, D. Gratadour, O. Martin, Z. Hubert, A. Sevin, D. Perret, F. Chemla, G. Rousset, N. Dipper, G. Talbot, E. Younger, R. Myers, D. Henry, S. Todd, D. Atkinson, C. Dickson, and A. Longmore, "First on-sky SCAO validation of full LQG control with vibration mitigation on the CANARY pathfinder," Opt. Express **22**, 23565 (2014).
13. B. Le Roux, C. Kulcsár, L. M. Mugnier, T. Fusco, H.-F. Raynaud, and J.-M. Conan, "Optimal control law for classical and multiconjugate adaptive optics," JOSA A **21**, 1261–1276 (2004).
14. C. Kulcsár, H.-F. Raynaud, C. Petit, J.-M. Conan, and P. V. de Lesegno, "Optimal control, observers and integrators in adaptive optics," Opt. Express **14**, 7464 (2006).
15. D. P. Looze, "Discrete-time model of an adaptive optics system," J. Opt. Soc. Am. A **24**, 2850–2863 (2007).
16. C. Kulcsár, H.-F. Raynaud, C. Petit, and J. M. Conan, "Minimum variance prediction and control for adaptive optics," Automatica **48**, 1939–1954 (2012).
17. B. D. O. Anderson and J. B. Moore, *Optimal Filtering* (Prentice-Hall, London, 1979).
18. V. Kucera, *Analysis and design of discrete linear control systems* (Prentice Hall London, 1991).
19. L. Marquis, C. Kulcsár, I. Montilla, H.-F. Raynaud, J. M. de la Rosa, Ó. T. Araújo, A. Basden, and M. R. García-Talavera, "Linear quadratic Gaussian predictive control for the Gran Telescopio Canarias AO system: design issues and first bench results," in *Adaptive Optics Systems VIII,* vol. 12185 (SPIE, 2022), pp. 909–916.
20. D. P. Looze, "Linear-quadratic-gaussian control for adaptive optics systems using a hybrid model," JOSA A **26**, 1–9 (2009).
21. L. Marquis, "High performance control for the Gran Telescopio Canarias Adaptive Optics system," Ph.D. thesis, Université Paris-Saclay & Universidad de La Laguna (2023).
22. P. V. Overschee and B. D. Moor, "N4sid: Subspace algorithms for the identification of combined deterministic-stochastic systems," Automatica **30**, 75 – 93 (1994). Special issue on statistical signal processing and control.
23. I. Montilla, J. M. de la Rosa, Ó. Tubío Araújo, J. Rosich, M. Reyes García-Talavera, M. L. Aznar, E. González, R. López, R. Simoes, J. Patrón Recio, M. Puga, and V. Sánchez Béjar, "Laboratory acceptance and telescope integration readiness of the Gran Telescopio Canarias adaptive optics system," https://doi.org/10.1117/12.2630109 **12185**, 660–667 (2022).
24. A. Basden, D. Geng, R. Myers, and E. Younger, "Durham adaptive optics real-time controller," Appl. Opt. **49**, 6354–6363 (2010).

Chapter 5
Adaptive optics system modeling and calibration for linear predictive control

5.1 Introduction

We have seen in chapter 3 and 4 that the implementation of an LQG regulator intrinsically required the modeling of the AO system and as a result its calibration. We will explore in this chapter some aspects linked to the telescope itself, like the way the primary and secondary mirrors are structured, the pupil rotation/derotation or how the windshake is modeled. We will also describe some calibration methods and their implementation on GTCAO to obtain an efficient controller. In particular, we propose a simple method to estimate the fractional loop delay, which needs to be known to simulate properly the AO loop and to design the controller. To build some of the models, the inner functions of the Object-oriented Matlab adaptive optics toolbox (R. Conan and Correia, 2014) (OOMAO) will be used.

This chapter starts with the descriptions related to the telescope in section 5.2 and the GTCAO system in section 5.3. Interaction matrix calibration is tackled in section 5.4, fractional loop delay estimation in section 5.5 and measurement noise covariance matrix in section 5.6.

5.2 Gran Telescopio Canarias

5.2.1 Primary mirror: an alt-azimuth mounted segmented pupil

5.2.1.1 Telescope pupil

The Gran Telescopio Canarias has a 36-hexagonal-segment primary mirror, with a total peak-to-peak width of $D_{\text{pup}} = 11.35\,\text{m}$. This parameter will mainly intervene in the turbulence and tip-tilt vibration energy. In terms of light collection, it is equivalent to a 10.4-meter diameter circular mirror. The spider holding the secondary mirror has six thin legs of uniform width of 2.5 cm. It is neglected since sufficiently small not to have led to any petal mode problem on the Keck telescope which has the same architecture. The central obstruction is a circle of size 2.5 m. The pupil is in the end a collection of hexagonal segments, as illustrated in figure 5.1.

5.2.1.2 Alt-azimuthal mount

The GTC location is at latitude $\Phi_{\text{a}} = 28°45'$. Its mount is alt-azimuthal. As a result, to allow long exposure time scientific images, a de-rotator manages the de-rotation of the images, defined by the parallactic angle (η_{a}). This angle variation is a function

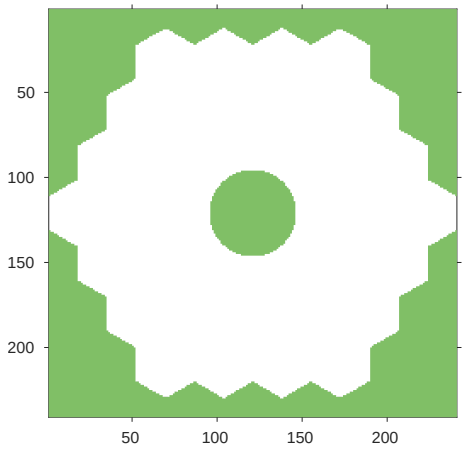

Figure 5.1: (OOMAO) Footprint of the GTC input pupil.

of the zenith angle (Z_a), the declination (δ_a) and the hour angle (h_a). All are shown in the celestial illustration, figure 5.2. The sinus law gives us

$$\sin(\eta_\mathrm{a}(t)) = \sin(h_\mathrm{a}(t))\frac{\sin(\pi/2 - \Phi_\mathrm{a})}{\sin(Z_\mathrm{a}(t))}\,. \tag{5.1}$$

The definition of the hour angle is

$$h_\mathrm{a}(t) = \frac{360}{24}(12 - t)\,, \tag{5.2}$$

taking for t the time convention that the target is at its zenith at $t = 12$. The zenith angle is obtained with:

$$Z_\mathrm{a}(t) = \arccos\left(\sin(\delta_\mathrm{a})\sin(\Phi_\mathrm{a}) + \cos(\delta_\mathrm{a})\cos(\Phi_\mathrm{a})\cos(h_\mathrm{a}(t))\right)\,. \tag{5.3}$$

The azimuth angle A_a can also be given:

$$A_\mathrm{a}(t) = \arcsin\left(\frac{\cos(\delta_\mathrm{a}\sin(h_\mathrm{a}(t))}{\sin(Z_\mathrm{a}(t))}\right)\,. \tag{5.4}$$

It is then possible to see what is the de-rotator speed as illustrated in figure 5.3. For example, for an object at declination 45°, it is invisible until the hour -8 because under the horizon. Once visible and tracked by the telescope, the de-rotator speed goes from about 0.4° per 120 seconds to 1.6° per 120 seconds at time 0. The second half of the object "day" (time 0 to 12) is symmetrical. Therefore, in this example, if one imposes that the modeling should be done at most every 1° of pupil rotation, as e.g. in (Van Dam, Le Mignant, and B. A. Macintosh, 2004), we should update the controller every minute. This insures nearby the zenith a maximum rotation of 0.8° (speed of 1.6° for 2 minutes). This will be used later when evaluating the validity of LQG models.

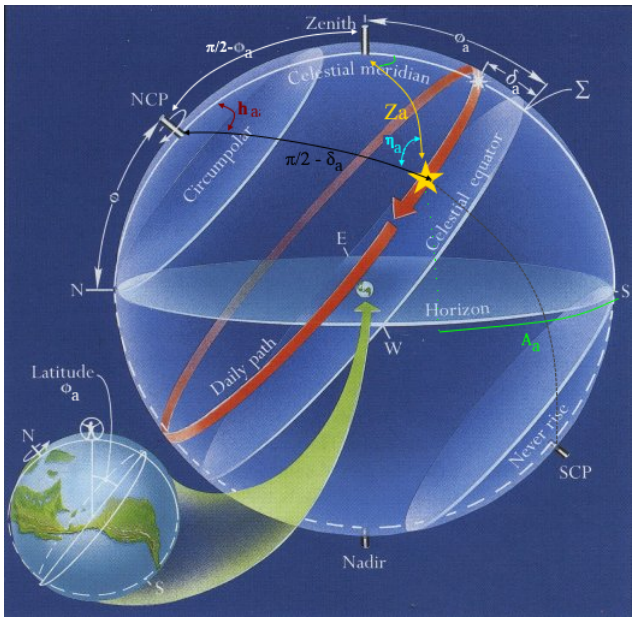

Figure 5.2: Diagram of celestial angles definitions (Kaler, 2002). The target travels at its declination δ_a, at constant hour angle speed ($\frac{dh_a}{dt} = 360°$ per day). The GTC mount manages the angles of zenith $Z_a(t)$ and azimuth $A_a(t)$, and the internal de-rotator manages the parallactic angle $\eta_a(t)$.

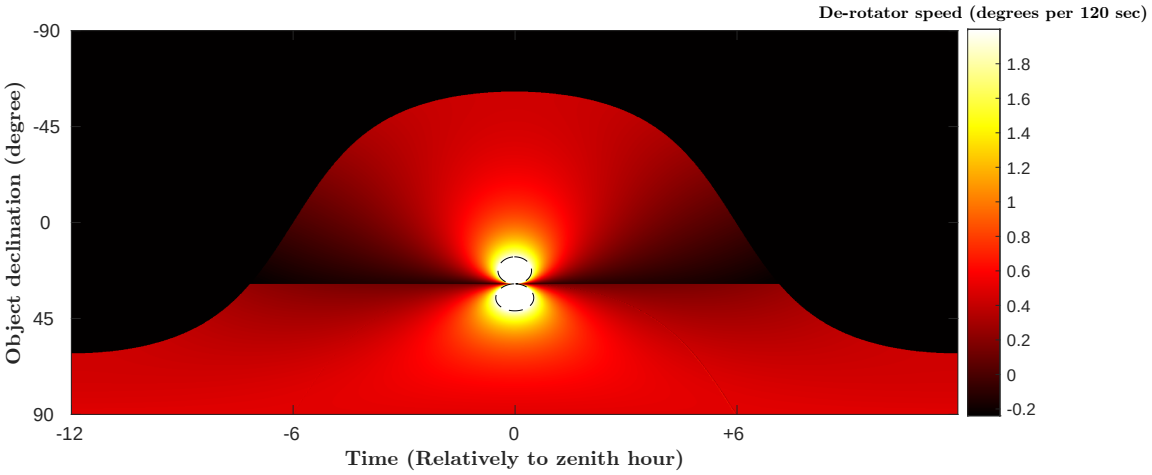

Figure 5.3: Parallactic angle evolution speed (in degree per 120 sec) as a function of the time (x-axis) and the target declination (y-axis). The dashed circles in the middle are delimiting the area where the speed exceeds 2 degrees per 120 second (maximum value set in the color bar). The outside black area corresponds to coordinates of objects that are invisible from the GTC (under the horizon of La Palma).

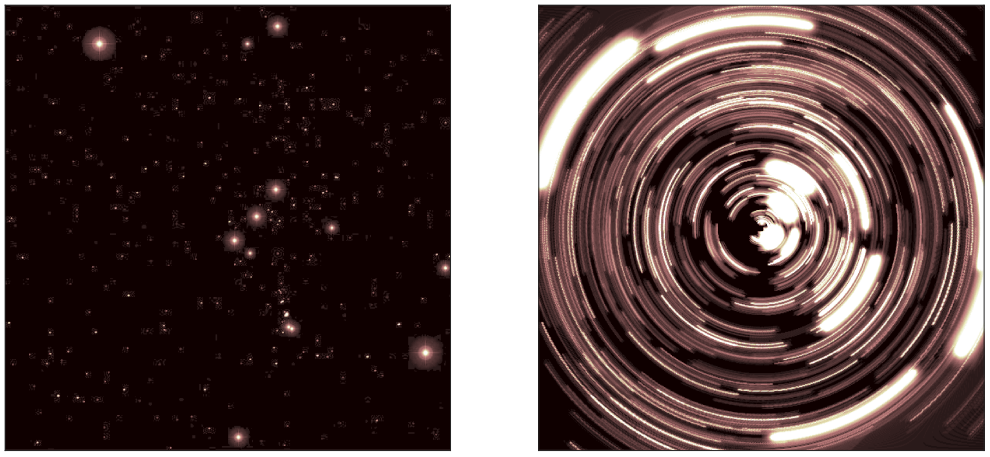

Figure 5.4: Illustration of the parallactic angle effects on a 2-hour exposure image of Orion with an alt-azimuthal tracking. Left: with parallactic angle de-rotation (Credit: Scott Levine). Right: Matlab simulation without de-rotation. All stars are describing circle arcs of angle η_{a}.

5.2.2 Tip-tilt secondary mirror and tip-tilt correction

The secondary mirror M2 is a tip-tilt mirror whose support makes a central obstruction of 2.5 m. The effect of windshake can be important as described in section 5.2.2.1, due to the vibrations induced by the spider structure that supports M2. This mirror has also its proper servo-loop, described in section 5.2.2.2.

5.2.2.1 Windshake-induced tip and tilt disturbance

Taking into account the low-order aberrations due to the windshake is mandatory and all the more so important as we are on a very large telescope. Other non-atmospheric aberration sources may also be present, like vibrations induced by coolers, fans, etc. We are going to describe the basic approach implemented to generated phase disturbances that mimic the M2 related vibrations.

Windshake-induced aberrations spectrum

An analytical expression of the power spectral density (PSD) of the mechanical excitation due to the windshake has been provided by the IAC mechanics team and reported in (Femenía, Icíar Montilla, and Núñez, 2017):

$$S_{\mathrm{wind}}(f) = \frac{f}{(1+f^2)^{\frac{4}{3}}\left(1+\left(\frac{f}{0.77}\right)^{\frac{4}{3}}\right)^2}, \tag{5.5}$$

where f is the temporal frequency in Hz. This is filtered by the response of the telescope to produce the windshake. The telescope is considered as a spring-damp

system of natural frequency $\omega_{\text{vib}} = 2\pi f_{\text{vib}} = 75.4\,\text{rad}\,\text{s}^{-1}$ and damping coefficient $\xi_{\text{vib}} = 0.01$. Noting $p = 2i\pi f$ the Laplace variable, the transfer function can be written as:

$$H_{\text{tel}}(p) = \frac{1}{\left(\frac{p}{\omega_{\text{vib}}}\right)^2 + \frac{2\xi_{\text{vib}}}{\omega_{\text{vib}}}p + 1}\,. \tag{5.6}$$

The PSD of the windshake perturbation is thus:

$$PSD_{\text{windshake}}(f) = S_{\text{wind}}(f)|H_{\text{tel}}(2i\pi f)|^2\,. \tag{5.7}$$

Figure 5.5 illustrates the windshake PSD and its different components: the PSD S_{wind} in red, the telescope square gain $|H_{\text{tel}}|^2$ in blue, and the total disturbance $PSD_{\text{windshake}}$ in bold black.

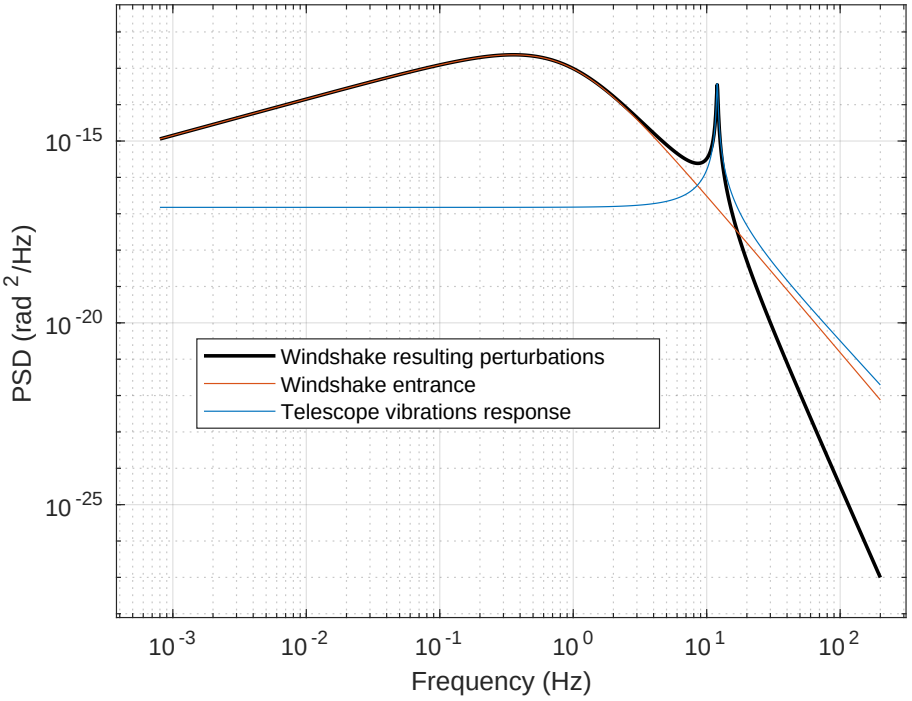

Figure 5.5: (Optical disturbance models resulting from mechanical models) Windshake-induced aberrations: power spectral density for tip or tilt Zernike modes (angle of arrival in radians). The windshake entrance S_{wind} multiplied by the telescope response H_{tel} results in the disturbance PSD $PSD_{\text{windshake}}$.

Generation of windshake phase aberrations

Knowing the expression of the windshake PSD in equation (5.7), we can generate a discrete-time vibration signal ϕ^{vib} to be added to the atmospheric tip (or tilt) mode for a n_{iter}-frame long (n_{iter} even) simulation at frequency F_{s}. The following standard steps lead to the generation of the temporal data:

- Calculate from equation (5.7) the amplitude $PSD_{\text{windshake}}(f_k)$ where $f_k = k\frac{F_{\text{s}}}{n_{\text{iter}}+1}$ for $k \in I_{\text{iter}} = [\![1, \frac{n_{\text{iter}}}{2}]\!]$ (the 0 frequency is not calculated here).
- Compute a discrete Fourier transform of the desired vibration signal, $\Phi^{\text{vib}} = \mathcal{F}\left(\phi^{\text{vib}}\right)$, by assigning phases Θ_k as pseudo-random numbers following the continuous uniform distribution over $[-\pi, \pi]$:

$$\forall k \in I_{\text{iter}}, \Phi^{\text{vib}}(f_k) = \sqrt{PSD_{\text{windshake}}(f_k)}\exp(i\Theta_k)\,. \tag{5.8}$$

- Build a discrete Fourier transform respecting hermitian symmetry (vibration signal must be real with zero mean):

$$\left\{0, \left\{\Phi^{\text{vib}}\left(f_k\right)\right\}_{k=1,\ldots,\frac{n_{\text{iter}}}{2}}, \left\{\Phi^{\text{vib}*}\left(f_k\right)\right\}_{k=\frac{n_{\text{iter}}}{2},\ldots,1}\right\}.$$

  This allows to generate $n_{\text{iter}}+1$ data at the right sampling frequency F_{s}.

- Go back to temporal space by inverse Fourier transform $\phi^{\text{vib}} = \mathcal{F}^{-1}\left(\Phi^{\text{vib}}\right)$ and adjust the scalar temporal RMS of the signal from any initial arbitrary value σ_ϕ to the desired value σ_{vib}: $\frac{\sigma_{\text{vib}}}{\sigma_\phi}\phi^{\text{vib}}$. In our case, $\sigma_{\text{vib}} = 10\,\text{rad}$ (path-way difference) allows a standard deviation of $\sigma_{\text{AoA}} = 63\,\text{mas}$ (angle of arrival, corresponding to an amplitude of $\sqrt{2}\sigma_{\text{AoA}} \approx 0.1''$ as in (Femenía, Icíar Montilla, and Núñez, 2017)). In other words, knowing that the Airy disk is of size $FWHM_{\text{Airy}} = \lambda_{\text{sci}}/D_{\text{pup}} = 0.033''$, a long exposure with pure vibration (no atmosphere, no correction) leads to a 2D-Gaussian-shaped image with a FWHM of $FWHM_{\text{vib}} = 2.355\sigma_{\text{AoA}} \simeq 4.5FWHM_{\text{Airy}}$ as visible in figure 5.6. An example of windshake temporal evolution obtained with the procedure above, together with the atmospheric tip generated under OOMAO are displayed in figure 5.7.

5.2.2.2 Secondary mirror tip/tilt correction

The measurements coming from the WFS of GTCAO will be also used to drive the secondary mirror M2. The latter will manage a part of the tip and tilt (TT) correction, with its sampling frequency set to 100 Hz. There is no TT mirror on GTCAO optical table, so the DM will have to manage M2 TT residual disturbance. The M2 loop will be positioned ahead of GTCAO so that the DM works in closed loop from M2 residuals without knowing the values of the M2 commands. The

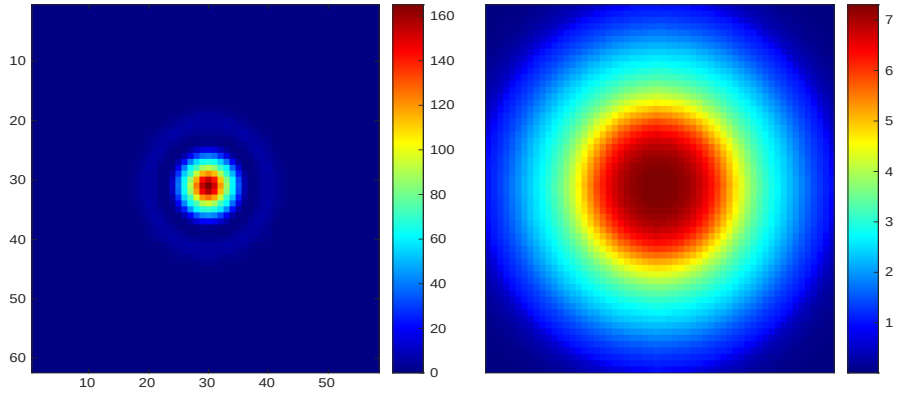

Figure 5.6: (OOMAO simulation) PSF in the focal plane. Left: diffraction limited. Right: long exposure image with windshake aberrations (no atmosphere, no correction) as simulated for GTC.

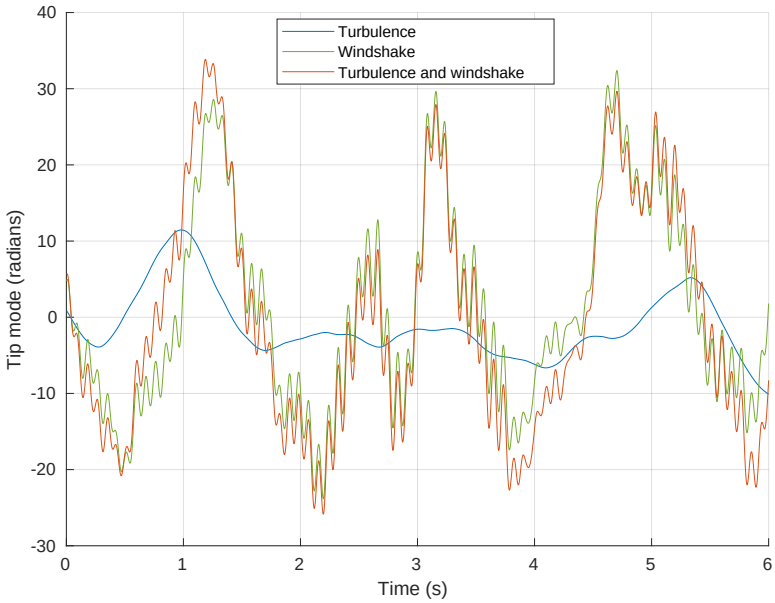

Figure 5.7: (OOMAO simulation) Example of windshake aberrations (green curve, tip Zernike mode), atmospheric turbulence tip generated by OOMAO (blue color, standard scenario of $r_0 = 20\,\mathrm{cm}$ and $V_0 = 10\,\mathrm{m\,s^{-1}}$), and sum of turbulence and windshake (red curve). The three sets come from one single simulation. The windshake is clearly dominant in this scenario.

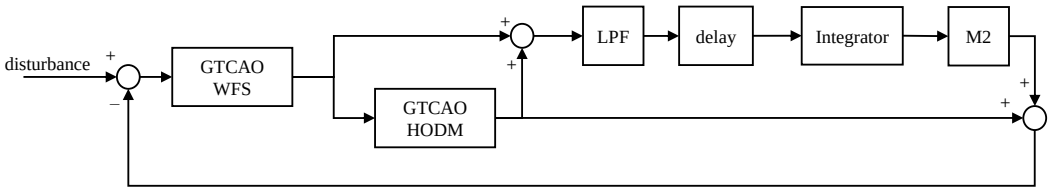

Figure 5.8: Structure of the servoing with GTCAO and M2 in the loop. The M2 loop receives measurements where the effect of the high-order DM (HODM) of GTCAO is removed. The low-pass filter (LPF) is a Butterworth filter with cut-off frequency 50 Hz. The M2 loop has a frequency sampling of 100 Hz. Data transfer rates are not indicated.

block-diagram of this control structure has been proposed in an internal technical report (Núñez Cagigal, 2018) and is illustrated in figure 5.8 in a simplified version.

To simulate the existence of M2 on the bench (while being of course already in the spider web of the operational GTC), first, the related windshake vibrations must be introduced as explained in 5.2.2.1. Then, the M2 related tip-tilt transfer function needs to be accounted for. In the report of (Núñez Cagigal, 2018), M2 has a time response modeled with a second order filter (damping 0.7 and cut-off frequency 70 Hz), a time delay of 3 ms, and is managed by a standard integrator with a best-tuned loop gain. The measurements received by this integrator are pre-filtered by a Butterworth with a cut-off frequency of 50 Hz. Therefore, the disturbance entering GTCAO needs to be pre-processed by the M2 loop when simulated on the bench or in OOMAO. This was done in particular for all the additional disturbances we introduced on the bench, such as the windshake. An example of such processed windshake time-series is shown in figure 5.9.

5.3 GTCAO system and components

At the time of this manuscript writing, the single-conjugated AO bench GTCAO is in its final test campaign in the AIV of the IAC (Iciar Montilla et al., 2022).

Wavefront sensor

The GTCAO system features an on-axis Shack-Hartmann sensor with 20×20 lenslets (Marco de la Rosa et al., 2018). The camera is an OCAM2 with EMCCD and 240×240 pixels, each pixel having an image scale on sky of $0.35''$. This leads to 12×12 pixels for each subaperture. That CCD can be moved left-right and up-down, allowing for choosing what is the global reference centroid position. The read-out is done with an electronic gain, possible to set from around 50 to 1000. The related noise is of $0.4\,\mathrm{e}^-\,\mathrm{px}^{-1}$ RMS. There are 312 active lenslets, thus leading to 624 measurements

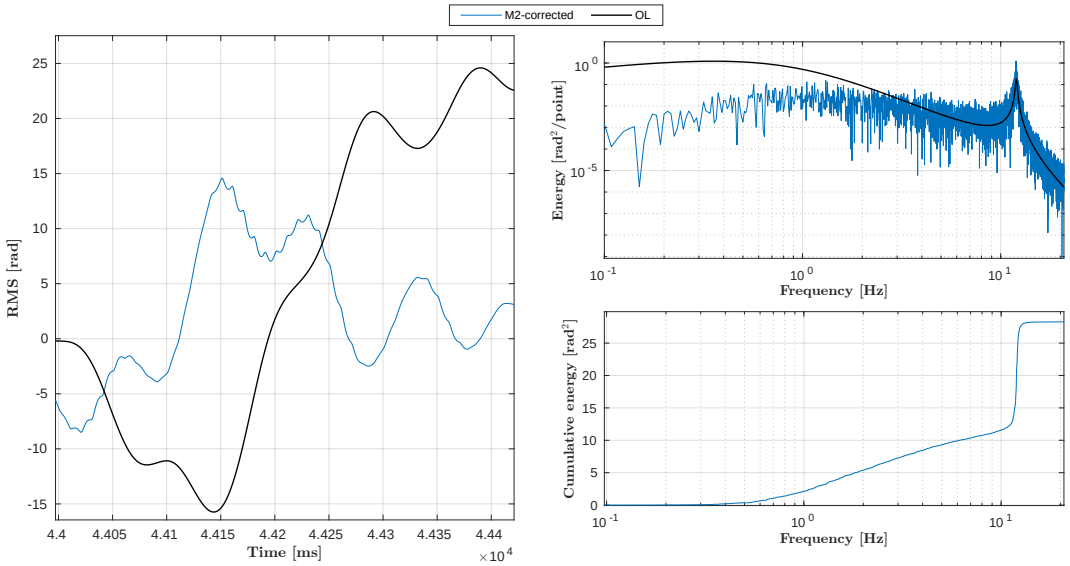

Figure 5.9: (simulation) Example of windshake signal in open-loop (black) and M2-corrected (blue) with a sampling time of $T_s = 1000\,\text{Hz}$. Left: time-series. Right: energy (cumulative on the bottom). The temporal response of M2 is visible on the time-series, most of all around the frame 44200 (time resolution of 1 ms). The OL signal has a total energy of $150\,\text{rad}^2$ (not represented in cumulative energy graph because too high). The 12-Hz resonance peak is not corrected by M2: the DM will have to fully manage it. This residual time-series will be used as a disturbance signal for the bench tests.

(contained in the vector y).

Deformable mirror

The DM is a Cilas of 21×21 piezoelectric actuators, among which 373 are used (Marco de la Rosa et al., 2018) but with the 330th out of order. The commands unit is called "count", such as $1\,\text{count} = 0.0065\,\text{V} = 0.0449\,\text{nm}$. The command stroke limit of each actuator is a voltage of $\pm 400\,\text{V} = \pm 3.07 \times 10^4\,\text{count} = \pm 1.35\,\mu\text{m}$. The stroke of an actuator is increased when the neighbours are actuated, due to the coupling factor of $C_{\text{DM}} \approx 0.14$.

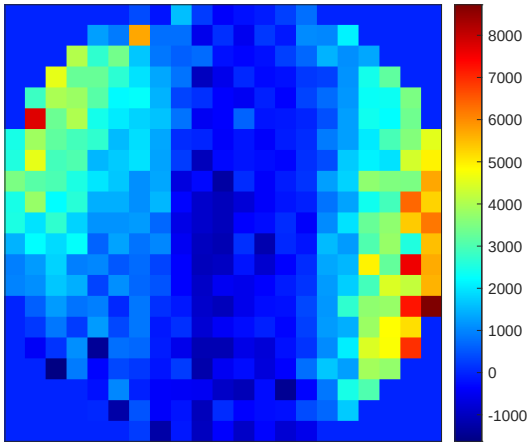

Figure 5.10: 2D display of the control vector (in counts) necessary to flatten the DM (November 2022). The highest values of about 6×10^3 counts on the very right side is not negligible: it corresponds to one fifth of the maximum allowed value $u_{\text{clip}} = 3.07 \times 10^4$ counts.

The command vector is actually containing $373 + 2$ commands. The two additional ones are called "pseudo-actuators", corresponding to a tip and a tilt command. The latters are still performed by the DM, simply allowing for increasing the integrator loop gain dedicated to tip and tilt. The actuators grid is not Fried aligned with the WFS, mainly due to a 3.0° rotation between the DM and the WFS. The DM response time is lower than 0.5 ms. We estimated this by sending some steps commands to the DM and recording WFS data at a frame of 2000 Hz, as illustrated in figure 5.11. The values plotted at each sampling time kT_{s} correspond to the average values of the DM position on the whole interval $[(k-1)T_{\text{s}}, kT_{\text{s}}]$.

Real-time calculator

The real-time computer software is DARC (A. Basden et al., 2010; Marco de la Rosa et al., 2018). At each frame, the centroid of each subaperture is computed by using the 16 most illuminated pixels. Below a chosen total illumination, the vertical and

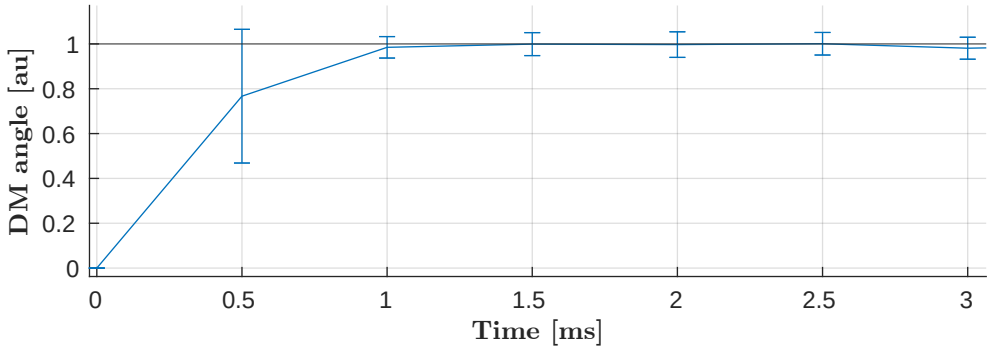

Figure 5.11: DM average angle on each sampling period (cadence of 2000 Hz). The DM rises between 0 and 0.5 ms. It means that it has a time response inferior to 0.5 ms.

horizontal measurements of a subaperture is automatically set to 0. The computation is done by a Superserver RTC. The baseline of GTCAO concerning the regulator is a leaky integrator with a gain dedicated to the TT modes and another for the higher orders. The output telemetry gives access to time-series of the slopes (units: pixels of the WFS CCD), the actuators commands (in counts), the subapertures illumination (in electrons) and other variables that are not used in our case. The DARC software also allows in its baseline distribution for the implementation of an LQG controller, as it was used on CANARY at a frequency of about 150 Hz, as described in detail in (Sivo, 2014). The LQG real-time implementation corresponds to the scheme given in section 3.3.6. It was modified in the beginning of my PhD by Jose Marco de la Rosa (software engineer at IAC) to allow an LQG implementation on GTCAO at high frequency rate. It was also improved by Nicolas Galland (post-doc at Institut d'Optique, Laboratoire Charles Fabry) to take into account the commands clipping and the time delay. All these modifications have been validated by Ali Basden (Durham University).

Bench disturbance simulator

The system must work for faint guide star magnitudes reaching $M_{\text{ngs}} = 14$ with a performance of still 10% in terms of Strehl ratio in K band. With guide stars brighter than $M_{\text{ngs}} = 10$, the Strehl ratio must be upper than 65% (Núñez Cagigal et al., 2017). The bench test allows to implement some simulations with a telescope simulator (on the left in figure 5.12). The atmospheric turbulence disturbance is introduced by one of the two available phase screens (PS):

- a first phase screen (PS1) corresponds to a favorable atmosphere of $r_0 = 23$ cm
- a second phase screen (PS2) corresponds to a challenging atmosphere of $r_0 = 8.5$ cm.

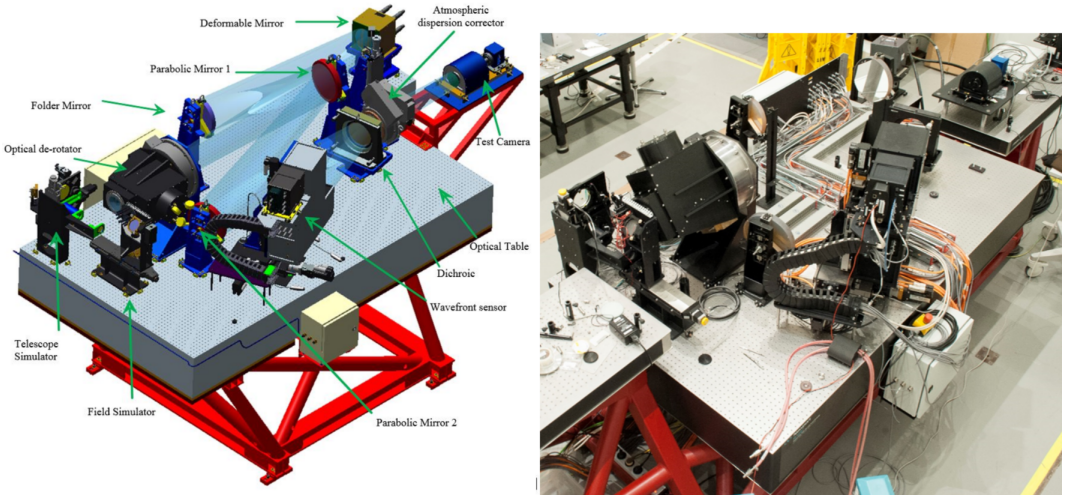

Figure 5.12: Scheme (left) and photograph (right) of the GTCAO bench in the AIV. Credit: (Béjar et al., 2018)

Both PSs were manufactured with low TT energy to mimic M2 effect. The vibrations are simulated by sending to the deformable mirror some pre-computed vibration time-series, at the loop sampling frequency F_s (Jose Marco function added on the GUI). An internal source can simulate a visible-NGS of magnitude 10 to 14.

The performance is assessed through:

- the near-IR test camera (very right in figure 5.12) and its corresponding internal halogen light source (central wavelength of 1.6 μm) with pixel size 11 mas. This mimics the record of scientific images.
- the residual slopes given by the WFS.

On the bench, the pupil of GTC, M1, is simulated with a mask on the optical path of the NGS and of the scientific source. It is rotated of 3.6 degrees. However, it does not represent the central obscuration, as visible in figure 5.13.

5.4 Pseudo-synthetic interaction matrix and phase-to-commands projector

The interaction matrix enters the LQG formulation (see 3.3.4) to compensate the effect of the DM commands in the Kalman filter. It is also used to reconstruct POL slopes from which is built the state-space model of the disturbances.

In first subsection 5.4.1, we show the discrepancy noticed when comparing the bench OL measurements with:

- the POL slopes obtained with an experimental interaction matrix $M_{\text{int}}^{\text{exp}}$,
- the POL slopes obtained with a pseudo-synthetic interaction matrix $M_{\text{int}}^{\text{synth}}$.

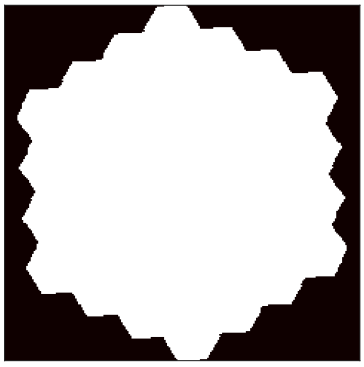

Figure 5.13: GTCAO test bench M1 pupil. It has no central obscuration (and no spider), and the orientation corresponds to a spin of 3.6 degrees.

In subsection 5.4.2, we describe the way the WFS matrix D is calculated, which is used in subsection 5.4.3 to obtain the pseudo-synthetic interaction matrix. Then, as we have the influence matrix N through the optimization of the pseudo-synthetic interaction matrix, we get a mapping of the actuators positions in subsection 5.4.4. From that, we can build in subsection 5.4.5 the phase-to-commands matrix P_u that allows the predicted phase to be projected on the actuators space, see equation (5.13).

5.4.1 Experimental interaction matrix issues and pseudo-synthetic matrix

Limited linearity for GTCAO

We can start showing some potential limits of the interaction matrix (linear model) in our GTCAO case. The pixel size of the WFS CCD is of $\mu_{\text{wfs}} = 0.35''$ for a subaperture of $d_{\text{SA}} = 0.568\,\text{m}$. At $\lambda_{\text{wfs}} = 500\,\text{nm}$, the pixels are thus Nyq times smaller than the FWHM of the subapertures diffraction-limited spots:

$$Nyq \triangleq \frac{0.5\lambda_{\text{wfs}}/d_{\text{SA}}}{\mu_{\text{wfs}}} = 0.260\,. \tag{5.9}$$

The value of Nyq would be 1 in the Shannon-Nyquist resolution case. As a result, the linearity of the measurement is compromised. For each subaperture image, when the light spot happens to be in the middle of a – twice bigger – CCD pixel, a small displacement is almost undetectable. On the contrary, when the light spot is exactly between two pixels, a small displacement will be measured with a too high sensitivity. This non-linearity is visible in the OOMAO simulation on figure 5.14. This simulation simply consists in measuring, with a same-defined Shack-Hartmann WFS as GTCAO one, a varying tip phase and extracts the tip measurement as the median of all horizontal displacement measurements. We notice that the measured tip (continuous line) is either flatter or steeper than the real tip (dashed line). The same type of behaviour has been pointed out in (Kolb et al., 2012) for a source whose FWHM was of 0.5 pixels (that is to say $Nyq = 0.25$). For simplicity reasons, the

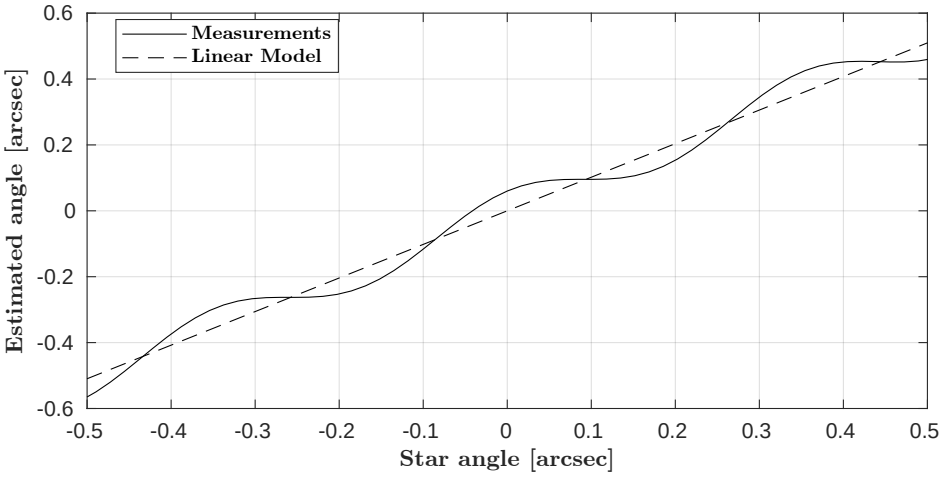

Figure 5.14: (OOMAO simulation) Comparison of the measured tip (full line) with the real linear tip (dashed lined, which is also the model-based value).

linear model in our case will be the same dashed line for all the subapertures.

Measurement noise within $M_{\text{int}}^{\text{exp}}$

We highlight here the problem of measurement noise intrinsically existing in the interaction matrix $M_{\text{int}}^{\text{exp}}$ measured on the bench. To favor a proper reconstruction of some pseudo-open loop slopes, the interaction matrix is thresholded with a value of $1.8 \times 10^{-6}\,\text{px}\,\text{count}^{-1}$ (figure 5.15). This value has been experimentally defined through the evaluation of $\|y - M_{\text{int}}^{\text{exp}} u\|$. We send to the DM some turbulence-like commands (recorded during a previous close-loop run) and compare the tip and tilt measured with the one we expected knowing the interaction matrix. As it can be seen in figure 5.16, the comparison of $M_{\text{int}}^{\text{exp}} u$ with the slopes measured after application of u is better for the thresholded interaction matrix.

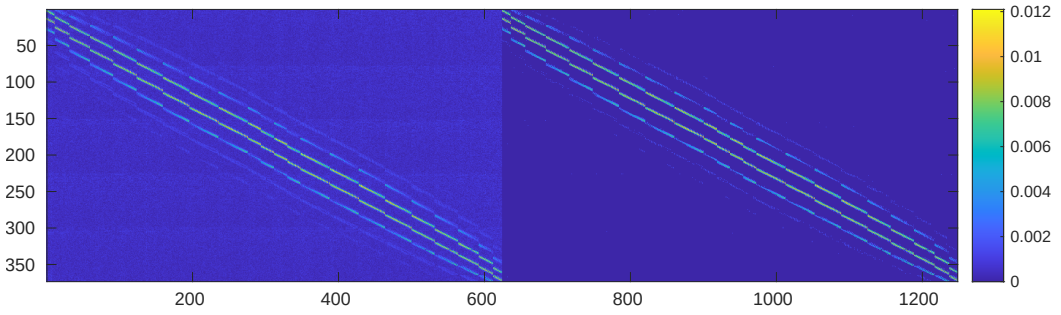

Figure 5.15: (bench data). Comparison of the interaction matrix $M_{\text{int}}^{\text{exp}}$ without (left) and with (right) threshold. Square root displayed (the threshold has a square root $(1.8 \times 10^{-6})^{0.5} = 0.0013$).

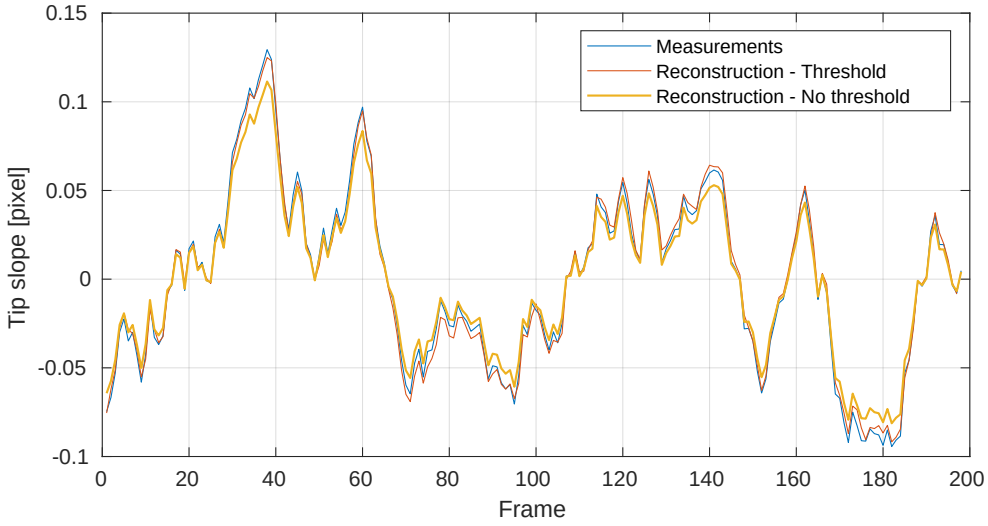

Figure 5.16: (Bench data). Comparison of the tip (angle of arrival) of the slopes measured on the bench (blue) with the slopes reconstruction $M_{\text{int}}^{\text{exp}}u$, with (red) and without (yellow) thresholding $M_{\text{int}}^{\text{exp}}$. Without thresholding, the reconstruction is 15% too weak. The angle of arrival is computed as the average of horizontal slopes.

Pseudo-open loop reconstruction with a pseudo-synthetic interaction matrix

However, we noticed that the POL slopes were still not well matching the OL slopes. We record some OL slopes of a full phase screen rotation. We close the loop and record a new batch of a full phase screen rotation. We build back a POL sample from the latter, using either $M_{\text{int}}^{\text{exp}}$ or a pseudo-synthetic interaction matrix $M_{\text{int}}^{\text{synth}}$. The way $M_{\text{int}}^{\text{synth}}$ is constructed will be detailed later in section 5.4.3. We then compare these POL samples with the OL one. To compare the samples, we use a Zernike MMSE reconstructor and compute the first Zernike modes variance.

After doing the noise filtering (figure 5.15), the $M_{\text{int}}^{\text{exp}}$-based POL have still around 15% error when using the phase screen 2 (PS2) data while the pseudo-synthetic interaction matrix allows a better reconstruction of the POL for all Zernike modes as shown in figure 5.17. Something unexplained nevertheless happens when estimating OL slopes directly from the commands, as in figure 5.16: when using the pseudo-synthetic matrix, the result is further from the real measurement than when using $M_{\text{int}}^{\text{exp}}$, as shown in figure 5.18. This means that POL reconstruction is better done with the pseudo-synthetic interaction matrix whereas reconstruction OL measurements from command vectors is more accurate with the –thresholded– experimental interaction matrix. In the following, each matrix will be used according to the situation. For the $M_{\text{int}}u$ estimation as in section 5.5 (loop delay estimation), $M_{\text{int}}^{\text{exp}}$ is used. Otherwise, for POL slopes fabrication, $M_{\text{int}}^{\text{synth}}$ is used (including in the Kalman

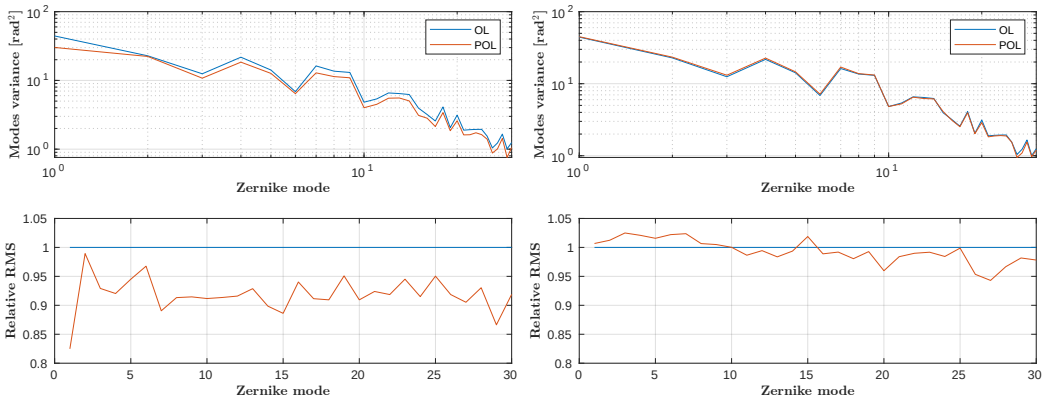

Figure 5.17: (bench data). Modal comparison of the OL (blue) with the POL (red). Top: modal variances. Bottom: ratio of square root of the respective modal variances. Left: using $M_{\text{int}}^{\text{exp}}$ for POL. Right: using $M_{\text{int}}^{\text{synth}}$ for POL.

filter).

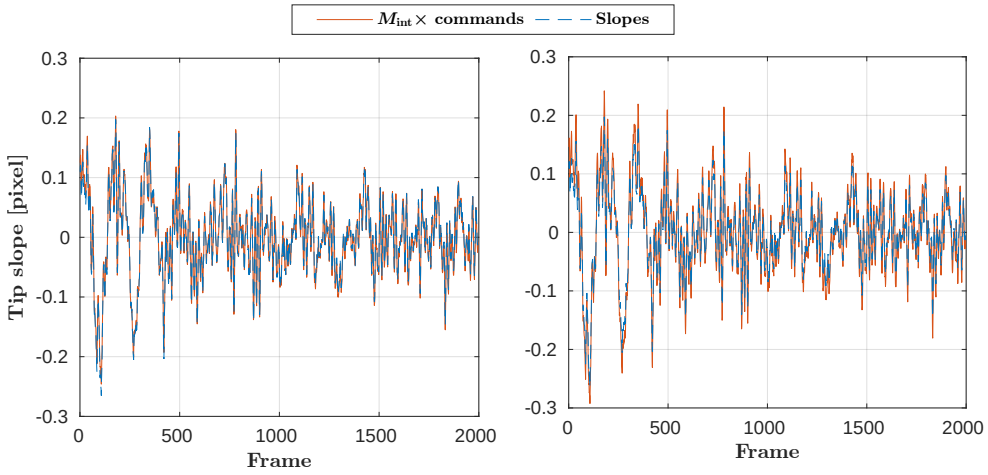

Figure 5.18: (bench data). Comparison in OL without turbulence of the measurement OL (blue) with the expected slope $M_{\text{int}}u$ (red) when sending some commands u to the DM. Left: using $M_{\text{int}}^{\text{exp}}$. Right: using $M_{\text{int}}^{\text{synth}}$. The latter leads to 20% overestimation

5.4.2 modeling of WFS matrix D

The WFS matrix D, as described in section 3.3.4, is used to describe the slopes measurements from the phase. It is also used to build the pseudo-synthetic interaction matrix in the next subsection. The linear operation that relates the phase ϕ to the non-noisy WFS measurement y can be written:

$$y = D\overline{\phi}. \tag{5.10}$$

For the sake of simplicity, we have used the typical matrix D_{O}, calculated in the software OOMAO, that can be easily transformed into D. It has been commonly used in the on-sky LQG implementations by Sinquin (Sinquin et al., 2020) on CANARY. Each of its j-th and $(j + n_{\mathrm{SA}})$-th column contains proper coefficients to compute respectively the horizontal and vertical phase gradient for the j-th subaperture. It uses only the subapertures edge pixels as described in figure 3.3.The unit is pixel per radian (pixels of the OOMAO WFS camera).

It remains to adapt D_{O} to the dimensions and conventions of GTCAO. This is done by comparing the interaction matrice (PMX) of OOMAO with the GTCAO one.

1. We notice that the subapertures indexes concur: for both, the first SA is up-left and the order of range is up-down and then left-right. It remains to simply rearrange the slopes order (that is the lines order of D_{O}) since OOMAO separates the horizontal slopes (first 312 lines) from the vertical slopes (last 312 lines) while the RTC DARC gathers the horizontal and vertical slopes of each subaperture together: $D_{\mathrm{O}} = [D_{x1}, D_{x2}, ..., D_{x312}, D_{y1}, ..., D_{y312}]^{\mathrm{T}}$ rearranged to DARC order $[D_{x1}, D_{y1}, ..., D_{x312}, D_{y312}]^{\mathrm{T}}$.

2. The sign convention of the x-slopes is matching but not the y-slopes one, visible on the example of figure 5.19. The signs of the D matrix columns should be modified as follows:

$$[D_{x1}, D_{y1}, ..., D_{x312}, D_{y312}]^{\mathrm{T}} \rightarrow [D_{x1}, -D_{y1}, ..., D_{x312}, -D_{y312}]^{\mathrm{T}} .$$

3. Eventually, the scaling must be fitted. In OOMAO, D_{O} is scaled so as to satisfy Shannon criteria whatever the wavelength of the guide star λ_{wfs} used in the simulations: the FWHM of one diffraction-limited lenslet spot $\lambda_{\mathrm{wfs}}/d_{\mathrm{SA}}$ is tacitly supposed to be equal to two CCD pixels (2px $= 2 \times 0.35''$ on sky for GTCAO). So the scaling factor to apply is $Nyq = 0.26$ for a 500-nm guide star (same logic as for equation (5.9)).

In the end, when working in Zernike space (ϕ is a vector of Zernike coefficients), we use an orthogonalized Zernike-to-zonal projector $C^{\mathrm{ZernToZon}}$ (to account for pixellisation and central obstruction). From the OOMAO matrix $D_{\mathrm{O}} = [D_{x1}, D_{x2}, ..., D_{x312}, D_{y1}, ..., D_{y312}]^{\mathrm{T}}$, the D matrix used in the LQG implemented in DARC RTC has therefore the following expression:

$$D = Nyq \times [D_{x1}, -D_{y1}, ..., D_{x312}, -D_{y312}]^{\mathrm{T}} \, C^{\mathrm{ZernToZon}}. \tag{5.11}$$

5.4.3 Construction of $M_{\mathbf{int}}^{\mathbf{synth}}$

The method to compute a pseudo-synthetic interaction matrix is fully based on (Heritier et al., 2018; Heritier-Salama, 2019). We generate numerically the interaction

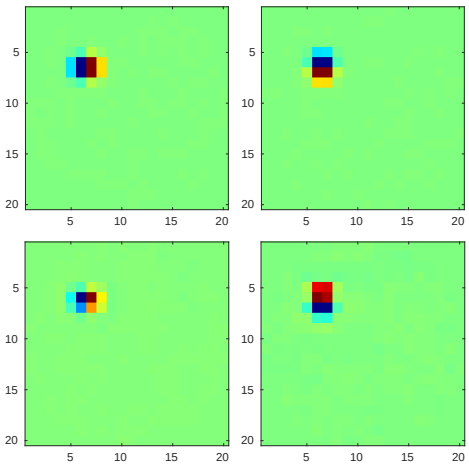

Figure 5.19: 2D representation (WFS slopes space) of the interaction matrix for the actuator number 99: OOMAO (top) and GTCAO (bottom), showing separately horizontal slopes (left) and vertical slopes (right). We notice that the sign of the vertical slopes is inverted between OOMAO and GTCAO.

matrix, identifying the key-parameters of the model from experimental inputs. The principle is to solve:

$$\arg\min_{X} ||M_{\text{int}}^{\text{synth}}(X) - M_{\text{int}}^{\text{exp}}||^2 \,, \tag{5.12}$$

where the vector X contains the necessary parameters to geometrically transform the DM actuators grid into the WFS subaperture grid. In the case where the DM and the WFS are in Fried geometry (all actuators at the corners of the microlenses), this geometrical transformation is the identity. In OOMAO, it is possible to define a DM through the map of the actuators with their respective complex coordinates $z^{\text{synth}} = x^{\text{synth}} + jy^{\text{synth}}$. The default OOMAO case is the Fried geometry, and the coordinates of the actuators are integers, corresponding to the WFS subaperture edges. The origin is the center of the pupil (the down-right corner of the subaperture located in the 10th column and the 10th line). In our case, the parameters X are defined as follow:

- The term $X(1)$ is the horizontal shift, $X(2)$ is the horizontal homothety (magnification) and X(3) is the horizontal quadratic displacement: $x^{\text{synth}} = x^{\text{fried}} + X(1) + X(2)x^{\text{fried}} + X(3)(x^{\text{fried}})^2$
- The three next terms $X(4)$, $X(5)$ and $X(6)$ are the vertical ones: $y^{\text{synth}} = y^{\text{fried}} + X(4) + X(5)y^{\text{fried}} + X(6)(y^{\text{fried}})^2$
- The rotation of angle $\theta_{\text{DM}} = X(7)$ is made once the grid has been distorted by the 6 first terms X: $z^{\text{synth}} = \exp(jX(7))\left(x^{\text{synth}} + jy^{\text{synth}}\right)$
- The influence function is also a synthetic one, a 2-D symmetric Gaussian calculated by OOMAO. This was tested in simulation in (Heritier-Salama, 2019) and

showing as good results as using an experimental influence function. The only parameter that remains to be defined is then the coupling factor $C_{\mathrm{DM}} = X(8)$, supposed identical for all the actuators

- The last parameter is a rescaling factor $X(9)$. Without figuring out the reason why, it appeared to be quite different from the expected Nyquist factor $Nyq = 0.26$ (around $X(9) = 0.45$).

With those parameters, we can define the OOMAO interaction matrix $M_{\mathrm{int}}^{\mathrm{synth}} = X(9) \times (DN)(X)$, and the Matlab function *lsqnonlin* is used to optimize equation (5.12) with respect to the nine components of X. We go until quadratic order for the shifts as indicated in a technical IAC document (Femenía, Icíar Montilla, and Núñez, 2017). The resulting pseudo-synthetic interaction matrix is very close to the measured one, as seen for example in figure 5.20 for the actuator number 70.

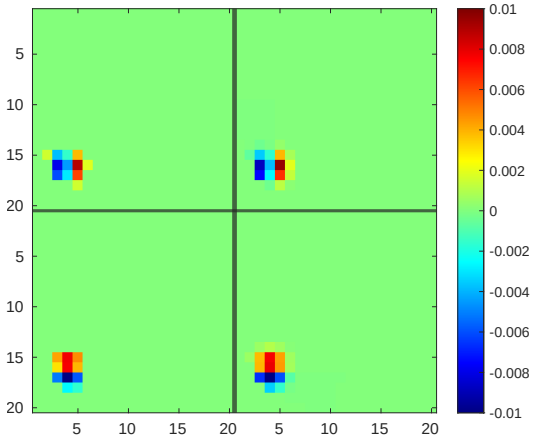

Figure 5.20: 2D representation of the GTCAO measurements for the poke of actuator number 70. Top: horizontal slopes. Bottom: vertical slopes. Left: experimental interaction matrix. Right: pseudo-synthetic interaction matrix. The square root is displayed so as to see the pixels erased by the threshold applied to the experimental interaction matrix.

5.4.4 DM actuators positions and influence functions

Together with the pseudo-synthetic interaction matrix, we obtain the distribution map of the actuators in the WFS plan, as shown in figure 5.21. The coupling factor estimated is $C_{\mathrm{DM}} = 18\%$. It is higher than the DM calibration one ($C_{\mathrm{DM}} = 14\%$), perhaps because of the GTCAO optical mount between the DM and the WFS (while the DM calibration with a Zygo was performed before its installation in GTCAO optical path). Because of a lack of time, we could not properly try to adjust each respective actuator sensitivity (we have one unique coefficient X(9) for the whole DM). Anyway, the OOMAO simulations seemed to show a very low dependency of

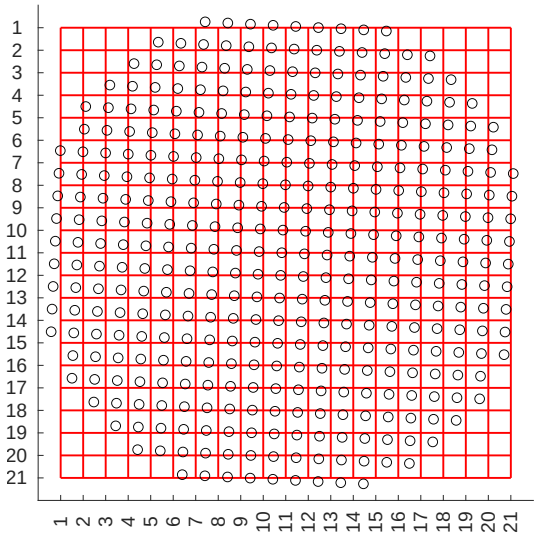

Figure 5.21: 2D representation of the GTCAO DM actuators positions (black circles) relatively to the microlenses grid (red).

the performance (less than one Strehl point) to an error on the actuators sensitivity. We have tried higher variations than those given in the technical IAC report and shown in figure 5.22 (Núñez and Martin, 2018).

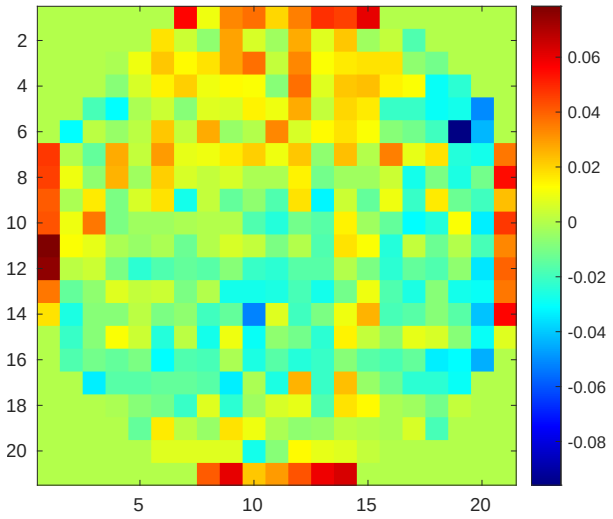

Figure 5.22: 2D representation of the GTCAO DM actuators sensitivity relatively to the average value. The actuators at the very edges are about 6% more sensitive than others.

5.4.5 Phase-to-commands projector

Let us suppose that we dispose of a prediction of the state vector $\hat{X}_{k+1|k}$. We must project it onto the DM space. As said in section 3.3.4 (equation (3.21)), the LQG control commands are computed as:

$$u_k = P_u C_\phi \hat{X}_{k+1|k}\,, \tag{5.13}$$

where the phase-to-commands projector P_u can be either $P_u^N = N^\dagger$ or $P_u^{M_{\rm com}} = M_{\rm com} D$. The behaviour was studied with OOMAO simulations with a set of parameters mimicking the GTCAO bench phase screen PS2 with a wind speed of $10\,{\rm m\,s^{-1}}$. In simulation, we can use the exact DM influence functions matrix N.

In the case of Fried geometry (between the DM and the WFS) the performance is the same for both projectors, around 51% of SR. Otherwise, when the actuator map is warped as for GTCAO (figure 5.21), simulation results change, with a drop of 5 points of SR for P_u^N and of 9 points of SR for $P_u^{M_{\rm com}}$. This matches the fact that the phase field description is limited (correction phase of the DM not well measured). This is logically worse for $P_u^{M_{\rm com}}$ due to the lower sensitivity of the WFS to the actuators that are away from the Fried geometry (example in figure 5.20).

However, the gap between the two projectors was not so high on the bench, limited to around 1 point of SR which is probably originated from the dead actuator management. Nevertheless, as explained below, P_u^N is useful to manage the dead actuators. We did not have time to pinpoint the reason of this limited improvement.

Dead actuators management

The actuator number $i^{\rm dead} = 330$ is out of order. The membrane of the DM at this actuator location can however still be reshaped by moving the neighbours thanks to the coupling. It means that the actuator is not frozen. It is simply probably not a mechanic but electronic problem, such that no voltage can be applied to that actuator. Its influence function is thus set to zero in the influence matrix N. In this way, the neighbours keep the same influence functions as if no actuator was dead. This was checked by sending some pistons to the DM and noticing that the resulting slopes measurements are matching with the such-defined pseudo-synthetic matrix as shown in figure 5.23.

Two methods to limit the impact of $i^{\rm dead}$ on the performance have been tested:

1. The first method is using the piston mode of the DM. The piston mode is normally invisible to the Shack-Hartmann WFS. But when one unique actuator is broken, a piston command sent to the DM will provoke a global up/down motion of the DM membrane, excepted for the area related to the dead actuator. In this way, the wavefront will undergo a deformation corresponding to a simple down/up motion of exclusively that 330th actuator. This is clear in figure 5.23. It is simpler to take advantage of this if the coupling of the DM

is very low, so that the piston performed by the neighbours is not moving the i^{dead} actuator too much.

The drawback of this piston method is that it may limit the dynamics of the DM. Since all actuators are moving all together, there is the risk of reaching the saturation threshold. This did not happen on the bench but was nearly to with the challenging atmosphere phase screen PS2.

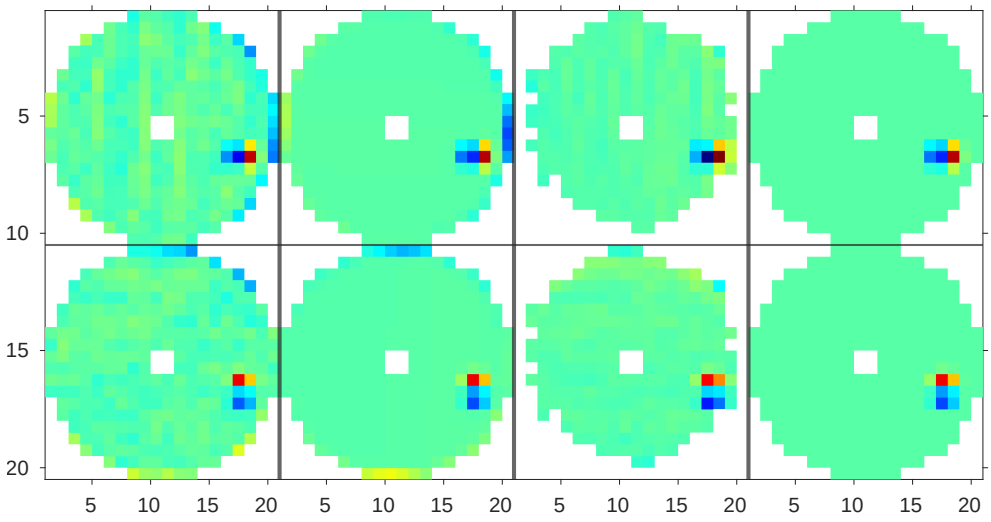

Figure 5.23: 2D comparison between the expected measurement of a piston. Top: horizontal slopes. Bottom: vertical slopes. Left to right: $M_{\text{int}}^{\text{exp}} \times u_{\text{piston}}$, $M_{\text{int}}^{\text{synth}} \times u_{\text{piston}}$, on-bench piston measurement, and $M_{\text{int}}^{\text{synth}}(:, 330)$ (330th actuator's pseudo-synthetic effects). White measurements correspond to the absence of measurement (subapertures that are invalid because not enough flux or located outside the telescope pupil).

A simple way to allow the use of the piston is to compute P_u with a pseudo-synthetic model which includes the dead actuator (not put to zero). Then, the command expected from the dead actuator command is taken off from each Zernike mode number z by subtracting a full piston:

$$P_u^z \leftarrow P_u^z - P_u^z(i^{\text{dead}})\,. \tag{5.14}$$

The tip and spheric modes example is shown in figure 5.24. The same process is possible with P_u^N and $P_u^{M_{\text{com}}}$ using $M_{\text{int}}^{\text{synth}}$. For the $P_u^{M_{\text{com}}}$ case, if no pseudo-synthetic interaction matrix is available, another way is to keep the piston-like mode among the SVD commands modes of $M_{\text{int}}^{\text{exp}}$ to compute M_{com}. Such a mode is shown in figure 5.25. Allowing the piston has improved the SR of some 1.5 point for challenging atmosphere case and around 0.5-1 point for the favorable atmosphere case.

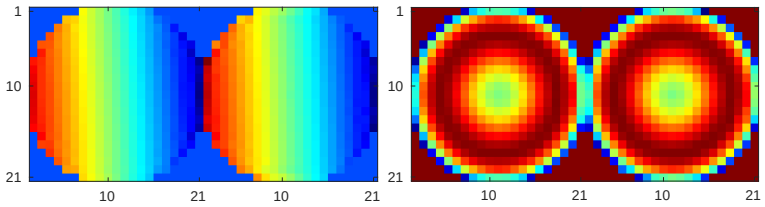

Figure 5.24: 2D display of the projectors using the piston mode (tip on the left, spherical on the right). Subleft: P_u^N. Subright: $P_u^{M_{\text{com}}}$. They are very similar, but the N-based projector manages better the conversion. The angle of spin of the DM (3°) is visible on the tip mode.

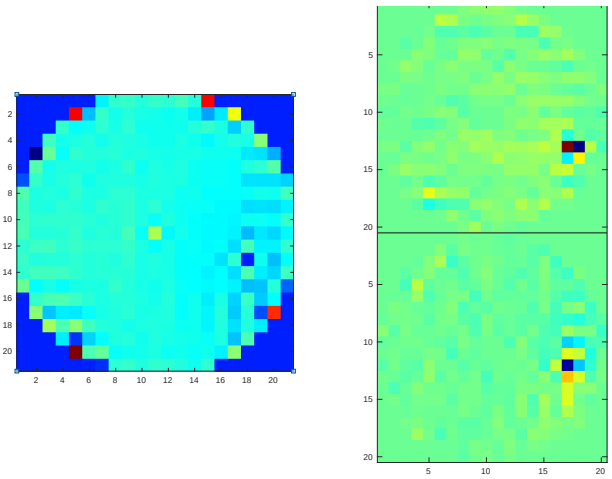

Figure 5.25: 2D display of the GTCAO DM piston mode obtained from $M_{\text{int}}^{\text{exp}}$ SVD (mode number 369 out of 373). The 4 or 5 strong outlier commands on the edge of the DM should be truncated to the average turquoise value to avoid useless strong edge commands.

2. A second and preferable method to manage the dead actuator is to use its neighbourhood. This is actually automatically done when performing the pseudo inverse of M_{int} or N when the dead actuator influence function is simply set to zero. The first advantage compared with the differential piston method above is that the actuators stroke is way decreased, with only a very few saturation issues at the neighbourhood (in some simulations, but never on the bench). The second big advantage is that it is applicable even if more than one actuator is dead. The inconvenient is that it is slightly less precise than the piston since exciting all the neighbourhood around the dead actuator. Some examples of projector modes are given in figure 5.26.

   On bench tests, this P_u^N projector improves the SR compared with a filtered $M_{\text{com}}D$ (filtered piston mode). It gives 1 point SR more (instead of 1.5 point with the piston method 1.) for the challenging atmosphere case and 0.5 point for the favorable atmosphere case. With $P_u^{M_{\text{com}}}$, filtering or not the high order SVD modes that excite the actuators in the neighbourhood of the dead one does not allow a proper management of i^{dead}.

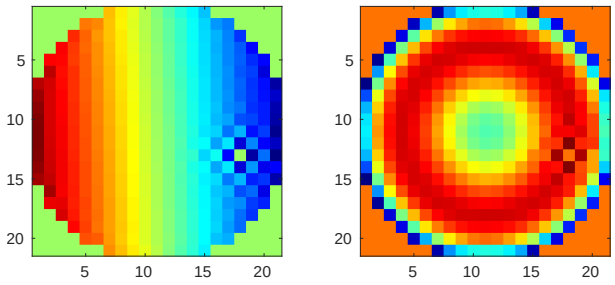

Figure 5.26: 2D display of the projector P_u^N using the dead actuator neighbourhood. Left: tip mode. Right: spherical mode.

5.4.6 Conclusion on the use of a pseudo-synthetic interaction matrix

When using the formula $M_{\text{int}}^{\text{exp}} \times u$, it is important to apply a noise threshold to the measured interaction matrix, and the result is in our case closer to the corresponding OL slopes obtained on the bench using the same commands. It is quite simple to build from $M_{\text{int}}^{\text{exp}}$ a pseudo-synthetic interaction matrix. The latter appears to better reconstruct the pseudo-open loop slopes. It also gives access to a DM influence functions matrix N that accounts for the bench geometry and that is used for the phase-to-commands projector P_u^N. The latter appeared in OOMAO simulations to be 10% better than $P_u^{M_{\text{com}}}$ due to the limited visibility of some actuators in the middle of some subapertures ($SR_N \approx 1.1 SR_{M_{\text{com}}}$ with $SR_{M_{\text{com}}} \simeq 40\%$).

On bench tests, both yet appeared (without explanation) to be of practically the same quality: only one SR point better for P_u^N, just due to a better account of the dead actuator. Using the piston mode of the DM to replace the dead actuator

(inside $P_u^{M_{\text{com}}}$ or P_u^N) is more advantageous. However, if several actuators came to die, the piston method would probably not bring any improvement while the neighbourhood method would stay satisfactory. Another advantage of the pseudo-synthetic interaction matrix is that it adapts easily to any change on the bench, as noted in (Heritier-Salama, 2019; Kolb et al., 2012). We therefore retained P_u^N for our bench tests.

5.5 Fractional loop delay estimation

We presented in chapter 4 an in-depth study of how the loop delay intervenes in the high-performance predictive controller definition, how it affects the stability margins and vibration mitigation. In this section, we will describe various methods to estimate the loop delay in our AO system.

5.5.1 Problem description

We will describe three methods to carry out off-line estimations of the loop delay Δ starting from the end of the WFS CCD integration to the end of the related DM reshaping. This delay includes the camera read-out, the slopes computation (from the received WFS image), the corresponding commands computation and the DM settling time. The total loop delay, defined in chapter 4 as $d + \delta$ frames, is thus expressed here under the form $1 + \Delta$ frames, where Δ can be bigger than 1 frame contrarily to δ. This way, the 1-frame exposure time of the WFS camera will not be part of the estimation.

We will describe three methods to compute the delay Δ: the DM step response, the Fourier transform with interspectrum, and the least-squares (LS) resolution. This last method appears to be the most versatile as shown in simulation and easier to implement than the Fourier one. This delay will be for sure function of the state vector size.

5.5.2 Measurement model

The three methods compare the data recorded on the bench without disturbance with the WFS model. In this section, the WFS measurement is denoted by y^{wfs}, the measurement noise w as usual, and the command-based reconstructed slopes by y^{dm}, with $y_k^{\text{dm}} = M_{\text{int}}\, u_k$. With the ceiling and floor rounding of Δ denoted by $\lceil\Delta\rceil$ and $\lfloor\Delta\rfloor$ respectively, we have:

$$y_k^{\text{wfs}}(\Delta) = M_{\text{int}} \left((\Delta - \lfloor\Delta\rfloor) u_{k-\lceil\Delta\rceil} + (\lceil\Delta\rceil - \Delta) u_{k-\lfloor\Delta\rfloor} \right) + w_k \tag{5.15}$$

$$= (\Delta - \lfloor\Delta\rfloor) y^{\text{dm}}_{k-\lceil\Delta\rceil} + (\lceil\Delta\rceil - \Delta) y^{\text{dm}}_{k-\lfloor\Delta\rfloor} + w_k \,. \tag{5.16}$$

In many typical cases on AO systems, GTCAO included when operating below $F_{\text{s}} \sim 600\,\text{Hz}$, the delay Δ is below one frame so that $\lfloor\Delta\rfloor = 0$ and $\lceil\Delta\rceil = 1$. Equation (5.15)

then becomes:

$$y_k^{\text{wfs}}(\Delta) = M_{\text{int}} \left(\Delta u_{k-1} + (1-\Delta)u_k\right) + w_k. \tag{5.17}$$

In these equations, we have supposed that the settling time is small enough (inferior to 1 frame) to involve in equation (5.15) only two successive commands frames in the model $y^{\text{wfs}}(\Delta)$. This was checked on the bench as shown in GTCAO DM description, figure 5.11.

5.5.3 Estimation methods for the delay Δ

5.5.3.1 Step response

Principle

The step response method consists in sending to the DM a tip command in open-loop and catch the moment when it starts to take its final shape by plotting the WFS slopes average (ex. in figure 5.27). The last point before the final plateau, point number k of value noted ϵ, is the frame within which the DM reached its final shape (at frame $k+1$ the shape has already been established). The value of ϵ can be seen as the percentage of the unitary step that has been integrated. The delay is then simply computed as $(k-\epsilon)$ frame. At high FPS, we can roughly distinguish the calculation time and the DM settling time. The drawback is how irrelevant a step command is compared with what the DM does when operating in real time to compensate turbulence.

Application

The used data sequences are similar to that of figure 5.27. For instance, looking at yellow curve in the $F_{\text{s}} = 500\,\text{Hz}$ case, we obtain a delay $\Delta = (k-\epsilon)T_{\text{s}} = (2-0.83) \times 2 = 2.34\,\text{ms}$. Another example, looking at purple curve in the $F_{\text{s}} = 1000\,\text{Hz}$ case, we obtain a delay $\Delta = (k-\epsilon)T_{\text{s}} = (3-0.4) \times 1 = 2.6\,\text{ms}$. All results are gathered in the figure 5.28.

5.5.3.2 Fourier

Principle

Fourier method uses the standard properties of Fourier transform of two signals of same frequency f, one being shifted by Δ. In our case, the delay equation (5.15) becomes:

$$\forall f, \mathcal{F}\left(y^{\text{wfs}}(\Delta)\right)(f) = \exp(2i\pi\Delta f)\mathcal{F}\left(y^{\text{dm}}\right)(f) + \mathcal{F}(w)(f). \tag{5.18}$$

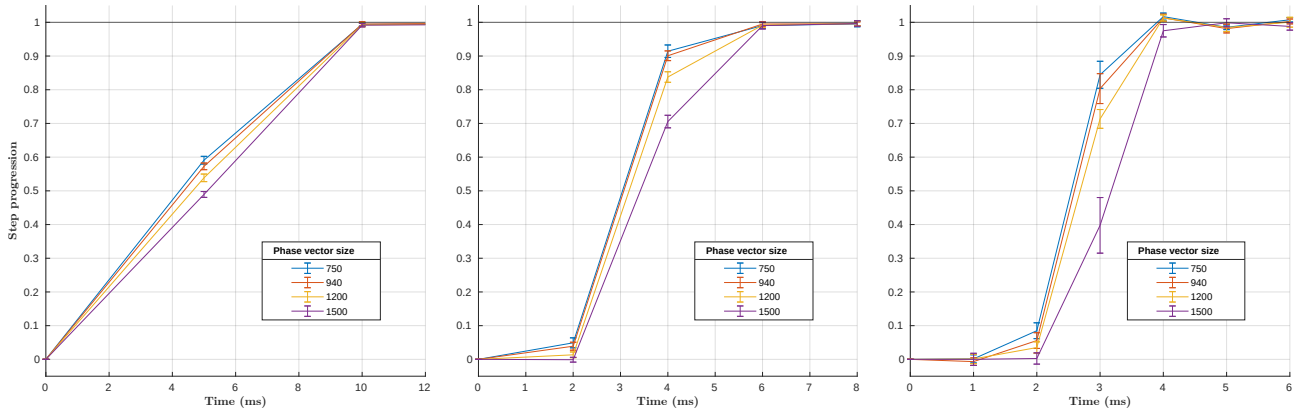

Figure 5.27: (bench) Plots of the step measurements used to compute the delay. Left to right: 200, 500 and 1000 FPS. For each graph, the first point (frame number 0 at arbitrary time position $t_0 = 0\,\text{ms}$) corresponds to the integration frame that ends at t_0. Even if it is in open loop, the command is still calculated by the RTC so that the calculation time is accounted for: the next command vector is applied only after the command calculation is finished. Each plot is the average of ten step responses, and the error bars correspond to $\pm\sigma$.

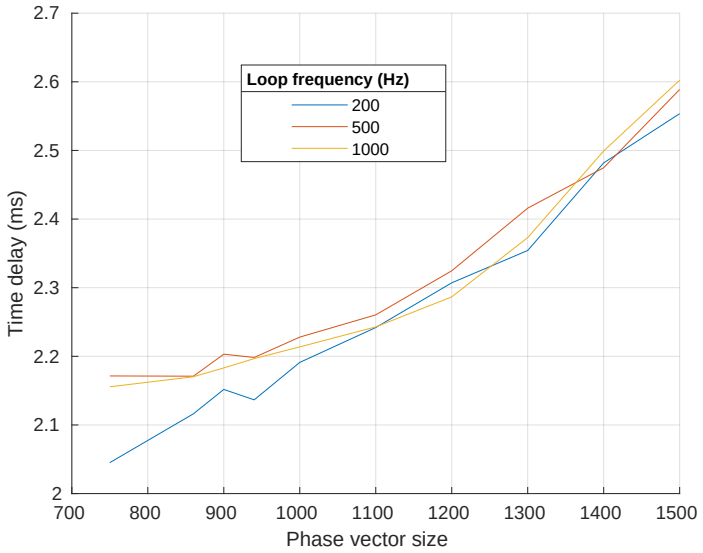

Figure 5.28: (bench) Plots of the loop delays estimated with the step method for different phase vector sizes at different FPS.

After multiplying left and right by the conjugate $\overline{\mathcal{F}\left(y^{\mathrm{dm}}\right)}$, we get the interspectrum $\mathcal{I}$ written as:

$$\forall f, \mathcal{I}(f) = \mathcal{F}\left(y^{\mathrm{wfs}}\right)\overline{\mathcal{F}\left(y^{\mathrm{dm}}\right)}(f) \tag{5.19}$$

$$= \exp\left(2i\pi\Delta f\right)\left|\mathcal{F}\left(y^{\mathrm{dm}}\right)(f)\right|^2 + \mathcal{F}(w)\,\overline{\mathcal{F}\left(y^{\mathrm{dm}}\right)}(f)\,. \tag{5.20}$$

If the noise w is negligible compared with y^{dm} at frequency f, the argument of $\mathcal{I}$ will be a straight line of slope $2\pi\Delta$. Only remains to catch the desired variable Δ:

$$\Delta = \frac{slope\left(\arg(\mathcal{I})\right)}{2\pi} = \frac{k_{\mathcal{I}}}{2\pi}\,. \tag{5.21}$$

This method had been proposed by Jose Marco de la Rosa at the IAC in the case where the commands sent to the DM are an oscillating tip of single frequency f_{vib} and amplitude A. The expected average of horizontal slopes is then:

$$y^{\mathrm{dm}^{\mathrm{tip}}} = A\cos(2\pi f_{\mathrm{vib}}t + \phi_1)\,,$$

while the average of measured horizontal slopes is

$$y^{\mathrm{wfs}^{\mathrm{tip}}} = A\cos(2\pi f_{\mathrm{vib}}t + \phi_2) = A\cos\left(2\pi f_{\mathrm{vib}}(t-\Delta) + \phi_1\right)\ .$$

We notice simply that $\Delta\phi = 2\pi f_{\mathrm{vib}}\Delta$, which is a particular case of equation (5.21) for the case of single-frequency signal:

$$\Delta = \frac{\Delta\phi}{2\pi f_{\mathrm{vib}}}\,. \tag{5.22}$$

Jose Marco made it then possible to be entirely implemented with one GTCAO GUI button (commands sequence fabrication, application to the DM, recording of the slopes y^{wfs}, computation of Δ).

For broader-frequency-covering signals, the slope $k_{\mathcal{I}}$ has to be estimated by linear interpolation of $\arg(\mathcal{I})$.

With many tests in simulation and on bench data, we have shown that for the case where u is a sequence of turbulence-like commands (not only one single vibration), the interpolation of $\arg(\mathcal{I})$ is way better by weighting the cost-function V with the square norm $|\mathcal{I}(f)|^2$:

$$V(k) = \sum_{f=f_{\min}}^{f_{\max}} |\mathcal{I}(f)|^2 \times \left(kf - \arg(\mathcal{I}(f))\right)^2\,. \tag{5.23}$$

This weight allows to account for the relative reliability of the $\arg(\mathcal{I})$ curve points. Then:

$$k_{\mathcal{I}} = \underset{k}{\mathrm{argmin}} V(k)\,. \tag{5.24}$$

The frequency interval $[f_{\min}, f_{\max}]$ (and there could be more if desired) on which the slope is estimated is self-chosen. This is useful for on-sky delay estimation, when

the spectral analysis is to be performed on frequency ranges where the turbulence disturbance is not too strong. It works in simulations when the command signal is at least twice stronger than the parasite turbulence one. This optimization of equation (5.24) is done for both the horizontal slopes average (1D tip time-series) and vertical slopes average (1D tilt time-series) giving out their respective slopes estimations. It also appeared to be possible on other Zernike modes (tested for modes 1 to 5) doing a phase reconstruction, if the SNR is high enough. The final slope $k_{\mathcal{I}}$ used to apply equation (5.21) is then:

$$k_{\mathcal{I}} = \frac{k_{\mathcal{I}_{\text{tip}}}/V(k_{\mathcal{I}_{\text{tip}}}) + k_{\mathcal{I}_{\text{tilt}}}/V(k_{\mathcal{I}_{\text{tilt}}})}{1/V(k_{\mathcal{I}_{\text{tip}}}) + 1/V(k_{\mathcal{I}_{\text{tilt}}})}\,. \tag{5.25}$$

Application

The interspectrum process is illustrated in figure 5.29. Estimation results are in figure 5.32, together with those of the least-squares method described hereafter.

5.5.3.3 Least-squares

Principle

We propose to perform a least-squares (LS) estimation of Δ by writing the delay equation (5.15) for n_{iter} frames, leading to a linear parametric equation (Walter and Pronzato, 1997) that is solved for Δ. With the hypothesis that $\Delta < 1$, this writes:

$$\begin{aligned}
y_2^{\text{wfs}} - M_{\text{int}}\,u_2 &= M_{\text{int}}\,(u_1 - u_2) \times \Delta + w_2 \\
y_3^{\text{wfs}} - M_{\text{int}}\,u_3 &= M_{\text{int}}\,(u_2 - u_3) \times \Delta + w_3 \\
&\vdots \\
y_{n_{\text{iter}}}^{\text{wfs}} - M_{\text{int}}\,u_{n_{\text{iter}}} &= M_{\text{int}}\,(u_{n_{\text{iter}}-1} - u_{n_{\text{iter}}}) \times \Delta + w_{n_{\text{iter}}}
\end{aligned} \tag{5.26}$$

with w_k the measurement noise vector. This can be concatenated into a unique vectorial equation

$$Y = R \times \Delta + W, \tag{5.27}$$

where Y and the regressor R are composed of only known terms. This can be straightforwardly solved with the LS method:

$$\hat{\Delta} = R^{\dagger} Y\,. \tag{5.28}$$

Using the noise statistics Σ_w to weight the estimation of Δ (more noisy subapertures measurements have a smaller weight in Δ estimation) did not modify the results. This method also works with on-sky open-loop data, that is to say with a parasite turbulence-induced signal $D\phi$ added to the self-introduced one y^{dm}. It is just necessary to either extend the batch size n_{iter} or increase the strength of the injected signal $M_{\text{int}}\,u$.

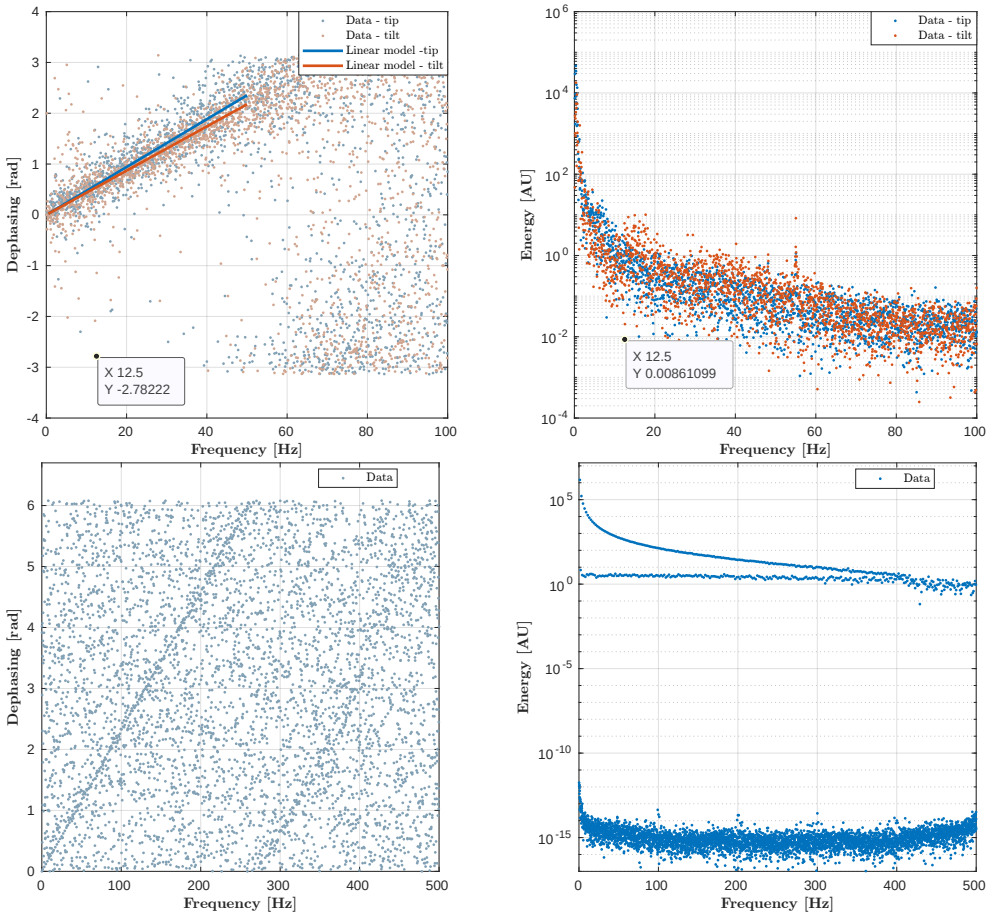

Figure 5.29: Examples of interspectra phases ($\arg(\mathcal{I})$, left) and energy ($|\mathcal{I}|$, right). Top: using turbulence-like commands. Bottom: using tip steps commands. The point at 12.5 Hz shows the relevance of the energy ponderation we suggested in equation (5.24). It is even clearer with tip steps interspectrum (bottom) with many purely noisy frequencies.

If the result happens to be negative, the first responsible is the hypothesis of $\Delta < 1$. It was confirmed by simulation. This means that the delay may actually be between $\Delta = 1$ and 2 frames, so equation (5.26) must simply use y_{k+1}^{wfs} instead of y_k^{wfs} for $k = 2, ..., n_{\text{iter}}$.

The LS theory gives access to an estimation σ^{Δ} of the estimation error standard deviation. Denoting by $e \triangleq Y - R\hat{\Delta}$ the estimation residues, and by σ_e its scalar standard deviation, then:

$$\sigma^{\Delta} = \sigma_e \left(\frac{1}{R^{\mathrm{T}} R} \right)^{1/2} \quad . \tag{5.29}$$

Application

We can show in figure 5.30 the validity of equation (5.29). The delay estimations are performed on the bench putting the RTC either on integrator mode (red curve) or in LQG mode (blue curve). We see that the experimental results of Δ estimations have an RMS matching rather well with the theoretical formula of equation (5.29). It can thus be used as an indicator of whether the data sample used for delay estimation will allow a sufficient precision. In figure 5.32, it can be seen that the LS method

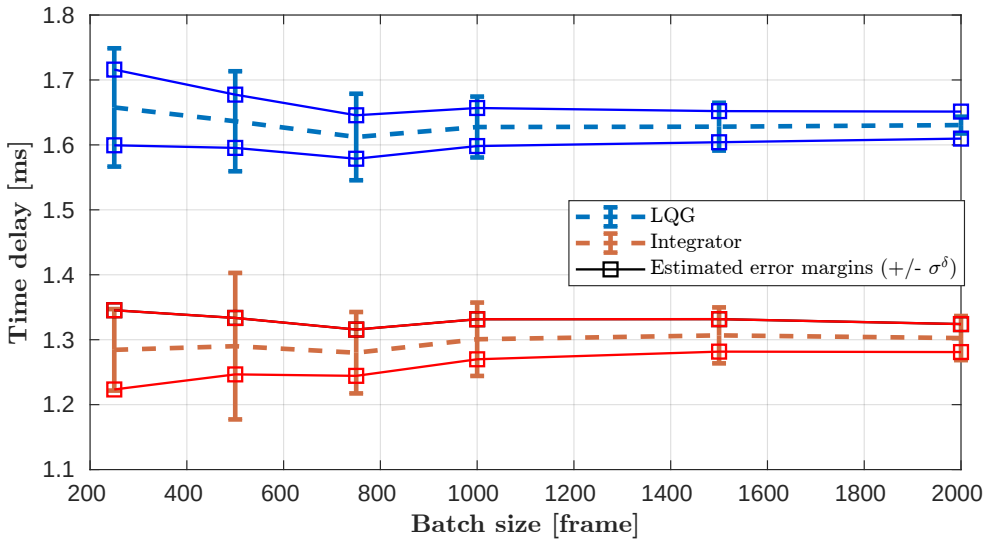

Figure 5.30: (bench) Delay Δ estimations with LS method for different sample sizes n_{iter}. Each point shows the average and $\pm$ the STD of 8 different samples. The squares show the expected STD. The commands data sent to the DM were a Keck batch.

tends to give more reliable results in the case of turbulence-like injected commands.

5.5.3.4 Simulation tests

The methods based on FFT and LS are tested by generating more or less noisy measurements y^{wfs} using some past bench commands batches u and applying equation (5.15) with self-chosen value of $\Delta = 2\,\text{ms}$. Results are given in figure 5.31. It shows that both methods are perfectly working in case of a vibration command, with a better repeatability in the LS results. However, in the case of turbulence-like AO commands, the Fourier method is getting limited in terms of precision. This simulation allows to conclude that the Fourier method should only be used with sine wave commands to get enough precision of the linear interpolation of $arg(\mathcal{I})$.

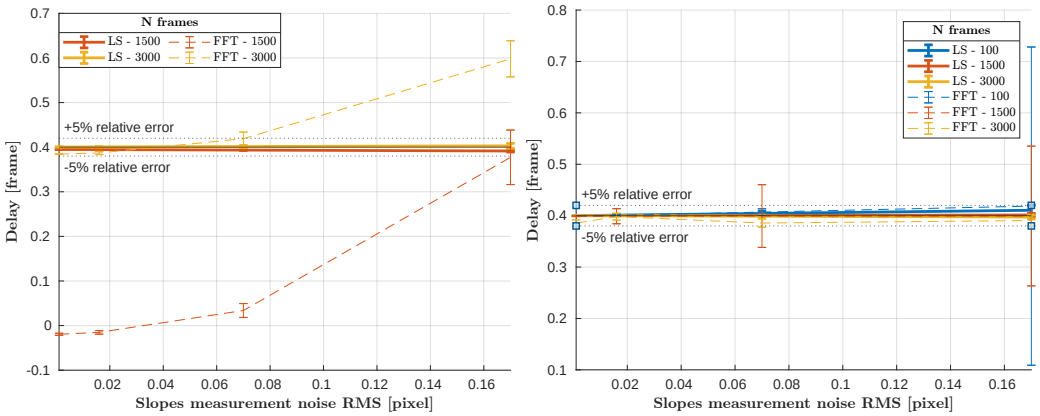

Figure 5.31: Simulated slopes data. Plots of the obtained delays for different noise values and different sample sizes. The used commands are turbulence-like on the left, 12-Hz vibration on the right. Internal source without turbulence.

5.5.3.5 Bench results and conclusion

We notice on the results of figure 5.32, that both FFT and LS delay estimation methods are quite consistent, the time-delay increasing with the size of LQG phase vector. The case of turbulence-like commands (left) at 100 Hz (blue curves) confirms the limits of the FFT method as predicted in simulations before. The use of vibration commands (right) allows to avoid being subject to this issue, with moreover a simpler interspectrum process (needs only equation (5.22), without the need of linear interpolation). On GTCAO, the delay estimations were consistent between the two methods whatever the commands sent were some sky-like or some vibrations. No distinguishable dependence on the Zernike modes appeared, as expected from the negligible time response of the DM (tests done for tip, tilt, focus and astigmatism).

We have also tested cases in presence of a disturbance signal $D\phi$. Such cases estimation results are not displayed on the graphs, but a time-series example is given in figure 5.33. It appeared that the LS method is more robust (as expected

from the simulation tests of sensitivity to the measurement noise), with a variation in the estimation lower than 0.1 ms.

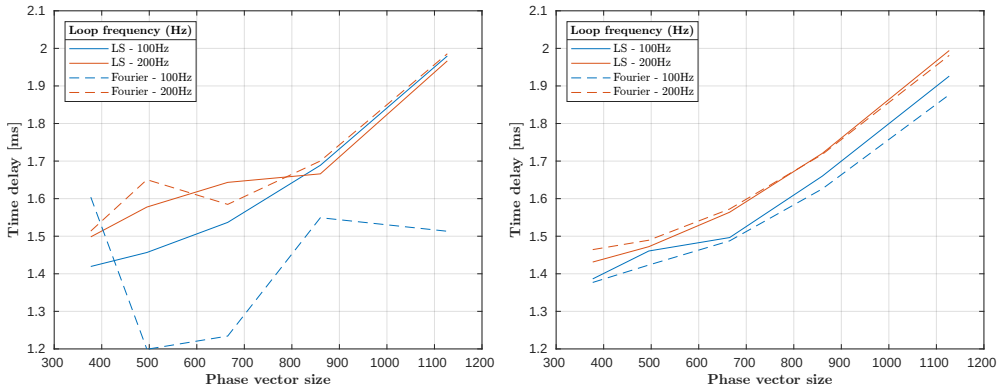

Figure 5.32: Plots of the estimated delays for various LQG phase vector sizes and FPS. The commands are turbulence-like on the left and a pure tip vibration $f_{\text{vib}} = 20\,\text{Hz}$ on the right ($n_{\text{iter}} = 4000$). Internal source without turbulence.

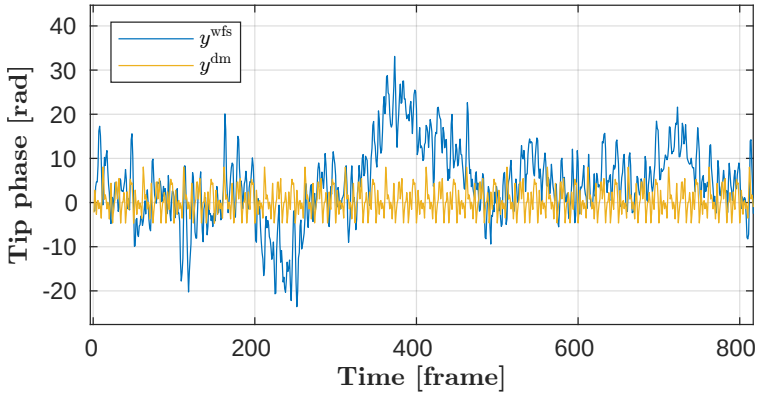

Figure 5.33: (bench) Example of expected signal y^{dm} (yellow) and actually measured disturbed signal (blue). The LS method still extracts the delay existing between both, the FFT method does not.

In any case, a good way to check the validity of the estimations is to make it for various growing size samples as shown in figure 5.30 and see whether it indeed converges with similar STD as expected with equation (5.29). In terms of implementation complexity, the LS is very simple (no transition towards frequency space is needed).

As for the step response method with results in figures 5.28 and 5.34, the delay is about 0.5 ms bigger. This discrepancy is significant enough to discard this method.

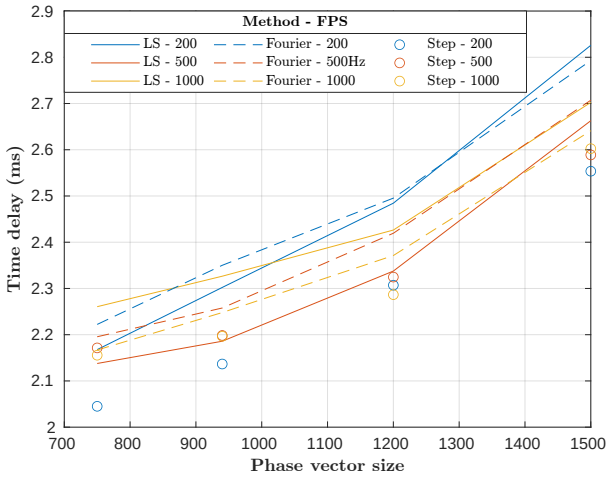

Figure 5.34: (bench) Plots of the delay estimations obtained for various phase vector size and FPS. The commands are tip steps. Internal source without turbulence.

5.6 Measurement noise covariance matrix

5.6.1 Telemetry-based construction method

As explained in section 3.3.4, the computation of the Kalman gain L_∞ calls for the definition of the measurement noise covariance matrix Σ_w. We conduct a telemetry-based procedure, based on WFS measurements and flux per subaperture, that delivers a Kalman gain leading to both a stable and efficient closed-loop controller, notably well adapted to the case of segmented primary mirror with unilluminated subapertures. It is described in the article of the SPIE conference at Montréal in July 2022 (Marquis et al., 2022), included hereafter. This matrix Σ_w can also be used for the MAP phase reconstruction.

Linear Quadratic Gaussian predictive control for the Gran Telescopio Canarias AO system: design issues and first bench results

Lucas Marquis[a], Caroline Kulcsár[a], Icíar Montilla[b], Henri-François Raynaud[a], José Marco de la Rosa[b], Óscar Tubío Araújo[b], Alastair Basden[c], and Marcos Reyes García-Talavera[b]

[a]Institut d'Optique Graduate School, Laboratoire Charles Fabry - CNRS, Université Paris-Saclay, Palaiseau, France
[b]Instituto de Astrofísica de Canarias, La Laguna, Spain
[c]Durham University, United Kingdom

ABSTRACT

The Gran Telescopio Canarias (GTC) will be soon equipped with an Adaptive Optics (AO) system. The GTCAO system[1,2] is currently at the Instituto de Astrofisica de Canarias (IAC), where tests and performance assessment are ongoing. The Institut d'Optique Graduate School-Laboratoire Charles Fabry (IOGS-LCF), through a collaboration with IAC, is exploring high performance control solutions. In this proceeding, we present first bench results for such a controller, namely a Linear Quadratic Gaussian regulator (LQG). First, we briefly describe the GTCAO bench and the principle of the LQG regulator. Second, an aspect of this development is outlined, namely the wavefront sensor measurement noise variance characterization. It is conveniently based on the use of telemetry data (wavefront sensor closed-loop slopes power spectral densities and subapertures flux) allowing for an easy-to-update and best-tuned controller. Finally, on-bench performance results are presented with an LQG regulator in the line of the previous on-sky experiments with full LQG regulator,[3,4] implemented in DARC,[5] the GTCAO RTC. Comparison is performed with the integrator as baseline controller, through evaluation of the Strehl ratio from point spread functions acquired on the scientific camera, rejection transfer functions and stability margins.

Keywords: Adaptive Optics, discrete-time LQG control, asymptotic Kalman filter, measurement noise covariance, vibration filtering

1. INTRODUCTION

1.1 GTC telescope

The Gran Telescopio Canarias telescope is until now the biggest telescope in visible/infrared wavelength range. Located in La Palma (Canaries Islands, Spain), it has a segmented primary mirror (37 segments) of equivalent diameter 10.4 m. It will be equipped next year with an adaptive optics system: the GTCAO.

1.2 GTCAO

The GTCAO is a Single Conjugated AO (SCAO) system, currently in laboratory at the Instituto de Astrofisica de Canarias (IAC), where tests and performance assessment are ongoing. It is composed of those three main components:

1. Deformable mirror (DM): Cilas piezo-electric, size 21 × 21 with 373 used actuators
2. Wavefront sensor (WFS): Shack-Hartmann with OCAM2 camera (EMCCD), size 20 × 20 with 312 used subapertures
3. Real-time controller: Durham AO Real-Time Controller[5] (DARC), which embeds an LQG controller

The typical loop sampling frequencies extend from 50 Hz to 1000 Hz, corresponding respectively to NGS magnitudes of around 14 and 10 (or less).

Further author information: lucas.marquis@institutoptique.fr

1.3 GTCAO controller

The controller baseline for GTCAO is the integrator, with a tip/tilt loop separated from the higher orders loop. The core of our work is the design of a high-performance controller based on data-driven models: the LQG controller.

1.3.1 Integrator

When closing the loop with a sampling time of T_s, the calculation of an integrator command u^{INT} at time kT_s using the residual wavefront slopes measurement y_k is given by

$$u_k^{\mathrm{INT}} = u_{k-1}^{\mathrm{INT}} - \left(gM_{\mathrm{com}}y_k + g^{\mathrm{TT}}M_{\mathrm{com}}^{\mathrm{TT}}y_k\right) \tag{1}$$

where M_{com} is the DM command matrix and $M_{\mathrm{com}}^{\mathrm{TT}}$ the tip/tilt modes command matrix. The loop gains g and g^{TT} are optimized on the bench according to the disturbance (phase screen, vibration) and measurement noise (variance σ_w^2, depending on the NGS magnitude M_{NGS} and the sampling frequency F_s).

1.3.2 Linear Quadratic Gaussian controller

For the sake of simplicity, we suppose here that GTCAO has a total loop delay of exactly two frames (one for the WFS exposure time, one for WFS camera read-out, slopes and command computation and DM reshaping).

Principle Our goal is to compute the command u_{k-1} that minimizes the residual phase variance $J(u) = \mathrm{var}(\phi_k^{\mathrm{res}}) = \mathrm{var}(\phi_k - \phi_k^{\mathrm{cor}})$. The correction phase ϕ_k^{cor} is related to the command vector u through $\phi_k^{\mathrm{cor}} = Nu_{k-1}$, N being the DM influence matrix.

To design an LQG controller, we need a state space representation of the AO system (including wavefront perturbations), obtained for example in the form

$$\begin{cases} X_{k+1} = AX_k + \Gamma v_k \\ \phi_k = C_\phi X_k \\ y_k^{\mathrm{OL}} = CX_k + w_k \end{cases} \tag{2}$$

where X_k is the state vector at time k, A is the state matrix containing the dynamics of the perturbation model. The disturbance ϕ_k is expressed on a Zernike base and is obtained as an output thanks to the matrix operator C_ϕ. The process noise v is zero-mean, white and Gaussian with covariance matrix Σ_v insuring that ϕ has the desired Von Kármán statistics. The matrix Γ simply ensures consistency with the dimensions of the state vector X_k. The open-loop WFS measurement Y^{OL} is affected by a zero-mean white Gaussian measurement noise w with covariance matrix Σ_w, and C is the observation matrix that encodes the WFS operations.

The optimal control which minimizes $J(u)$ is an LQG regulator. The control takes the form

$$u_k = N^\dagger \hat{\phi}_{k+1|k} \tag{3}$$

where $\hat{\phi}_{k+1|k} = \mathrm{E}(\phi_{k+1}|\mathcal{I}_k) = C_\phi \hat{X}_{k+1|k}$ is the output of the asymptotic Kalman filter built from (2), $\mathcal{I}_k = \{y_k, y_{k-1}, ..., u_{k-1}, u_{k-2}, ...\}$ representing all available information at time k.

Kalman filter calculation The real-time part of the asymptotic Kalman filter corresponds to the equation

$$\widehat{X}_{k+1|k} = A\widehat{X}_{k|k-1} + L_\infty \left(y_k - \widehat{y}_{k|k-1}\right) \tag{4}$$

where $\widehat{y}_{k|k-1} = C\widehat{X}_{k|k-1} - M_{\mathrm{int}}u_{k-2}$ is the prediction of the closed-loop residual slopes, and M_{int} is the interaction matrix.

The prediction Kalman gain L_∞ is computed off-line:

$$L_\infty = A\Sigma_\infty C^{\mathrm{T}} \left(C\Sigma_\infty C^{\mathrm{T}} + \alpha_{\mathrm{ff}}\Sigma_w\right)^{-1} \tag{5}$$

with Σ_∞ the asymptotic estimation error covariance matrix and α_{ff} is a fudge factor that allows to tune the global signal-to-noise ratio. The matrix Σ_∞ is then obtained as the solution of the following discrete algebraic Riccati equation, computed off-line:

$$\Sigma_\infty = A\Sigma_\infty A^{\mathrm{T}} + \Gamma\Sigma_v\Gamma^{\mathrm{T}} - A\Sigma_\infty C^{\mathrm{T}}\left(C\Sigma_\infty C^{\mathrm{T}} + \alpha_{\text{ff}}\Sigma_w\right)^{-1} C\Sigma_\infty A^{\mathrm{T}}. \tag{6}$$

The state matrix A and state noise covariance matrix $\Gamma\Sigma_v\Gamma^{\mathrm{T}}$ embed the disturbance model. The matrix Σ_w embeds the WFS measurement noise model. We need to model the disturbance and the measurement noise faced by the AO system as efficiently as possible in terms of control performance. We focus in this paper on the computation of Σ_w, and we explain in next section how we compute it using telemetry data.

2. AO SYSTEM MODELLING FOR LQG CONTROLLER: THE MEASUREMENT NOISE COVARIANCE MATRIX

The computation of the Kalman gain through (5) and (6) calls for the definition of the measurement noise covariance matrix $\Sigma_w = \mathrm{E}\left(w_k w_k^T\right)$. As the measurement noise is supposed here to be spatially white, Σ_w is a diagonal matrix in the form $\Sigma_w = \mathrm{diag}[\sigma_w^2(i)]_{i=1,\ldots,n_{\text{s}}}$ where n_{s} is the number of slopes ($n_{\text{s}} = 624$ slopes).

In the case of GTCAO, the telescope pupil is not circular and moreover rotates with time, see figure 1.

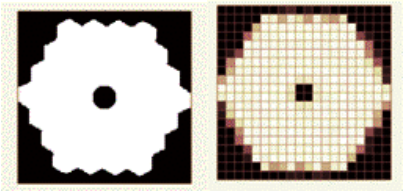

Figure 1. The non circular pupil of GTC (left) rotates with time, inducing a strongly variable flux on the WFS camera for the edges subapertures (right).

The purpose of this Section is to propose a method that computes Σ_w automatically while accounting for the flux per subaperture for a given batch of pseudo-open-loop slopes measurements. This method has been used successfully for LQG bench tests.

1. First, we need the median of the measurement noise variances of the well illuminated subapertures (that is to say subapertures with a flux level above the threshold stipulated to DARC). These are easy to pinpoint since they are delivering a non-zero measurement at every frame, so that the validity ratio is equal to 1 (never beneath the threshold). We need to have an idea of the minimal length the considered batch should have (n_{iter}) and of the bandwidth of high frequencies taken into account (n_{freq}) so as to obtain a good estimation of the noise variance from the Power Spectral Density (PSD).

   Figure 2 shows the ratios r of validation of the WFS illumination criterion according to the subaperture (left), and an example of the PSD of a y-slope for a batch size of 12000 open-loop samples recorded at 1000 Hertz (right).

   Figure 3 shows on the left the medians calculated when increasing the batch size used to compute the Power Spectral Density (PSD) and on the right when increasing the number of frequency PSD samples used for the variance calculation. In our case, either at $F_{\text{s}} = 100$ FPS or 1000 FPS, $n_{\text{iter}} = 2000$ frames and $n_{\text{freq}} = 200$ points are satisfying values as it can be seen in figure 3.

2. Secondly, we attribute a variance to the partially illuminated slopes from the estimations mentioned above. They correspond to the subapertures in which the availability ratio r (figure 2, left) is between 0 and 1 excluded. Knowing that the measurement noise variance is proportional to the light flux, we decided on the following rule:

$$\forall i \in [\![1, 624]\!], r(i) \in]0, 1[\implies \sigma_w^2(i) = \frac{1}{r(i)}\mathrm{median}\left(\{\sigma_w^2(j) | r(j) = 1\}\right). \tag{7}$$

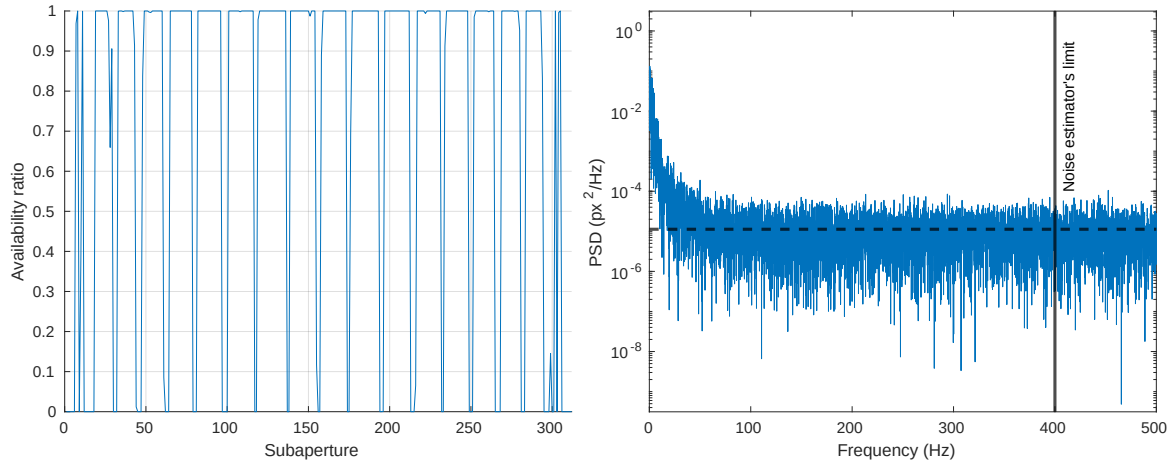

Figure 2. Left: typical ratios r of validation of the WFS illumination criteria according to the subaperture. Right: example of PSD of a y-slope (here, slope number 610/624 for a 1000-Hertz 12000-frame long OL sample), the black dashed line showing the estimated noise in $\mathrm{px}^2/\mathrm{Hz}$ as the median of the last 200 points (high frequencies 400 Hz to 500 Hz here, $n_{\mathrm{freq}} = 1200$ frequency samples): $\sigma_w^2(610) = 1.2 \times 10^{-5} \times F_{\mathrm{s}}/2 = 6.0 \times 10^{-3}$ px^2.

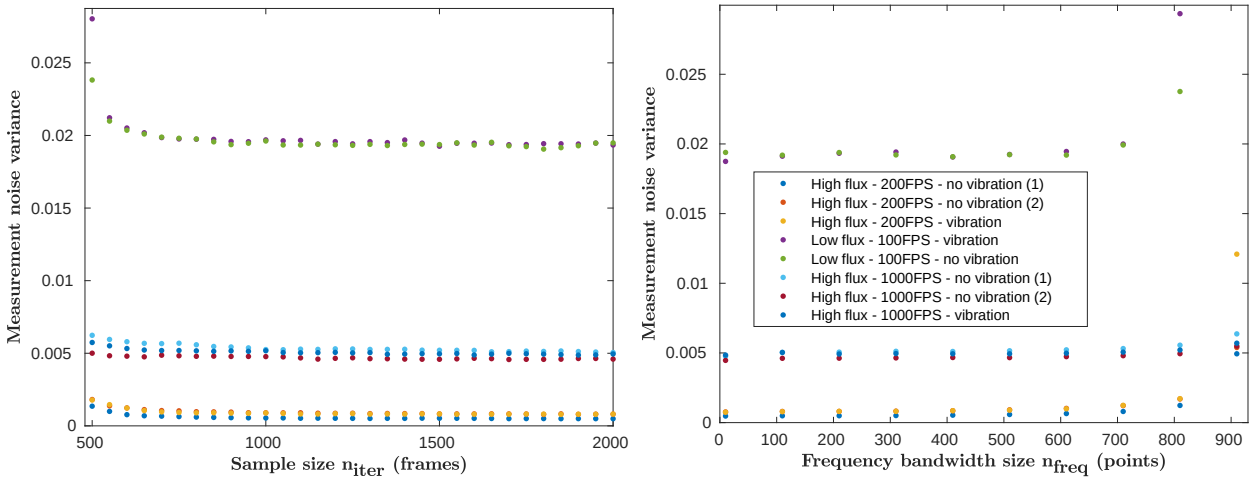

Figure 3. Slopes measurement noise variance estimations (median of the fully-illuminated slopes among the 624 obtained the same way as in figure 2). Left: for different sample sizes n_{iter}; case with $n_{\mathrm{freq}} = 200$. Right: for different numbers n_{freq} of high-frequency points; case with $n_{\mathrm{iter}} = 2000$.

3. Then, we attribute a high value $\sigma_{\mathrm{w,lim}} = c \times \mathrm{median}\left(\{\sigma_w^2(j)|r(j) > 0\}\right)$ to the never-illuminated subapertures. It needs to be extremely high since corresponding to missing measurements, but small enough to avoid numerical problems when solving the Riccati equation. Different coefficients c are leading to negligeable performance gaps when carrying out tests on the bench (those unilluminated subapertures are set to zero by DARC), allowing to take c roughly between 20 and 1000. It was decided to take $c = 100$.

Once the three steps are completed (requiring not even one second of computation on a standard laptop) we dispose of an appropriate matrix Σ_w (example in figure 4) that allows for starting the Kalman gain matrix computation.

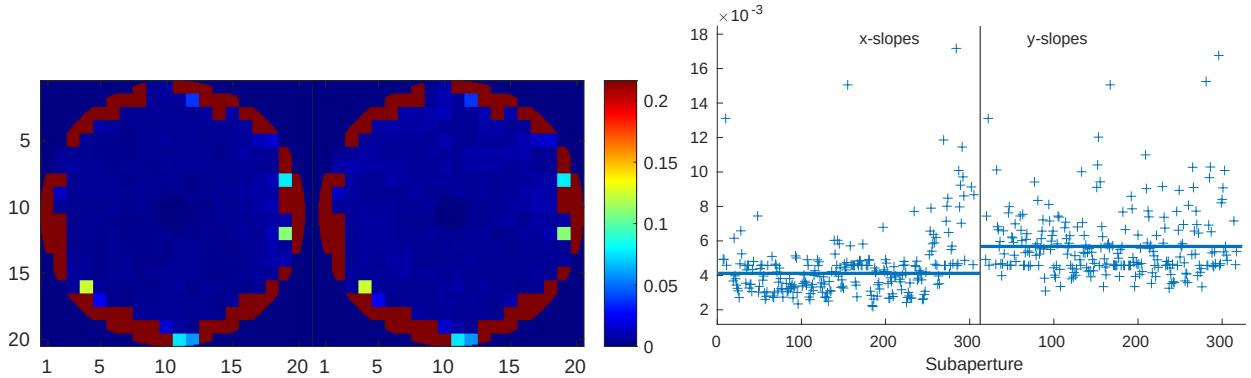

Figure 4. Slopes measurement noise variance estimations, in px^2, following the procedure described above (using a batch of slopes at high flux recorded at 1000 FPS). Left: in 2D pupil plan. Right: on a graph, unilluminated subapertures cut out, with median drawn as a horizontal blue bar. Both: x-slopes on the subleft and y-slopes on the subright

Notes For some reasons, the y-slopes clearly seem to be more subject to measurement noise than the x-slopes are (cf figure 4).

Also, it is clear that setting a high variance value for a given slope (like taking $c = 100$) roughly amounts to nullify the corresponding column in the Kalman gain L_∞ or equivalently to replace the corresponding measurement by its prediction.

3. ON-BENCH RESULTS

We present here some of the results obtained on the GTCAO bench when closing the loop with an integrator or with an LQG controller.

3.1 Bench parameters

The turbulence (rotating phase screen) corresponds to a single layer of Fried parameter $r_0 = 9\,\mathrm{cm}$ and wind speed $V_0 = 10\,\mathrm{m\,s^{-1}}$. We have also independently some windshake-induced vibrations: we introduce artificially with the DM a peak of energy in both tip and tilt PSD, at 12 Hz and of RMS 20 mas as described by the GTC mechanics team,[2] as illustrated in figure 5 with the OL tip-mode PSD.

3.2 Strehl ratios

We consider in this paper two NGS magnitude cases: first, magnitude 10.2 (with 900 FPS sampling rate) and second, magnitude 11.3 (400 FPS). All regulators have been tuned in order to get their best performance in each case (integrator tip-tilt and DM gains, and LQG fudge factor).

The LQF regulator reaches 37.5 % of Strehl Ratio (SR) for both magnitudes, while the integrator gives a value of 34.5 % SR for magnitude 10.2 and 32 % SR for magnitude 11.3. It is worth noting that despite the loop frequency decrease (from 900 FPS to 400 FPS), the LQG regulator maintains its performance at the same level thanks to its predictive capacity. Figure 6 presents the profiles associated with the four corresponding Point

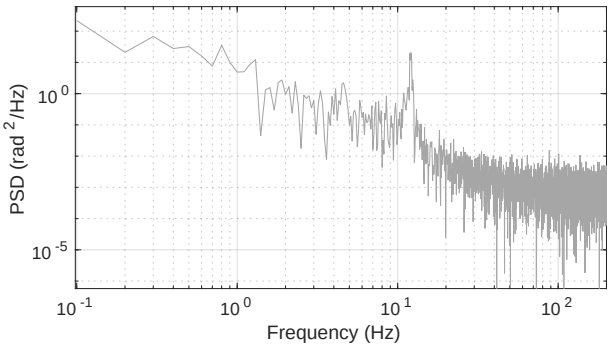

Figure 5. PSD of tip perturbations: turbulence and 12-Hz vibration (20 mas RMS).

Spread Functions (PSFs), showing the increase of the peak intensity provided by the LQG (9 % increase for magnitude 10.2 and 19 % for magnitude 11.3).

The use of the procedure presented above for the calculation of Σ_w has allowed an increase of 1.5 to 3.5 points of SR (depending on the turbulence strength, magnitude and presence of vibration where highest increases have been obtained) with respect to using a standard calculation where all measurement noise variances are deduced only from the slopes PSDs plateaus. The LQG thus allows better performances than the integrator while closing

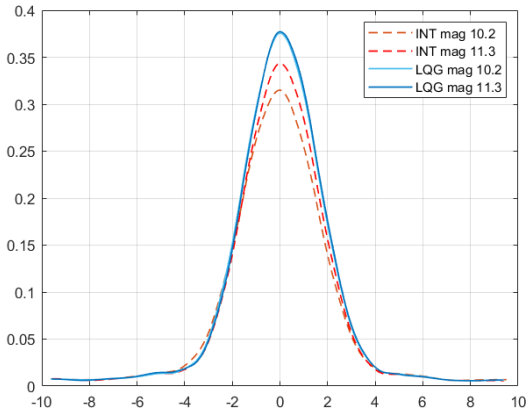

Figure 6. Profiles of the PSFs (in Airy disk peak unit) obtained with integrator and LQG regulator in two cases: magnitude 10.2 (900 FPS sampling rate) and magnitude 11.3 (400 FPS sampling rate). The x-axis is in pixels of the scientific camera.

the loop with lower sampling frequency. It allows thus to possibly decrease the WFS camera gain in order to increase the camera longevity.

3.3 Behavior

We describe hereafter some behavioral aspects for the case with magnitude 11.3 (400 FPS).

3.3.1 Rejection transfer functions

Figure 7 presents the Rejection Transfer Functions (RTFs) for the LQG regulator (top) and for the integrator (bottom). The theoretical RTFs are in good agreement with the ones calculated from the bench telemetry data. This shows that the models and calibrations are well describing the bench behaviour. It is worth noting that the tilt PSD presented in figure 5 exhibits a peak at 12 Hz that is nicely compensated by the LQG RTF shown in figure 7.

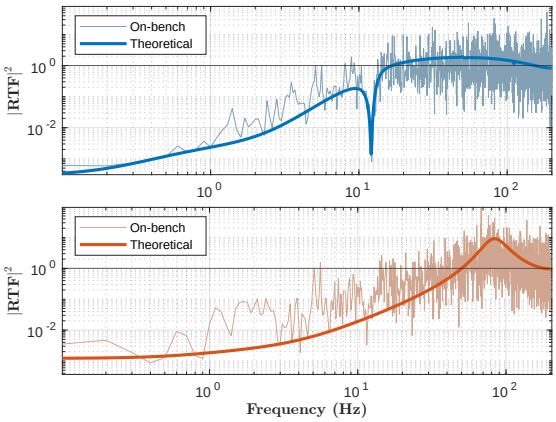

Figure 7. Rejection Transfer Functions for the LQG regulator (top) and the integrator (bottom) in the case of bad atmospheric conditions and windshake-induced vibration for magnitude 11.3. The loop rate is 400 FPS.

3.3.2 Stability and actuator solicitation

The LQG regulator has excellent stability margins, see also.[4] For the case of magnitude 11.3 (400 FPS), as shown in figure 8, the tip phase margin of the LQG is 53° and the gain margin is 13.6 dB. This is respectively around 22° and 9 dB above the integrator margins.

In addition to that, the actuators are less solicited when operating with a well-tuned LQG regulator, with on average −13 % rms of actuator stroke with respect to the integrator as shown in figure 9. Only the integrator has some commands above the DM clipping value of 3 µm.

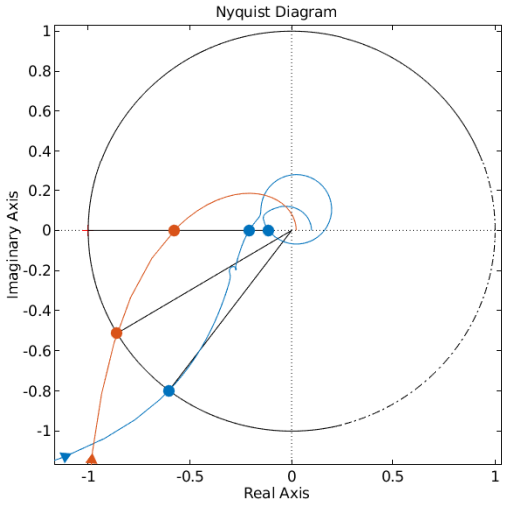

Figure 8. Tip correction Nyquist diagram for the LQG regulator (blue) and the integrator (red). The loop rate is 400 FPS.

4. CONCLUSION

In this paper, we have presented a procedure for the calculation of the measurement noise covariance matrix used in the LQG design. This procedure is fast (less than 1 s on a standard laptop), easy to update during operation

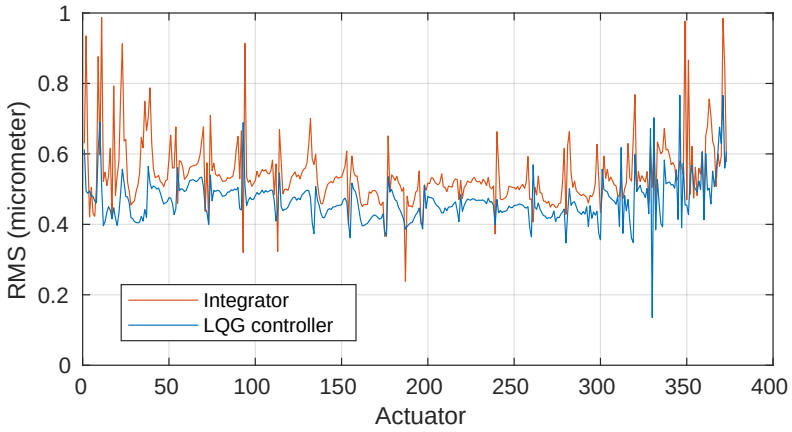

Figure 9. Example of actuators stroke temporal rms for the LQG regulator (blue) and the integrator (red).

and utilizes closed-loop measurements and a map of average flux per subaperture. It allows an increase of the Strehl ratio of 1.5 to 3.5 points depending on the observation conditions (turbulence strength, NGS magnitude, presence of vibration).

On-bench results have been presented in the case of windshake-induced vibrations and strong turbulence for two different NGS magnitudes (10.2 and 11.3). Rejection transfer functions are also displayed. The LQG regulator overpasses the integrator both in terms of SR and of stability margins.

More cases with magnitudes until 14 are left for future work, which possibly includes on-sky tests in 2023.

ACKNOWLEDGMENTS

This work is supported by the "Investissements d'Avenir" project funded by the IDEX Paris-Saclay ANR-11-IDEX-0003-02. This work has also received funding from the European Union Horizon 2020 research and innovation program, ORP Pilot, grant agreement No 101004719.

REFERENCES

[1] Bello, D., Boucher, L., Rosado, M., Castro López, J., and Feautrier, P., "Characterization of the main components of the gtcao system: 373 actuators dm and ocam2 camera," in [*Proceedings of the Third AO4ELT Conference*], 31 (2013).

[2] Cagigal, M. N., Ramosa, L. R., Araujoa, O. T., de la Rosaa, J. M., Basdenb, A., Montillaa, I., Minguell, J. R., López, R. L., Antolín, M. P., García-Talavera, M. R., et al., "Feedback control baseline for gtc adaptive optics with ngs," in [*AO4ELT5*], (2017).

[3] Sivo, G., Kulcsár, C., Conan, J.-M., Raynaud, H.-F., Éric Gendron, Basden, A., Vidal, F., Morris, T., Meimon, S., Petit, C., Gratadour, D., Martin, O., Hubert, Z., Sevin, A., Perret, D., Chemla, F., Rousset, G., Dipper, N., Talbot, G., Younger, E., Myers, R., Henry, D., Todd, S., Atkinson, D., Dickson, C., and Longmore, A., "First on-sky scao validation of full lqg control with vibration mitigation on the canary pathfinder," *Optics Express* **22**, 23565–23591 (September 2014).

[4] Sinquin, B., Prengere, L., Kulcsár, C., Raynaud, H.-F., Gendron, E., Osborn, J., Basden, A., Conan, J.-M., Bharmal, N., Bardou, L., et al., "On-sky results for adaptive optics control with data-driven models on low-order modes," *Monthly Notices of the Royal Astronomical Society* **498**(3), 3228–3240 (2020).

[5] Basden, A., Geng, D., Myers, R., and Younger, E., "Durham adaptive optics real-time controller," *Applied Optics* **49**, 6354–6363 (Nov. 2010).

5.6.2 Measurement noise variance values on GTCAO bench

In figure 5.35, we show the estimations obtained for various bench flux and phase screen cases. To convert to an on-sky angle, the RMS must be multiplied by the WFS pixel size $\mu_{\text{wfs}} = 0.35''$. To convert to the wavefront peak-to-peak difference of the edges of the subapertures, this angle RMS must be multiplied by $2\pi d_{\text{SA}}/\lambda_{\text{wfs}}$. The typical RMS value for GTCAO is of 10^{-1} px $= 35$ mas $= 1.2$ rad for $\lambda_{\text{wfs}} = 500$ nm.

The photon noise formula suggested a power law $flux^{-1}$ in section 3.2.1.1. Here, probably because of the undersampling (Roddier, 1999), it is rather $\sigma \propto flux^{-1.2}$, drawn in black on the figure 5.35. Whatever the flux, there is no change in the slope of the exponential model. It means that even with low flux, the read-out noise ($\sim flux^{-2}$) is still lower than the photon noise thanks to the EMCCD gain of about $G \sim 500$. We see a coefficient between the two phase screens of about $1.5 \leq 2$, meaning that as expected the photon noise depends on the seeing, but way less than the formula-based expectations of $\left(r_0^{\text{PS1}}/r_0^{\text{PS2}}\right)^2 \sim 5$ because of the undersampling.

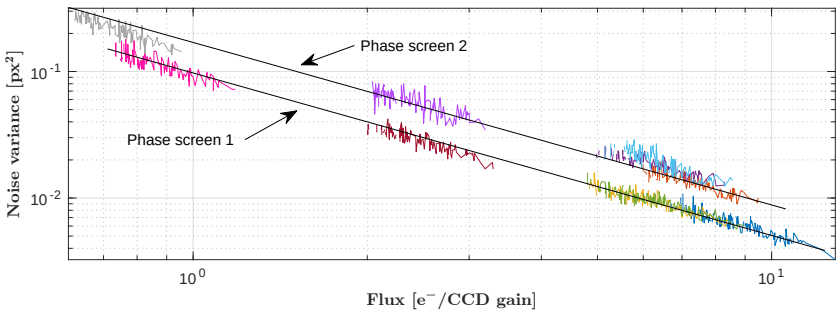

Figure 5.35: Plots of the measurement noise variances (diagonal of each Σ_w) with respect to the flux (median value of the sample, normalized by the respective WFS CCD gain $G \sim 500$ of each case). One color corresponds to one case of NGS magnitude with its fitted sampling frequency. One dot corresponds to one of the 624 values of the diagonal of Σ_w.

5.6.3 Extension: substitution for invalid measurements

As concluded in the second section of the proceeding (Marquis et al., 2022) presented in this chapter, the unilluminated subapertures measurement noise variances are set to a strong value. This corresponds to set to zero the corresponding columns of the Kalman gain. Another way to see this is within the Kalman filter equation: it is equivalent to the numerical substitution of those unilluminated subapertures corresponding slopes by their predicted measurement $\widehat{y}_{k|k-1} = C_y \widehat{X}_{k|k-1} - DNu_{k-2}$. This operation is not possible yet with DARC RTC, so it has been tested in simulation only. But it would be doable in real-time, as DARC sets to zero the low-flux subaperture measurements that are considered not valid. In simulation, we compare the

difference between LQG regulators where slopes are simply set to zero versus substituting the measurements with their Kalman prediction. Some advantages appeared when using the substitution:

- First advantage, a reinforced stability, noticed with the increase of the allowed range of fudge factor

- Second advantage, a slight increase of the performance, with a little less than one SR point without vibration and a little more than one in vibration cases. On the bench, a test was carried out to mimic this substitution method in the case where a whole part of the pupil was deprived of measurements (local burst of turbulence for instance). It was done with phase screen one ($r_0 = 23\,\mathrm{cm}$) and a wind speed of $V_0 = 10\,\mathrm{m\,s^{-1}}$ at 200 Hz with GTC windshake disturbance (section 5.2.2.1). The flux threshold of the WFS CCD was artificially set to a higher value than the usual one, so as to have more invalid subapertures even within the hexagonal pupil.

  The noise covariance matrix was then similar to that of the left image in figure 5.36. In this high-invalidity case, closing the loop with the adjusted Σ_w (adjusted in such a way that it would be equivalent to replacing the invalid measurements by the slopes predicted by the Kalman filter) was giving 1.5 SR point more than without adjusting Σ_w (keeping into account the DARC null measurements of the invalid subapertures).

  The residual tip and astigmatism are shown in figure 5.37 for the PSDs and in table 5.1 for the SR performance. In those conditions, the integrator was of course more severely concerned. The loss of valid subapertures inflicted a decrease of 12 SR points to the integrator (63% to 51%), while of 8 points for the LQG (68% to 60%) and 6.5 points with the substitution method. The loss of only 8 points without stability issue suggests that the LQG would be robust to this kind of sudden unmodeled events, such as a burst of turbulence.

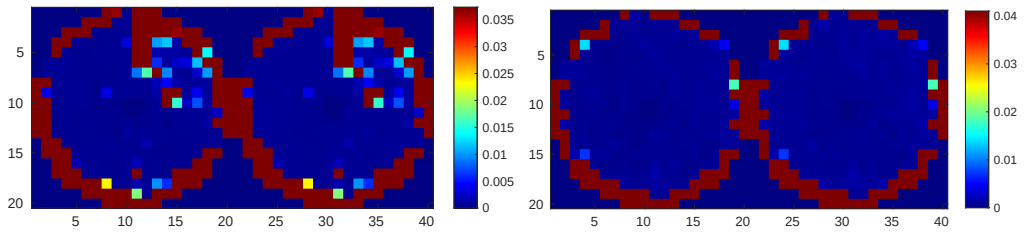

Figure 5.36: (bench) 2D representation of the diagonal of the measurement noise covariance matrix diag(Σ_w). Left: case of high flux threshold, there are some invalid subapertures inside the telescope pupil. Right: case of standard flux threshold.

- Third advantage, a back-up solution to the hexagonal M1 pupil rotation problem. In a simulated situation where the pupil rotation is faster than is the

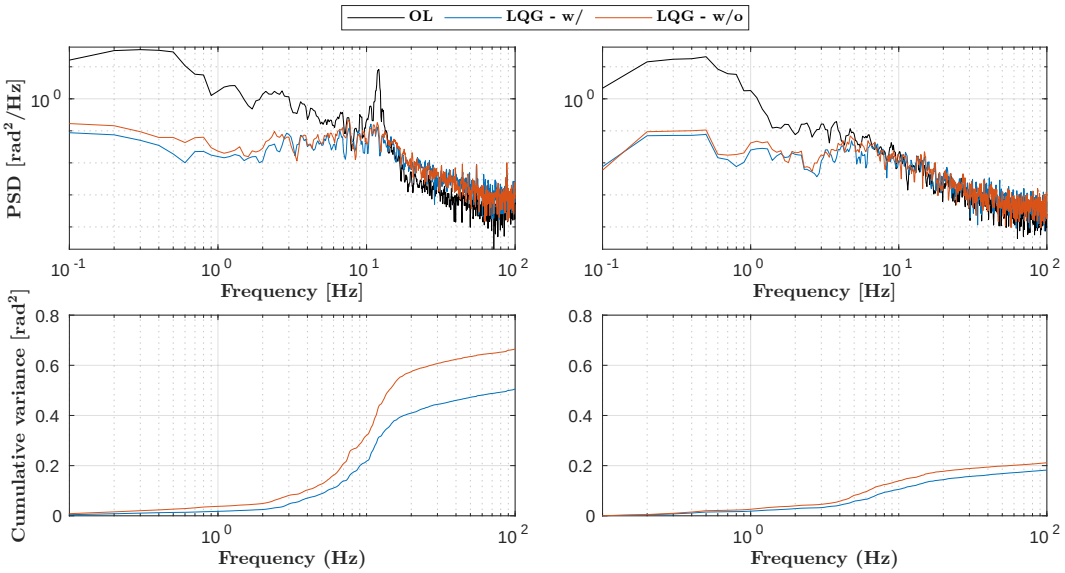

Figure 5.37: (bench) PSDs of reconstructed phases. Left: tip mode. Right: astigmatism mode. Residual phases of the LQG are shown with (blue) or without (red) substitution. The main improvement is due to the attenuation of the tip vibration at 12 Hz.

	Standard validity		**Reduced validity**	
Regulator	**no vibration**	**vibration**	**no vibration**	**vibration**
Integrator	69	63	59	51
LQG	71	68	64 + 0.5	60 + 1.5

Table 5.1: (bench) Strehl ratio (%) with and without the decrease of slopes validity rate. The substitution method related gain of points is indicated with $+pnt$.

LQG regulator matrices update (near the zenith, cf figure 5.3), the substitution allows to take a simple circular model for Σ_w with a loss of only 1 SR point. A circular model but with usual zeroing of invalid subapertures measurements leads to a loss of 5 SR points and with a more restricted range of good fudge factors.

5.7 Conclusion

We started this chapter clarifying the effect M2 would have during on-sky tests: correct low-frequency disturbance, but introduce a vibration peak at 12 Hz that the DM will have to counteract.

We have seen how to model each part of an AO system in order to apply high performance control. We have calibrated the interaction matrix. The pseudo-synthetic interaction matrix allows an accurate POL reconstruction and produces the right geometry for the influence matrix used for the projector P_u (phase-to-commands projector). It also allows to manage easily the dead actuator. We have proposed a simple and efficient delay measurement method based on least-squares estimation. We have also proposed the calibration of the measurement noise covariance matrix based on the flux per subaperture, combined with a specific processing of invalid subapertures in real time (replacement of invalid measurements by their Kalman prediction). This allows to account easily for a non-circular pupil and its rotation.

All this will be used in chapter 6 for the phase modeling and to obtain the results presented in chapter 7.

Chapter 6
Methodology for data-driven disturbance modeling

6.1 General presentation of the disturbance models

As already mentioned, the implementation of a high-performance controller as the LQG requires not only the modeling of the AO system (chapter 5) but also the spatio-temporal modeling of the disturbances. In this chapter, we will present telemetry-based methods to achieve this. The optimal modeling developed in chapter 4 could not be tested through end-to-end simulations due to a lack of time. It is besides not needed on bench where vibrations are piece-wise constant signals introduced with the DM.

We are following the modeling methods recently confirmed with on-sky tests (Sinquin et al., 2020), using thus the Zernike representation of the phase. Those methods consist in two complementary disturbance stochastic dynamical models:

- A first model describes for the global turbulence-induced wavefront disturbance as a list of second order auto-regressive models based on turbulence priors (Sivo et al., 2014), encapsulated inside matrices A_1 and A_2 such as:

$$\phi^{\text{tur}}_{k+1} = A^{\text{tur}}_1 \phi_k + A^{\text{tur}}_2 \phi^{\text{tur}}_{k-1} + \Gamma^{\text{tur}} v_k \,. \tag{6.1}$$

  The state space representation will then be:

$$\begin{cases} \begin{bmatrix} \phi^{\text{tur}}_{k+1} \\ \phi^{\text{tur}}_{k} \end{bmatrix} = \underbrace{\begin{bmatrix} A^{\text{tur}}_1 & A^{\text{tur}}_2 \\ I & 0 \end{bmatrix}}_{A^{\text{tur}}} \begin{bmatrix} \phi^{\text{tur}}_{k} \\ \phi^{\text{tur}}_{k-1} \end{bmatrix} + \begin{bmatrix} \Gamma^{\text{tur}} \\ 0 \end{bmatrix} v_k \\ \phi^{\text{tur}}_k = \underbrace{\begin{bmatrix} I & 0 \end{bmatrix}}_{C_{\phi^{\text{tur}}}} \begin{bmatrix} \phi^{\text{tur}}_{k} \\ \phi^{\text{tur}}_{k-1} \end{bmatrix} \end{cases} \tag{6.2}$$

  In our GTCAO case, the wavefront ϕ^{tur}_k is expressed in a Zernike basis. It could be defined in another basis. For instance, Léonard Prengère showed in simulations the efficiency of using the Yule-Walker equations to define AR2 models in a Karhunen–Loève basis (Prengere, 2021).

  The signal $\{v\}$ is a zero-mean Gaussian process noise with unitary covariance matrix, so that the corresponding process noise variance is $\Sigma^{\text{tur}}_v = \Gamma^{\text{tur}}(\Gamma^{\text{tur}})^{\text{T}}$. We list in section 6.2 the methods used to estimate all the required priors.

- A second model is used for the low order (LO) Zernike modes, the parameters of which being identified with the N4SID subspace identification method (Overschee and Moor, 1994) used on sky in (Sinquin et al., 2020). The method

has been coded by Baptiste Sinquin with insured stability of the identified model. Subspace identification methods belong to the set of machine learning methods. They are also based on a linear state-space model but without parametric structure (which is sometimes referred to as "model-free"). The state-space model is in the form:

$$\begin{cases} x_{k+1}^{\mathrm{LO}} = A^{\mathrm{LO}} x_k^{\mathrm{LO}} + \Gamma^{\mathrm{LO}} v_k \\ \phi_k^{\mathrm{LO}} = C^{\mathrm{LO}} x_k^{\mathrm{LO}} \end{cases}, \tag{6.3}$$

where x_k^{LO} is a state without any obvious physical interpretation and ϕ_k^{LO} is a vector containing the Zernike coefficients of low-order modes. This method is described in section 6.3. In section 6.3, we show the interest of defining the LO matrices with coupling between Zernike modes (rather than sparse definition with decoupled dynamics). In section 6.4, we highlight some precautions to take about the loss of validity of the low-order models when the parallactic angle varies.

These two dynamical models are concatenated by taking the sum $\phi = \phi^{\mathrm{tur}} + \phi^{\mathrm{LO}}$ for the low-order modes and $\phi = \phi^{\mathrm{tur}}$ for all the other ones. The open-loop measurement y^{OL} is modeled as the noisy measurement of the sum of the delayed phases of the two disturbance models:

$$\begin{cases} \begin{bmatrix} \phi_{k+1}^{\mathrm{tur}} \\ \phi_k^{\mathrm{tur}} \\ x_{k+1}^{\mathrm{LO}} \\ x_k^{\mathrm{LO}} \end{bmatrix} = \underbrace{\begin{bmatrix} A_1^{\mathrm{tur}} & A_2^{\mathrm{tur}} & 0 & 0 \\ I & 0 & 0 & 0 \\ 0 & 0 & A^{\mathrm{LO}} & 0 \\ 0 & 0 & 0 & I \end{bmatrix}}_{A} \begin{bmatrix} \phi_k^{\mathrm{tur}} \\ \phi_{k-1}^{\mathrm{tur}} \\ x_k^{\mathrm{LO}} \\ x_{k-1}^{\mathrm{LO}} \end{bmatrix} + \underbrace{\begin{bmatrix} \Gamma^{\mathrm{tur}} & 0 \\ 0 & 0 \\ 0 & \Gamma^{\mathrm{LO}} \\ 0 & 0 \end{bmatrix}}_{\Gamma} v_k \\ y_k^{\mathrm{OL}} = \underbrace{\begin{bmatrix} 0 & D & 0 & DC^{\mathrm{LO}} \end{bmatrix}}_{C_y} \begin{bmatrix} \phi_k^{\mathrm{tur}} \\ \phi_{k-1}^{\mathrm{tur}} \\ x_k^{\mathrm{LO}} \\ x_{k-1}^{\mathrm{LO}} \end{bmatrix} + w_k \\ \phi_k = \underbrace{\begin{bmatrix} I & 0 & C^{\mathrm{LO}} & 0 \end{bmatrix}}_{C_\phi} \begin{bmatrix} \phi_k^{\mathrm{tur}} \\ \phi_{k-1}^{\mathrm{tur}} \\ x_k^{\mathrm{LO}} \\ x_{k-1}^{\mathrm{LO}} \end{bmatrix} \end{cases} \tag{6.4}$$

The two covariance matrices of the process noise for the AR2 and the low-order models, namely Σ_v^{tur} and Σ_v^{LO}, are computed by solving separately two Lyapunov equations, once all the parameters have been defined and the low-order model identified. The global covariance matrix Σ_v for the model in (6.4) is then obtained as the block-diagonal formed with Σ_v^{tur} and Σ_v^{LO}. We can then follow the Kalman gain calculation and filter implementation as described in section 3.3.4.

6.2 AR2 modeling for control

As seen in section 2.4, the spatio-temporal statistics of phase disturbance induced by the atmospheric turbulence can be described in our case by three main parameters: the Fried parameter r_0, the large scale factor L_0 and the wind speed V_0. The values identified during the definition of our LQG controller will be denoted respectively by V_0^{LQG}, r_0^{LQG} and L_0^{LQG}. One more parameter to be tuned is the fudge factor α_{FF}. We present in this section some methods to do so, based on the reconstructed OL phase trajectories in Zernike base (using equations (3.31) and (3.32)).

6.2.1 Number of modes to describe the phase

As explained in chapter 2, the number of Zernike modes used to represent the phase depends on the spatial resolution we want to achieve. A simple order of magnitude for the necessary radial order is twice the linear number of actuators, $n_{\mathrm{rad}} \simeq 2 \times n_{\mathrm{act}}$. In some CANARY on-sky tests with full LQG (Sivo et al., 2014), a radial order of $n_{\mathrm{rad}} = 14$ was used. For CANARY, it corresponded to a little less than twice its linear number of actuators of 8. In (Sinquin et al., 2020) with the new DM of CANARY, $n_{\mathrm{rad}} = 2 \times n_{\mathrm{act}} = 30$ radial orders were used.

On GTCAO, the radial order n_{rad} was set to 37 (total of 740 Zernike modes). This was decided noticing that the computation time was significantly increasing above this value (figure 5.32), while performance was not significantly improved even in simulations (less than one SR point until $n_{\mathrm{rad}} = 2 \times n_{\mathrm{act}} = 42$), as shown in figure 6.1. We see on that figure that if the computation time of the models becomes an issue, it would be conceivable to drop to a radial order of 34 without too much performance sacrifice.

6.2.2 Coherence length, outer scale factor and fudge factor

As commonly done in the community (see e.g. (Andrade et al., 2018)), the estimation of atmosphere characteristic lengths is done from a data set of WFS slopes $Y = (y_k)_{1 \leq k \leq n_{\mathrm{iter}}}$ by optimizing (with Matlab *lsqnonlin* function) the cost function:

$$\hat{p} = \arg\min_{p} \sum_{z \in Z} \left\{ \log\left(\left\langle \phi_z^2 \right\rangle_{\mathrm{vK}(p)} \right) - \log\left(\left\langle \phi_z^2 \right\rangle_{\mathrm{MAP}(p)} \right) \right\}^2 , \tag{6.5}$$

where Z is a list of Zernike modes z which depends on the parameter p to be optimized (coherence length, outer scale, or fudge factor). The two main terms in equation (6.5) are:

1. $\left\langle \phi_z^2 \right\rangle_{\mathrm{vK}(p)}$, corresponding to the theoretical variance expectation of mode number z, based on Von Kármán statistics (depending on parameters $p = r_0$ or $p = L_0$, cf section section 2.4.2), plotted in blue in the next figures 6.3, 6.4, and 6.7.

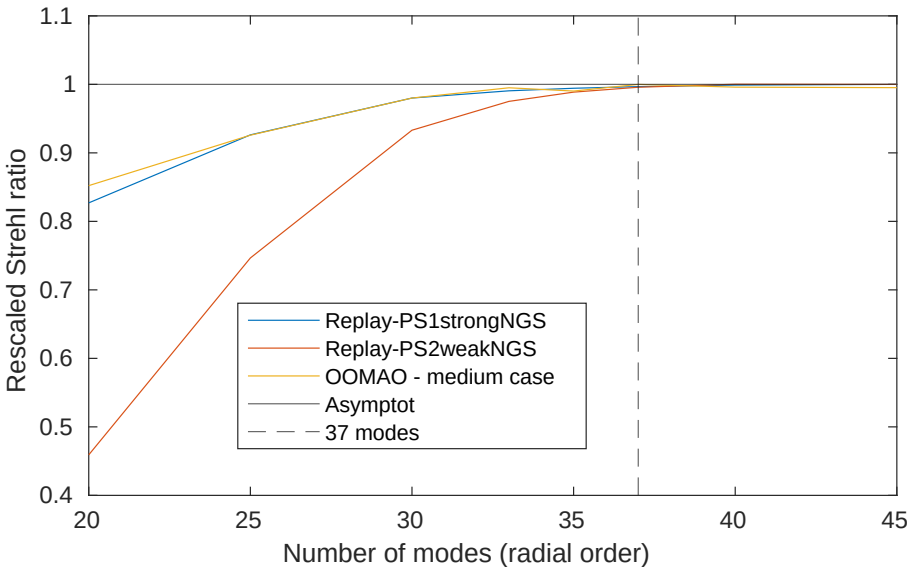

Figure 6.1: (GTCAO replay and OOMAO simulation) Optimization of the radial order to define the Zernike basis of the LQG controller on GTCAO. The value of $n_{\text{rad}} = 37$ was selected. On-bench tests with phase screen 2 and an LQG of radial order $n_{\text{rad}} = 30$ showed a decrease of the performance slightly bigger than one SR point compared with $n_{\text{rad}} = 37$.

2. $\left\langle \phi_z^2 \right\rangle_{\text{MAP}(p)} = \text{var}\left(R_{\text{MAP}\,z} Y\right)$, corresponding to the temporal variance of the reconstructed phase time-series (mode number z). It is plotted in red in the next figures 6.3, 6.4, and 6.7. As mentioned, the reconstructor R_{MAP} is defined from Von Kármán statistics (thus depending on parameters $p = r_0$ or $p = L_0$) and with a SNR-tuning regularization parameter $p = \alpha_{\text{MAP}}$.

With an iterative process, the three parameters r_0^{LQG}, L_0^{LQG} and α_{FF} are sequentially optimized.On OOMAO simulations, with three such iterations (one iteration for equation (6.5) corresponds to one loop on the three parameters r_0^{LQG}, L_0^{LQG} and α_{FF}), we were converging towards a consistent set of values. The same with two iterations on GTCAO bench data or with Keck on-sky data. Those three variables govern different parts of the Zernike modes distribution.

Due to the segmented shape of M1, the Zernike modes with high energy concentrated on the edge of the circular pupil are particularly inaccurately reconstructed. They are thus not used for the parameters optimization. They correspond to the first and the two last azimuthal modes of each radial order past the 20th mode, looking as the ones shown in figure 6.2. The MAP approach does not succeed to avoid this problem despite the high noise level attributed to the out-of-M1 subapertures.

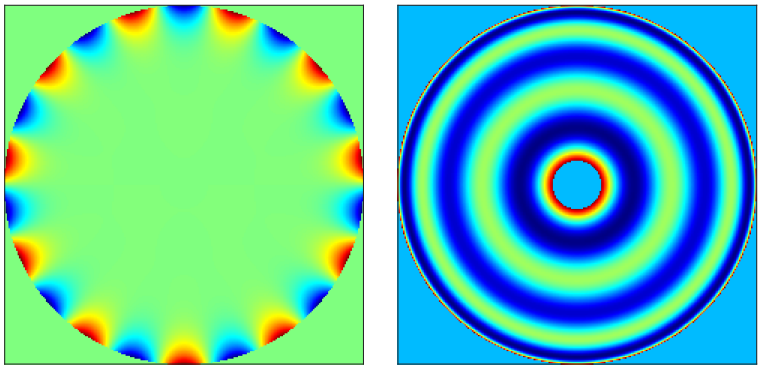

Figure 6.2: Example of Zernike modes (number 77 and 78) tricky to reconstruct from hexagonal-M1 slopes measurements.

Coherence length $r_0^{\mathbf{LQG}}$

The value r_0^{LQG} defines the global level of energy of all Zernike modes. We take the set of Zernike modes $Z = [\![35, 135]\!]$, since it corresponds to the spatial frequencies where neither L_0 nor α_{FF} intervene. An example is shown in figure 6.3.

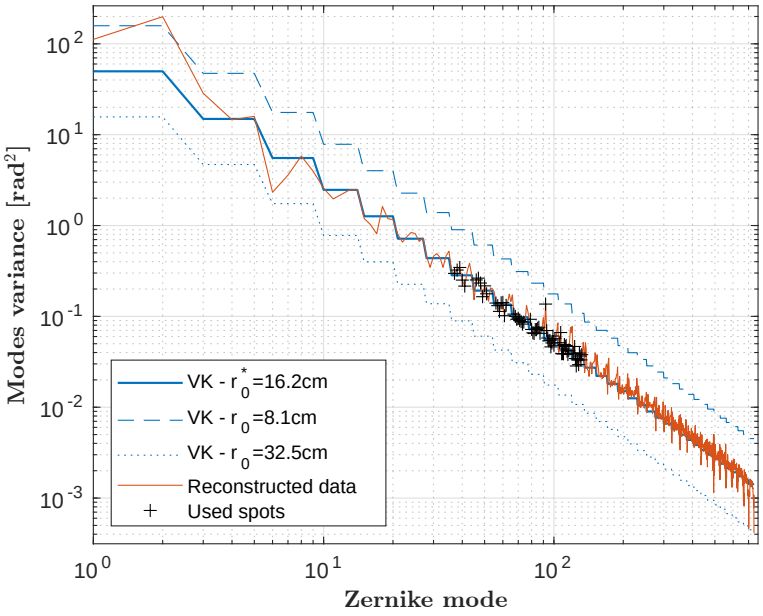

Figure 6.3: (Keck on-sky data) Example of r_0^{LQG} optimization from Zernike modes of orders 35 to 135 whose spots are in black.

Outer scale factor $L_0^{\mathbf{LQG}}$

The value L_0^{LQG} determines the relative energy levels of the low order Zernike modes. This prior is used only by the AR2 models to distribute the modal energy, since the

subspace identification of the low-order model simply uses the data variances to fit its energy. We take for the estimation of L_0^{LQG} $Z = [\![1, 34]\!]$, corresponding to the spatial frequencies where L_0 intervenes. An example is shown in figure 6.4. On

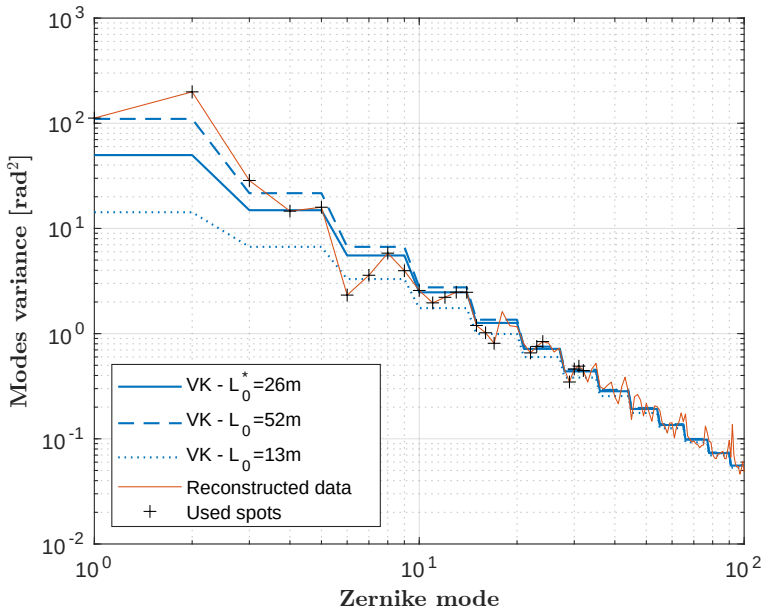

Figure 6.4: (Keck on-sky data) Example of L_0^{LQG} optimization from Zernike modes of orders 1 to 34 whose spots are in black.

some OOMAO simulations, the performance did not change when taking a value of 10 m or 100 m, as long as the ratio $L_0^{\mathrm{LQG}}/\alpha_{\mathrm{FF}}$ was kept the same. Surprisingly, on the bench, it did have an unexplained impact. Indeed, when setting the estimated value of $L_0^{\mathrm{LQG}} = 20\,\mathrm{m}$ in the LQG regulator definition, $L_0 \simeq 20\,\mathrm{m}$ being the value for phase screen 1, the performance was 1 SR point lower than with $L_0^{\mathrm{LQG}} = 12\,\mathrm{m}$ itself again 1 SR point lower than with 6 m. Yet, keeping the largest value of L_0^{LQG} and multiplying the fudge factor by 4 did not yield the same performance as with $L_0^{\mathrm{LQG}} = 6\,\mathrm{m}$ as it would be the case in the simulations. Moreover, the residual phase reconstructed from the residual slopes of the bench tests suggest that the best setting was the one with the estimated L_0^{LQG} on figure 6.5, with rejection transfer functions matching the theoretical ones in figure 6.6. The identified LO models (section 6.3) are not the reason of the smallness of that best-tuned value $L_0^{\mathrm{LQG}} = 6\,\mathrm{m}$. Indeed, one could think that because they are already quite accurate, the energy allocated to the AR2 models for low Zernike orders should be diminished. Yet, even when doing tests without LO identified models (full AR2 Zernike modeling for all Zernike modes), the same low-L_0 preference appeared.

In practice, a good compromise –from experimental intuition– would be to start from $L_0^{\mathrm{LQG}} = 12\,\mathrm{m}$. Taking low values such as less than 6 m repeatedly caused model stability issues. This remain to be further investigated.

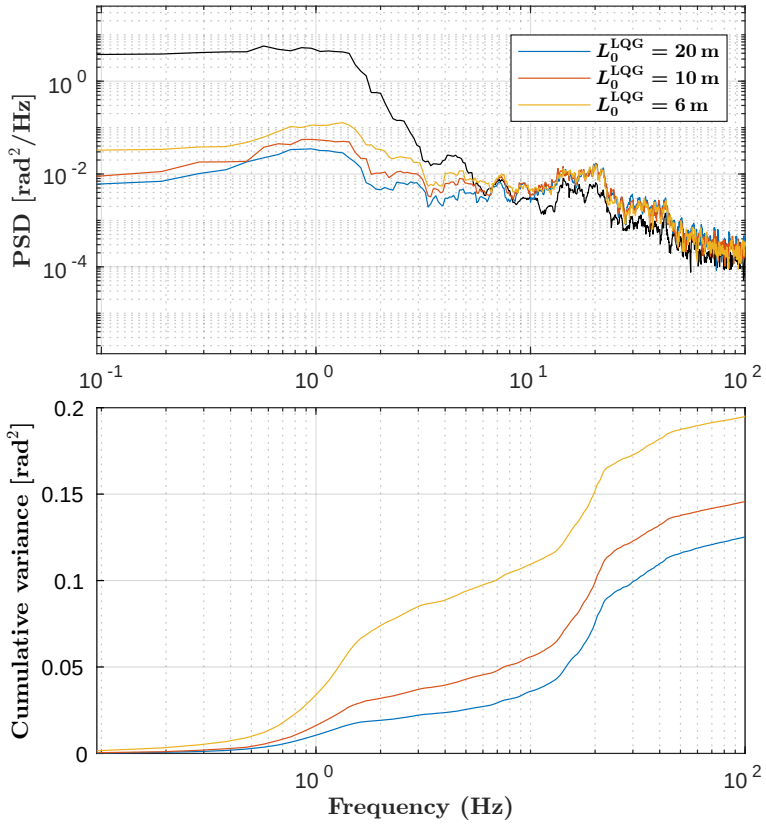

Figure 6.5: (bench) PSD of the residual astigmatism with closed-loop LQG regulator with three different L_0^{LQG}. The yellow curve ($L_0^{\mathrm{LQG}} = 6\,\mathrm{m}$) has the worst reconstructed residual phase, but the best Strehl ratio on the bench. Black: open-loop phase

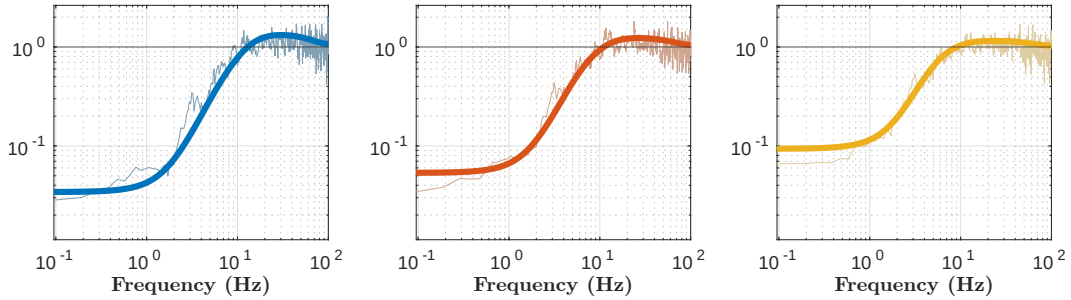

Figure 6.6: (bench) LQG rejection transfer function of the astigmatism mode for three different L_0^{LQG} (and thus three different datasets, the same ones as used in figure 6.5).

Fudge factor $\alpha_{\mathbf{FF}}$

As L_0^{LQG} sets the level of energy of low-order Zernike modes, α_{FF} determines the energy of the high order Zernike modes. We take for its estimation $Z = [\![200, 740]\!]$, corresponding to the Zernike modes where the changes of α_{MAP} in R_{MAP} impact the reconstructed modes variance. (The expression of R_{MAP} is given in (3.32) and recalled here: $R_{\mathrm{MAP}} = \Sigma_\phi D^{\mathrm{T}} \left(D\Sigma_\phi D^{\mathrm{T}} + \alpha_{\mathrm{MAP}}\Sigma_w\right)^{-1}$.) This sensitivity is shown in figure 6.7. To optimize α_{MAP}, we keep using equation (6.5). Let us point out that in that equation, we did not take off any term of noise: we do not write the reconstructed phase variance with a noise term as

$$\left\langle \phi_z^2 \right\rangle_{\mathrm{MAP}(p)} = \mathrm{var}(R_{\mathrm{MAP}\,z} Y) - R_{\mathrm{MAP}\,z}\Sigma_w {R_{\mathrm{MAP}\,z}}^{\mathrm{T}}, \tag{6.6}$$

but rather without subtracting the noise term $R_{\mathrm{MAP}\,z}\Sigma_w {R_{\mathrm{MAP}}}_z^{\mathrm{T}}$. Thus, we mimic the principle of the LQG regulator, in which the measurement noise must be filtered. Indeed, when closing the loop, the Kalman gain has to manage the noise contained in the slopes measurements y. For this reason, we tune α_{MAP} to manage the measurement noise, as it has a big impact on the variance of the high order reconstructed modes (figure 6.7).

For some yet unexplained reason, a good fudge factor for the LQG implementation, in OOMAO simulation as on the bench, happened to be $\alpha_{\mathrm{FF}} = \alpha_{\mathrm{MAP}} \times 10$. If it is reaching big values, say, $\alpha_{\mathrm{FF}} = 100 >> 1$, it means that the observing situation is with a very high NGS flux (seen on bench and in simulations) and thus a very low-value covariance noise matrix Σ_w has been calculated. This rule of $\alpha_{\mathrm{FF}} = \alpha_{\mathrm{MAP}} \times 10$ always led to stable controllers with better performance than the integrator. However, it sometimes did not give the best performance on the bench, as in some cases $\alpha_{\mathrm{FF}} = \alpha_{\mathrm{MAP}} \times 3$ was optimal. A last thing to precise is that on GTCAO, the value given to α_{FF} is quite flexible: if α_{FF}^* is the value giving the best performance, less than one SR point would be lost by defining the LQG matrices with a fudge factor value in the range $[\alpha_{\mathrm{FF}}^*/2, \alpha_{\mathrm{FF}}^* \times 2]$.

6.2.3 Modal speed $V_0^{\mathbf{LQG}}$

The determination of the modal "wind" speed is based on the cut-off frequency of the Zernike coefficients PSD, see (Sivo et al., 2014). It relies on the typical one-layer Von Kármán shape to which the PSD of radial orders i_{rad} should resemble (section 2.4.2.2):

- a low frequency plateau extending from null-frequency until F_{cut}, given by

$$F_{\mathrm{cut}} = 0.3(i_{\mathrm{rad}} + 1)\frac{V_0}{D_{\mathrm{pup}}} \tag{6.7}$$

- a $f^{-\frac{17}{3}}$ (or $f^{-\frac{11}{3}}$ if the Shack-Hartmann aliasing occurs, see e.g. (E. Gendron and G. Rousset, 2012)) asymptote from F_{cut} to F_{noise} (frequency where noise plateau starts)

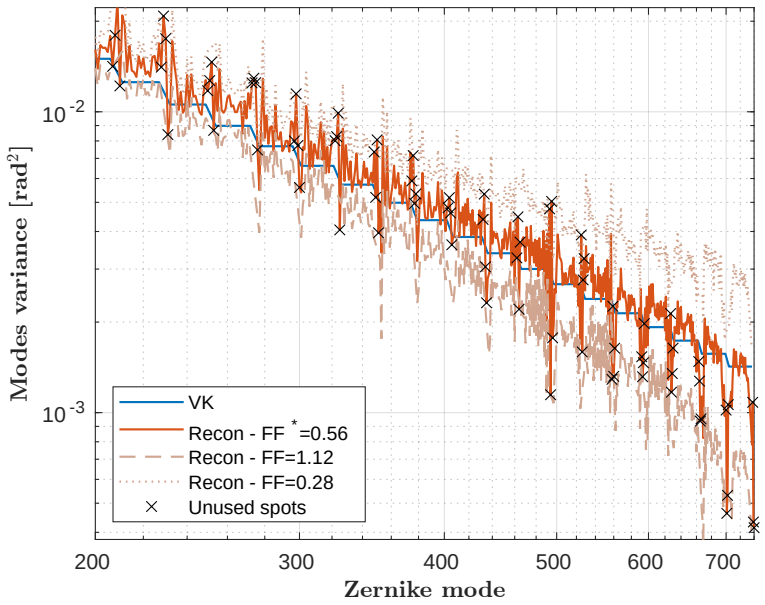

Figure 6.7: (Keck on-sky data) Example of α_{MAP} optimization. Black cruxes correspond to the unused values (Zernike modes with poor reconstruction within a segmented pupil).

- A high frequency plateau purely composed by the measurement noise

This model is not appropriate for low order modes. These have more complex PSDs because of additional perturbations such as vibrations or windshake. We will use the terminology of modal speed rather than wind speed, since V_0^{LQG} determines the model wind speed for each mode.

Instead of one unique wind speed identical for all modes as in (Sivo et al., 2014), we will determine one modal speed for each Zernike radial orders. We will then apply the same formula to define the AR2 model. For each of the $(i_{\mathrm{rad}}+1)$ Zernike modes of radial order i_{rad}, the coefficients a_1 and a_2 of matrix A^{tur} will be:

$$\begin{aligned} a_1 &= 2\exp(-\xi\omega_0^{i_{\mathrm{rad}}}T_{\mathrm{s}})\cos(\omega_r^{i_{\mathrm{rad}}}T_{\mathrm{s}}) \\ a_2 &= -\exp(-2\xi\omega_0^{i_{\mathrm{rad}}}T_{\mathrm{s}}) \end{aligned} \tag{6.8}$$

with $\xi = 0.9$ and

$$w_r^{i_{\mathrm{rad}}} = 2\pi 0.3(i_{\mathrm{rad}}+1)V_0^{\mathrm{LQG}\,i_{\mathrm{rad}}}/D_{\mathrm{pup}}\sqrt{1-\xi^2} = \omega_0^{i_{\mathrm{rad}}}\sqrt{1-\xi^2}, \tag{6.9}$$

where the modal speeds can reach values higher than $V_0^{\mathrm{LQG}} \sim 100\,\mathrm{m\,s^{-1}}$. Figure 6.8 shows that the LO modes are better corrected with LQG controllers built from higher modal speeds. Switching from $V_0^{\mathrm{LQG}} = 15\,\mathrm{m\,s^{-1}}$ (real bench wind speed) to $V_0^{\mathrm{LQG}} = 40\,\mathrm{m\,s^{-1}}$ appeared to improve the SR by about two points. It is thus interesting to conclude that it is preferable to increase the cut-off frequency to filter out the additional energy induced by the aliasing of the Shack-Hartmann subapertures.

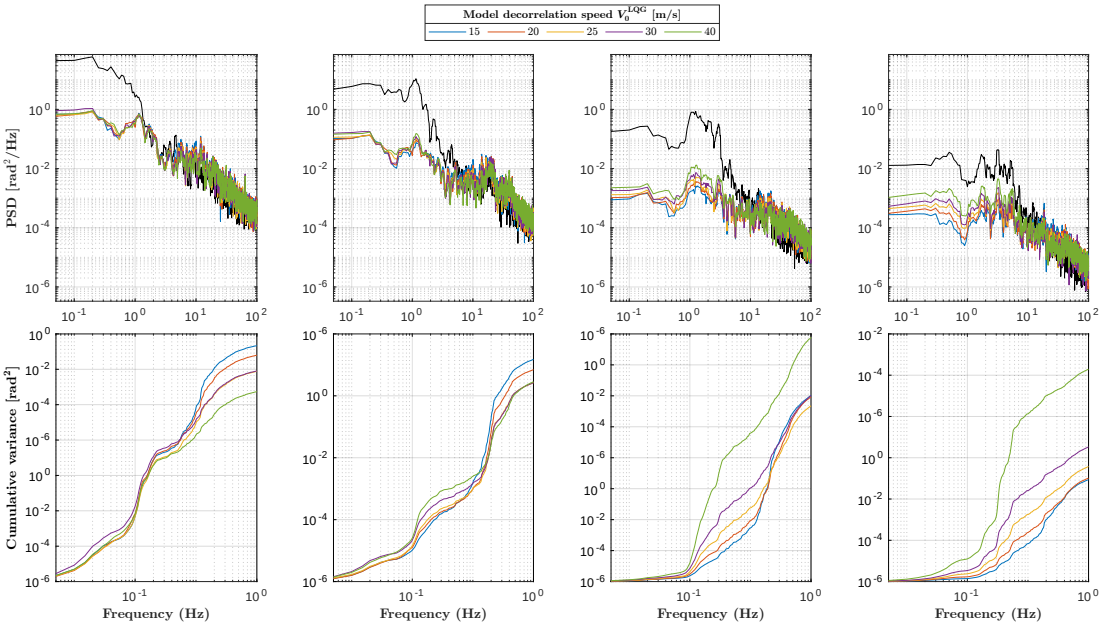

Figure 6.8: (bench) Examples of PSDs calculated from some GTCAO closed-loop residual reconstructed phase modes. LQG regulators defined with different modal speeds V_0^{LQG}. Left to right: Zernike modes 1, 5, 25 and 100. Black: open-loop. The actual wind speed was of $V_0 = 10\,\mathrm{m\,s^{-1}}$.

We present here a way to extract appropriate modal speeds V_0^{LQG} from the open-loop data, in a simple and fast way. Given a batch of (pseudo-)open-loop data Y^{OL}, the procedure is for each radial order:

1. Reconstruct Zernike open-loop phase $\phi^{\mathrm{OL}} = R_{\mathrm{MAP}} Y^{\mathrm{OL}}$ ($n_{\mathrm{rad}} + 1$ modes of radial order n_{rad})

2. Compute their respective PSDs and average them to a single one PSD_{avrg}, assuming all should be more or less identical for a given radial order (example in figure 6.9)

3. Compute the low-frequency plateau value (*plateau*) of the theoretical PSD as the average of the first 4 points and the high-frequency noise value as the average of the last 20 points.

4. For F_{cut} from $\frac{F_{\mathrm{s}}/2}{n_{\mathrm{iter}}}$ to $F_{\mathrm{s}}/2$, compute model PSDs $PSD_{\mathrm{model}}(F_{\mathrm{cut}})$ as a long plateau until F_{cut} followed by a f^{-4}-slope line down to the previously calculated noise level (examples in figure 6.10). This is a simple way to represent the AR2 model. As said before with the example of figure 6.8, a condition to optimize the performance is to encompass the whole frequency domain. This is ensured by constraining the f^{-4}-slope line to reach the noise plateau of the data PSD (for instance, in figure 6.10 the dashed line is not satisfying).

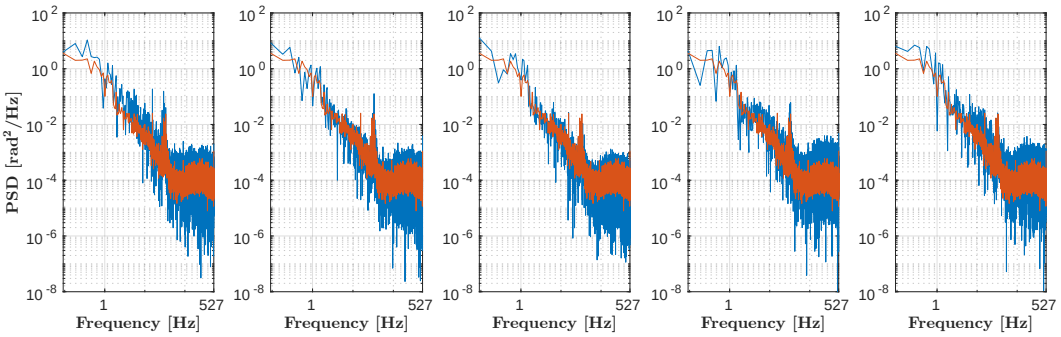

Figure 6.9: Examples of PSDs calculated from Keck pseudo-open loop slopes. Zernike modes of radial order $n_{\mathrm{rad}} = 4$ (left to right, modes 10 to 14). Red: n_{rad}-th radial order average PSD_{avrg}.

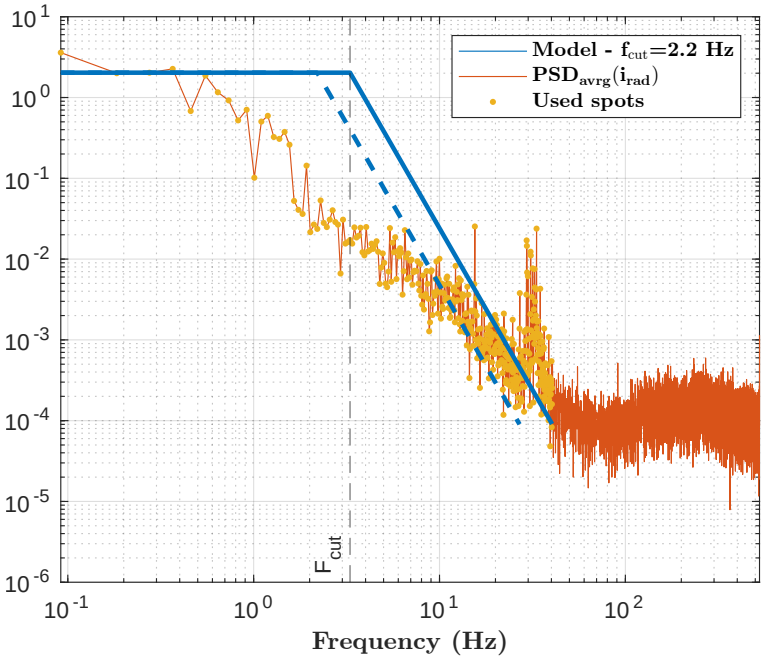

Figure 6.10: Blue: examples of PSD_{model} obtained for two different cut-off frequencies. The dashed one reaches the noise plateau values below noise plateau frequencies: it was thus discarded despite a better fitting (figure 6.11). Red: n_{rad}-th radial order average $PSD_{\mathrm{avrg}}(n_{\mathrm{rad}} = 4)$.

5. Calculate the average of the logarithm of the error gap ϵ between modeled and data-based PSDs (example in figure 6.11):

$$\epsilon(F_{\text{cut}}) = \overline{|\log(PSD_{\text{avrg}}) - \log(PSD_{\text{model}}(F_{\text{cut}}))|^2}\,. \tag{6.10}$$

   Its argmin is the F_{cut} we are looking for, which gives $V_0^{\text{LQG}}(i_{\text{rad}})$ thanks to equation (6.7).

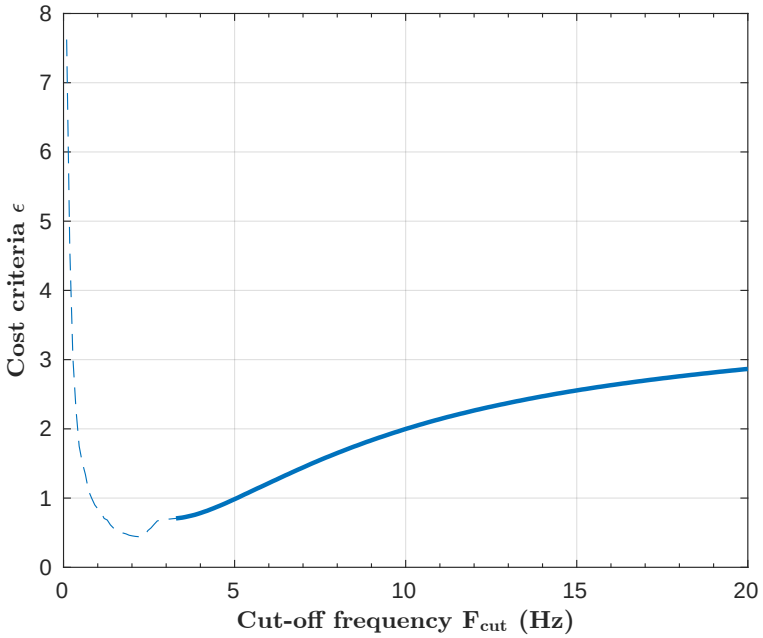

Figure 6.11: Example of error function $\epsilon(F_{\text{cut}})$. The dashed line represents the values where F_{cut} is too small for the PSD model to reach the noise plateau of the data PSD. The best frequency is thus here 3 Hz.

6. Once all the n_{rad} modal speeds are computed, set all modal speed values for radial orders greater than 12 to the median value thereof. This is done knowing that the speed estimations are getting trickier for very high Zernike orders (noisier data), as in figure 6.12. It avoids instability problems exposed below.

7. A last thing to check is whether the respective modal estimations are decreasing with the radial order. It appeared that sometimes, when some estimations $V_0^{\text{LQG}}(j_{\text{rad}})$ are lower than for some higher order ones, the Riccati equation solving becomes difficult to solve: either the doubling algorithm does not converge, or it does converge but yields an unstable Kalman filter ($\max|(\text{eig}(A - L_\infty C))| > 1$, equation (3.25)). A satisfying solution is to insure that all the higher order modal speeds are decreasing by setting a constant value

$$\forall k_{\text{rad}} \geq j_{\text{rad}}, V_0^{\text{LQG}}(k_{\text{rad}}) = \text{med}(V_0^{\text{LQG}}(i_{\text{rad}} > 12))\,.$$

The last resort in case of stability problems is to set one same unique average speed for all the Zernike radial orders.

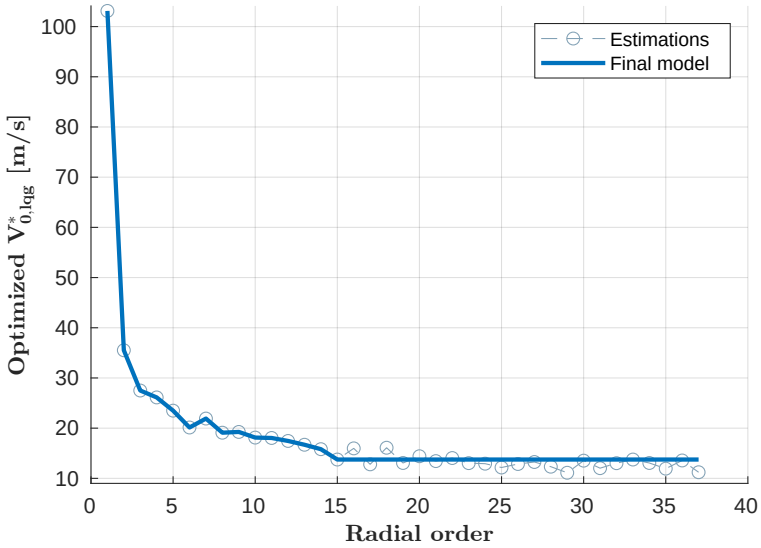

Figure 6.12: (Keck on-sky data) Example of modal speeds estimations.

Simulation tests

We performed simulations on OOMAO to check the efficiency of this method. We first estimated the modal speeds V_{esti} on a batch of open-loop data, and then performed several closed-loop simulations with LQG controllers for which the AR2 model was parameterized with various modal speeds V_0^{LQG} around the estimated value V_{esti}: $V_0^{\mathrm{LQG}} = \{0.5V_{\mathrm{esti}}, 0.75V_{\mathrm{esti}}, V_{\mathrm{esti}}, 1.25V_{\mathrm{esti}}, 1.5V_{\mathrm{esti}}\}$. We expected the performance to be the best or at least at a good level for $V_0^{\mathrm{LQG}} = V_{\mathrm{esti}}$, which would be the value used in an unsupervised identification. This was done for two extreme cases: $[M_{\mathrm{ngs}}, F_{\mathrm{s}}] = [10, 1000\,\mathrm{Hz}]$ and $[13, 100\,\mathrm{Hz}]$. Results are displayed in figure 6.13. Note that the case with challenging atmosphere and high sampling frequency is the only one for which the estimated wind speed is not the best tuning to define the LQG controller. However, the loss of performance is less than one SR point.

Concerning the repeatability, the modal speed estimations $V_{\mathrm{esti,i}}$ of a same parameterized atmosphere but using different batches vary of $\frac{\sigma_{V_{\mathrm{esti}}}}{V_{\mathrm{esti}}} < 5\%$ in the four cases.

6.3 Low-order models identification

6.3.1 Zernike modes and state-space size

A subspace identification is done for the first 9 Zernike modes (radial order 3). Each mode corresponds to 18 states. This means that x_k^{LO} has $9 \times 18 = 162$ components.

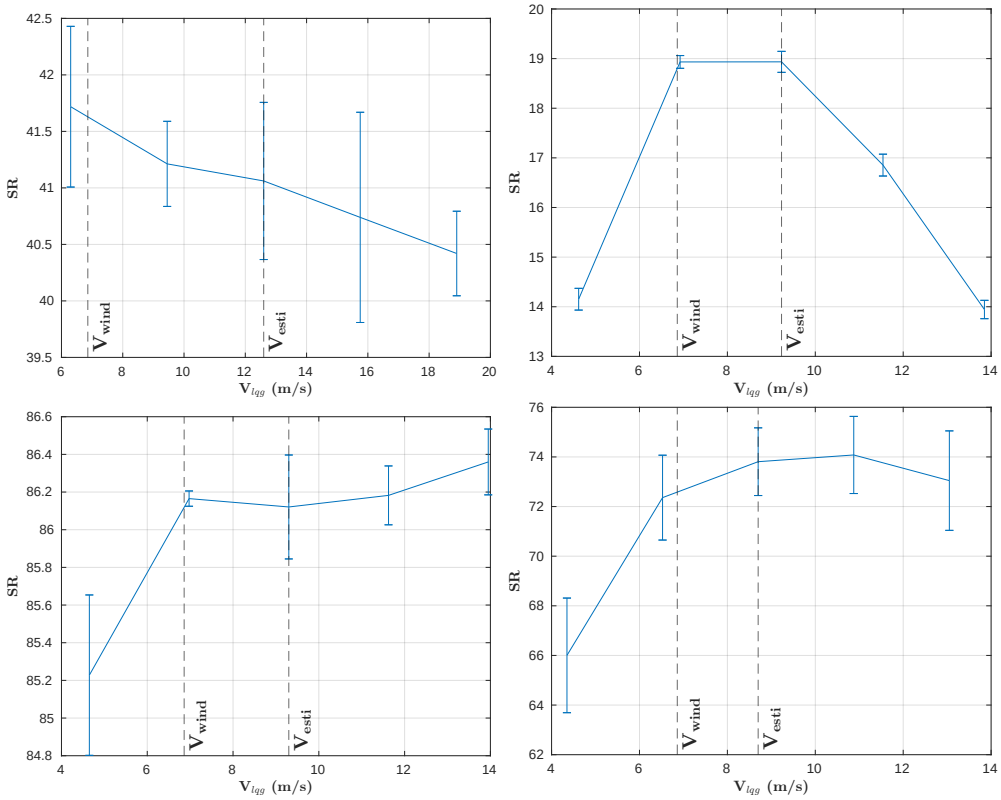

Figure 6.13: Example of estimated modal speeds tests. Left: $[M_{\text{ngs}}, F_{\text{s}}] = [10, 1000\,\text{Hz}]$. Right: $[M_{\text{ngs}}, F_{\text{s}}] = [13, 100\,\text{Hz}]$. Top: $r_0 = 8\,\text{cm}$. Bottom: $r_0 = 20\,\text{cm}$.

These two values (9 modes, 162 state components) were decided with replays using Keck on-sky data, noting that for higher values (more Zernike modes, or bigger state vector) the performance almost did not change. The same limit value was found at the WHT in (Sinquin et al., 2020), above which the performance did not improve. We could have expected that for Keck telescope, with its structure bigger than the one of WHT, more Zernike modes would have been necessary. Yet, keeping the number to 9 is still enough. It might be explained by the increase in the AR2 cut-off frequencies, while in (Sinquin et al., 2020) the modal speed V_0^{LQG} was constant for all modes and had not been optimized.

6.3.2 Identification method

The same LO modeling algorithm as in (Sinquin et al., 2020) is used, based on N4SID (Overschee and Moor, 1994), but modified to insure the stability of the identified model by an adequate regularization of the last resolution of a linear matrix equation. An additional optimization step in the identification could be implemented with the prediction error minimization (PEM). However, it led several times to unstable models (maximal modulus of eigenvalues of identified matrix A^{LO} higher than one) and was thus discarded.

During our work, a particular interest towards coupled dynamics was given. Without coupling, independent N4SID models are defined for each Zernike mode z, leading in the end to a block-diagonal matrix A^{LO} assembling the separately identified A_z^{LO} models. Coupled identification gathers all the data for the 9 Zernike modes and produce one non-diagonal model. The advantages that have arisen are:

- Gain in performance: on the GTCAO bench (with Keck-like disturbances) and on replay with on-sky Keck data, the use of coupling in the definition of A^{LO} was improving the SR by some 2 points.
- Reduced size of the state vector: the mechanical coupling existing between the different parts of the structure (e.g. an oscillating arm inducing both defocus and tip/tilt disturbances), and the coupling between the disturbance sources (e.g., is one fan rotating now?) leads to the possibility to gather the disturbances into particular modes involving several Zernike modes. The coupling allows it, so as to diminish the choice of the size of the state vector to embed all disturbances.
- No need to wonder about the respective order to grant to each Zernike mode model: a total size of $9\times18 = 162$ is given, and the algorithm will automatically optimize the importance given to each.

The disadvantage we can state is the computation complexity to build the matrices. For instance, in our simulations Matlab needs several minutes to build the matrices in the coupling case, compared with a total of $\sim 10\,\mathrm{s}$ with successive independent identifications. This problem with coupling was solved by using the script

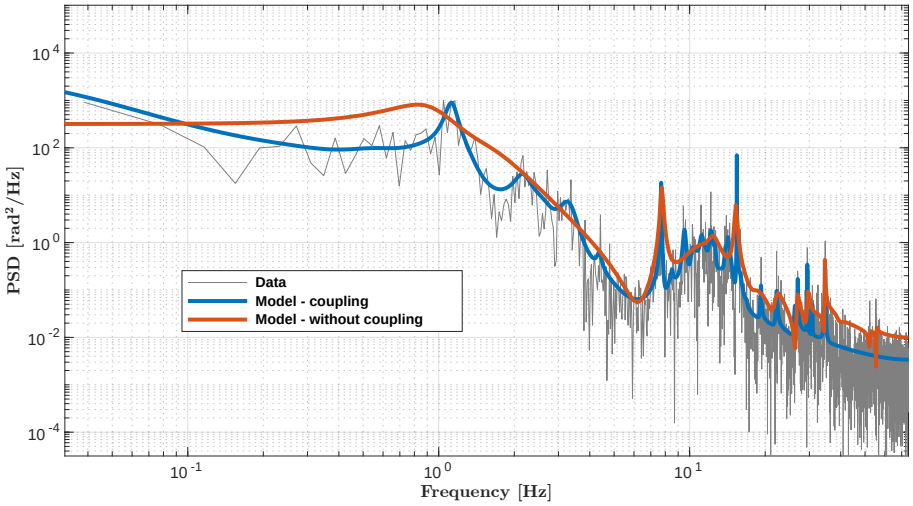

Figure 6.14: (Keck on-sky data) Example of identified PSD to see the coupling advantage in disturbance modeling. Tip mode. The coupling allows more accurate modeling, leading to more than 2 SR points improvement. The coupled model is yet of order 18 only, while of order 30 for the coupling-free one.

coded by Sinquin (whose principle is explained in the annex of (Sinquin et al., 2020)), with a computation time of some 20 s. Those times are given for a model of total order ~ 100 from telemetry data of length 10000 samples. Another disadvantage is the supplementary steps towards the absence of physical meaning of the subspace identification. If for some reasons one Zernike mode appeared to be badly corrected when closing the loop, it would be difficult to point out what part of A^{LO} is responsible.

6.4 Switch and stitch successive models

6.4.1 Needs of update

Atmosphere evolution

The models, whether based on priors or identifications, depend on the observation conditions. The classical conditions are those of the atmosphere, such as the wind speed. The very good robustness of LQG control to those changes were highlighted in (Prengère et al., 2020). It has not been deeply examined on the GTCAO bench during my PhD, always keeping the phase screen wind speed to $V_0 = 10\,\mathrm{m\,s^{-1}}$. Anyway, the performance variation for some LQG defined with modal speeds V_0^{LQG} from one to even four times the actual value V_0 did not lead to stability problem, with a loss of SR inferior to 3 points, matching with (Prengère et al., 2020). A study about the impact of bursts of turbulence has also been conducted by Nicolas Galland (pending COAT proceeding), showing that it is still better to have an LQG regulator with a non-optimized $r_0^{\mathrm{LQG}} >> r_0$ decorrelation length than an integrator.

A more serious issue for the LQG is the evolution of vibration spectra. It can be induced for instance by the activation/deactivation of some mobile machine components of the telescope, such as cooling systems. It can also be the result of changes in the position of the M2 carrying spider, leading to changes in the mechanical vibration modes of the structure and thus in the resulting optical disturbances PSDs, even with a constant wind.
On bench tests and in simulation, the non-modeling of existing vibrations almost systematically made the LQG underperform the integrator. Conversely, modeling a nonexistent vibration had almost no impact on the performance (less than one SR point). A bench example is shown with the PSDs of residual reconstructed phases for those two situations in figure 6.15 (low flux, $F_s = 100\,\text{Hz}$, phase screen 1 with $r_0 = 23\,\text{cm}$). Without modeling the vibrations, the SRs collapse from 65% to 24% when the vibrations occur. However, with the vibration model, the SR still reaches 64.5% in absence of vibrations and remains at 54% with vibration. Thus, if the same

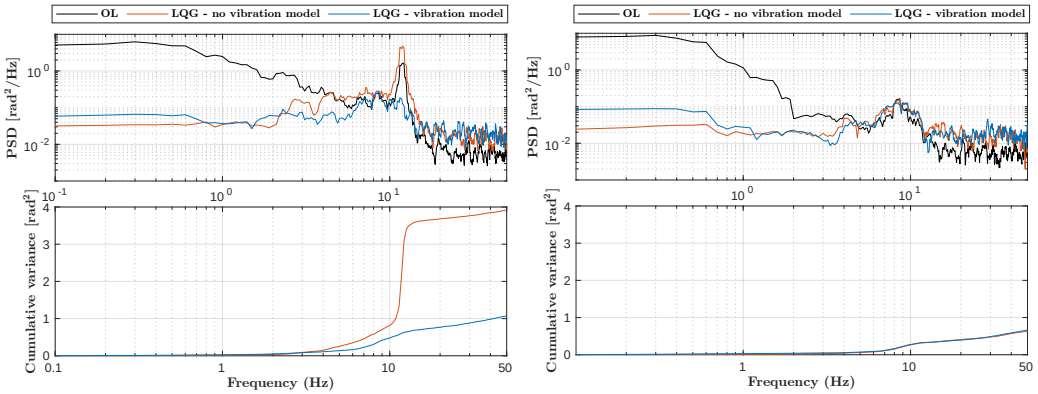

Figure 6.15: (bench tests) PSD of the residual tip. Left: with vibrations. Right: without vibrations. Red: regulator defined from vibration-free data. Blue: regulator defined from vibration-including data.

vibration peak happens to be regularly present on some Zernike modes of a telescope, the safer course would be to include its analytical AR2 model at the specific vibration frequency.

Parallactic angle evolution

Another interesting problem we investigated is the variation of the parallactic angle described in figure 5.3. This pertains to the identified low-order models. It was confirmed on the bench, with DM-injected Keck-like disturbances of LO Zernike modes 1 to 9. The LQG regulator matrices are defined with the on-sky data, but on the bench the DM-injected disturbances have been applied a spatial rotation of 90 degrees or 180 degrees. We see on results figure 6.16 that it led to a loss of 11 SR points (from 49% to 38%) in the worst case of 90 degrees rotation, and 9 points (from

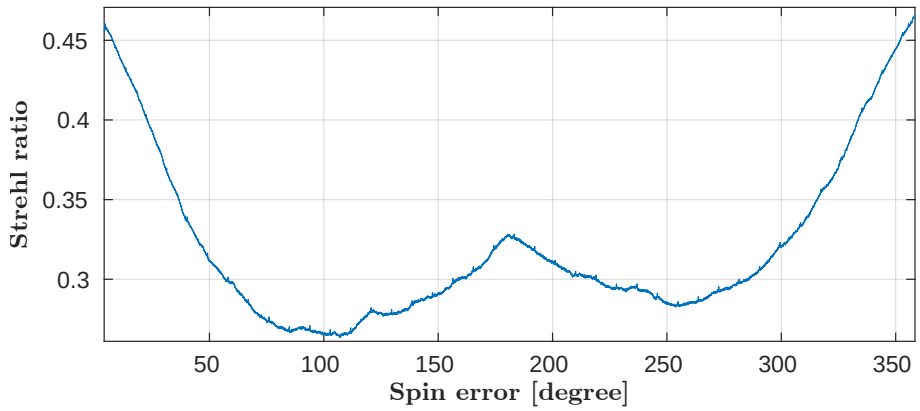

Figure 6.16: (OOMAO simulation with Keck on-sky LO disturbances) Effect on the LQG controller SR (y-axis) of the parallactic angle changes relatively to the model identification data (x-axis). A law of 0.3 point per degree is a good order of magnitude for the first (and last) 50 degrees. Integrator SR (not displayed) always around 30%.

49% to 40%) for the 180 degrees one. The integrator, as expected, was not sensitive to it (staying to its 39% SR). As expected from its rotation invariance, the defocus mode was still reasonably corrected by the LQG whatever the angle, as visible in modal results in figure 6.17.

An idea (but not yet properly implemented in simulation) is to include in real-time some spin-angle dependent linear operators, that allow to spin off the measurements (retrieve a spin-free measurement vector), compute the command with a same initial unique spin-free model, and then spin back the commands thanks to Zernike basis rotation formulas. For now, the only solution is to update the models often enough (depending on the location of the celestial object and the LO models singularities) so as not to have a too strong modeling error and therefore a limited loss of performance.

6.4.2 Model stitching in real-time systems

As seen in section 6.4.1, an on-the-fly model update will be necessary to guaranty the high performance. We use in this section the regulator state space representation to describe commands calculation from the slopes. It is defined by:

$$\begin{cases} X_{Rk+1} &= A_R X_{Rk} &+ B_R y_k \\ u_k &= C_R X_{Rk+1} & \end{cases} . \tag{6.11}$$

Let $\{A_R^1, B_R^1, C_R^1\}$ be the set of current regulator matrices. A new one $\{A_R^2, B_R^2, C_R^2\}$ has been defined: a controller switch is then necessary. The RTC will keep performing the computations, but at the switch iteration $k = k_s$, the state-vector calculation

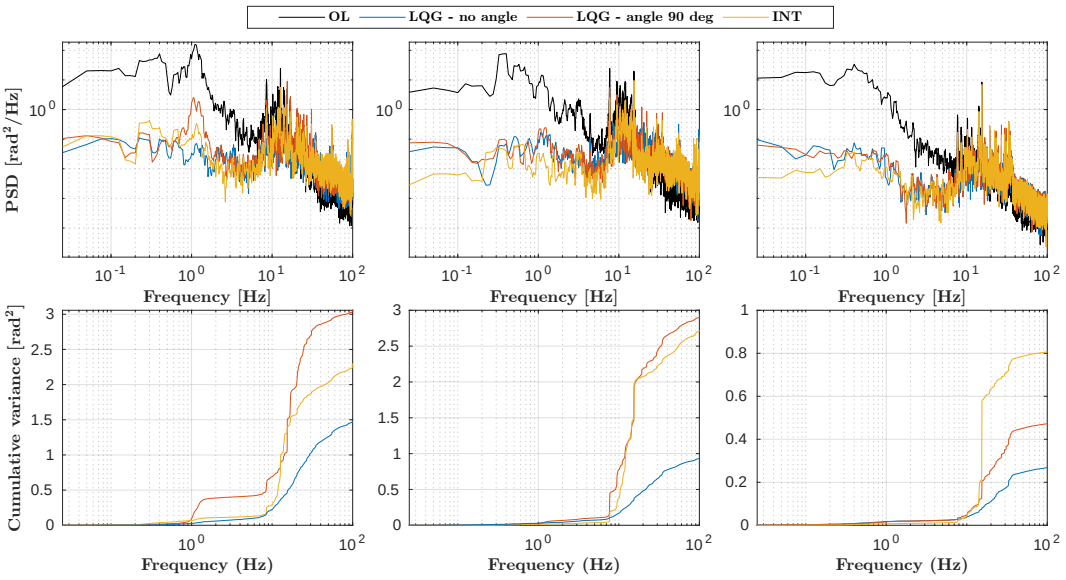

Figure 6.17: (bench) Modal spectra analysis of the effects on of parallactic angle changes. Left to right: tip, tilt and defocus. The worst are the peaks specific to the tip (1.2 Hz) and to the tilt (7.6 Hz) that are not covered anymore with a 90 degrees rotation. The turbulence correction does not depend on the angle, since more or less of same PSD for all the Zernike modes of a same radial order. Moreover, the models used for turbulence are not caring about the propagation direction ("boiling" models).

will mix the two models, multiplying the state 1 vector by the state 2 matrix:

$$X^2_{Rk_\mathrm{s}} = A^2_R X^{\mathrm{switch}}_R + B^2_R y_{k_\mathrm{s}-1}\,, \tag{6.12}$$

with $X^{\mathrm{switch}}_R = X^1_{Rk_\mathrm{s}-1}$. A first thing to notice is that it is not a problem for the AR2 models that represent mainly atmospheric turbulence: whatever 1 or 2, the state vectors should contain the same physical values of the phase at the two past iterations. However, the subspace identified models may not.

6.4.2.1 Basic methods and resulting issues

A solution to this switching problem was theoretically described in (H.-F. Raynaud, Kulcsár, et al., 2016).

The idea is to compute at the instant $k_\mathrm{s}-1$, by least square, the vector $X^2_{Rk_\mathrm{s}-k_\mathrm{h}}$ that would have led to the same sequence of commands $u_{k_\mathrm{s}-k_\mathrm{h}}, ..., u_{k_\mathrm{s}-1}$ actually obtained with the first regulator and to propagate this controller state through (7.6) from $k = k_\mathrm{s} - k_\mathrm{h}$ to $k = k_\mathrm{s} - 1$. It was tested in replay with bench data and appeared to be working well, as shown in figure 6.18. It requires a horizon value of about $k_\mathrm{h} = 50$, below which some jumps might occur at switching moment. In that figure is tested another method, which simply consists in doing a replay at instant $k_\mathrm{s} - 1$ on the last k_h iterations and use the last obtained $X^2_{Rk_\mathrm{s}-1}$ as the switching value X^{switch}_R. For $k_\mathrm{h} >> 1$, the two methods give the same result X^{switch}_R. The second method gives at least as good performance as the first method, with moreover a smaller necessary horizon, around $k_\mathrm{h} \sim 20$, according to some switching simulations (results in figure 6.19. This smaller horizon, with moreover less operations to do, makes this second replay method preferable to the first one. The order of magnitude on my computer to perform the replay is of 10 ms for $k_\mathrm{h} = 50$, making thus completely imaginable the implementation on an RTC. However, this is assuming that the RTC could have immediately access to the data of the past k_h iterations. Since the switching was not a sensitive issue in my PhD (see next section), it was not developed further for GTCAO.

6.4.2.2 Simple solution: keep state

In DARC, the RTC was always keeping the last state when changing the LQG regulator matrices, just on condition that the size of the new matrices was the same as the current matrices. Jose Marco added an option to DARC to allow the user to choose whether or not to keep the state on the frame when the RTC changes the LQG matrices. On GTCAO, the default was to keep the state during the switch. To make sense, this requires that the two successive models involved have the same number of Zernike modes with the same number of LO modes. This is not much of a constraint in our case where these numbers are set (cf previous sections). In simulations, this solution of keeping the state appeared to work very well in most of the cases (no residual phase jump at switching frame, e.g. figure 6.18 top) but

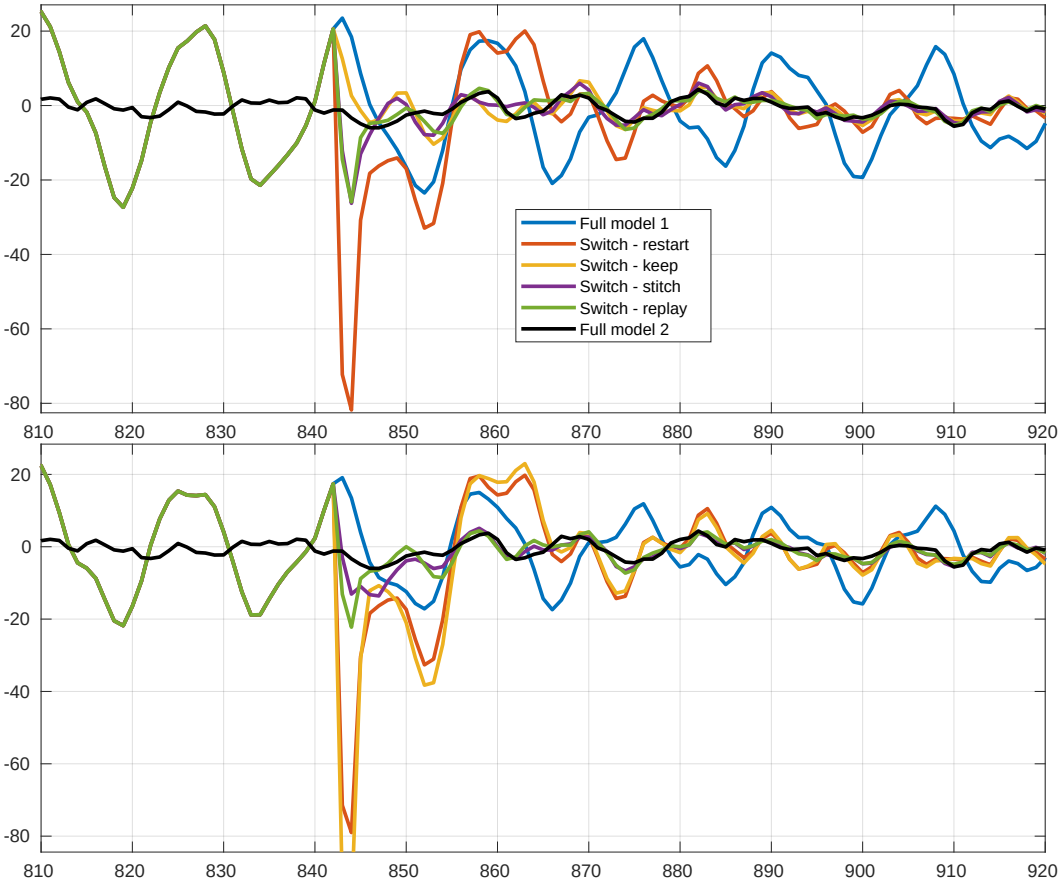

Figure 6.18: (replay) Residual phase before and after regulator switching. The switching occurs at $k_s = 845$. Top: switch from one set of matrices with wrong vibration modeling ($f_{vib} = 12\,\text{Hz}$ and $25\,\text{Hz}$) to another set with right vibration modeling ($f_{vib} = 15\,\text{Hz}$ and $30\,\text{Hz}$). Bottom: switch from one set of matrices without vibration modeling to another set with right vibration modeling ($f_{vib} = 15\,\text{Hz}$ and $30\,\text{Hz}$).

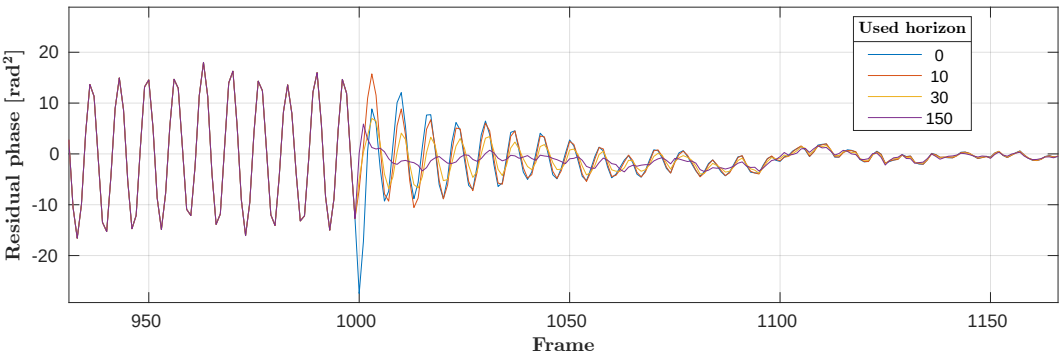

Figure 6.19: (replay) Residual phase before and after regulator switching. The switching occurs at $k_s = 1000$ from one set of LQG matrices without vibration modeling to another set of LQG matrices with vibration modeling. The horizon represents the number of iterations used in the replay mode to initialize the new state vector X_R^{switch}.

sometimes made the switch occur worse than $X_R^{\text{switch}} = 0$ (residual phase jump at switching frame, e.g. figure 6.18 bottom). We made a test on the bench to see how the system was reacting during the switches with and without keeping the state, as shown in figure 6.20. It was a case with maximal sampling frequency $F_s = 900\,\text{Hz}$ to challenge the RTC during the switches. There is a DM-injected vibration peak at 12 Hz. The switch is done between two regulators, one being defined from with-vibration data and the other without. With a reset to zero of the state vector (blue curve), there is no loss of stability, with very small transient times. Keeping the state, they are invisible. But we can precise that the things would not be so easy if the regulator matrices were modeling vibration peaks at two different resonant frequencies. In that case, the red curve would have probably looked like the blue one.

Another thing to say is that this type of peak is often happening naturally on the RTC, during usual runs (without switch), probably because some slopes are missed by DARC (about every 5 seconds). This is enough for us at the moment not to dig deeper the issues of optimal stitching.

6.5 Conclusion

We have detailed the telemetry-data-based methods developed to acquire the necessary parameters for disturbance modeling. This allows to cope with all type of disturbances, in an autotuning way. Some warnings about the needs of model update and the switching instants have been detailed, but in the following we will stay in the case of stationary conditions.

The next chapter describes the results obtained on bench with those modeling methods, comparing the autotuning strategy with the best-tuned LQG regulators.

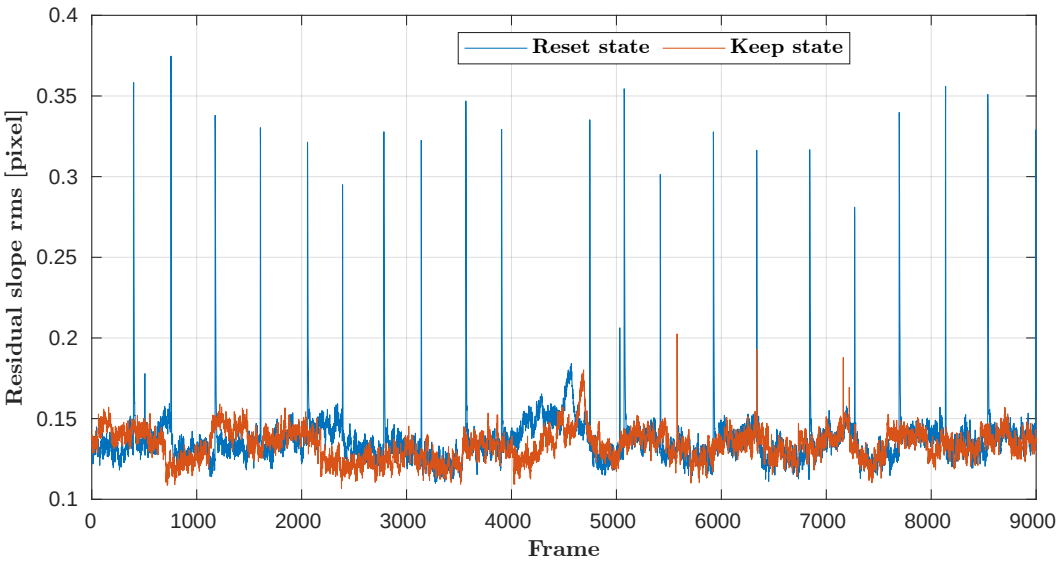

Figure 6.20: (bench) Residual slopes RMS. A switch between two preset regulators is done every half second. Red: keep state, SR 64%. Blue: reset state, SR 62.5%. The non regularity of peaks is due to data recording difficulties of the RTC at high sampling frequency.

Chapter 7
Performance analysis for LQG control: GTCAO bench tests and Keck on-sky data

We have developed in chapter 5 some procedures to calibrate and model the AO system.In chapter 6, we have designed the disturbances models together with their identification procedures. The previous chapter explained the methods to model the disturbances. In this chapter, we evaluate the performance of this work applied to the GTCAO system. First, we define the performance and behavior evaluation tools in section 7.1. Then, in section 7.3, we gather the performance results obtained on bench with GTCAO. Unfortunately, the whole control design procedure could not be tested on sky. We have thus contacted Peter Wizinowich at Keck Observatory, with the idea of carrying out some tests using on-sky data sets. Sam Ragland has kindly made available several hundreds of data sets. The performance results obtained in replay are presented in section 7.4. Let us precise that the work developed in chapter 4 was not implemented on bench tests: the vibrations on GTCAO are simulated with DM commands, that is to say in discrete time, while the chapter 4 is dedicated to the correction of continuous disturbances.

7.1 Performance evaluation from residual slopes

7.1.1 Residual phase reconstruction

The study of residual slopes is particularly inappropriate for performance evaluation. What matters for scientific images is the residual phase variance, which needs to be minimized. This is illustrated in figure 7.1, where the LQG has more than 20% higher residual slopes variance than the integrator. Yet, its SR is 10 points higher than the integrator one. The difference between residual slopes and phase on GTCAO might be even stronger than some other AO systems due to the non-Fried geometry (limited measurement of the actuators related dephasing). To reconstruct the residual phase time-series Φ^{CL}, the same projector R_{MAP} as in equation (3.32) is used, applied to time-series of closed-loop slopes Y^{CL} time-serie of :

$$\phi^{\mathrm{CL}} = R_{\mathrm{MAP}} Y^{\mathrm{CL}} \,. \tag{7.1}$$

Even if R_{MAP} is defined based on open-loop atmospheric statistics, it appeared that this reconstruction was giving almost the same results as doing: $\Phi^{\mathrm{CL}} = R_{\mathrm{MAP}}(Y^{\mathrm{CL}} - M_{\mathrm{int}}U) + NU$, in which R_{MAP} does multiply pseudo-open loop measurements (U is the matrix containing time-series of command vectors u_k) . Once the time-series are computed, it is possible to take the squared modulus of the Fourier transform to obtain the PSD. This is a very interesting graph to plot to determine what are the

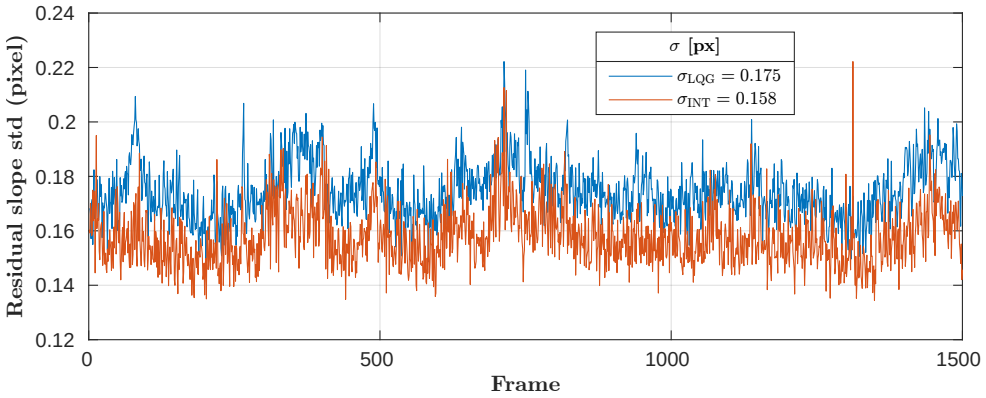

Figure 7.1: (bench) Residual slopes STD in a case with vibrations.

problems of a regulator, displaying its cumulative sum to highlight the actual zone of importance among the frequency spectrum. This is done in results sections 7.3.4 and 7.4.1.3.

7.1.2 Rejection transfer function computation

The rejection transfer function (RTF) shows the spectral rejection of the disturbances. Its modulus can be computed in two different ways. The first is based on experimental data, and the second on theoretical formula resting on the models.

Empirical calculation

The RTFs are standardly calculated from the empirical PSDs. For each mode, the PSDs in open-loop (or pseudo open-loop) and closed-loop are computed. Then, the empirical RTF gain is obtained as the ratio of closed-loop PSD by (pseudo-)open-loop PSD for each temporal frequency.

Theoretical calculation

The format of matrices in DARC allows to write the regulator matrices $[A_R, B_R, C_R]$ as in equation (7.6). From it, it is possible to build a state-space representation $[A^P, B^P, C^P, D^P]$ of the closed-loop system with the phase disturbance ϕ^{OL} as input and the residual ϕ^{CL} as output. For instance, for the case of a system delay Δ inferior to one (meaning that $\Delta = \Delta - \lfloor \Delta \rfloor \triangleq \delta$), it is written:

$$A^P = \begin{bmatrix} A_R + (1-\delta)B_R M_{\text{int}} C_R & \delta B_R M_{\text{int}} \\ C_R & 0 \end{bmatrix} \tag{7.2}$$

$$B^P = \begin{bmatrix} B_R D \\ 0 \end{bmatrix} \tag{7.3}$$

$$C^P = \begin{bmatrix} N(1-\delta)C_R & \delta N \end{bmatrix} \tag{7.4}$$

$$D^P = I \tag{7.5}$$

and the state-space representation writes:

$$\begin{cases} X^P_{k+1} &= A^P X^P_k &+ B^P \phi^{\text{OL}}_k \\ \phi^{\text{CL}}_k &= C^P X^P_{k+1} &+ D^P \phi^{\text{OL}}_k \end{cases} . \tag{7.6}$$

Then, Matlab allows to plot the Bode diagram corresponding to this system, that is to say of the rejection transfer function.

7.1.3 Stability margins from Nyquist diagram

The Nyquist diagram is used to visualize the stability margins. It is obtained with Matlab by defining the transfer function in open-loop. The latter needs the regulator transfer function, which is

$$TF_{\text{regul}}(z) = zC_R(zI - A_R)^{-1}B_R\,, \tag{7.7}$$

where $z = \exp(2i\pi T_{\text{s}})$ is the z-transform variable. Then, the open-loop transfer function of the mode number i is:

$$TF_{\text{OL}}(z) = N^i \left(\delta z^{-1} + (1-\delta)\right) TF_{\text{regul}}(z) D^i z^{-1}\,, \tag{7.8}$$

where N^i and D^i are respectively the line and the column of matrices N and D (corresponding to the mode of interest i). The Matlab function *nyquist* is then used directly with each mode in (7.8), the transfer function being defined as a symbolic expression.

7.2 Study of scientific images: Strehl ratio computation

The estimation of SR has been widely studied, see e.g. (Roberts Jr et al., 2004; Soummer and Ferrari, 2007; Gladysz et al., 2008). In this section, we present two standard ways to compute the SR from a given PSF:

- in image space, computing the ratio between the scientific image peak and the diffraction-limited PSF, as presented in section 2.6 (the left hand side of equation (2.35))
- in Fourier space, computing the ratio between the scientific image FFT –the optical transfer function (OTF)– total energy and the diffraction-limited PSF FFT total energy (the right hand side of equation (2.35)).

7.2.1 Methods description

Camera parameters

Both methods need the value of the oversampling $\mu_{\text{sci}}^{\text{ov}}$ of the scientific camera:

$$\mu_{\text{sci}}^{\text{ov}} = 0.5\frac{\lambda_{\text{sci}}/D_{\text{pup}}}{\mu_{\text{sci}}} = 1.32\,, \tag{7.9}$$

with $\lambda_{\text{sci}} = 1600\,\text{nm}$, $D_{\text{pup}} = 11.4\,\text{m}$ and $\mu_{\text{sci}} = 11 \times 10^{-3}$ arcsec.

7.2.1.1 Airy reference

Both methods need a diffraction-limited reference to determine how far from the maximum possible intensity the scientific images peaks are.

- The pupil of M1 on the bench is simulated with OOMAO (segmented pupil) and is rotated of 3.6 degrees, as is GTCAO M1 pupil simulator shown in figure 5.13.
- To have the right oversampling in the focal plane, the pupil of current size n is padded (basic Matlab function) up-down and left-right with $n(2\mu_{\text{sci}}^{\text{ov}} - 1)/2$ lines and columns.
- The padded pupil is resized with the propper coefficient to reach afterwards the desired scientific image number-of-pixel size $n_{\text{px}}^{\text{SR}}$.
- Eventually, the square module of the FFT of the padded array (example of result in figure 7.8) gives the diffraction-limited PSF I_{diffr}.

7.2.1.2 Image pre-processing

Both methods are applied after a pre-processing of the images:

- The image to be processed is made of the average of n_{img} images. It has already its background subtracted. In our case, it represents 11 s, that is to say one full rotation of the phase screen at $V_0 = 10\,\text{m}\,\text{s}^{-1}$.
- To counteract the effect of salt & pepper noise and of some vertical noise bands (visible for instance on figure 7.2), a median filter of size 1×3 (horizontal band) is applied to the image. It enables to find the PSF peak of intensity without being trapped by strongly noisy pixels. For the 13×13 pixels around that peak pixel, the unmedianned original image is kept to avoid filtering the maximum intensity pixel. The median filtering mostly helps the OTF method, whose results precision otherwise can drop by some 3 Strehl points. The residual noise mean and STD values, $\mu_{\text{sci}}^{\text{noise}}$ and $\sigma_{\text{sci}}^{\text{noise}}$, are then estimated on a far-from-flux area (figure 7.3).

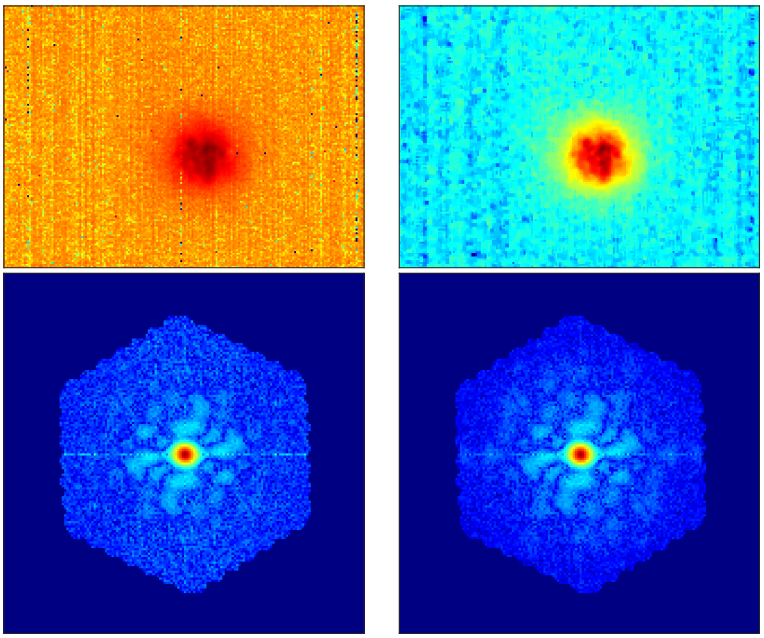

Figure 7.2: (bench) Example of image without (left) and with (right) median filtering. Effects on the image (top, with square root to highlight the noise) and their OTF real part (bottom).

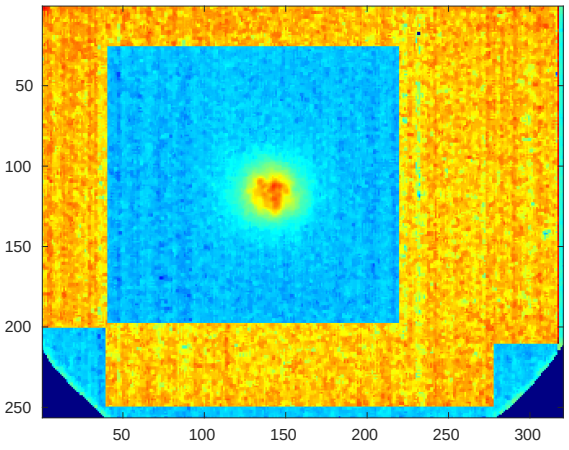

Figure 7.3: (bench) Example of scientific image noise area (yellow-orange highlighted pixels). Noise STD $\sigma_{\text{sci}}^{\text{noise}}$ and average $\mu_{\text{sci}}^{\text{noise}}$ are evaluated on those pixels.

- The PSF is centered. To allow an accurate centering, an interpolation is first made, using zero-padding in Fourier space. An interpolation factor of $q = 3$ (linear) appeared sufficient, beyond which the SR estimation is not changing (typical value for an image with pixels oversampling of $\mu_{\text{sci}}^{\text{ov}} = 1.32 \simeq 1.5$). This interpolation is of course also done for the Airy reference image.
- The image is cropped to the desired square image size $qn_{\text{px}}^{\text{SR}}$ pixels linear. The Airy reference image too.

Once prepared in such a way, the image I can be processed by the OTF algorithm and/or the PSF one. Note that the total fluxes are adapted later, within each of both methods.

7.2.1.3 OTF method

The OTF is obtained by taking the FFT of the image I: $OTF = \mathcal{F}(I)$. Then:

- The image I is assumed to be composed of a useful signal part I_{sci} plus two components of noise, one main white I_{white} and the other spatially correlated $I_{\text{non-white}}$: $I = I_{\text{sci}} + I_{\text{white}} + I_{\text{non-white}}$ (example in figure 7.4). In this way, almost the whole noise signal in the OTF is concentrated in OTF_{white} at the 0-px^{-1} point (first point of the OTF matrix). The effect of the noise at this frequency should thus be removed. This is done by performing a second order extrapolation of the OTF in zero using the next four points of the real part of the OTF, as illustrated in figure 7.5.

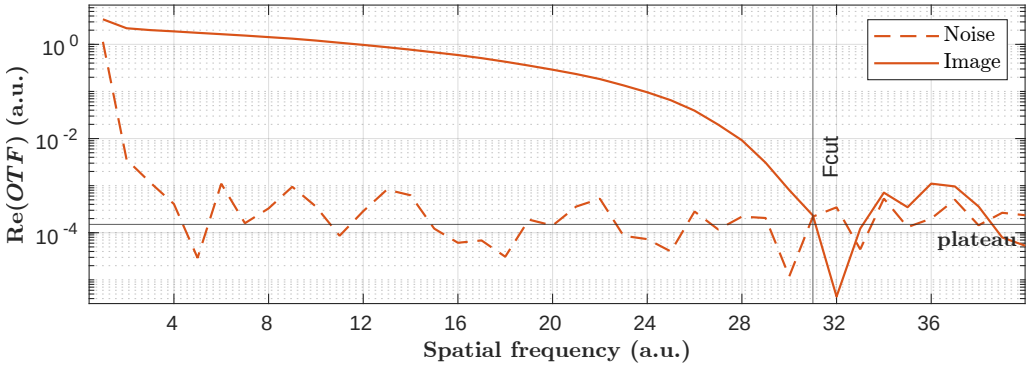

Figure 7.4: (bench) Example of noisy OTF real part (continuous red line) and image noise (real part of spectral content, dashed red line) using a window of $n_{\text{px}}^{\text{SR}}$=80 pixels. The cut-off frequency $F_{\text{cut}} = \frac{n_{\text{px}}^{\text{SR}}}{2\mu_{\text{sci}}^{\text{ov}}} = 31$ pixels is indicated by a vertical line and is consistent with the OTF behavior. These 1-D curves correspond to the circular averages of the OTFs real part.

- The OTF of the diffraction-limited image is taken, $OTF_{\text{diffr}} = \mathcal{F}(I_{\text{diffr}})$.

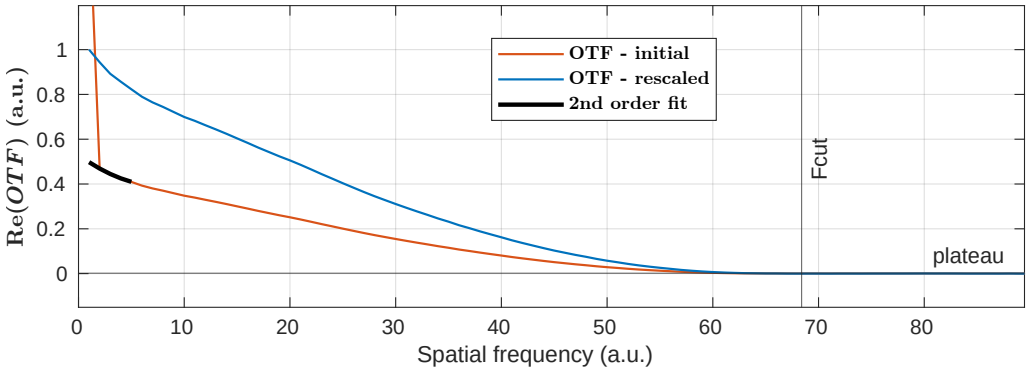

Figure 7.5: Example of OTF for a noisy PSF (red), the OTF extrapolation (black) and the rescaled denoised OTF (blue). These 1-D curves correspond to the circular averages of the OTFs real part.

- The total fluxes are made unitary for both the studied image and the diffraction-limited image, in the spectral domain, by dividing their respective OTFs by their respective first value (the images were centered on their respective maximum value during the images pre-processing, so $OTF(0\,\mathrm{px}^{-1}) = \overline{I}$).
- The SR is then computed using:

$$SR = \frac{\max(I)}{\max(I_{\mathrm{diffr}})} = \frac{I(0\,\mathrm{rad})}{I_{\mathrm{diffr}}(0\,\mathrm{rad})} = \frac{\overline{OTF}}{\overline{OTF_{\mathrm{diffr}}}} = \frac{\sum OTF}{\sum OTF_{\mathrm{diffr}}}\,. \tag{7.10}$$

7.2.1.4 PSF method

The pre-processed image I is used this way:

- The average noise scalar value previously computed (figure 7.3) is substracted from the image: $I \leftarrow I - \mu_{\mathrm{sci}}^{\mathrm{noise}}$.
- In the case of a very noisy image (SNR below 100), a 2-D Gaussian fitting can be done (with a least-square optimization of the Gaussian amplitude, center and variances, Matlab code of Gero Nootz (2022)), giving thus an estimation of the peak value of the image. It also gives the possibility to have an estimate of the FWHM of the scientific PSF by using the x and y RMS:

$$FWHM = 2.335\frac{\sigma_x + \sigma_y}{2}\frac{1}{q}\,[\mathrm{px}]\,. \tag{7.11}$$

  Note that if the SNR is over 100, as it is the case on the bench or in our SR computation simulations, it is not necessary to make this Gaussian fitting and it can be even prejudicial. We see for instance on images of figure 7.6 that AO closed-loop images may be not really Gaussian. Red and green lines on the images are the two principal directions of the 2-D Gaussian models. Black

lines on the plots are the Gaussian models. Model is strongly wrong for the 10%-SR case (20% relative underestimation of the SR), good for the medium case (less than 0.5% relative error) and acceptable for the 95%-SR case (3% relative error).

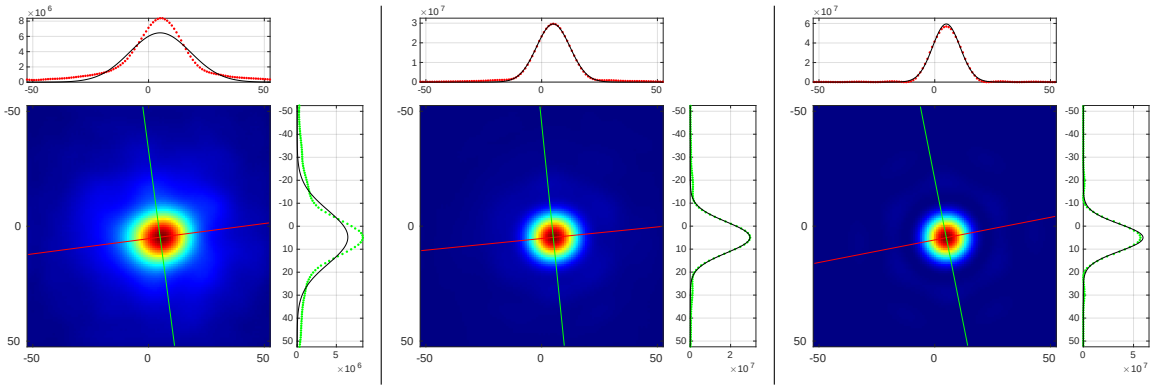

Figure 7.6: (simulation) Example of 2-D Gaussian fitting of a long exposure scientific image with SNR higher than 100. SR cases (left to right): 10%, 50% and 95%. The fitting clearly fails for the 10%-SR case. Interpolation factor of 5. Figure code Gero Nootz (2022).

- The total fluxes are made unitary for both the studied image I and the diffraction-limited image I_{diffr}.
- The SR is computed as:

$$SR = \frac{\max(I)}{\max(I_{\text{diffr}})}\,. \tag{7.12}$$

Automated computation on GTCAO bench

On GTCAO bench, the SR is continuously displayed aside the RTC windows using a slightly different PSF method. It is setting the window size to the value $n_{\text{px}}^{\text{SR}}$ such that the edge pixels of the cropped image have an STD twice as big as $\sigma_{\text{sci}}^{\text{noise}}$.

7.2.2 Simulation study of the pros and cons

To figure out the pros and cons of these two methods, we performed simulations with different SRs, scientific camera noise levels and window sizes $n_{\text{px}}^{\text{SR}}$. Note that, since having SNRs over 100 in the simulations, no Gaussian fitting has been done.

7.2.2.1 Simulations conditions

Wavefront distortion

The closed-loop images are simulated by computing a wavefront error on 495 Zernike modes following a typical Gaussian distribution with Zernike residual variance cal-

culated from bench data. The variance values are averaged for each radial order (figure 7.7). The variances are obtained as then scaled to have more or less challenging wavefront distortions. Long exposure scientific images are the sum of 75 "short exposure" PSFs, each computed with independent realisations of wavefronts (example in figure 7.8).

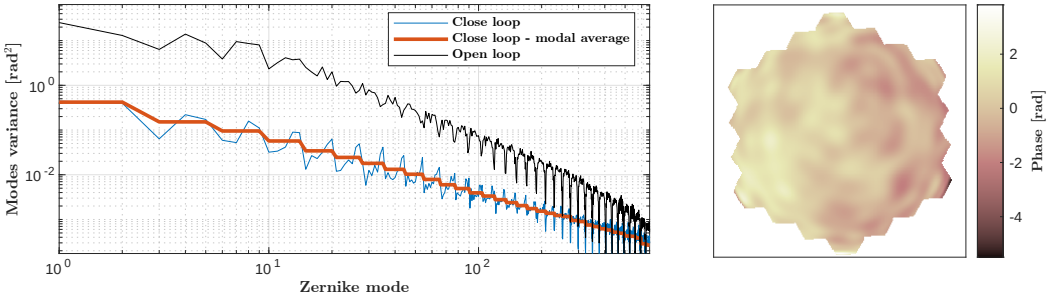

Figure 7.7: Modal statistics used for generating residual wavefronts (red, left). Example of residual wavefront on the right (as on the testbench, there is no central obscuration).

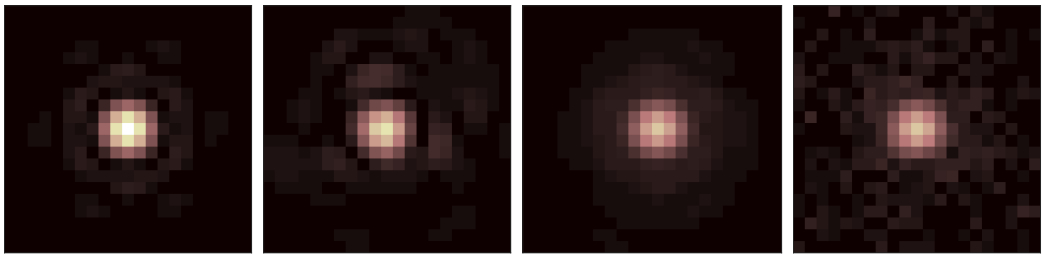

Figure 7.8: Simulated PSF for SR computation. Left to right: diffraction limited, short exposure, long exposure with added noise. The last one is the simulated scientific image. Case of a residual wavefront of 0.8 rad RMS (50% SR) with noise of SNR=100 and window size of $n_{\text{px}}^{\text{SR}} = 20$ pixels.

Computation of the "true" Strehl ratio

The SR is computed with the noise-free image, to which the PSF method is applied (section 7.2.1). Since there is no noise yet, we can consider that the PSF method delivers the right SR value.

Noisy images

A read-out noise is then added as a zero-mean Gaussian white noise. The values taken for the SNR are based on typical bench values, which is around 5000: $\sigma_{\text{sci}}^{\text{noise}} \simeq 2\,\text{au} \simeq \frac{\max(I_{\text{diffr}})}{5000}$. Two other values are tested: an SNR of 500 ($\sigma_{\text{sci}}^{\text{noise}} = 20$) and 100 ($\sigma_{\text{sci}}^{\text{noise}} = 100$).

Computation with different window sizes

The two SR computation methods described above are both implemented, cropping the images with different window sizes $n_{\text{px}}^{\text{SR}}$. As it can be seen in figure 7.8, the minimum size should be around 20 px. In simulations, the sizes extend from $n_{\text{px}}^{\text{SR}} = 20$ to 160 pixels.

7.2.2.2 Simulations results

Results are gathered in figure 7.9. For the sake of clarity, the STD are plotted on another graph instead of adding error bars on the median error graphs.

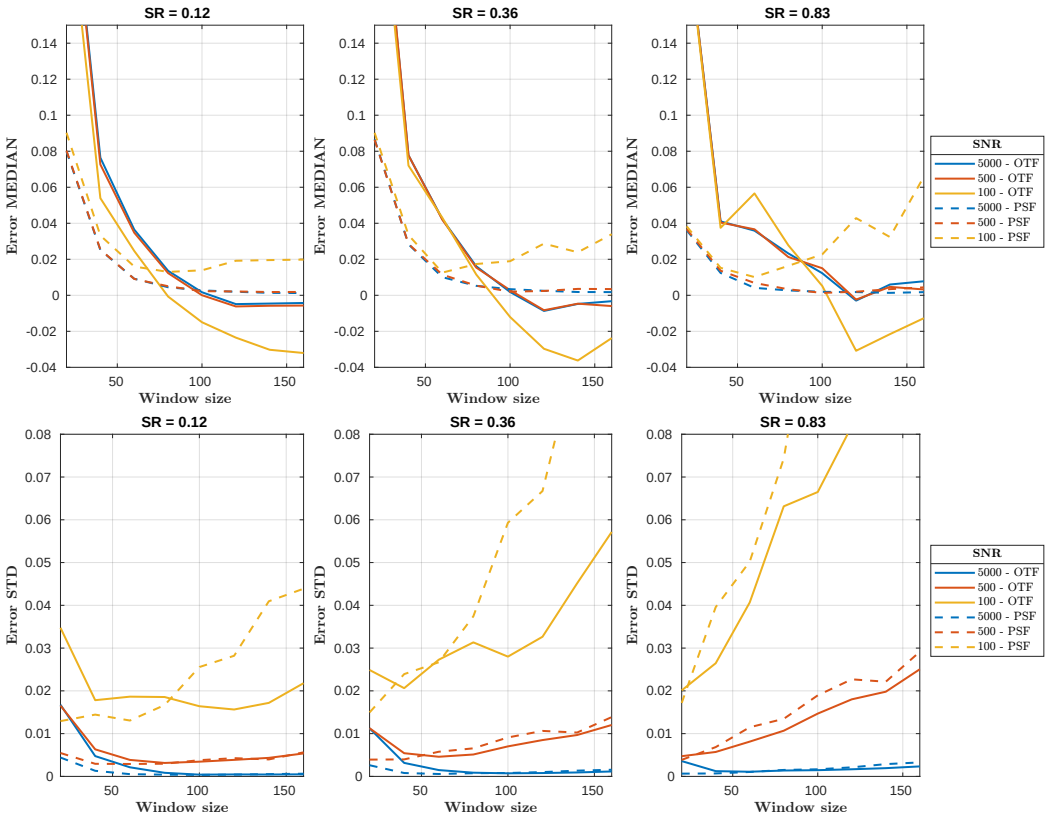

Figure 7.9: (simulation) Comparison of SR estimation errors as a function of the window sizes $n_{\text{px}}^{\text{SR}}$. Continuous lines: OTF method. Dashed lines: PSF method. Top: medians of the estimation errors. Bottom: STDs of the estimation errors. Window sizes $n_{\text{px}}^{\text{SR}}$ are in pixels. Errors STD are reaching 0.2 (outside the graph) for the low flux case at high SR=0.83 for SNR=100 (down-right yellow graphs).

From the analysis of figure 7.9, we can state that

- The high flux cases, SNR 5000 (blue curves), correspond to the bench test conditions. The OTF method works well when the window is sufficiently wide

($n_{\text{px}}^{\text{SR}} > 130\,\text{px}$), giving an estimation error inferior to 0.01. The PSF method exhibits however an even better behaviour (lower error median values and similar STDs) with only $n_{\text{px}}^{\text{SR}} \simeq 60\,\text{px}$. We see in these simulations that the values of $n_{\text{px}}^{\text{SR}} = 32\,\text{px}$ for high SRs or $n_{\text{px}}^{\text{SR}} = 64\,\text{px}$ for lower SRs slightly overestimates the SRs (about 1 point).

- With a SNR of 500 (red curves), both estimators still converge to the right SR when the window size increases. The PSF is again preferable. With this SNR, the error STD starts increasing for both methods. Setting the window sizes to the best estimation values (130 pixels for OTF method and 60 pixels for PSF method), the PSF method has again slightly lower error STDs than the OTF method.

- With a SNR of 100 (low flux, yellow curves), both estimators stop converging when increasing the window size. The SR is still well estimated using the local minimum of PSF method estimations, around $n_{\text{px}}^{\text{SR}} = 60\,\text{px}$ in those simulations. The OTF estimator has more bias and seems to underestimate the SR past $n_{\text{px}}^{\text{SR}} \simeq 90\,\text{px}$. Looking at the STDs of the estimation errors, the repeatability is here quite damaged, rising about 0.02 even for the smallest window size. When setting the window sizes to the values of 60 and 90 pixels, the PSF method has again lower error STDs.

As a conclusion, we favor the PSF method, granting better accuracy and precision on the whole SR scale, notably with our high-flux GTCAO scientific source.

7.2.3 Assessment with bench test images

Using some CL images obtained on the bench for various phase screens and NGS fluxes, in OL or CL, it is possible to appreciate whether the simulations results (figure 7.9) match with experimental ones. Figure 7.10 analysis leads to similar behaviour but with changes in the numerical values:

- Due to high flux condition, the estimations are all converging with the window size (unlike yellow curves). For the PSF method a value of $n_{\text{px}}^{\text{SR}}$ between 80 and 100 px is correct, similarly to simulations (SNR close to 5000). For OTFs, $n_{\text{px}}^{\text{SR}} \simeq 130\,\text{px}$ as indicated for simulations.

- As in simulations, the OTF probably underestimates the SR for large window sizes, getting typically a few points under the PSF method estimations

- A difference between the bench results and the simulation results is the stronger sensitivity of bench images SR to the window size. For instance, the red curve case shows now a decrease of 20 points between the SR estimations at $n_{\text{px}}^{\text{SR}} = 20$ pixels and at $n_{\text{px}}^{\text{SR}} = 150$ pixels, while it was of only 4 points in simulations.

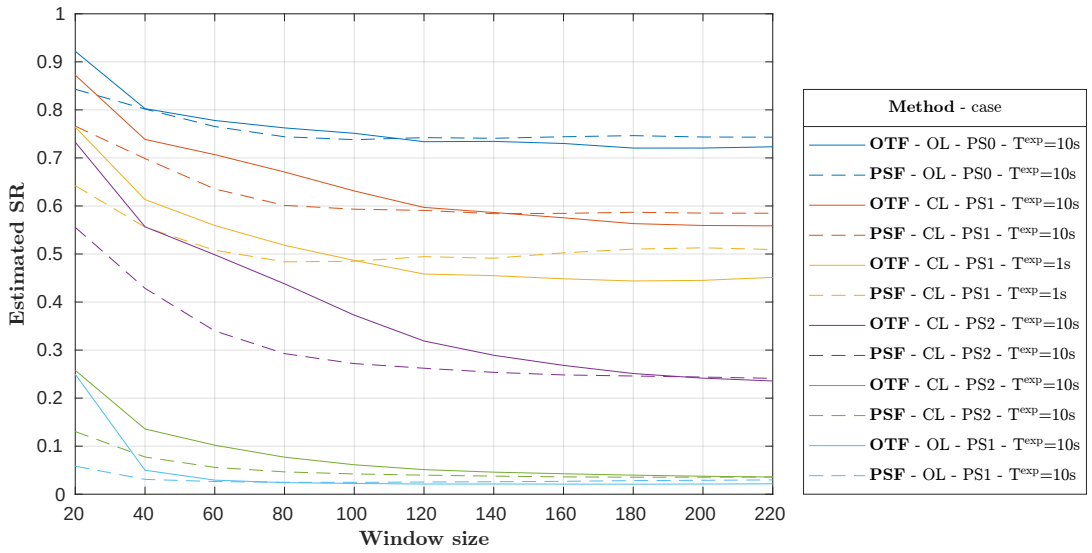

Figure 7.10: (bench) Example of SR estimation methods application on GTCAO scientific images. Window sizes $n_{\text{px}}^{\text{SR}}$ are in pixels. PS1: phase screen 1 (favorable atmosphere). PS2: phase screen 2 (challenging atmosphere). PS0: no phase screen (disturbance-free and with flatened DM).

Conclusion

The SR estimator based on the PSF is the best for the GTCAO bench tests scientific images. Despite a similar behaviour, the bench images are more strongly sensitive to the window size than in simulation. It is probably due to the absence of central obscuration: a badly corrected phase in the central part of the pupil is affecting the scientific images. This produces a strong decrease of the SR when increasing the window size. The values retained for the bench SR estimations are $n_{\text{px}}^{\text{SR}} = 32\,\text{px}$ for phase screen 1 and $n_{\text{px}}^{\text{SR}} = 64\,\text{px}$ for phase screen 2 to balance this effect.

7.3 GTCAO on-bench tests: performance results and behaviour analysis

In this section, we start in subsection 7.3.1 by precising the pipeline we followed to carry out on-bench tests.

Then, we present some results obtained on GTCAO bench. In section 7.3.2 are gathered the SR results for the basic cases with pure turbulence (phase screens PS1 and PS2), to which is added in section 7.3.3 only the windshake TT disturbance (section 5.2.2.1). Afterwards, in section 7.3.4, the performance is analysed in a case where Keck-like disturbances on all the first 9 Zernike modes (not only TT) are injected (made possible here again by the DM on GTCAO optical path).

7.3.1 Pipeline of on-bench tests

The main steps we followed for the tests on the bench (we suppose that all the system power is already turned on and the WFS CCD cooled down) are the following:

1. At the beginning of the day, the WFS reference centroids positions is loaded. Those centroids references are everyday the sames: they were optimized during a bench calibration to give the best possible SR. Then, the WFS CCD is shifted up-down and left-right to minimize the measured slopes relatively to the just-loaded reference centroids. Then, the loop is closed (with an integrator with any small loop gain) to finalize the alignment on the reference centroids. Finally, the such-obtained DM offset voltages are taken (average of the commands on one second) as the flattening reference command of the day.

2. For each test of the day, the bench simulator parameters are set to the desired experimental conditions: the NGS flux (playing with the NGS source power or setting some filter at the entrance of the WFS), the vibrations (loading a time-series of DM commands on the GUI) and the phase screen (setting PS1 or PS2 and their rotating speed).

3. For each test, the GTCAO RTC parameters are set to the desired control conditions: the sampling frequency F_{s}, the WFS CCD optical gain and the WFS CCD flux threshold (with python DARC commands on the RTC computer, or on the WFS GUI window)

4. The regulator is adjusted: setting the desired loop gains on the integrator GUI or setting the desired LQG matrices timestamp on the LQG GUI.

5. The loop is closed. The RTC is asked to collect some telemetry data for a user-defined duration, say ten seconds. This is done using the GUI interface.

6. Past those ten seconds, the headers which describe the RTC and simulator parameters are automatically added to the saved fits files (the list of headers we defined with Jose Marco are listed in Appendix A (page 193), and are joined to fits files thanks to "with_cards" GUI function). The fits files are copied towards the GUI-indicated working directory. From our computer (linked to the IAC AIV internal folders) we copy those files to our own computer LQG directory: the Matlab code can be run to define LQG matrices as in section 6, a flow chart that gives the sequence of the calculations is given in Appendix B (page 197).

7. The state-space model is recast into DARC-format LQG matrices that are saved in their respective fits files, with their timestamp. The fits files are given headers to describe the controller parameters (example in Appendix A (page 193)).

8. These matrices are sent to the RTC computer (reverse path as the data path), the GUI timestamp is adapted, and reloaded by DARC (i.e. go back to step 4 to test the updated LQG controller)

7.3.2 Results for pure atmospheric turbulence

The on-bench results in terms of SR are displayed in figure 7.11. They correspond to cases with atmospheric turbulence only. On the left are the cases with favorable atmosphere (PS1), while challenging on the right (PS2). The sampling frequency for each NGS magnitude is written in black (in Hertz). Blue lines correspond to the LQG results obtain with the best tuning of the fudge factor α_{FF}, red lines to the integrator results with the best tuning of the loop gains.

In good atmospheric conditions (PS1), with NGS magnitudes 10.2 or 11.3, both integrator and LQG regulator have the same maximal SR of 72%, with the sharpest PSF of FWHM 35 mas. We see that the LQG performance outperforms the integrator when the magnitude increases. The prediction capability of the LQG is well illustrated for magnitude 11.3 (500 Hz) and 12.6 (250 Hz): the performance is at same level despite the lower loop frequency and flux.

For bad atmospheric conditions (PS2), the advantage is broader, with a minimum gain of 4 SR points and a maximum of 10 SR points. The prediction here allows keeping the same performance level when going from magnitude 10.2 (900 Hz) to magnitude 11.3 (400 Hz). In terms of resolution, at $F_{\mathrm{s}} = 50\,\mathrm{Hz}$, the LQG is sharpening the critical FWHM of the integrator PSF from 400 mas to 69 mas.

With each phase screen, some tests were performed using the data-based algorithm to adjust the fudge factor automatically (section 6.2.2).

For the case of phase screen 2, these autotuned fudge factor values led to the same performance as with the best values tuned manually.

For phase screen 1, we observed that the autotuned fudge factors led to a reasonable performance degradation of half of the improvement with respect to the integrator (e.g. 63.5% SR instead of 66.5% at $F_{\mathrm{s}} = 100\,\mathrm{Hz}$). We could envision several options to avoid this:

- a look-up table, depending on the NGS magnitude and the estimated AR2 parameters
- revisit the criterion we built for the fudge factor in section 6.2.2
- optimize the fudge factor based on a short loop replay, which may be time consuming in situations where model updates are to be performed on short time scales.

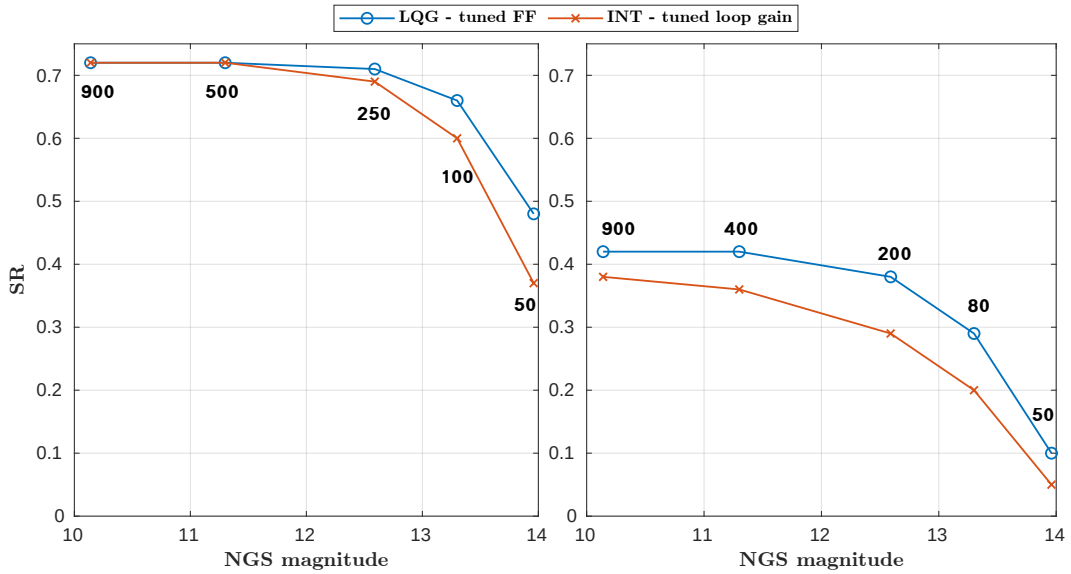

Figure 7.11: (bench without vibration, 2022/06/02) SR as a function of the guide star magnitude. Left: phase screen 1 $r_0 = 23\,\text{cm}$. Right: phase screen 2 $r_0 = 8\,\text{cm}$. Sampling frequencies are written in black for each NGS magnitude.

7.3.3 Effect of windshake on performance

The on-bench SRs with turbulence and windshake are displayed in figure 7.12. On the left are the cases with favorable atmosphere (PS1), while challenging on the right (PS2).

In good atmospheric conditions (PS1), we see that the advantages of the LQG appear from magnitude 11.3. Despite the windshake, the LQG controller can still keep the same performance when diminishing the sampling frequency from 900 Hz to 500 Hz. For magnitudes higher than 11.3, the gain of SR with respect to the integrator increases from a minimum of 4 points to a maximum of 12 points. In terms of resolution, at $F_s = 50\,\text{Hz}$, the LQG is sharpening the FWHM of the integrator PSF from 81 mas to 52 mas.

For bad atmospheric conditions (PS2), the LQG succeeds to keep the same performance between sampling frequencies of 900 Hz and 400 Hz. Compared with the integrator, the gain in SR extends from a minimum of 4 points to a maximum of 12 points. For magnitudes higher than 13, the LQG is more than doubling the maximal intensity of the integrator. In terms of resolution, at $F_s = 50\,\text{Hz}$, the LQG is sharpening the FWHM of the integrator PSF from 440 mas to 140 mas.

With each phase screen, some tests were performed using the data-based algorithm to adjust the fudge factor automatically (section 6.2.2). It gave similar performance as with the manual best tuning. In the case of phase screen 2, the performance was however sometimes lower (about 3 SR points for magnitudes 12.6 and 13.3). Nevertheless, it is worth noting that the autotuned procedure tends to

favor higher values of the fudge factor. As a results, the regulator sees its stability margins increased. On sky, the good compromise may well be to prefer a method which ensures more robust stability.

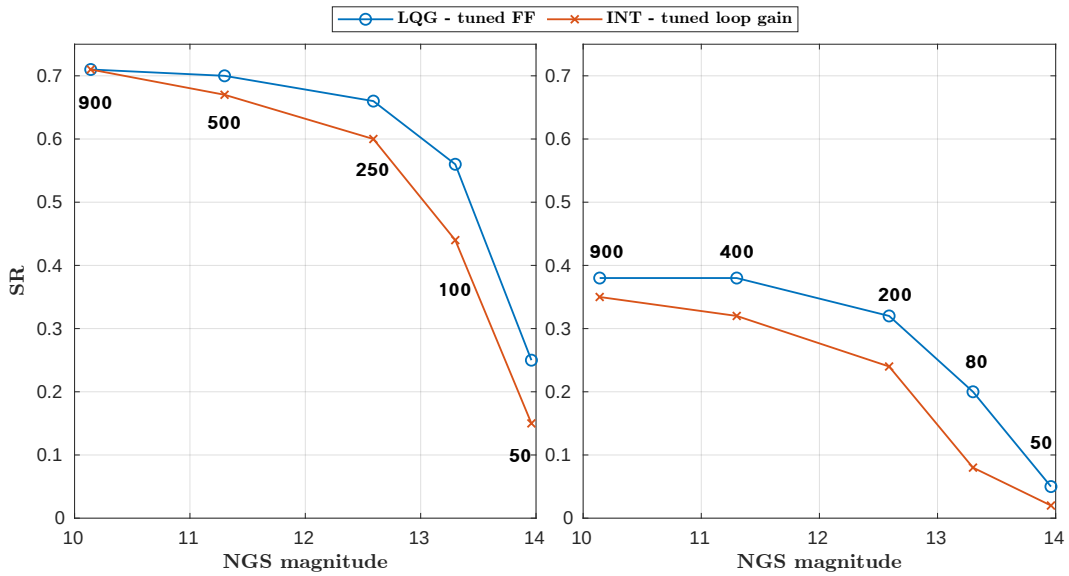

Figure 7.12: (bench with vibration, 2022/06/13) SR as a function of the guide star magnitude. Left: phase screen 1 $r_0 = 23\,\text{cm}$. Right: phase screen 2 $r_0 = 8\,\text{cm}$. Sampling frequencies are written in black for each NGS magnitude.

7.3.4 Performance and behavior analysis for Keck-like disturbances

7.3.4.1 Global tests description

Used data

We use here Keck on-sky data recorded in 2020 which were made accessible to us thanks to Peter Wizinowich, Sam Ragland (and of course thanks to the work of the staff at Keck Observatory).

On-bench disturbances

To obtain the corresponding phase disturbances, a Keck MAP reconstructor is defined with the same procedure as for GTCAO (matrices D, Σ_w, Σ_ϕ). For bench tests, we keep the Zernike modes 1 to 9 that seemed the main containers of vibration disturbances judging from the PSDs. The two first modes (tip and tilt) are filtered by M2 the same way as detailed in section 5.2.2.2. The phases are finally converted into GTCAO commands with a phase-to-command GTCAO projector, to allow their injection with the DM.

Those synthetic disturbances are added to phase screen 1, the latter rotating at $V_0 = 10\,\mathrm{m\,s^{-1}}$.

Regulator matrices construction

The LQG controller matrices are generated following the autotuning procedure (including for the fudge factors, which resulted to give indeed the best performance), using OL data. In the last subsection, a brief performance study is conducted with an MMSE reconstructor (same defined regulator as in section 3.3.5, possible to implement with DARC LQG module).

7.3.4.2 Detailed analysis for a low-FPS Keck-like case

For this case, the chosen Keck data had a particularly strong tip and tilt energy with a low sampling frequency. The phase disturbances are resampled from their initial sampling frequency of 149 Hz to $F_\mathrm{s} = 200\,\mathrm{Hz}$ which is the GTCAO frequency sampling used for these tests.

The data length recorded during the closed-loop tests on the bench corresponds to a duration of half of the Keck disturbances (4000 iterations out of 8000). Using the same data for the training as for the test has not appeared to particularly favor performance during bench tests, as shown in the example given in figure 7.13. The integrator loop gains were tuned, leading to the maximal TT loop gain allowed value on the GUI, $g^{\mathrm{TT}} = 1.8$, and $g^{\mathrm{HO}} = 0.8$ for the other modes.

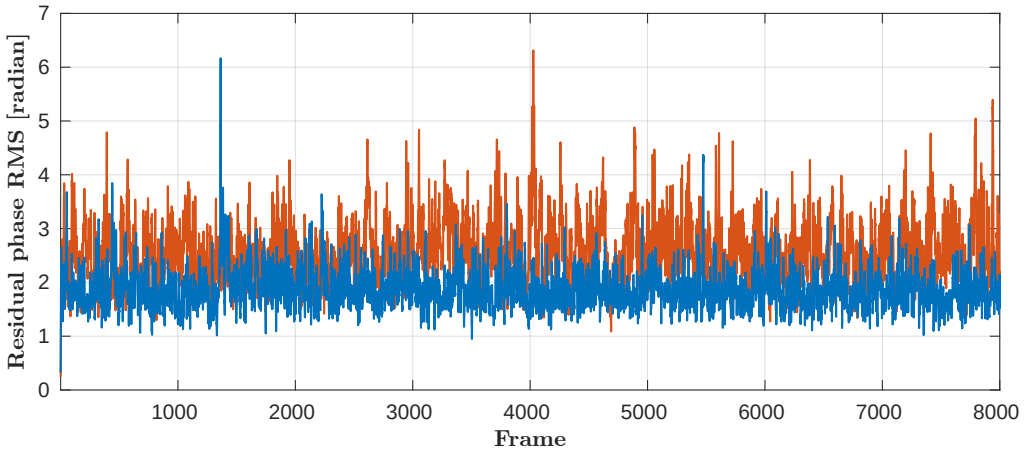

Figure 7.13: (bench with vibration) Residual phase variances of the first 9 Zernike modes with Keck-like LO disturbance. For the LQG, no particular 4000-iteration long interval appears better than the other half: the identification was performed using the first half of the data and this interval is not favored in terms of variance. Blue: LQG. Red: integrator.

Performance results on scientific images

In figure 7.14 are shown the long exposure scientific images ($\lambda_{\text{sci}} = 1600\,\text{nm}$). They have been upsampled by a factor two and recentered.

The left one is in open-loop. The center is the closed-loop with the integrator, and the right one with the LQG controller. The maximum intensity of the latter is 30% higher than the integrator one, increasing the Strehl ratio from 38% to 49%. The PSF is sharpened with a FWHM decreased from 47 to 41 mas. Without any disturbance, the FWHM is of 33 mas.

Residual modal phase energy and spectral analysis

We analyze in this paragraph the advantages of the LQG regulator in terms of spatial (modal) variances and frequency PSDs. We see in figure 7.15 that the advantage of the LQG comes mainly from the vibration mitigation. The tip and tilt are the main concerned modes, with a total of more than $2\,\text{rad}^2$ energy difference seen on their two cumulative variance graphs. The defocus (mode 3) is also significant, with $0.6\,\text{rad}^2$ difference. On this Keck sample, the astigmatism is not preponderant. It mainly has a reasonable vibration peak at 29 Hz, that is to say in the overshoot of the rejection, but leads to a penalty of some $0.1\,\text{rad}^2$, that is to say around 0.5 point of SR at λ_{sci}. In some other Keck samples, a strong vibration peak of astigmatism (around $1.5\,\text{rad}^2$) exists at very high frequency, around 315 Hz. It is investigated in subsection 7.3.4.3.

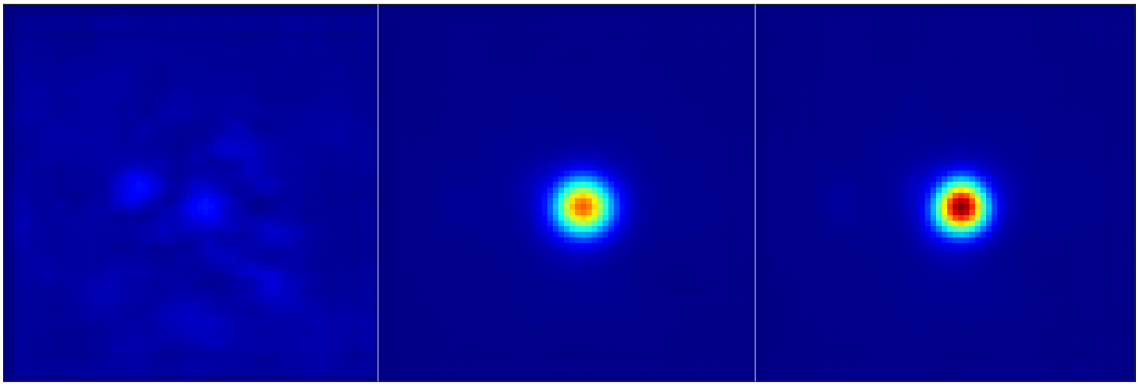

Figure 7.14: (bench with vibration, 2022/11/08) Scientific images with Keck-like LO (9 modes) disturbance. Left: open-loop. Middle: integrator (SR 38%). Right: LQG controller (SR 49%).

Also in figure 7.15 we can see that the higher Zernike orders (number 23 is shown here) are as well corrected by both the LQG controller and the integrator with a very small advantage to the integrator. This is visible in figure 7.16, where the modal residual phase variances are displayed. The two cumulative variances curves (bottom) have a similar increase past mode number 7. The two variances curves

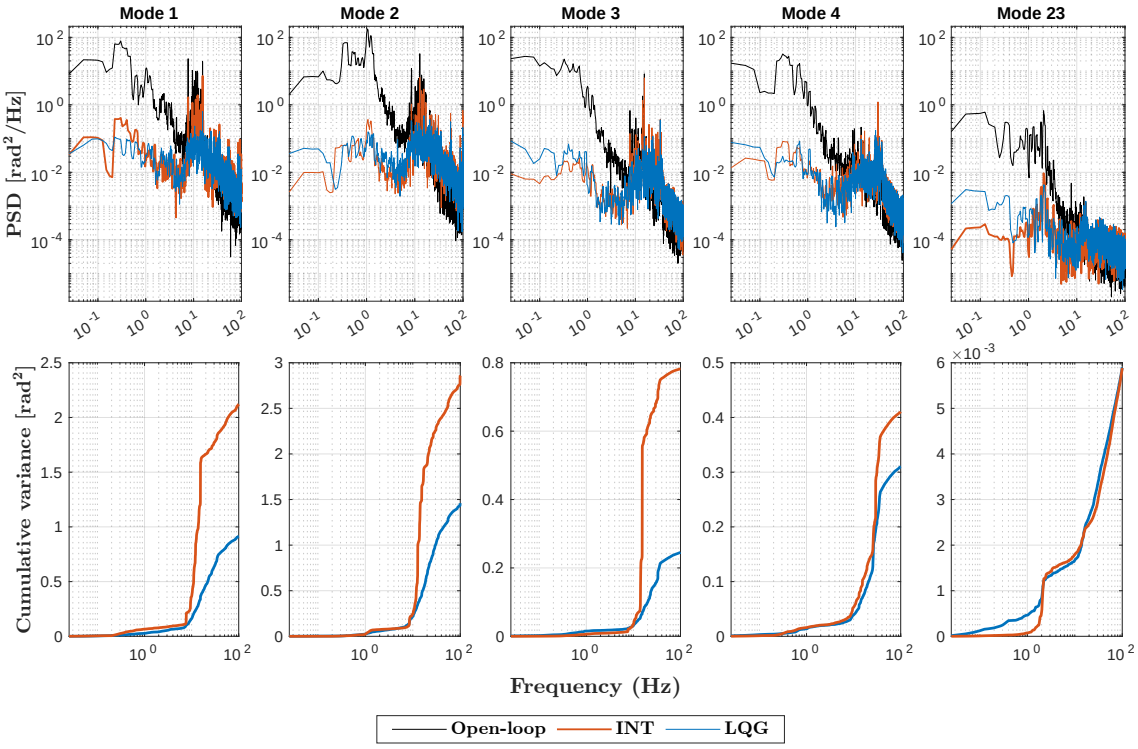

Figure 7.15: (bench with vibration) Residual phases with Keck-like LO (9 modes) disturbance. Up: modal PSDs. Down: cumulative energy. Left to right: Zernike modes 1, 2, 3, 4 and 23.

(top) show however a slightly better correction of high orders by the integrator. In terms of commands, this leads to a stronger solicitation of the DM as shown in figure 7.17. This is another positive side effect of the LQG controller, avoiding to grant to much stroke to some Zernike modes that are yet not preponderant in terms of performance. Thus, in situations with strong turbulence, the LQG would lead to a significant increase of the SR gap thanks to a clipping limitation and with a better DM behavior.

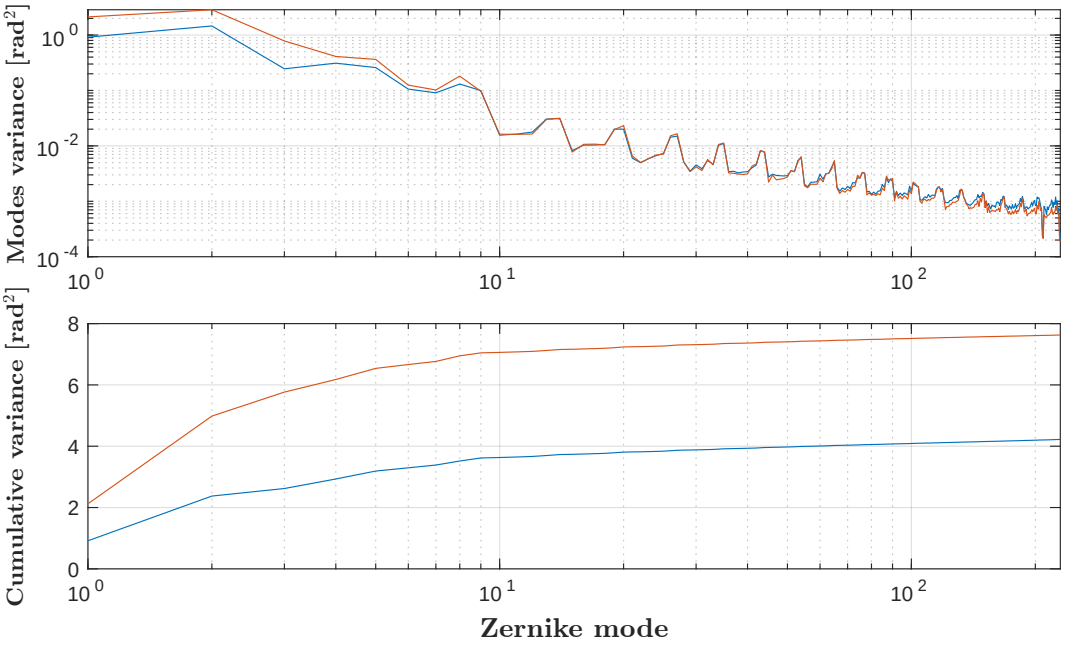

Figure 7.16: (bench with vibration) Modal residual phase variance with Keck-like LO (9 modes) disturbance. Blue: LQG. Red: integrator.

Disturbance modeling and rejection transfer functions

In figure 7.18, we see that the N4SID-identified models (four first modes) are encompassing many of the numerous non-turbulent energy peaks. The AR2 model on the very right (mode 23) is covering both the entire plateau of turbulence energy and the high frequency blob of energy (around 10 Hz). This includes the Shack-Hartmann aliasing that visibly increases slighter the energy past 5 Hz. This broad coverage comes from the high modal speed and allows good performance (section 6.2.3).
Note: We might believe here that the modeling could be improved by using the N4SID identification with order 2 models. But doing so did not improve the performance on the bench, with even a negative impact of the DM behaviour (creation of some commands peaks on some actuators).

In figure 7.19 are shown the rejection transfer functions, both model-based (dark bold plots) and bench data based (light slim plots). When comparing those RTFs

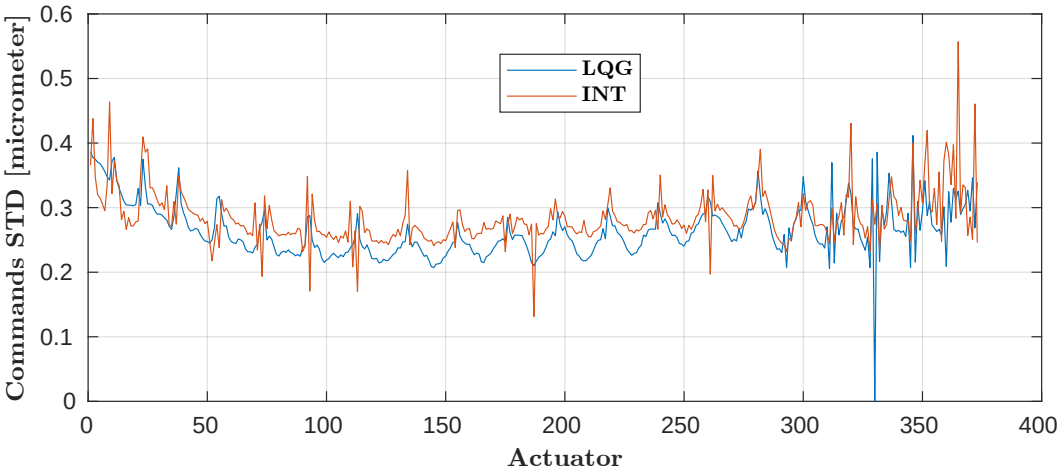

Figure 7.17: (bench with vibration) Standard deviation of each actuator command series. Blue: LQG. Red: integrator.

with the previous disturbance models of figure 7.18, we notice that what has been modeled is indeed well rejected.

We can notice that the low-frequency plateau in the tip (mode 1) disturbance rejection of the integrator (bottom red curves) is higher than for the tilt (mode 2) or defocus (mode 3) disturbance rejection by a factor greater than 3. This is due to the broken actuator located on the right of the middle horizontal axis of the pupil. Indeed, the DM cannot easily shape a proper tip mode, needing a strong stroke of actuators on the left and right edges of the DM where the dead actuator is located (see section 5.4.5. This is provoking a static error, therefore visible in the low frequencies. On the contrary, the tilt or defocus modes are almost not affected, since the dead actuator is not much degrading theses modes.

Stability margins

In figure 7.20 are displayed the stability margins of the LQG and the integrator.

For the tip and tilt modes, the integrator has a phase margin of 28 degrees and the LQG 38 degrees. Despite the large rejection improvement, the LQG has thus 10 degrees more phase margin than the integrator. In terms of temporal delay, it corresponds to increasing from 0.33 to 0.65 frame margin. The integrator is already below the usual limit of 30 degrees, meaning that increasing more the tip/tilt gain g^{TT} would not be done in on-sky tests (even if the GUI allowed it). The gain margins are of 7 dB for the integrator and 10 dB for the LQG.

For the defocus and astigmatism modes, the integrator with its lower g^{HO} loop gain sees its margins jumping to 11 dB and 55°. For LQG, the margins go to 41° and 11 dB: only slightly larger than for tip and tilt. This similarity is due to the fact that defocus and astigmatism are also among the Zernike modes managed with identified LO models.

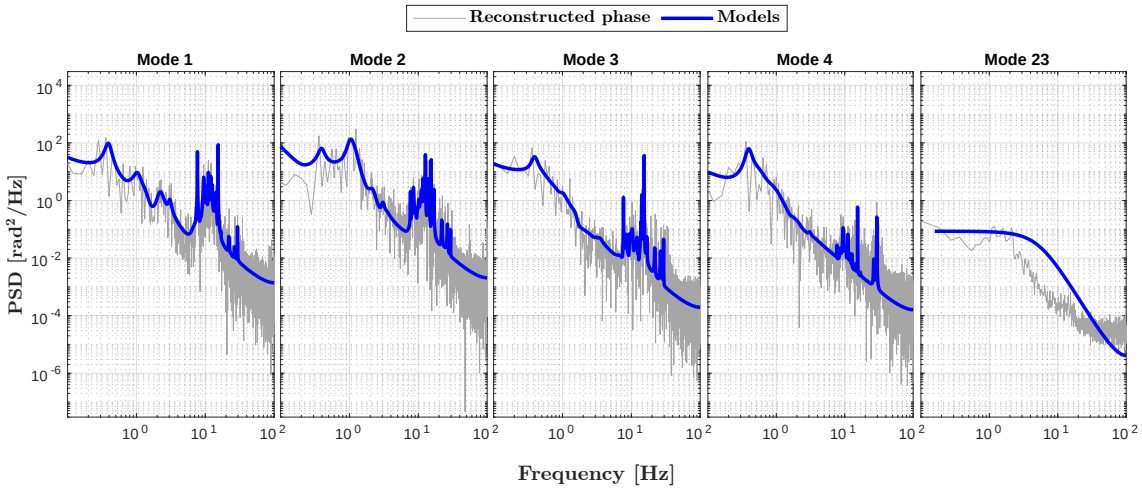

Figure 7.18: (bench with vibration) PSDs of open-loop phase disturbances and corresponding LQG temporal models. Left to right: Zernike modes 1, 2, 3, 4 (N4SID-identified models) and 23 (AR2 model).

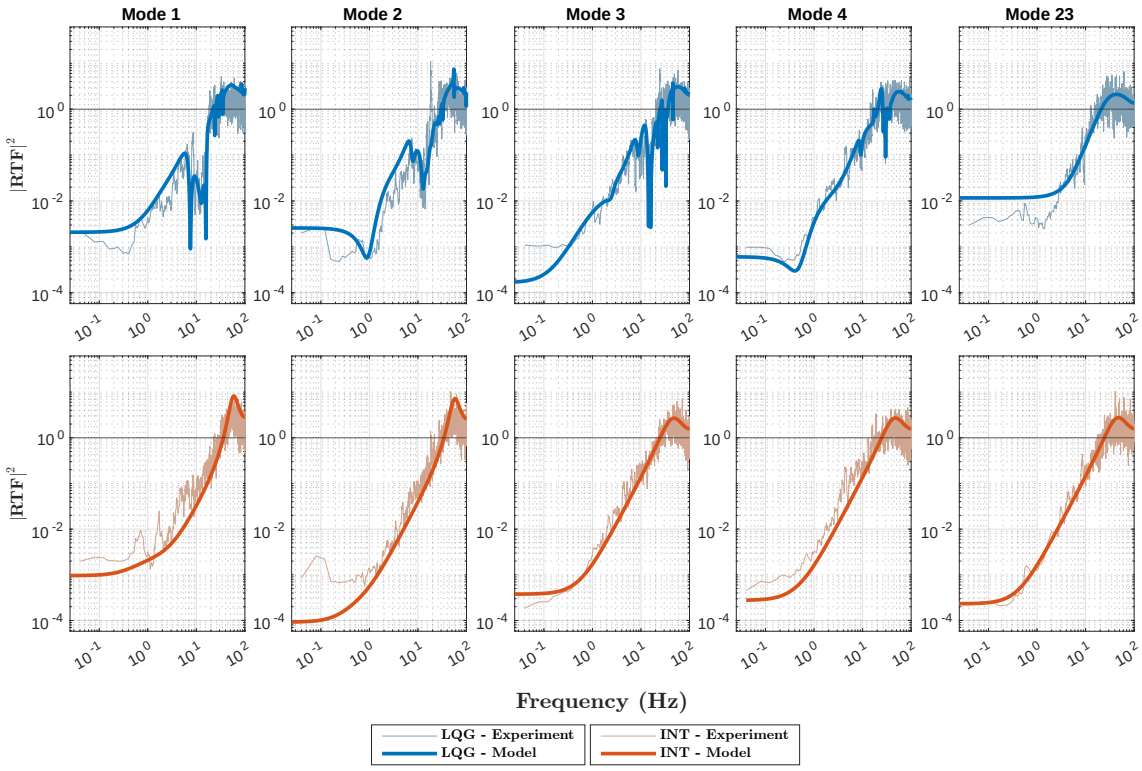

Figure 7.19: (bench with vibration) Modal RTFs with Keck-like LO (9 modes) disturbance. Up blue: LQG. Down red: integrator. Left to right: Zernike modes 1, 2, 3, 4 and 23.

For the high order modes (number 23 here), the stability margins get similar for both controllers. The LQG and its AR2 model gets 12 dB and 52°, the integrator 11 dB and 53°.

Concerning modeling error impact on the LQG, the parameter of interest is the loop delay δ^{ctrl}. Looking at tip/tilt modes, with a pessimistic error of 0.25 ms, the phase margin loses 4° and the gain margins 1 dB. To increase the margins, a possibility is to increase the fudge factor. An augmentation from $\alpha_{\mathrm{FF}} = 6$ to 30 improves the margins by 5° and 2 dB, leading to a modest SR decrease of 1 point on the bench. Although such an error on the loop delay is unlikely to occur, it shows that it could be considered to impose minimum stability margins by adjusting the fudge factor, with a potentially limited impact on performance.

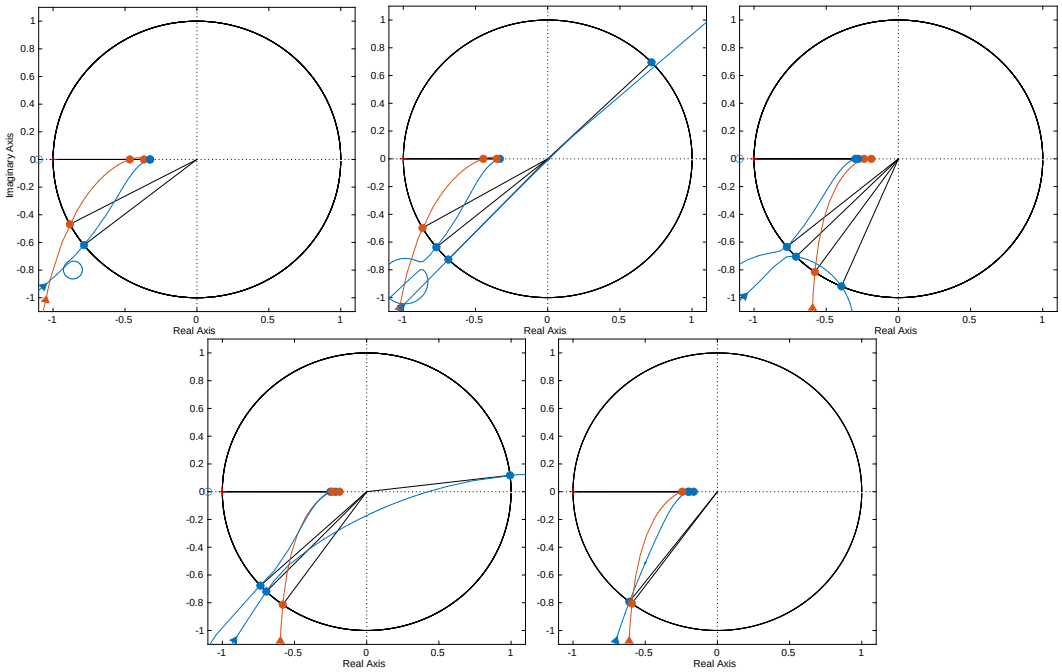

Figure 7.20: (bench with vibration) Regulators modal Nyquist diagrams with Keck-like LO (9 modes) disturbance. Blue: LQG. Red: integrator. Reading direction: Zernike modes 1, 2, 3, 4 and 23.

7.3.4.3 Analysis for a high-frequency vibration Keck-like case

Description of the case

Numerous on-sky data sets among the ones of September 2020, with sampling frequencies of $F_{\mathrm{s}} \simeq 1\,\mathrm{kHz}$, appear to show a vibration peak at a frequency of $f_{\mathrm{vib}} = 315\,\mathrm{Hz}$. It is notably visible in the PSDs of the astigmatism and defocus modes. They can reach an energy of some $2\,\mathrm{rad}^2$. This level of energy at this frequency ($\sim F_{\mathrm{s}}/3$) corresponds to the study made in chapter 4. For the bench tests, we kept ourselves

from implementing this critical situation and took a case with a similar PSD shape but with nicer energy peaks of around $0.1\,\mathrm{rad}^2$. The RTC LQG code version which is used for this test is the one synchronizing the models with the DM, as we took $\delta^{\mathrm{ctrl}} = \delta$, a value which should give good performance results when vibrations are injected by the DM, as shown in chapter 4.

The LQG in this modest-vibration case allowed to increase the Strehl ratio from 60% (integrator) to 63%. One of the three points comes from the high-frequency vibrations correction.

Results in vibration rejection

We see in figure 7.21 that similarly to the bench test of previous section 7.3.4.2 and the analysis on high-order modes, mode 23 is slightly better corrected by the integrator. We can appreciate here the neutralization by the LQG regulator of the vibration peaks at $f_{\mathrm{vib}} = 315\,\mathrm{Hz}$, visible in modes 3 and 5. The integrator could not prevent from amplifying those peaks despite the loop gains tuning.

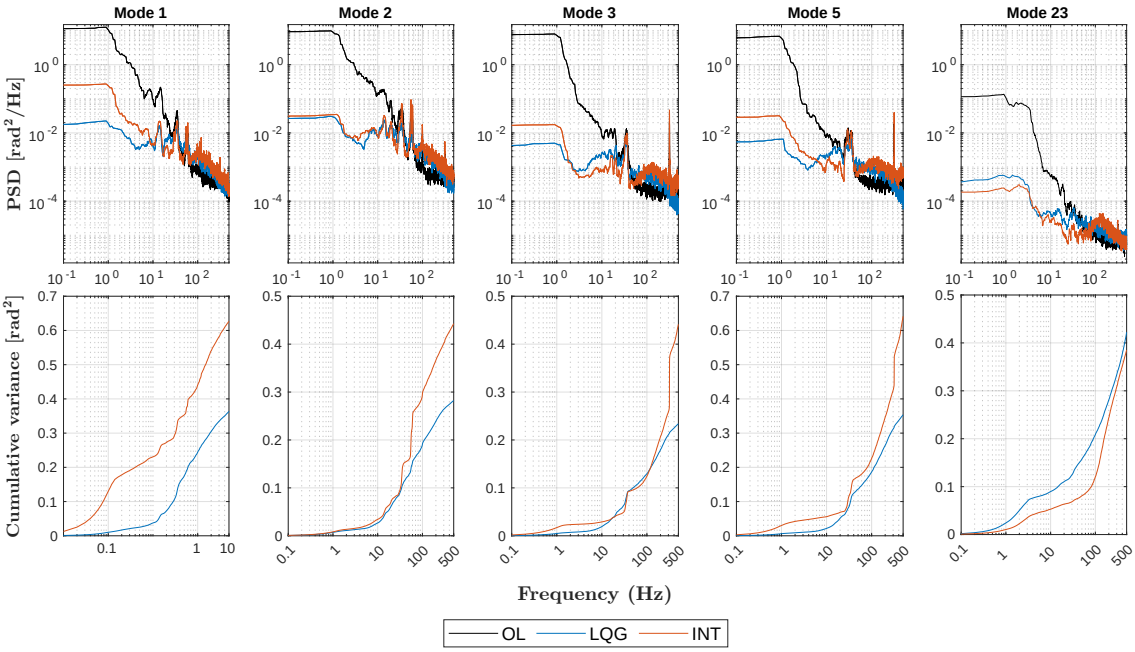

Figure 7.21: (bench with vibration) Residual phases with Keck-like high-frequency vibrations. Up: modal PSDs. Down: cumulative energy. Left to right: Zernike modes 1, 2, 3, 5 and 23.

The RTFs shown in figure 7.22 illustrate very well the vibration peak rejections for modes 3 and 5, validating the efficiency of the modeling (the curves are dashed to let the experimental RTFs visible behind). The difficulty of tip compensation due to the dead actuator is here also very well visible (mode 1), with a much higher low-frequency plateau than for modes 2 and 3.

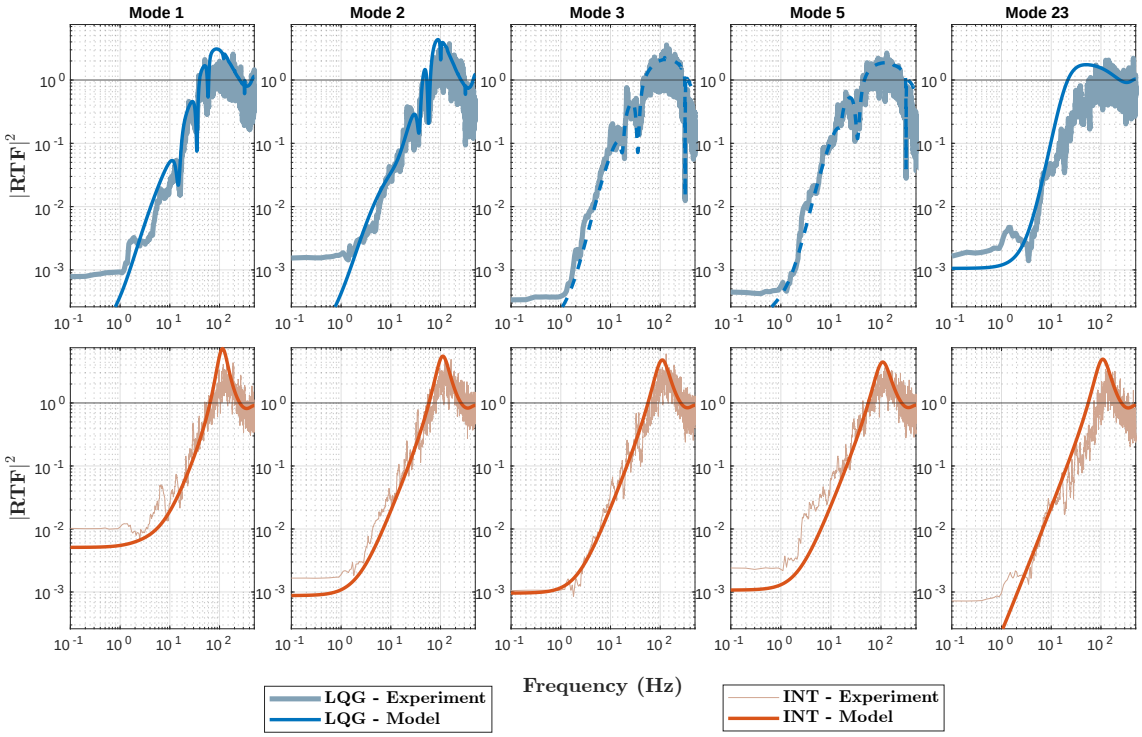

Figure 7.22: (bench with vibration) Modal RTF with high-frequency vibrations Keck-like case. Up and blue (dashed or continuous line): LQG. Down and red: integrator. Left to right: Zernike modes 1, 2, 3, 5 and 23.

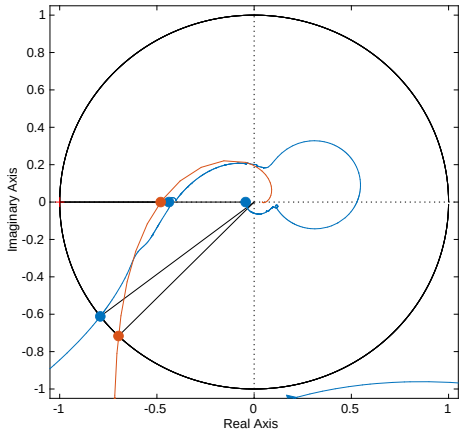

Figure 7.23: (bench with vibration) Regulators modal Nyquist diagrams with high-frequency vibrations Keck-like case. Blue: LQG. Red: integrator. Zernike defocus mode.

The Nyquist diagram of the defocus mode (mode 3) shown in figure 7.23 also displays the stability margins of the integrator and the LQG. The integrator and the LQG have respective gain margins of 6 and 7 dB, at respective frequencies 133 Hz and 122 Hz. The respective phase margins are of 46 and 38 degrees, at respective frequencies 67 Hz and 58 Hz. It leads to time delay margins of respectively 1.9 and 1.8 frames. The stability margins are similar to those obtained in the other Keck-like test (cf. figure 7.20), the 315-Hz vibration compensation having thus no stability issue. The account in the modeling of high frequency peaks should thus not compromise regulator stability.

Conclusion

This case of high-frequency vibration definitely highlights the ability of LQG controllers to reject vibration in a very wide frequency range. This also confirms our previous hypothesis of considering that the DM response is instantaneous. Indeed, the vibrations at 315 Hz being completely suppressed by the LQG, we can say that our temporal model is valid. The total loop delay for these tests is 2.6 frames ($\Delta = 1.6$ ms at 1 kHz), which corresponds to a fractional delay of $\delta = 0.6$ frames: a critical case as seen in chapter 4. In the real life (continuous vibration disturbance instead of DM-synchronized one), the developments of chapter 4 would need to be implemented so as to take optimally into account the fractional delay.

Globally, these results are also very promising news regarding the GTCAO system, showing that its components and RTC allow for extreme vibration management.

7.3.4.4 Performance with an MMSE reconstructor

Description of the case

An MMSE reconstructor (principle described in section 3.3.5) for GTCAO was built and tested on the bench. The same system modeling is used for the MMSE as for the LQG (phase-to-command matrix $N^\dagger$, measurement matrix D, measurement noise covariance matrix Σ_w, delay Δ), the same number of Zernike modes (740), and the same atmosphere priors necessary for R_{MAP} computation (r_0, L_0). A fudge factor was hand-tuned separately to optimize the SR of the MMSE reconstructor (the α_{MAP} of section 6.2.2 was fine).

Concerning the tests conditions, the guide star magnitude is of 12.5, with a sampling frequency of $F_{\text{s}} = 150$ Hz. The PS2 is used to introduce challenging atmospheric disturbance, to which is added (or not) the same vibration spectra as in section 7.3.4.2.

Results on the bench

In figure 7.24 are shown the rejection transfer functions of the MMSE, computed either from theoretical models or from the experimental residual PSDs of the recon-

structed modes. Both match, as seen previously with the integrator and the LQG controllers (e.g figure 7.22). We can see that similarly to the integrator, the absence of temporal modeling constrains the delay-related overshoot to be fully localized on high frequencies.

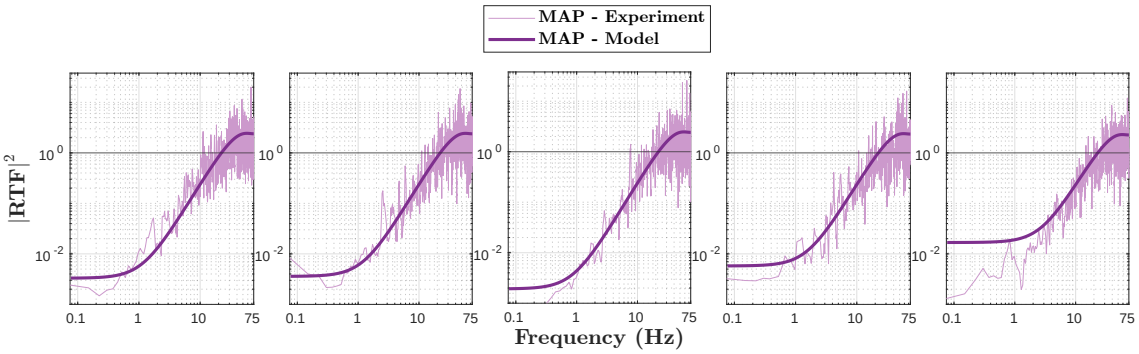

Figure 7.24: (bench and model) Modal RTF of the MMSE reconstructor. Left to right: Zernike modes 1, 2, 3, 4 and 23.

An advantage of the MMSE is the modal reconstruction, giving a strong reduction of the DM commands STD, with an evener shape, as presented in figure 7.25.

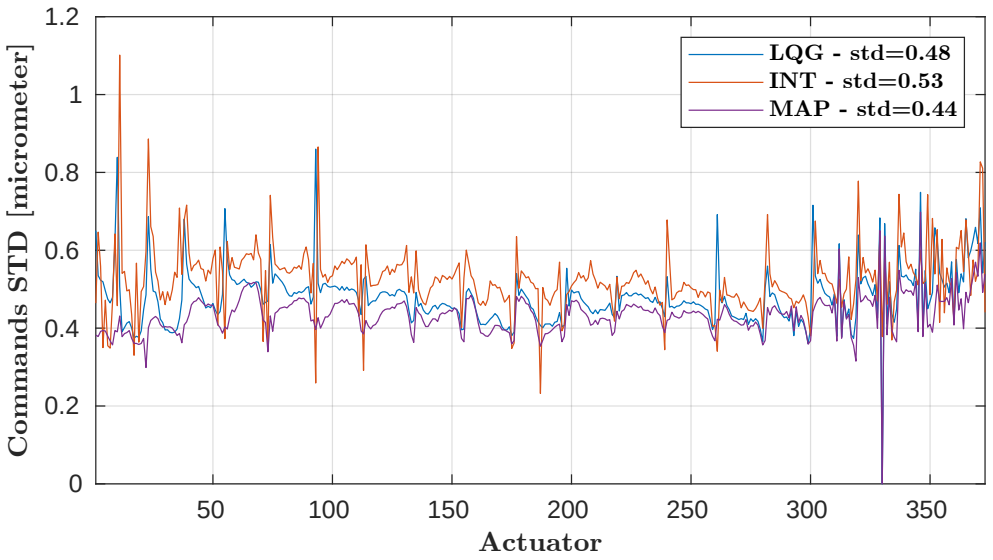

Figure 7.25: (bench) Commands STD for the case without vibration.

The results in terms of SR are shown in table 7.1. Thanks to a better noise rejection, the MMSE allows an improvement (around +15%) of the initial integrator SR. The extra performance improvement then allowed by the LQG (temporal modeling) is still of +20% (4 points, no-vibration case) to +50% (5 points, vibration case).

Regulator	Integrator	MMSE	LQG
SR (fwhm) - w/o vibration	15 (47)	18 (44)	22 (42)
SR (fwhm) - w/ vibration	8 (75)	9 (71)	14 (58)

Table 7.1: (bench) Strehl ratio (%) and FWHM (mas) with and without vibration for the three standard regulators.

7.4 Performance results in replay with W. M. Keck telescope on-sky data

The purpose of this section is to present the results obtained by applying our work in replay mode using Keck telescope AO system on-sky data from 2013 and 2020. As mentioned at the beginning of section 7.3.4, we are grateful to the Keck Observatory staff and in particular to Peter Wizinowich and Sam Ragland for making it possible to use these data. We also would like to thank Olivier Beltramo-Martin who has made available the three initial ready-to-use datasets from 2013.

After a preliminary study on the three initial datasets in section 7.4.1, we have extended the analysis to two more data sets of September 2020 in section 7.4.2.

7.4.1 Replay procedure and preliminary results on 3 datasets

We describe briefly in sections 7.4.1.1 to 7.4.1.3 the procedures, tests and analysis done in replay mode with three data sets of nights of August 2013 (all being full NGS cases):

- Data set 1, $r_0 = 23\,\text{cm}$, 1054 FPS
- Data set 2, $r_0 = 17\,\text{cm}$, 1054 FPS
- Data set 3, $r_0 = 25\,\text{cm}$, 149 FPS

The replay procedure is described in section 7.4.1.1.

The two same regulators have been tested. One is an LQG regulator designed in the same way than the one designed for GTCAO, see section 7.4.1.2 readily adapted to the Keck AO system parameters. The second is a leaky integrator similar to the one used for Keck AO.

First performance results and behavior studies are in section 7.4.1.3.

7.4.1.1 Replay mode and information used to perform the tests

We use pseudo-open-loop (POL) data to replay the closed-loop AO system with various regulators. To reconstruct the POL data, we use the loop delays (DM and TTM may have different delays but run at the same loop frequency), in order to perform a

correct compensation. The delay values for DM and TTM loops as described in (Van Dam, Le Mignant, and B. A. Macintosh, 2004) are:

$$\Delta_{\mathrm{DM}}^{\mathrm{loop}} = 2.1\,\mathrm{ms}\,,\ \Delta_{\mathrm{TTM}}^{\mathrm{loop}} = 1.65\,\mathrm{ms}\,, \tag{7.13}$$

WFS exposure time excluded. Then, if y are the slopes contained in the slopes file, G_{cent} is the centroids gain, u^{DM} the DM commands, and u^{TTM} the TT commands, the POL slopes are computed using the Keck interaction matrix M_{int} as:

$$\begin{aligned} y_k^{\mathrm{POL}} &= y_k/G_{\mathrm{cent}} \\ &- M_{\mathrm{int}} \left(\delta_{\mathrm{DM}}^{\mathrm{loop}} u_{k-2}^{\mathrm{DM}} + (1-\delta_{\mathrm{DM}}^{\mathrm{loop}}) u_{k-1}^{\mathrm{DM}}\right) \\ &- \left(\delta_{\mathrm{TTM}}^{\mathrm{loop}} u_{k-2}^{\mathrm{TTM}} + (1-\delta_{\mathrm{TTM}}^{\mathrm{loop}}) u_{k-1}^{\mathrm{TTM}}\right)\,, \end{aligned} \tag{7.14}$$

with here the delays expressed in frames and in a case where $\Delta_{\mathrm{DM}}^{\mathrm{loop}} = \Delta_{\mathrm{DM}}^{\mathrm{loop}} - \lfloor \Delta_{\mathrm{DM}}^{\mathrm{loop}} \rfloor = \delta_{\mathrm{DM}}^{\mathrm{loop}} \leq 1$. In a case where $\Delta_{\mathrm{DM}}^{\mathrm{loop}} > 1$, the commands indexes must be adjusted (one additional frame delay).

For simplicity reasons, we used in our replays the same unique value of 1.8 ms for both the DM and the TTM delays. We could thus use our pre-existing replay code without modification (one unique delay value). As shown in the following sections, it is close enough to the real Keck AO system delay values to mimic the on-sky behavior.

To calculate the command matrix M_{com}, we have done a pseudo-inversion of the interaction matrix M_{int} and have also optimized the number of filtered mode, so as to minimize the distance between on-sky and in-replay residual slopes variances. It leads us to filter 4 modes out of 349.

Figure 7.26 shows the POL data obtained after DM and TTM commands compensation with the loop delays defined above.

Figure 7.27 shows the in-replay results using a leaky integrator with leak gain $g^{\mathrm{leak}} = 0.999$ and compare them with on-sky data: on the left the on-sky and in-replay residual slopes variances for all subapertures, and on the right the on-sky and in-replay residual angle of arrival. The residuals in replay have slightly higher variances on the subapertures corresponding to pupil edges, but otherwise they are very close.

Furthermore, figure 7.28 compares on-sky and in-replay tilt commands for the leaky integrator. The discrepancy is small.

In addition, it is visible in figure 7.29 that the replay reproduces the modal distribution of the residual phase (left graphs), and also rather well the temporal frequency behaviors we get from residual phase reconstruction (MMSE estimation, the first 4 Zernike modes PSDs are shown in figure 7.29).

In conclusion, the procedure that allows to build POL data from the on-sky data sets can be validated, and so is the replay procedure. We are now in the position to test the two regulators of interest using POL slopes in replay.

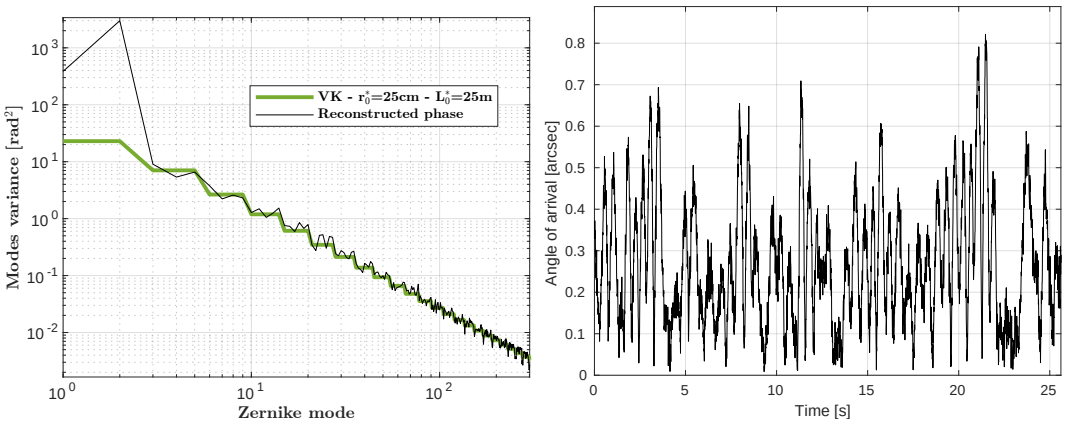

Figure 7.26: POL data obtained by compensating DM and TTM commands. Data set 3. Left: POL phase Zernike modes variance compared with Von Kármán statistics. Right: angle of arrival norm evolution.

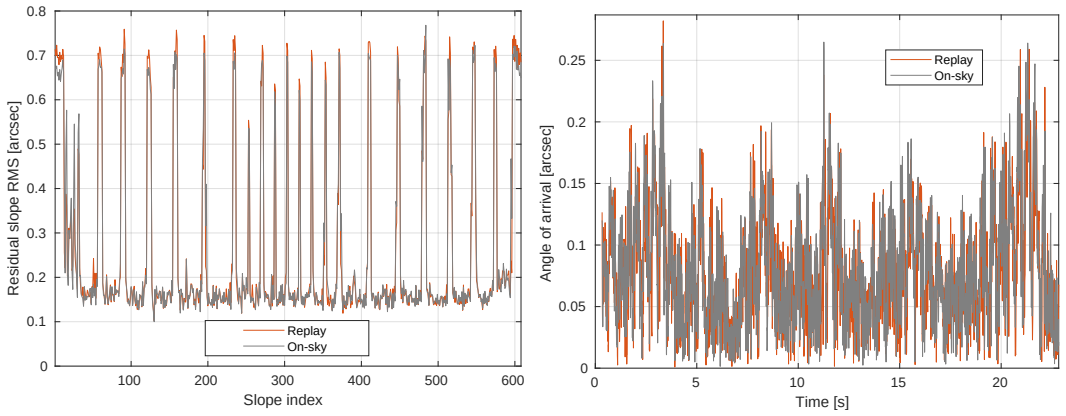

Figure 7.27: Left: on-sky and in-replay residual slopes variances for all sub-apertures; Right: on-sky and in-replay residual angle of arrival with leaky integrator. Data set 3. Integrator loop gains in the replay: $g^{\mathrm{TT}} = 0.3$, $g^{\mathrm{HO}} = 0.5$, $\alpha_{\mathrm{leak}} = 0.999$.

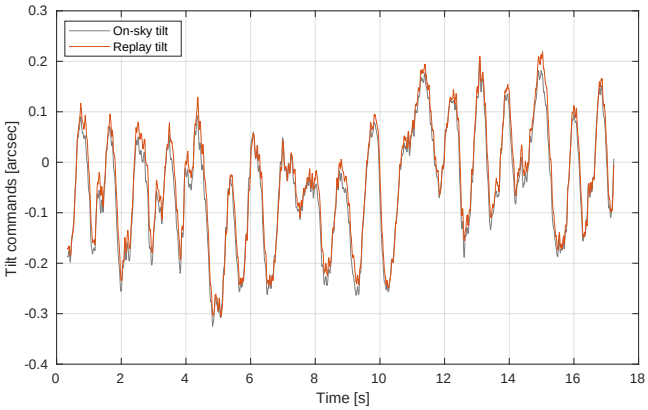

Figure 7.28: On-sky and in-replay tilt commands. Data set 3. Integrator loop gains in the replay: g^{TT}, $g^{\mathrm{HO}} = 0.5$, $\alpha_{\mathrm{leak}} = 0.999$.

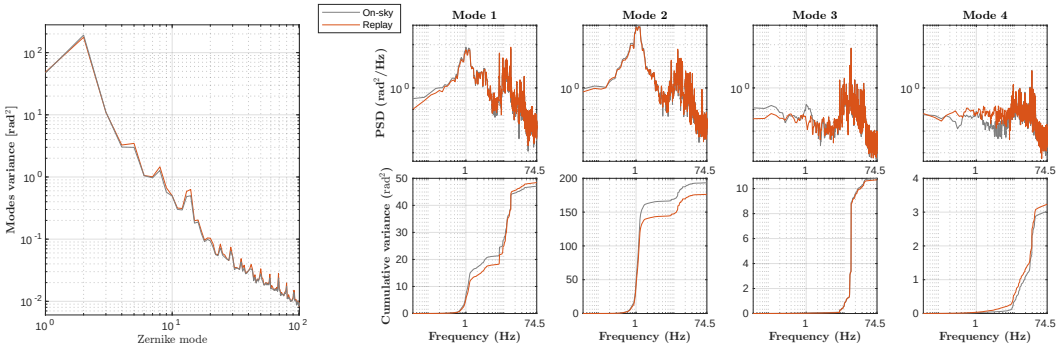

Figure 7.29: Left: on-sky and in-replay residual modal phase variances; Right: PSDs of on-sky and in-replay residual modal phase (tip, tilt, defocus, astigmatism, for a wavelength of 500 nm). Data set 3. Integrator loop gains in the replay: $g^{\mathrm{TT}} = 0.3$, $g^{\mathrm{HO}} = 0.5$, $\alpha_{\mathrm{leak}} = 0.999$. Centroids gain: 0.53.

7.4.1.2 Designing the LQG regulator

The definition of the LQG regulator is the same as done for GTCAO, with matrices obtained following the procedure described in chapter 6. The first half of the POL dataset is used to identify the disturbance models, the remaining half being used for performance evaluation in replay.

The commands u^{TTM} are supposed to correspond directly to the phase tip and tilt $\phi^{\hat{\mathrm{TT}}}$ predicted by the Kalman filter. To calculate the commands u^{DM}, the remaining predicted phase $\hat{\phi} - \phi^{\hat{\mathrm{TT}}}$ is projected onto the DM space using here the WFS measurement matrix model D (phase-to-slopes), left-multiplied by the command matrix M_{com} (slopes-to-commands):

$$u^{\mathrm{DM}} = M_{\mathrm{com}} D \hat{\phi} \triangleq P_u^{M_{\mathrm{com}}} \hat{\phi}\,. \tag{7.15}$$

This choice of projector rather than P_u^N aimed at simplifying the modeling of Keck AO system, which has anyway a Fried geometry as shown in figure 7.30 and no broken actuator. The influence functions matrix N was still computed as in section 5.4.3 (with a tuning of TT modes due to the existence here of a TT mirror), for the calculation of theoretical RTFs.

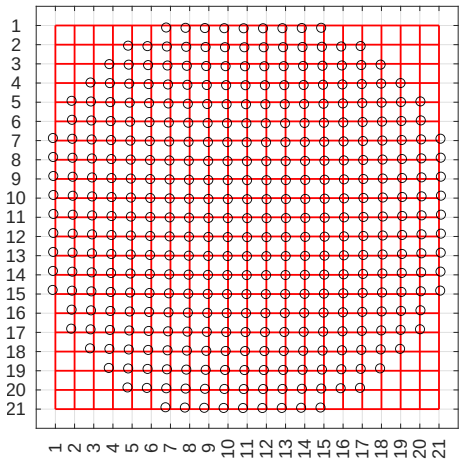

Figure 7.30: 2D representation of the Keck DM actuators estimated positions (black circles) relatively to the microlenses grid (red). Rotation angle estimated to -0.1061 degree, coupling factor of $C_{\mathrm{DM}} = 0.108$.

7.4.1.3 Performance results and analysis on the 3 datasets

Table 7.2 gathers the results obtained with the leaky integrator and the LQG regulator. The same leak gain $\alpha_{\mathrm{leak}} = 0.999$ has been used for all the data sets.

The results are given as the residual wavefront error RMS, computed as the square root of the sum of the first 300 Zernike modes average power.Residual wavefronts

have been estimated from residual slopes using the MMSE estimator (equation (7.1)). The data of Table 1 are the only ones that exhibit a significant discrepancy between on-sky and in-replay performance with the integrator. This was not the case for the data of Section 7.4.2.

Data set	1	2	3
Integrator (on-sky)	189 (0.5 & 0.3)	206 (0.5 & 0.3)	677 (0.5 & 0.3)
Integrator (best loop gain values in replay)	221 (0.5 & 0.55)	230 (0.55 & 0.7)	352 (0.9 & 1.2)
LQG	188	199	247

Table 7.2: Replay results. Residual wavefront error RMS in nanometers (300 Zernike modes). For the two leaky integrator cases, DM and TTM gains values are given under the form (DM loop gain & TTM loop gain).

To understand the behavior of the regulators, figures 7.31 and 7.32 report various results related to closed-loop behaviors. The PSDs for different Zernike modes, for the leaky integrator and the LQG, as well as the PSDs of the POL data, are shown in figure 7.31.

Thanks to the data-driven part of the LQG controller based on subspace identification for the LO modes, the controller automatically balances its RTF for each mode as seen on the bench in section 7.3.4: strong rejection when needed, relaxation when possible. In figure 7.31, when comparing the PSDs of the integrator and the LQG, we see that the respective cumulative PSD curves exhibit several behaviors of the LQG regulator: for mode 2 (tilt), it dampens the large 1.25-Hz vibration peak; for mode 3 (defocus), the 15-Hz vibration peak is strongly rejected, and for mode 4 (astigmatism) the correction is distributed throughout the large 10-to-40-Hz range of energy. This behavior can be easily appreciated thanks to the empirical and theoretical RTFs shown in figure 7.32. Those RTFs are obtained the same way as explained in section 7.1.2.

These results show similarities with the tests we have conducted on the GTCAO bench at IAC:

- When it is possible to close the loop with a bright guide star, at $F_\mathrm{s} = 1054\,\mathrm{Hz}$, the integrator can deliver good performance despite the presence of vibrations in the low order Zernike modes spectra. LQG may improve by some 5 to 10 SR points when compared with replayed integrator (based on the Mahajan approximation $\exp^{-\sigma^2}$ applied to the results of table 7.2). Similarly to what we have on GTCAO bench, the stronger the atmospheric disturbance (about $r_0 = 17\,\mathrm{cm}$ in set 2 while about $23\,\mathrm{cm}$ in set 1), the better the improvement in performance with LQG.

- When the loop is closed with lower frame-per-second rate, as is the case for the data set 3 ($F_\mathrm{s} = 149\,\mathrm{Hz}$), the integrator rejection is poor in the 10Hz-to-50Hz frequency range (populated with several vibrations) and the performance

drastically drops down. However, in spite of the low FPS which tends to lower performance for all controllers, the LQG built from our data-based models provides much better wavefront correction than the integrator (the corresponding increase in terms of SR should be in the order of 20 points).

After these preliminary good results, we have processed in next section numerous recent data of 2020 to extend the performance analysis.

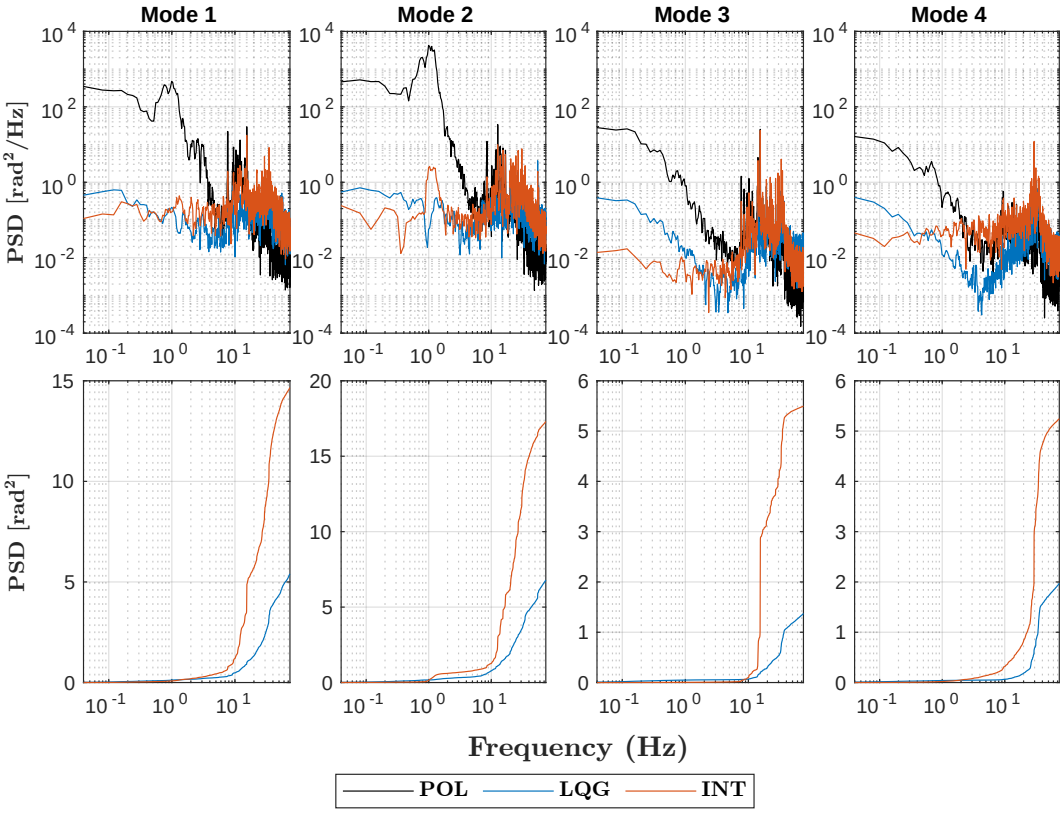

Figure 7.31: Replay results, data set 3. Top row: power spectral densities. Bottom row: cumulative power spectral densities. From left to right: tip, tilt, defocus, astigmatism. Black: pseudo-open-loop. Blue: closed-loop LQG. Red: closed-loop integrator.

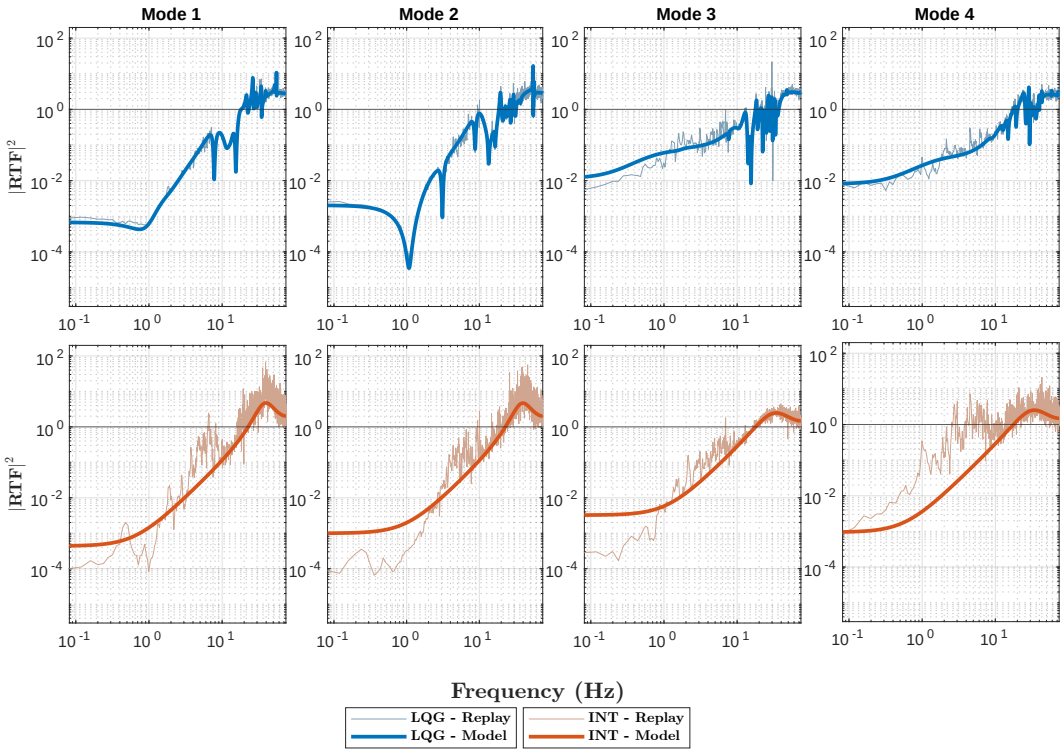

Figure 7.32: Replay results, data set 3. Rejection transfer functions (squared). From left to right: tip, tilt, defocus, astigmatism. Top row and blue: LQG. Bottom row and red: leaky integrator.

7.4.2 Performance results with datasets of September 2020

To identify and test the LQG regulators, we need enough seconds of data. When a data set is shorter than 4 seconds, the identification sometimes does not lead to good models. We thus retained all the data sets with duration greater than 4 seconds, and the same time-series were used for optimizing the integrator loop gains. In this way, the data sets recorded during the night of 9 September have not been used (their duration is less than 4 seconds).

When the data sets duration is greater than 4 seconds but less than 8 seconds, the same data are used for model identification and performance evaluation. We checked on a few sets that this did not lead to a significant overestimation of the LQG good performance.

The frequency sampling for these data is either $F_{\mathrm{s}} = 1054$ Hz or $F_{\mathrm{s}} = 438$ Hz. We are thus probably in cases of medium to high flux. Results in terms of wavefront error RMS in nm are displayed in figure 7.33 and show an impressive improvement with LQG. Wavefronts were estimated from residual slopes using MMSE reconstruction. Note the good agreement between on-sky and in-replay performance for the integrator.

Results in terms of slopes RMS in arcsec are displayed in figure 7.34. The slopes RMS are similar between integrator and LQG. However, the wavefront error RMS is much lower for LQG. We have pointed out the same standard behavior with GTCAO on-bench data in section 7.1. In another case with Keck-like vibrations that was not reported in that section (also a bench experiment with vibrations generated by the deformable mirror), the residual slopes RMS appeared to be 20% worse for LQG, while its SR on the science camera was of 25%, against the integrator one of 17%. And when looking at their respective MMSE-reconstructed residual phases, the LQG indeed achieved smaller residual wavefront error. Even better, the ratio between the two respective images SRs ($0.25/0.17 \approx 1.5$) was nearly the ratio between the two Mahajan-estimated SRs ($0.54/0.37 \approx 1.45$) based on residual phase reconstruction.

7.4.3 Keck replays conclusion

We can conclude that the LQG strategy designed in the framework of my PhD and tested on the GTCAO bench gives excellent results on these hundreds of data sets. More tests and analysis could be done with even more data sets to probe various observation conditions (high-flux/very-low-flux, high wind/low wind, more challenging atmospheres with lower r_0 values, etc.).

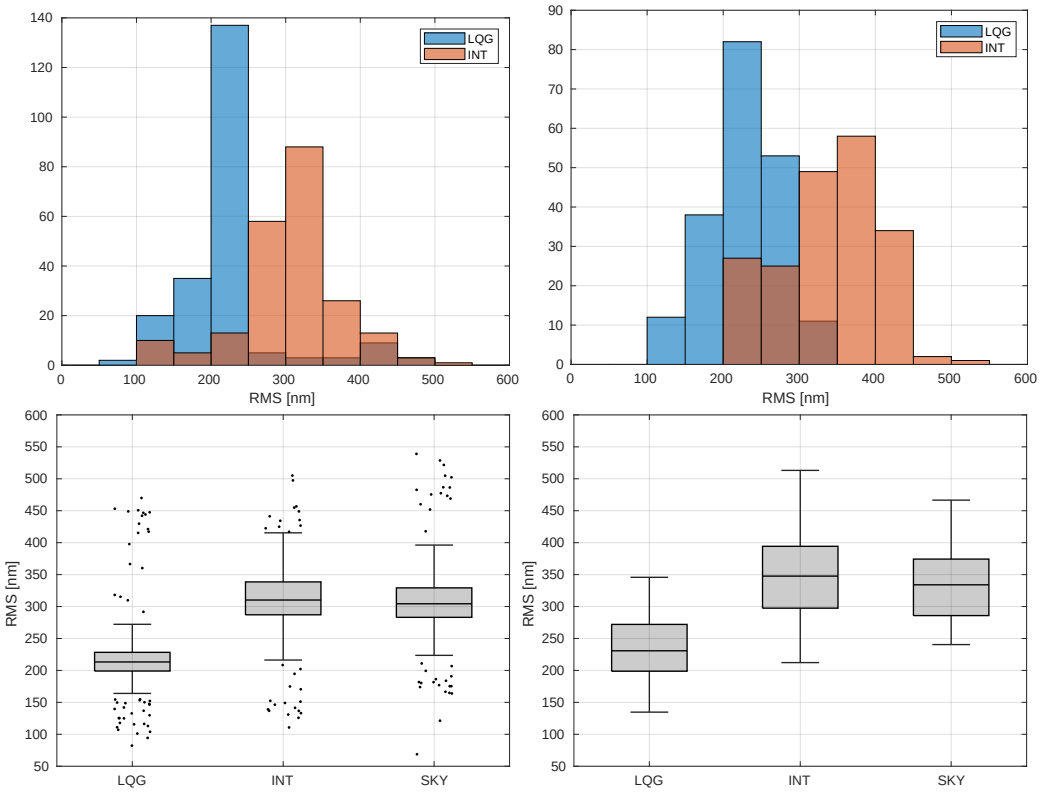

Figure 7.33: Performance comparison between integrator and LQG regulators in terms of wavefront error RMS in nm for the nights of 8 September (left) and 21 September (right).
Top: slopes RMS histograms.
Bottom: for replays with LQG and integrator (INT) and for on-sky integrator (SKY), box charts with median value, upper/lower quartiles, and whiskers extending until 1.5 times the interquartile range away from the top or bottom of the boxes. Results outside the range are displayed with dots.

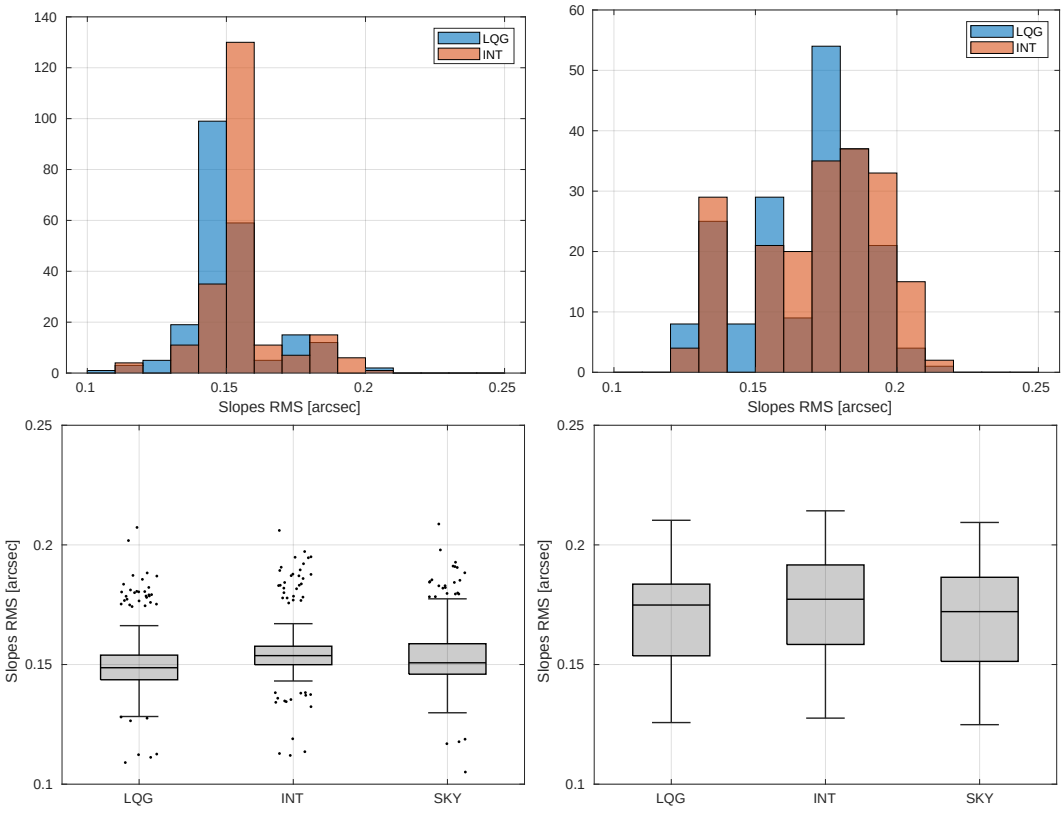

Figure 7.34: Performance comparison between integrator and LQG regulators in terms of slopes rms in arcsec for the nights of 8 September (left) and 21 September (right).
Top: slopes RMS histograms.
Bottom: for replays with LQG and integrator (INT) and for on-sky integrator (SKY), box charts with median value, upper/lower quartiles, and whiskers extending until 1.5 times the interquartile range away from the top or bottom of the boxes. Results outside the range are displayed with dots.

7.5 Conclusion

We started this chapter with a presentation in section 7.1 of some tools useful for performance analysis. We have in particular shown how to compute the theoretical open-loop transfer functions and RTFs using the state-space representation. The study on SR in section 7.2 led us to choose a method based on the PSF for our on-bench performance assessment.

The on-bench tests are conducted in section 7.3:

- For pure atmospheric turbulence, the gap between LQG and integrator performances is more important for stronger disturbances (low r_0). With strong turbulence, the SR is improved by the LQG from 5 to 10 points. The advantages in cases of favorable atmospheric turbulence appear for NGS magnitudes higher than 12, reaching 10 SR points for magnitude 14.

- In presence of windshake, the integrator is more affected than the LQG, making the gaps above increasing. The LQG succeeds to keep the same performance when it runs whether at 900 Hz (NGS magnitude 10) or 400 Hz (NGS magnitude 11).

- In a first case with Keck-like vibration disturbances, at magnitude 12.5, the LQG allowed a gain of 10 points against the integrator. In another Keck-like case, we could confirm that even very high frequency vibrations could be managed by the LQG on GTCAO.

  The modal analysis of those two cases showed that the integrator was better compensating the high order Zernike modes (mainly upper than order 70). If this is not simply due to the correction optimization of the LQG (concentrating the DM abilities on the most energetic modes), some model improvement should be envisioned.

In all those tests, the stability margins of the LQG are very comfortable. The data-based determination of the fudge factor happened to suit quite fine the balance between stability and performance, with some possibilities to improve it even more.

Numerous replays carried out using Keck on-sky data with the same calculations procedures have allowed to confirm the autotuning strategy developed in chapter 6. These good news come with the other part of our work: the simplicity to define an LQG controller on another AO system – on condition that the RTC disposes of the necessary control algorithm. The order of magnitude of the performance gain in average for these Keck datasets is estimated to about 100 nm RMS.

The maturity of the methodology would allow to go now for on-sky tests. These would be of great interest to confront the results with the ones obtained on bench and in replay, and confront the modeling to real and not really stationary disturbances over long enough intervals of time to test the controller stability.

Chapter 8
Conclusion and perspectives

8.1 Conclusion

The GTC and its 10.4-m segmented primary mirror has nowadays the biggest potential of resolution in the world. To exploit it, it will be soon equipped with a single-conjugated adaptive optics system: GTCAO. Its control baseline is the standard integral action controller (or integrator), which has been used as the default AO controller over the past three decades. It is particularly easy to implement while well adapted to atmospheric turbulence rejection.

However, it has been seen in the community of other 8-10m class telescopes that disturbances other than the atmosphere alone are present, and in particular vibration. These are induced by the wind blowing on the telescope's structure, or by components such as fans, coolers, etc. The temporal behaviour of these non-atmospheric disturbances generally exhibit higher frequencies than atmospheric turbulence so that they are poorly compensated (or even amplified) by the integrator due to the time delay affecting AO systems. This has led to consider optimal AO control, that is minimal variance LQG control design, which embeds an optimal prediction of the disturbances. As are many high-performance controllers, the LQG is based on a state-space representation of the AO system, to model both the dynamics of the disturbances and the AO loop. A Kalman filter predicts the short-upcoming time disturbances, this prediction being optimal in the sense of the minimum variance of the estimation error.

Despite the higher numerical complexity of this regulator, we show that it can be operated at more that 1 kHz on the GTCAO real-time computer DARC, including clipping management. The control design involves a disturbance modeling step which needs to deliver an accurate enough disturbances state-space model. It then allows a predictive control which is particularly efficient to suppress vibration, whatever their number and their spatio-temporal statistics. This proved effective in on-sky tests, with a significant gain in the quality of scientific images.

Thus, in seek of optimal control for the GTCAO system, we have proposed in this manuscript a complete methodology for calibrating and modeling the AO system with its disturbances. The validity of the approach has been confirmed by numerous on-bench laboratory tests. Our LQG disturbances modeling baseline is similar to the modeling defined in (Sinquin et al., 2020) and successfully tested on sky. Using a Zernike basis defined on a finite number of modes (740 modes in our GTCAO case), we identify a stochastic dynamical AR2 parametric model for all the modes. Conversely to what was done in (Sinquin et al., 2020), this AR2 modeling is adapted to the telemetry data. A specific treatment is made for 9 low order modes with an

additional stochastic dynamical model identified using subspace identification with the same implementation as in (Sinquin et al., 2020).

While the full LQG regulators tested on sky have been initially defined in Zernike basis with circular pupil shapes, the methodology we have developed accounts for a segmented pupil. The key difference comes from the measurement noise covariance matrix, for which we have proposed an estimation strategy adapted to a non-circular and rotating pupil such as M1 in GTC: a high value is attributed to the unilluminated wavefront sensor subapertures. The Kalman filter is thus predicting the phase in the circular Zernike basis by relying only on the in-pupil illuminated subapertures, which are updated at each model update, say every 2 minutes.

Another important part we developed is the estimation of temporal parameters. Our extensive study shows that the modeling requires special treatment in the presence of a fractional loop delay when high frequency disturbances need to be rejected. The problem of fractional loop delay in AO control has already been tackled in the literature, but we have highlighted behaviours that have not been pointed out so far and we have compared suboptimal control solutions in the way they should be implemented in a real system. In particular, we have shown through simulations and on bench that with atmospheric disturbance only, the effect of a fractional loop delay on suboptimal control performance was negligible, which is not the case in presence of vibration. We have also demonstrated that the optimal modeling and performance evaluation could be obtained using standard and simple methods, without resorting to multiple numerical integrations. We have also developed a method that derives the continuous-time state space model from a given discrete-time state-space model identified from telemetry data. This allows to build the optimal modeling based on the continuous-time state space matrices. We have also shown how to derive the open-loop and rejection transfer functions that are useful for stability and performance analysis. The implementation of the optimal regulator would need no modification of the RTC code.

This modeling is accompanied by the need to estimate the system loop delay, a task for which we have defined and tested a simple and accurate method. Concerning the disturbances modeling, the temporal cut-off frequencies for each mode of the AR2 state-space model appeared to have a significant impact on performance and require special attention. The equivalent wind speed in the pupil, usually used as a reference to compute these cut-off frequencies, is in many cases not adapted and leads to an undervaluation of the best modal speeds values for the AR2 model.

On the bench, the study of modal power spectral densities (PSDs) has confirmed that taking higher modal speeds V_0^{LQG} and thus having faster modal decorrelations in the AR2 model were beneficial for the performance. This allows a better handling of the measurement aliasing signal. It allowed a gain of at least 1 SR point, and even 3 SR points in some cases with vibration or high sampling frequency cases with strong atmospheric turbulence (900 Hz, $r_0 = 8$ cm).

In addition to the temporal parameters, the LQG controller we implemented

needs some spatial priors about atmospheric conditions, such as r_0 and L_0. We started with a basic existing identification methods (based on von Kármán statistics), with an important difference being the consideration of the poor reconstruction of some Zernike modes with a segmented pupil for which the edges are not measured. With the same identification method, we made an important progress in the evaluation of the "loop gain" of the LQG, that is, the fudge factor. It is a key factor to be tuned in terms of both stability and performance, and we have shown thanks to on-bench results that our evaluation of the fudge factor was a good compromise.

All the proposed disturbance models are identified in an unsupervised way from telemetry data. We only use the measurements provided by the wave front sensor (a Shack-Hartmann type in the case of GTCAO) in the form of slopes measurements and flux per sub-aperture. The regulator can therefore be easily updated at regular intervals (less than 1 minute is needed to build all the LQG matrices on a basic laptop computer) and is thus able to closely follow the evolution of the disturbance statistics.

As for the system modeling required by LQG control, we have shown that using a pseudo-synthetic interaction matrix gives better results than the experimental interaction matrix, even after noise thresholding. This gives moreover access to both the WFS measurement matrix and DM influence functions matrix. We unravelled the rules to fit the WFS measurement matrix to the system's geometry and CCD pixel size. The synthetic DM influence function matrix allows to define an efficient projector P_u^N for the projection of the Kalman filter phase predictions onto the DM actuator space. This projector has the advantage to avoid a detour via the measurement space, as done before. It thus avoids the lack of visibility some DM actuators have in the measurement space (because we are not really in a Fried geometry), and it avoids worrying about defining a command matrix from the interaction matrix. In OOMAO simulations, the use of this projector improved strongly the performance (5 SR points), while on the bench rather 1 SR point. This may be due to several factors, e.g., the lack of precision of the estimated actuators position or the lack of consideration of the non-linear relation between phase and WFS measurements due to the large size of CCD pixels.

In this work, we paid particular attention to the potential loss of performance implied by the rotation of the pupil. We noticed with simulations and bench tests that the model identification is sensitive to changes in the sky-to-WFS angle. This could be mainly a problem in case of observation very close to the observatory zenith where de-rotation higher than 2 degrees per 2 minutes might happen. The extreme case is 90 degrees per 2 minutes: it makes the LQG controller less efficient than the integrator when the disturbance energy (e.g., vibration peaks) is concentrated at different frequencies on modes that exhibit rotational symmetry with respect to each other (e.g., tip and tilt, astigmatism 1 and 2, etc.). This of course does not happen with the integrator as it is independent from this angle.

The LQG regulator we developed is based on a parametric model complemented

with a non-parametric one, a data-driven "model-free" part, with a design that insures to meet closed-loop stability conditions. As it is entirely built from telemetry data, it can be used in operation with a very limited learning stage (say in the order of 10 seconds). Its performance could be assessed through on-bench experiments conducted on GTCAO (with DARC real-time computer) at the IAC, and we warmly thank the team at IAC for having welcomed us and provided the necessary support. The on-bench performance revealed excellent, with a significant increase in the quality of scientific images compared to the best-loop-gain integrator, in particular in situations of low signal-to-noise ratio (SNR) (magnitude of the guide star greater than 12.5 in the visible) or in presence of vibration in the medium and high temporal frequencies. For example, we get about 10 points more of a Strehl ratio of 35% in a low SNR case, or on a Strehl ratio of 38% in a case of vibration similar to those of the Keck telescope. In situations of pure atmospheric turbulence with favorable observing conditions (large r_0 and magnitudes less or equal to 11.3 in the visible), the integrator and our predictive LQG controller have similar performance, albeit with a better robustness during on-sky operations, as reported in (Sinquin et al., 2020). Also, thanks to the kindness of Sam Ragland and Peter Wizinowich, and with the initial help of Olivier Beltramo-Martin, we could test the performance of our LQG design on hundreds of on-sky data recorded in 2013 and 2020 on the AO system of the Keck telescope. These tests, carried on in replay mode, have shown possible improvements of the same order of magnitude as those obtained on GTCAO. In addition, the LQG regulators exhibit very good stability margins, never seen below 35-degree phase margin and 7-dB gain margin.

8.2 Perspectives

The results presented in this manuscript motivate a fully unsupervised operation with LQG regulators, which should be the next stage of development in the short term. The first of the perspectives would thus be to validate the whole strategy with on-sky tests, as the agreement between in-lab bench results and on-sky replays makes it very promising. Besides, the development of the remaining articulations and GUIs to operate a fully autotuned LQG regulator on sky are the purpose of the H2020 ORP project (T. Morris et al., 2020).

Of course, this work has left aside certain aspects which could not be tackled for lack of time, certain in-depth studies would have required additional attention. To start with, the developments of chapter 4 could not be implemented and tested on the bench. As the modeling corresponds to continuous-time disturbances, it would be particularly interesting to be tested on sky. On a bench, when non-atmospheric disturbances are injected thanks to the DM, the modeling should be modified to account for piece-wise constant disturbances in addition to the atmospheric turbulence for a better appreciation of the global performance.

As for the AO system calibration, several points worth being looked at. First, the

calculation of the pseudo-synthetic interaction matrix, based on (Heritier et al., 2018; Heritier-Salama, 2019), led to obtaining an influence matrix with correct geometry allowing to derive a better phase-to-commands projector that naturally accounts for dead actuators. However, the relative improvement was not as good as what was expected when compared with simulations so that it is worth looking deeper into this problem to possibly derive a more efficient interaction matrix. Second, the simple method based on a least-squares solution of a linearly parameterized equation proved to deliver an efficient estimation of the loop delay in open-loop, even with turbulence. It would be useful to study a formulation for closed-loop on-sky operations in particular for systems without internal sources.

The modeling of the disturbances is ready to be fully autotuned. It is based on the Zernike basis and involves two different strategies: a machine learning-based method, N4SID, for the coupled low-order state space model, and a parametric state space model corresponding to a multivariable autoregressive model of order 2, the parameters of which are estimated from telemetry data. Although leading to stable and efficient regulators, the AR2 model deserves some attention, in particular for the high orders: we have seen that the model PSD was sometimes not fitting so closely the experimental data. It could thus be interesting to identify order 2 models for each mode using N4SID, as proposed in (Prengere, 2021). As for the low-order model, we have mentioned above its sensitivity to the sky-to-WFS angle when observing close to the zenith. To counteract this problem, it could be built differently, using a decoupled design where the modes with rotational symmetry are summed together. This is likely to produce a model that becomes insensitive to this angle.

A problem that has not been addressed is the effect of the aliasing on high-frequency vibrations: when sampled below the Shannon-Nyquist frequency, vibrations that are physically not present in the system appear in the measurements. If we let the regulator compensate for them, the performance will be degraded as the DM will generate a vibratory signal. If a table of possible high-frequency vibrations is available, the low-order model could be modified to cancel out the ghost vibrations by performing a canonical decomposition of the low-order state matrix. This should be possible in an automated way.

The switching between two successive controllers, which needs software modifications that are for the moment not available on DARC RTC, needs to be deepen in order to insure a good stitching. The simple solution that consists in keeping the previous state to perform a kind of warm restart is not efficient enough. The method described in (H.-F. Raynaud, Kulcsár, et al., 2016) insures bumpless switching but needs real-time operations to be performed in parallel of the control calculation. This would however concern only the low-order part of the regulator state. The rest of the state being related to smooth turbulence models, it could be initialized with warm restart.

Globally, having an index that indicates in real time whether the model is in good adequation with the disturbance would be of great interest. As we have seen in

the results, lowering the residual slopes variance does not necessarily lead to lowering the residual phase variance and this makes the task more difficult. However, taking advantage of the estimated phases given by the Kalman filter should be investigated.

To jump towards extreme AO or extremely large telescope sizes, the Zernike basis is not adapted since it is difficult to reach a number of modes greater than 900 (Prengere, 2021). We could transpose our methods towards other basis such as the Karhunen–Loève, as foreseen for the AO control of the MICADO first light instrument of the ELT (Clénet et al., 2018; Zidi et al., 2022). In combination with the use of N4SID for the AR2 model identification, as proposed in (Prengere, 2021) and mentioned above, this would allow the modeling methodology to be applied to any modal basis without specific knowledge about its spatio-temporal statistics. This could serve the next generation of instruments such as SPHERE+ (A. Boccaletti et al., 2022).

Appendix A
List of whole headers – examples

A.1 LQG controller headers

Keyword	Value	Description
MI	'20201116_104325_pmx_... rcond_0.1_stdThresh_1'	Interaction matrix (pmx)
MITHRESH	1.8e-6	Interaction matrix threshold value
MISYNTHE	'20220308_X_KlinKquadAngle... CouplingStrangecoeffXrotYrot.mat'	Synthetic interaction matrix parameters
PINVMINT	1	Recompute a new RMX?
PINVNFLT	4	Number of filtered PMX modes
PSEUDACT	0	Use TT pseudo-actuators?
FREQ	1000	Chosen FPS [Hz]
SYSDELTA	0.4	System delay (POL reconstruction) [frame]
LQGDELTA	0.4	Controller delay
ATMFILE	'20210730_131755_OPEN_LOOP_... _cents'	Data file for atmosphere priors estimation
FLATFILE	'20221123_163003_OPEN_LOOP_acts.fits'	File with DM flattening commands
ATMHANN	1	With/without Hann damping of time-series? [boolean]
ATMMAPFF	0.6232	Estimated fudge factor α_{MAP}
ATMNITER	2	Number of priors estimation iterations
DSUBAP	0.5675	Subapertures on-sky diameter [m]
DMSYNCHR	'poyneer'	Synchronizing method ('poyneer' or 'WFS'?)
LAMBDWFS	5×10^{-7}	WFS (and models) wavelength
PXSIZWFS	1.70e-6	WFS CCD pixel on-sky size
NOISDATA	'20210730_131755_OPEN_LOOP_... _cents'	Data file used for noise estimation
DZERCOEF	0.26	WFS CCD Shannon coefficient
ORADIAL	37	Zernike radial order (AR2)
KSI	0.9000	Damp factor ξ (AR2)
MEANWIND	9	Wind speed [$\mathrm{m\,s^{-1}}$] (AR2)
R0	0.3300	r_0 [m] (AR2)
L0	25	L_0 [m] (AR2)
WITHLO	1	Identification of low-order modes? [boolean]
SYSID	'n4sid'	Identification method
NMODLO	2	Number of low-orders (LO)
ORDERLO	15	Model order for (LO) modes
DATATOM	'20210730_131755_OPEN_LOOP_... _cents'	Data file used for LO modes modelling
FUDGE	50	Fudge factor α_{FF}
SWMA2MI	100	Superior limitation of Σ_w (min2max)
DARE	'doubling'	Method for solving Riccati equation
STOPCRIT	'normAlpha'	Criteria for solving Riccati equation
EPSILON	1.00e-09	Criteria value for solving Riccati equation
MAXITER	50	Max of iterations for solving Ricc. eq.
NHIGFREQ	100	Number of high frequency PSD points used for noise estimation
MEANWIND	38.138	Model decorrelation speed [m/s] (TipTilt modes)
DM1	11.35	M1 diameter [m]
DM2	0	Central obscuration diameter [m]
FILTNDAG	1	Number of filtered modes for $N^\dagger$
KNDAGTT	1.1936	Rescaling factor applied for $N^\dagger$
METHODPU	5	Projector Pu method (0->McomD, 5->$N^\dagger$)
NDAGPIST	0	Piston used to replace dead actu?
NDAGBROK	330	Index of dead actuator set to zero in N

Table A.1: List of LQG controller headers - example of the controller '20210730_13h58m49s'

A.2 Bench data headers

Keyword	Value	Description
MI	'20210208_121706_pmx_rcond_0.10_stdThresh_1.00'	Interaction matrix (pmx)
MC	'20210208_121706_rmx_rcond_0.10_stdThresh_1.00'	Command matrix (rmx)
TOTDELAY	1.7000	Total delay [frames]
SCIBGRMV	1	Was the scientifique background removed?
CTRLSTMP	'20210715_15h05m32s'	Controller timestamp
SCINIMAG	200	Number of scientific images
DATASTMP	'20210715_174843'	Timestamp of this data file
CTRLMODE	'INT'	Running darc-int or darc-lqg?
FPSWFS	100	Set FPS [Hz]
FPSDARC	99.9979	DARC FPS [Hz]
PHASCRN	2	Phase screen
CCDGAIN	990	WFS CCD gain
VWIND	33.0000	Wind speed [bench unit]
SCIEXPOS	50000	Scientific camera exposure time [μs/image]
WFSTHRES	1200	WFS light threshold [ADU]
NGSPOWER	0.9000	[bench units]
NGSFLTWH	3	Filter wheel position
INTGAIN	0.6000	Integrator global loop gain (NA if LQG mode)
INTLEAK	0.9900	Leaky factor (NA if LQG mode)
VIBRATOF	'KECKcommands_1000FPS_20221011_14h41m57s'	Vibration commands file (NA if no vibration)
VIBRATOG	0.5	Gain applied to VIBRATOF commands
COMPTIME	2.4199e-04	Computation time [s] (slopes-to-commands time)

Table A.2: List of bench data headers - example of the run '20210715_174843'

A.3 Vibration commands headers

Keyword	Value	Description
TIMESTMP	'20210730_12h23m07s'	Timestamp of this vibrations file
FPS	1000	Chosen FPS [Hz]
NITER	10750	Length [frames]
MODEVIB	'1 2'	Concerned modes [Zernike]
FVIB	'12and90'	Frequencies [Hz]
RMSAOA	'1.2125e-07and2.425e-08'	RMS angle of arrival [rad]
WFSLMBDA	6.5000e-07	WFS wavelength [m]
RMSPHI	'3.0473and0.60947'	RMS dephasing [rad@λ_{wfs}]
KSI	'0.01and0.0001'	Damping factor ξ
SEED	45	Seed for pseudo-random vibration phases
PINVMINT	1	Recompute a new RMX?
MI	'20201116_104325_pmx_rcond_0.10_stdThresh_1.00.fits'	Interaction matrix (PMX)
PINVNFLT	15	Number of filtered PMX modes
PSEUDACT	0	Use TT pseudo-actuators?

Table A.3: List of vibration commands fits file headers - example of the commands batch '20210730_12h23m07s'.

Appendix B
Building the LQG regulator

Procedure for the building of the LQG regulator matrices

We first gather here the expression of the global state space representation of the disturbances as given in (6.4), together with some notations that are used in the flow chart presented on next page.

$$\begin{bmatrix} x_{k+1}^{\text{tur}} \\ x_{k+1}^{\text{LO}} \\ x_{k}^{\text{LO}} \end{bmatrix} = \underbrace{\begin{bmatrix} A^{\text{tur}} & 0 & 0 \\ 0 & A^{\text{LO}} & 0 \\ 0 & 0 & I \end{bmatrix}}_{A} \begin{bmatrix} x_{k}^{\text{tur}} \\ x_{k}^{\text{LO}} \\ x_{k-1}^{\text{LO}} \end{bmatrix} + \underbrace{\begin{bmatrix} \Gamma_x^{\text{tur}} & 0 \\ 0 & \Gamma^{\text{LO}} \\ 0 & 0 \end{bmatrix}}_{\Gamma} v_k \tag{B.1}$$

$$y_k^{\text{OL}} = \underbrace{\begin{bmatrix} C_y^{\text{tur}} & C_y^{\text{LO}} \end{bmatrix}}_{C_y} \begin{bmatrix} x_k^{\text{tur}} \\ - - - \\ x_k^{\text{LO}} \\ x_{k-1}^{\text{LO}} \end{bmatrix} + w_k \tag{B.2}$$

$$\phi_k = \underbrace{\begin{bmatrix} C_\phi^{\text{tur}} & C_\phi^{\text{LO}} \end{bmatrix}}_{C_\phi} \begin{bmatrix} x_k^{\text{tur}} \\ - - - \\ x_{k+1}^{\text{LO}} \\ x_k^{\text{LO}} \end{bmatrix} \tag{B.3}$$

with the following notations:

$$A^{\text{tur}} = \begin{bmatrix} A_1^{\text{tur}} & A_2^{\text{tur}} \\ I & 0 \end{bmatrix} \tag{B.4}$$

$$C_y^{\text{tur}} = [0 \; D] \tag{B.5}$$

$$C_y^{\text{LO}} = [0 \; DC^{\text{LO}}] \tag{B.6}$$

$$C_\phi^{\text{tur}} = [I \; 0] \tag{B.7}$$

$$C_\phi^{\text{LO}} = [C^{\text{LO}} \; 0] \tag{B.8}$$

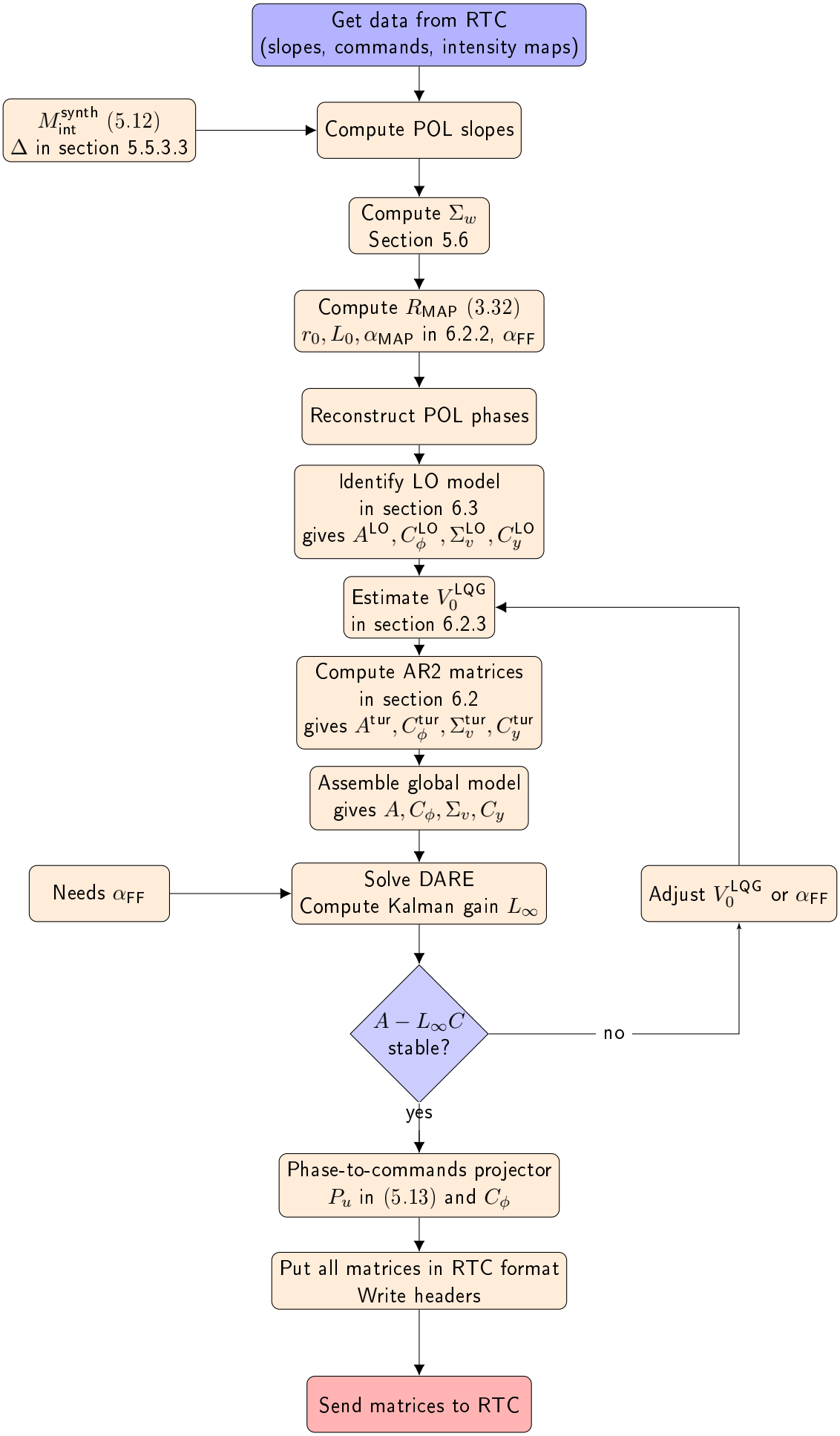
Get data from RTC
(slopes, commands, intensity maps)
$M_{\text{int}}^{\text{synth}}$ (5.12)
Δ in section 5.5.3.3
Compute POL slopes
Compute Σ_w
Section 5.6
Compute R_{MAP} (3.32)
$r_0, L_0, \alpha_{\text{MAP}}$ in 6.2.2, α_{FF}
Reconstruct POL phases
Identify LO model
in section 6.3
gives $A^{\text{LO}}, C_\phi^{\text{LO}}, \Sigma_v^{\text{LO}}, C_y^{\text{LO}}$
Estimate V_0^{LQG}
in section 6.2.3
Compute AR2 matrices
in section 6.2
gives $A^{\text{tur}}, C_\phi^{\text{tur}}, \Sigma_v^{\text{tur}}, C_y^{\text{tur}}$
Assemble global model
gives A, C_ϕ, Σ_v, C_y
Needs α_{FF}
Solve DARE
Compute Kalman gain L_∞
Adjust V_0^{LQG} or α_{FF}
$A - L_\infty C$
stable?
no
yes
Phase-to-commands projector
P_u in (5.13) and C_ϕ
Put all matrices in RTC format
Write headers
Send matrices to RTC

Bibliography

Anderson, Brian D O and John B Moore (1990). *Optimal Control: Linear Quadratic Methods*.

Andrade, Paulo P, Paulo J V Garcia, Carlos M Correia, Johann Kolb, and Maria Inês Carvalho (Nov. 2018). "Estimation of atmospheric turbulence parameters from Shack-Hartmann wavefront sensor measurements". In: *Monthly Notices of the Royal Astronomical Society* 483.1, pp. 1192–1201. ISSN: 0035-8711. DOI: 10.1093/mnras/sty3181. eprint: https://academic.oup.com/mnras/article-pdf/483/1/1192/27070331/sty3181.pdf. URL: https://doi.org/10.1093/mnras/sty3181.

Augusto, Astronomia, Righi Difa, and Elisabetta Rossi (2021). "Alma Mater Studiorum – Università di Bologna Unveiling the size of the Universe : the first accurate measurement of the Earth-Sun distance by Giovanni Domenico Cassini". In.

Babcock, H W (Oct. 1953). "The possibility of compensating astronomical seeing". In: *Publications of the Astronomical Society of the Pacific* 65.386, p. 229. ISSN: 1538-3873. DOI: 10.1086/126606. URL: https://iopscience.iop.org/article/10.1086/126606%20https://iopscience.iop.org/article/10.1086/126606/meta.

Barrell, H and J. E Sears (1939). "The Refraction and Dispersion of Air for the Visible Spectrum". In: *Philosophical Transactions of the Royal Society of London* 238.786, pp. 1–64.

Basden, A. G., D. Atkinson, N. A. Bharmal, U. Bitenc, M. Brangier, T. Buey, T. Butterley, D. Cano, F. Chemla, P. Clark, M. Cohen, J. -M. Conan, F. J. de Cos, C. Dickson, N. A. Dipper, C. N. Dunlop, P. Feautrier, T. Fusco, J. L. Gach, E. Gendron, D. Geng, S. J. Goodsell, D. Gratadour, A. H. Greenaway, A. Guesalaga, C. D. Guzman, D. Henry, D. Holck, Z. Hubert, J. M. Huet, A. Kellerer, C. Kulcsár, P. Laporte, B. Le Roux, N. Looker, A. J. Longmore, M. Marteaud, O. Martin, S. Meimon, C. Morel, T. J. Morris, R. M. Myers, J. Osborn, D. Perret, C. Petit, H.-F. Raynaud, A. P. Reeves, G. Rousset, F. Sanchez Lasheras, M. Sanchez Rodriguez, J. D. Santos, A. Sevin, G. Sivo, E. Stadler, B. Stobie, G. Talbot, S. Todd, F. Vidal, and E. J. Younger (Mar. 2016). "Experience with wavefront sensor and deformable mirror interfaces for wide-field adaptive optics systems". In: *Monthly Notices of the Royal Astronomical Society* 459.2, pp. 1350–1359. ISSN: 13652966. DOI: 10.1093/mnras/stw730. URL: http://arxiv.org/abs/1603.07527%20http://dx.doi.org/10.1093/mnras/stw730.

Basden, Alastair, Deli Geng, Richard Myers, and Eddy Younger (Nov. 2010). "Durham adaptive optics real-time controller". In: *Applied Optics* 49.32, pp. 6354–6363. ISSN: 15394522. DOI: 10.1364/AO.49.006354.

Béjar, V. J.S., M. R. García-Talavera, J. Patrón, E. Hernández, R. López, J. Marco de la Rosa, I. Montilla, M. Nuñez Cagigal, M. Puga Antolín, L. F. Rodríguez-Ramos, J. Rosich, J. Sánchez-Capuchino, R. Simoes, O. Tubio, J. A. Acosta-Pulido, A. Prieto, A. M. Watson, and M. R. Zapatero Osorio (2018). "The GTC Adaptive Optics system: The high spatial resolution Adaptive Optics facility at GTC". In: *Proceedings of the 13th Scientific Meeting of the Spanish Astronomical Society - Highlights of Spanish Astrophysics X, SEA 2018*. SEA, pp. 536–541. ISBN: 9788409093311.

Beuzit, J-L, Markus Feldt, David Mouillet, C Moutou, Kjetil Dohlen, P Puget, T Fusco, P Baudoz, A Boccaletti, S Udry, et al. (2005). "A planet finder instrument for the VLT". In: *Proceedings of the International Astronomical Union* 1.C200, pp. 317–322.

Blázquez-Bermejo, Zorba, Julio Hernández-Afonso, Antonio García-Quintana, José M. Medina, José J. Grillo, María D. García-Cosio, Laura Morán-Fernández, Pedro Caravaca-Pérez, Violeta Sánchez, Pilar Escribano-Subias, Emilio Renes, Fernando Arribas-Ynsaurriaga, José M. Cortina, and Juan F. Delgado (2020). "Heart transplantation in a distant island population: Accessibility and outcomes in patients from the Canary Islands transplanted in Madrid". In: *Transplantation* April, pp. 223–226. ISSN: 00411337. DOI: 10.1097/TP.0000000000002929.

Boccaletti, A., G. Chauvin, F. Wildi, J. Milli, E. Stadler, E. Diolaiti, R. Gratton, F. Vidal, M. Loupias, M. Langlois, F. Cantalloube, M. N'Diaye, D. Gratadour, F. Ferreira, M. Tallon, J. Mazoyer, D. Segransan, D. Mouillet, J.-L. Beuzit, M. Bonnefoy, R. Galicher, A. Vigan, I. Snellen, M. Feldt, S. Desidera, S. Rousseau, A. Baruffolo, C. Goulas, P. Baudoz, C. Bechet, M. Benisty, A. Bianco, B. Carry, E. Cascone, B. Charnay, E. Choquet, V. Christiaens, F. Cortecchia, V. Di Capprio, A. De Rosa, C. Desgrange, V. D'Orazi, S. Douté, M. Frangiamore, E. Gendron, C. Ginski, E. Huby, C. Keller, C. Kulcsár, R. Landman, S. Lagarde, E. Lagadec, A.-M. Lagrange, M. Lombini, M. Kasper, F. Ménard, Y. Magnard, G. Malaguti, D. Maurel, D. Mesa, G. Morgante, E. Pantin, T. Pichon, A. Potier, P. Rabou, S. Rochat, l. Terenzi, E. Thiébaut, I. Tallon-Bosc, H.-F Raynaud, D. Rouan, A. Sevin, F. Schiavone, L. Schrieber, and A. Zanutta (2022). "Upgrading the high contrast imaging facility SPHERE: science drivers and instrument choices". In: *Ground-based and Airborne Instrumentation for Astronomy IX*. Ed. by Christopher J. Evans, Julia J. Bryant, and Kentaro Motohara. Vol. 12184. International Society for Optics and Photonics. SPIE, 121841S. DOI: 10.1117/12.2630154. URL: https://doi.org/10.1117/12.2630154.

Chassat, F. (1992). "Propagation optique à travers la turbulence atmosphérique. Etude modale de l'anisoplanétisme et application à l'optique adaptative". PhD thesis. Université Paris 11.

Clénet, Yann, Tristan Buey, Eric Gendron, Zoltan Hubert, Fabrice Vidal, Mathieu Cohen, Frédéric Chapron, Arnaud Sevin, Pierre Fédou, Gaële Barbary, Pierre Baudoz, Bruno Borgo, Saber Ben Nejma, Vincent Chambouleyron, Vincent Déo, Olivier Dupuis, Sébastien Durand, Florian Ferreira, Julien Gaudemard, Damien Gratadour, Elsa Huby, Jean-Michel Huet, Bertrand Le Ruyet, Napoléon Nguyen-Tuong, Clément Perrot, Simone Thijs, Youssef Younès, Gérard Rousset, Philippe Feautrier, Gérard Zins, Emiliano Diolaiti, Paolo Ciliegi, Simone Esposito, Lorenzo Busoni, Josef Schubert, Michael Hartl, Veronika Hörmann, and Richard Davies (2018). "The MICADO first-light imager for the ELT: towards the preliminary design review of the MICADO-MAORY SCAO". In: *Adaptive Optics Systems VI*. Ed. by Laird M. Close, Laura Schreiber, and Dirk Schmidt. Vol. 10703. International Society for Optics and Photonics. SPIE, p. 1070313. DOI: 10.1117/12.2311481. URL: https://doi.org/10.1117/12.2311481.

Conan, Jean-Marc, Gérard Rousset, and Pierre-Yves Madec (1995). "Wavefront temporal spectra in high-resolution imaging through turbulence". In: *J. Opt. Soc. Am. A* 12.7, pp. 1559–1570. DOI: 10.1364/JOSAA.12.001559. URL: https://opg.optica.org/josaa/abstract.cfm?URI=josaa-12-7-1559.

Conan, Rodolphe (Feb. 2008). "Mean-square residual error of a wavefront after propagation through atmospheric turbulence and after correction with Zernike polynomials". In: *Journal of the Optical Society of America A* 25.2, p. 526. ISSN: 1084-7529. DOI: 10.1364/josaa.25.000526. URL: https://www.researchgate.net/publication/5606381_Mean-square_residual_error_of_a_wavefront_after_propagation_through_atmospheric_turbulence_and_after_correction_with_Zernike_polynomials.

Conan, Rodolphe and Carlos Correia (2014). "Object-oriented Matlab adaptive optics toolbox". In: *Proceedings of SPIE - The International Society for Optical Engineering*. Vol. 9148, p. 91486C. DOI: 10.1117/12.2054470.

Currie, Thayne, Olivier Guyon, Julien Lozi, Ananya Sahoo, Sebastien Vievard, Vincent Deo, Jeffrey Chilcote, Tyler Groff, Timothy D. Brandt, Kellen Lawson, Nour Skaf, Frantz Martinache, and N. Jeremy Kasdin (2020). "On-sky performance and recent results from the Subaru coronagraphic extreme adaptive optics system". In: *Adaptive Optics Systems VII*. Ed. by Laura Schreiber, Dirk Schmidt, and Elise Vernet. Vol. 11448. International Society for Optics and Photonics. SPIE, 114487H. DOI: 10.1117/12.2576349. URL: https://doi.org/10.1117/12.2576349.

Dhillon, V. S., N. Bezawada, M. Black, S. D. Dixon, T. Gamble, X. Gao, D. M. Henry, P. Kerry, S. P. Littlefair, D. W. Lunney, T. R. Marsh, C. Miller, S. G. Parsons, R. P. Ashley, E. Breedt, A. Brown, M. J. Dyer, M. J. Green, I. Pelisoli, D. I. Sahman, J. Wild, D. J. Ives, L. Mehrgan, J. Stegmeier,

C. M. Dubbeldam, T. J. Morris, J. Osborn, R. W. Wilson, J. Casares, T. Muñoz-Darias, E. Pallé, P. Rodríguez-Gil, T. Shahbaz, M. A.P. Torres, A. De Ugarte Postigo, A. Cabrera-Lavers, R. L.M. Corradi, R. D. Domínguez, and D. García-Alvarez (Aug. 2021). "HiPERCAM: a quintuple-beam, high-speed optical imager on the 10.4-m Gran Telescopio Canarias". In: *Monthly Notices of the Royal Astronomical Society* 507.1, pp. 350–366. ISSN: 0035-8711. DOI: 10.1093/MNRAS/STAB2130. URL: https://academic.oup.com/mnras/article/507/1/350/6328500.

Doelman, Niek, Rufus Fraanje, and Remco den Breeje (2011). "Real-sky adaptive optics experiments on optimal control of tip-tilt modes". In: *Second International Conference on Adaptive Optics for Extremely Large Telescopes*. Vol. 7736. URL: https://ui.adsabs.harvard.edu/abs/2011aoel.confP..51D/abstract%20http://adsabs.harvard.edu/abs/2011aoel.confP..51D.

Ellerbroek, Brent (2002). "Efficient computation of minimum-variance wavefront reconstructors with sparse matrix techniques." In: *Journal of The Optical Society of America A-optics Image Science and Vision*. DOI: 10.1364/josaa.19.001803.

Ellerbroek, Brent L. and Curt R. Vogel (2009). "Inverse problems in astronomical adaptive optics". In: *Inverse Problems* 25.6, p. 063001.

Esposito, Simone, Armando Riccardi, F Quirós-Pacheco, Enrico Pinna, Alfio Puglisi, Marco Xompero, Runa Briguglio, Lorenzo Busoni, Luca Fini, Paolo Stefanini, Guido Brusa, Andrea Tozzi, Piero Ranfagni, F Pieralli, Juan Carlos Guerra, Juan Carlos Guerra, Carmelo Arcidiacono, and Piero Salinari (2010). "Laboratory characterization and performance of the high-order adaptive optics system for the Large Binocular Telescope". In: *Applied Optics*. DOI: 10.1364/ao.49.00g174.

Femenía, Bruno, Icíar Montilla, and Miguel Núñez (2017). *GTCAO system error budget*. Tech. rep.

Fried, D L (Oct. 1966). "Optical Resolution Through a Randomly Inhomogeneous Medium for Very Long and Very Short Exposures". In: *J. Opt. Soc. Am.* 56.10, pp. 1372–1379. DOI: 10.1364/JOSA.56.001372. URL: https://opg.optica.org/abstract.cfm?URI=josa-56-10-1372.

Fusco, T., G. Rousset, D. Rabaud, E. Gendron, D. Mouillet, F. Lacombe, G. Zins, P. Y. Madec, A. M. Lagrange, J. Charton, D. Rouan, N. Hubin, and N. Ageorges (June 2004). "NAOS on-line characterization of turbulence parameters and adaptive optics performance". In: *Journal of Optics A: Pure and Applied Optics* 6.6, pp. 585–596. ISSN: 14644258. DOI: 10.1088/1464-4258/6/6/014. URL: https://www.researchgate.net/publication/231126587_NAOS_on-line_characterization_of_turbulence_parameters_and_adaptive_optics_performance.

Gendron, E. and G. Rousset (Sept. 2012). "Temporal analysis of aliasing in Shack-Hartmann wave-front sensing". In: *Adaptive Optics Systems III*. Vol. 8447. SPIE, 84476N-84476N–13. ISBN: 9780819491480. DOI: 10.1117/12.925554.

Gladysz, Szymon, Julian C Christou, L William Bradford, and Lewis C Roberts (2008). "Temporal variability and statistics of the Strehl ratio in adaptive-optics images". In: *Publications of the Astronomical Society of the Pacific* 120.872, p. 1132.

GTC (2023). *Introducing the Gran Telescopio CANARIAS*. URL: http://www.gtc.iac.es/.

Guo, Youming, Jiaying Wang, Ling Kong, Kele Chen, Naiting Gu, Xuejun Rao, and Changhui Rao (Mar. 2021). "Vibration mitigation experiment on the Chinese Large Solar Telescope based on the linear quadratic Gaussian control". In: *Optik* 230, p. 166333. ISSN: 0030-4026. DOI: 10.1016/J.IJLEO.2021.166333.

Guyon, Olivier, Yutaka Hayano, Motohide Tamura, Tomoyuki Kudo, Tomoyuki Kudo, Shin Oya, Yosuke Minowa, Olivier Lai, Nemanja Jovanovic, Naruhisa Takato, N Jeremy Kasdin, Jeremy Kasdin, Tyler D Groff, Masahiko Hayashi, Nobuo Arimoto, Hideki Takami, Colin Bradley, Hajime Sugai, Guy Perrin, Peter G Tuthill, and Ben Mazin (2014). "Adaptive optics at the Subaru telescope: current capabilities and development". In: *Proceedings of SPIE*. DOI: 10.1117/12.2057273.

Guyon, Olivier, Julien Lozi, Sebastien Vievard, Ruslan Belikov, Eduardo Bendek, Steven Bos, Thayne Currie, Vincent Deo, Michael Fitzgerald, Damien Gratadour, Tyler Groff, Nemanja Jovanovic, Hajime Kawahara, Takayuki Kotani, Tomoyuki Kudo, Coline Lopez, Hatem Ltaief, Jared Males, Frantz Martinache, Marc-Antoine Martinod, Benjamin A. Mazin, Kelsey Miller, Barnaby Norris, Mamadou Ndiaye, Eugene Pluzhnyk, Ananya Sahoo, Arnaud Sevin, Nour Skaf, Frans Snik, Motohide Tamura, and Alison Wong (2020). "Validating advanced wavefront control techniques on the SCExAO testbed/instrument". In: *Adaptive Optics Systems VII*. Ed. by Laura Schreiber, Dirk Schmidt, and Elise Vernet. Vol. 11448. International Society for Optics and Photonics. SPIE, 114481Z. DOI: 10.1117/12.2562723. URL: https://doi.org/10.1117/12.2562723.

Guyon, Olivier, Frantz Martinache, Vincent Garrel, Frederic Vogt, Kaito Yokochi, and Takashi Yoshikawa (2010). "The Subaru coronagraphic extreme AO (SCExAO) system: wavefront control and detection of exoplanets with coherent light modulation in the focal plane". In: *SPIE Astronomical Telescopes+ Instrumentation*. International Society for Optics and Photonics, pp. 773624–773624.

Hardy, John W and Laird Thompson (1998). *Adaptive Optics for Astronomical Telescopes*. ISBN: 0195090195. DOI: 10.1063/1.883053.

Helden, Albert Van (1974). "The Telescope in the Seventeenth Century". In: 83.3, pp. 171–186.

Heritier, Cédric Taïssir, Simone Esposito, Thierry Fusco, Benoit Neichel, Sylvain Oberti, Runa Briguglio, Guido Agapito, Alfio Puglisi, Enrico Pinna, and P.-Y. Madec (2018). "A new calibration strategy for adaptive telescopes with pyramid WFS". In: *Monthly Notices of the Royal Astronomical Society*. DOI: 10.1093/mnras/sty2485.

Heritier-Salama, Cédric Taïssir (2019). "Innovative calibration strategies for large adaptive telescopes with pyramid wave-front sensors". PhD thesis.

Hubin, Norbert, Bertrand Theodore, Patrick Petitjean, and Bernard Delabre (1994). "Adaptive optics system for the Very Large Telescope". In: *Astronomical Telescopes and Instrumentation*. DOI: 10.1117/12.176073.

Juvénal, Rémy, Caroline Kulcsár, Henri-François Raynaud, and Jean-Marc Conan (2018). "Linear controller error budget assessment for classical adaptive optics systems". In: *JOSA A* 35.8, pp. 1465–1476.

Kaler, James (2002). *Celestial Sphere*. URL: http://stars.astro.illinois.edu/celsph.html.

Kármán, Theodore Von (1948). "Progress in the Statistical Theory of Turbulence". In: *Proceedings of the National Academy of Sciences of the United States of America* 34.11, pp. 530–539. ISSN: 00278424. URL: http://www.jstor.org/stable/88224 (visited on 07/10/2023).

Kolb, Johann, P-Y Madec, M Le Louarn, N Muller, and C Béchet (2012). "Calibration strategy of the AOF". In: *Adaptive Optics Systems III*. Vol. 8447. SPIE, pp. 895–905.

Kolmogorov, A.N. (1941). "Local structure of turbulence in incompressible fluids with very high Reynolds number". In: *Dokl. Akad. Nauk. SSSR* 30.

Krajnovic, Davor (Oct. 2016). "The contrivance of Neptune". In: *Astronomy and Geophysics* 57.5. DOI: 10.1093/astrogeo/atw183. URL: http://arxiv.org/abs/1610.06424%20http://dx.doi.org/10.1093/astrogeo/atw183.

Kucera, Vladimir (1991). *Analysis and design of discrete linear control systems*. Prentice Hall London.

Kulcsár, Caroline, Henri François Raynaud, Cyril Petit, and Jean Marc Conan (Sept. 2012). "Minimum variance prediction and control for adaptive optics". In: *Automatica* 48.9, pp. 1939–1954. ISSN: 00051098. DOI: 10.1016/j.automatica.2012.03.030.

Kulcsár, Caroline, Henri-François Raynaud, Cyril Petit, Jean-Marc Conan, and Patrick Viaris de Lesegno (Aug. 2006). "Optimal control, observers and integrators in adaptive optics". In: *Optics Express* 14.17, p. 7464. ISSN: 10944087. DOI: 10.1364/OE.14.007464.

Kulcsár, Caroline, Gaetano Sivo, Henri-François Raynaud, Benoît Neichel, François Rigaut, Julian Christou, Andres Guesalaga, Carlos Correia, Jean-

Pierre Véran, Eric Gendron, Fabrice Vidal, Gérard Rousset, Tim Morris, Simone Esposito, Fernando Quiros-Pacheco, Guido Agapito, Enrico Fedrigo, Lorenzo Pettazzi, Richard Clare, Riccardo Muradore, Olivier Guyon, Frantz Martinache, Serge Meimon, and Jean-Marc Conan (Sept. 2012). "Vibrations in AO control: a short analysis of on-sky data around the world". In: *Adaptive Optics Systems III* 8447, pp. 84471C-84471C–14. ISSN: 0277786X. DOI: 10.1117/12.925984. URL: https://www.researchgate.net/publication/269318609_Vibrations_in_AO_control_A_short_analysis_of_on-sky_data_around_the_world.

Lainiotis, D G, Nicholas Assimakis, and Sokratis K Katsikas (1994). "New doubling algorithm for the discrete periodic Riccati Equation". In: *Applied Mathematics and Computation*. DOI: 10.1016/0096-3003(94)90109-0.

Le Roux, Brice, Jean-Marc Conan, Caroline Kulcsár, Henri-François Raynaud, Laurent M Mugnier, and Thierry Fusco (July 2004). "Optimal control law for classical and multiconjugate adaptive optics". In: *JOSA A* 21.7, pp. 1261–1276. ISSN: 1084-7529. DOI: 10.1364/josaa.21.001261. URL: https://www.researchgate.net/publication/8449889_Optimal_control_law_for_classical_and_multiconjugate_adaptive_optics.

Looze, Douglas P (2009). "Linear-quadratic-Gaussian control for adaptive optics systems using a hybrid model". In: *Journal of The Optical Society of America A-optics Image Science and Vision*. DOI: 10.1364/josaa.26.000001.

Macintosh, Bruce, James Graham, David Palmer, Rene Doyon, Don Gavel, James Larkin, Ben Oppenheimer, Leslie Saddlemyer, J Kent Wallace, Brian Bauman, et al. (2007). "Adaptive optics for direct detection of extrasolar planets: the Gemini Planet Imager". In: *Comptes Rendus Physique* 8, pp. 365–373.

Madec, Pierre-Yves (July 2012). "Overview of deformable mirror technologies for adaptive optics and astronomy". In: *Adaptive Optics Systems III, SPIE Proceedings* 8447.

Mahajan, Virendra N. (June 1983). "Strehl ratio for primary aberrations in terms of their aberration variance". In: *JOSA, Vol. 73, Issue 6, pp. 860-861* 73.6, pp. 860–861. ISSN: 00303941. DOI: 10.1364/JOSA.73.000860. URL: https://opg.optica.org/viewmedia.cfm?uri=josa-73-6-860&seq=0&html=true%20https://opg.optica.org/abstract.cfm?uri=josa-73-6-860%20https://opg.optica.org/josa/abstract.cfm?uri=josa-73-6-860.

Marco de la Rosa, Jose, J. Rosich, Miguel Núñez, Oscar Tubío, J. C. López, L. F. Rodríguez, A. Basden, J. Patrón, I. Montilla, R. L. López, M. Puga Antolín, R. Simoes, F. Tenegi, J. Sánchez-Capuchino, M. Reyes, and V.J.S. Béjar (2018). "GTCAO Real Time Control System software design". In: *AO4ELT5*.

Marquis, Lucas, Caroline Kulcsár, Icíar Montilla, Henri-François Raynaud, José Marco de la Rosa, Óscar Tubío Araújo, Alastair Basden, and Marcos Reyes García-Talavera (Aug. 2022). "Linear quadratic Gaussian predictive control for the Gran Telescopio Canarias AO system: design issues and first bench results". In: *https://doi.org/10.1117/12.2630257* 12185, pp. 909–916. DOI: 10.1117/12.2630257. URL: https://www.spiedigitallibrary.org/conference-proceedings-of-spie/12185/121852R/Linear-quadratic-Gaussian-predictive-control-for-the-Gran-Telescopio-Canarias/10.1117/12.2630257.full%20https://www.spiedigitallibrary.org/conference-proceedings-of-spie/12185/1.

Montilla, Iciar, José Marco de la Rosa, Óscar Tubío Araújo, Josefina Rosich, Marcos Reyes García-Talavera, Manuel Luis Aznar, Eduardo González, Roberto López, Roberto Simoes, Jesús Patrón Recio, Marta Puga, and Víctor Sánchez Béjar (Aug. 2022). "Laboratory acceptance and telescope integration readiness of the Gran Telescopio Canarias adaptive optics system". In: *https://doi.org/10.1117/12.2630109* 12185. Ed. by Dirk Schmidt, Laura Schreiber, and Elise Vernet, pp. 660–667. DOI: 10.1117/12.2630109. URL: https://www.spiedigitallibrary.org/conference-proceedings-of-spie/12185/1218523/Laboratory-acceptance-and-telescope-integration-readiness-of-the-Gran-Telescopio/10.1117/12.2630109.full%20https://www.spiedigitallibrary.org/conference-proceedings-of-spie/1218.

Morris, T., J. Osborn, M. Reyes, I. Montilla, G. Rousset, E. Gendron, T. Fusco, B. Neichel, S. Esposito, P. J. V. Garcia, C. Kulcsar, C. Correia, J.-L. Beuzit, N. A. Bharmal, L. Bardou, L. Staykov, and D. Bonaccini Calia (2020). "The ORP on-sky community access program for adaptive optics instrumentation development". In: *Adaptive Optics Systems VII*. Ed. by Laura Schreiber, Dirk Schmidt, and Elise Vernet. Vol. 11448. International Society for Optics and Photonics. SPIE, 114485H. DOI: 10.1117/12.2562805. URL: https://doi.org/10.1117/12.2562805.

Murgas, Felipe, Felipe Murgas, Guo Chen, Enric Palle, E Pallé, Enric Palle, Enric Palle, L Nortmann, Grzegorz Nowak, and Grzegorz Nowak (2019). "The GTC exoplanet transit spectroscopy survey X. Stellar spots versus Rayleigh scattering: the case of HAT-P-11b". In: *Astronomy and Astrophysics*. DOI: 10.1051/0004-6361/201834063.

Myers, Richard M, Zoltán Hubert, Timothy J Morris, Éric Gendron, Nigel A Dipper, Aglaé Kellerer, Stephen J Goodsell, Gérard Rousset, Eddy Younger, Michel Marteaud, et al. (2008). "CANARY: the on-sky NGS/LGS MOAO demonstrator for EAGLE". In: *Proc. SPIE*. Vol. 7015, 70150E.

Neichel, Benoit, Francois Rigaut, Matthieu Bec, and Aurea Garcia-Rissmann (2010). "Reconstruction strategies for GeMS". In: *1st AO4ELT conference-Adaptive Optics for Extremely Large Telescopes*. EDP Sciences, p. 02010.

Noll, R. J. (1976). "Zernike polynomials and atmospheric turbulence". In: *J. Opt. Soc. Am. A* 66, p. 207 211.

Núñez, Miguel and Yolanda Martin (2018). *Deformable Mirror test report*. Tech. rep.

Núñez Cagigal, Miguel (2018). *GTCAO RTC closed loop servo-control DED-DGAO_128v1*. Tech. rep.

Núñez Cagigal, Miguel, L. F. Rodriguez-Ramos, Óscar Tubío Araújo, Jose Marco de La Rosa, Alastair Basden, Iciar Montilla, Josefina Rosich, Roberto López, Marta Puga, Marcos Reyes García-Talavera, and Jesús Patrón Recio (2017). "Feedback control baseline for GTC adaptive optics with NGS". In: *Adaptive Optics for Extremely Large Telescopes, 2017 AO4ELT5*. Vol. 2017-June. DOI: 10.26698/ao4elt5.0182.

Osborn, J, R W Wilson, M Sarazin, T Butterley, A Chacón, F Derie, O J D Farley, X Haubois, D Laidlaw, M LeLouarn, E Masciadri, J Milli, J Navarrete, and M J Townson (Apr. 2018). "Optical turbulence profiling with Stereo-SCIDAR for VLT and ELT". In: *Monthly Notices of the Royal Astronomical Society* 478.1, pp. 825–834. ISSN: 0035-8711. DOI: 10.1093/mnras/sty1070. eprint: https://academic.oup.com/mnras/article-pdf/478/1/825/25698645/sty1070.pdf. URL: https://doi.org/10.1093/mnras/sty1070.

Osborn, J., T. Butterley, M. J. Townson, A. P. Reeves, T. J. Morris, and R. W. Wilson (Oct. 2016). "Turbulence velocity profiling for high sensitivity and vertical-resolution atmospheric characterization with Stereo-SCIDAR". In: *Monthly Notices of the Royal Astronomical Society* 464.4, pp. 3998–4007. DOI: 10.1093/mnras/stw2685. eprint: https://academic.oup.com/mnras/article-pdf/464/4/3998/8310802/stw2685.pdf. URL: https://doi.org/10.1093/mnras/stw2685.

Overschee, Peter Van and Bart De Moor (1994). "N4SID: subspace algorithms for the identification of combined deterministic-stochastic systems". In: *Automatica*. DOI: 10.1016/0005-1098(94)90230-5.

Pan, Jorge, Consolacion Asenjo, Alfredo Orden, and Angel Dilla (2000). "GTC telescope mechanics design". In: *Proceedings of SPIE - The International Society for Optical Engineering* 4004, pp. 92–103. ISSN: 0277786X. URL: http://www.scopus.com/inward/record.url?eid=2-s2.0-0033699602%5C&partnerID=40%5C&md5=d700dc9a005f98af02bf75c70bb2256b.

Paschall, RN, MA Von Bokern, and BM Welsh (1991). "Design of a linear quadratic Gaussian controller for an adaptive optics system". In: *Proceedings of the 30th IEEE Conference on Decision and Control*. IEEE, pp. 1761–1769.

Pease, F. G. (1921). "Measurement of Star Diameters by the Interferometer Method". In: *American Philosophical Society* 60.4, pp. 524–534.

Petit, C, C Petit, Cyril Petit, Jean-François Sauvage, Jean-François Sauvage, Thierry Fusco, A Sevin, Arnaud Sevin, M Suarez, Anne Costille, Arthur Vigan, Christian Soenke, D Perret, Denis Perret, Sylvain Rochat, S Rochat, A Barrufolo, Bernardo Salasnich, J L Beuzit, J L Beuzit, Kjetil Dohlen, David Mouillet, Pascal Puget, Pascal Puget, Francois Wildi, M Kasper, Jean-Marc Conan, Jean-Marc Conan, Caroline Kulcsár, and Henri-François Raynaud (2014). "SPHERE eXtreme AO control scheme: final performance assessment and on sky validation of the first auto-tuned LQG based operational system". In: *Proceedings of SPIE*. DOI: 10.1117/12.2052847.

Poyneer, Lisa, Robert J De Rosa, Robert J De Rosa, Bruce Macintosh, David W Palmer, David Palmer, D Palmer, David W Palmer, Marshall D Perrin, Naru Sadakuni, Dmitry Savransky, Brian J Bauman, Andrew Cardwell, Jeffrey Chilcote, Jeffrey Chilcote, Daren Dillon, D Gavel, Donald T Gavel, Donald Gavel, Stephen J Goodsell, Markus Hartung, Markus Hartung, Pascale Hibon, Pascale Hibon, Fredrik T Rantakyrö, Sandrine Thomas, Jean-Pierre Véran, Jean-Pierre Véran, and Jean-Pierre Veran (2014). "On-sky performance during verification and commissioning of the Gemini Planet Imager's adaptive optics system". In: *Proceedings of SPIE*. DOI: 10.1117/12.2057092.

Poyneer, Lisa and Jean-Pierre Véran (July 2008). "Predictive wavefront control for adaptive optics with arbitrary control loop delays". In: *JOSA A, Vol. 25, Issue 7, pp. 1486-1496* 25.7, pp. 1486–1496. ISSN: 1520-8532. DOI: 10.1364/JOSAA.25.001486. URL: https://opg.optica.org/viewmedia.cfm?uri=josaa-25-7-1486&seq=0&html=true%20https://opg.optica.org/abstract.cfm?uri=josaa-25-7-1486%20https://opg.optica.org/josaa/abstract.cfm?uri=josaa-25-7-1486.

Poyneer, Lisa A, S Mark Ammons, Mike K Kim, Brian Bauman, Jesse Terrel-Perez, Aaron J Lemmer, and Jayke Nguyen (2023). "Laboratory demonstration of the prediction of wind-blown turbulence by adaptive optics at 8 kHz with use of LQG control". In: *Applied Optics* 62.8, pp. 1871–1885.

Poyneer, Lisa A, David W Palmer, Bruce Macintosh, Dmitry Savransky, Naru Sadakuni, Sandrine Thomas, Jean-Pierre Véran, Katherine B Follette, Alexandra Z Greenbaum, S Mark Ammons, et al. (2016). "Performance of the Gemini Planet Imager's adaptive optics system". In: *Applied Optics* 55.2, pp. 323–340.

Prengere, Léonard (2021). "Commande haute performance des systèmes d'optique adaptative classique - des grands aux extrêmement grands télescopes (ELT)". PhD thesis. URL: http://www.theses.fr/2021UPAST028%5C%0Ahttps://github.com/rconan.

Prengère, Léonard, Caroline Kulcsár, Henri-François Raynaud, and Henri-François Raynaud (2020). "Zonal-based high-performance control in adaptive optics systems with application to astronomy and satellite tracking".

In: *Journal of The Optical Society of America A-optics Image Science and Vision*. DOI: 10.1364/josaa.391484.

Rappenglück, M. (1997). "The Pleiades in the "Salle des Taureaux", grotte de Lascaux. Does a rock picture in the cave of Lascaux show the open star cluster of the Pleiades at the Magdalénien era (ca 15.300 BC?"" In: *ascu*, pp. 217–225. URL: https://ui.adsabs.harvard.edu/abs/1997ascu.conf..217R/abstract.

Raynaud, Henri-François, Carlos Correia, Caroline Kulcsár, and Jean-Marc Conan (2011). "Minimum-variance control of astronomical adaptive optics systems with actuator dynamics under synchronous and asynchronous sampling". In: *International Journal of Robust and Nonlinear Control* 21.7, pp. 768–789.

Raynaud, Henri-François, Caroline Kulcsár, Rémy Juvénal, and Cyril Petit (2016). "The control switching adapter: a practical way to ensure bumpless switching between controllers while AO loop is engaged". In: *Adaptive Optics Systems V*. Ed. by Enrico Marchetti, Laird M Close, and Jean-Pierre Véran. Vol. 9909. International Society for Optics and Photonics. SPIE, 99094K. DOI: 10.1117/12.2234266. URL: https://doi.org/10.1117/12.2234266.

Roberts Jr, Lewis C, Marshall D Perrin, Franck Marchis, Anand Sivaramakrishnan, Russell B Makidon, Julian C Christou, Bruce A Macintosh, Lisa A Poyneer, Marcos A van Dam, and Mitchell Troy (2004). "Is that really your Strehl ratio?" In: *Advancements in Adaptive Optics*. Vol. 5490. SPIE, pp. 504–515.

Roddier, François (June 1999). *Adaptive Optics in Astronomy*. Cambridge University Press. ISBN: 9780521553759. DOI: 10.1017/cbo9780511525179. URL: https://www.cambridge.org/core/product/identifier/9780511525179/type/book.

Rodriguez-Espinosa, Jose Miguel and Pedro Alvarez (Mar. 1997). "Gran Telescopio Canarias: a 10-m telescope for the ORM". In: vol. 2871. SPIE, pp. 69–73. DOI: 10.1117/12.269113. URL: https://www.spiedigitallibrary.org/conference-proceedings-of-spie/2871/0000/Gran-Telescopio-Canarias--a-10-m-telescope-for-the/10.1117/12.269113.full.

Rose, J. (1964). "Galileo Galilei (1564-1642)". In: *Nature* 201.4920, pp. 653–657. ISSN: 00280836. DOI: 10.1038/201653a0.

Rousset, G, J. C Fontanella, P Kern, P Gigan, and F Rigaut (1990). "First diffraction-limited astronomical images with adaptive optics". In: *Astronomy and Astrophysics* 230, pp. L29–L32. URL: http://adsabs.harvard.edu/full/1990A%5C%26A...230L..29R.

Rousset, G., J. Primot, and J. C. Fontanella (1987). "Visible wavefront sensor development". In: *Workshop on Adaptive Optics in Solar Observation*.

Vol. 28. 28, pp. 17–34. URL: https://ui.adsabs.harvard.edu/abs/1987LFTR...28...17R/abstract.

Sánchez-Martínez and F. (2008). "Gran Telescopio Canarias: a key asset for Spanish astronomy". In: *LNEA* 3, pp. 103–112. URL: https://ui.adsabs.harvard.edu/abs/2008LNEA....3..103S/abstract.

Sinquin, Baptiste, Léonard Prengère, Caroline Kulcsár, Henri François Raynaud, Eric Gendron, James Osborn, Alastair Basden, Jean Marc Conan, Nazim Bharmal, Lisa Bardou, Lazar Staykov, Tim Morris, Tristan Buey, Fanny Chemla, and Matthieu Cohen (Oct. 2020). "On-sky results for adaptive optics control with data-driven models on low-order modes". In: *Monthly Notices of the Royal Astronomical Society* 498.3, pp. 3228–3240. ISSN: 0035-8711. DOI: 10.1093/MNRAS/STAA2562. URL: https://academic.oup.com/mnras/article/498/3/3228/5897378.

Sivo, Gaetano (2014). "Validation ciel d ' une commande haute performance en optique adaptative classique et multi-objet sur le démonstrateur CANARY". PhD thesis.

Sivo, Gaetano, Caroline Kulcsár, Jean-Marc Conan, Henri-François Raynaud, Éric Gendron, Alastair Basden, Fabrice Vidal, Tim Morris, Serge Meimon, Cyril Petit, Damien Gratadour, Olivier Martin, Zoltan Hubert, Arnaud Sevin, Denis Perret, Fanny Chemla, Gérard Rousset, Nigel Dipper, Gordon Talbot, Eddy Younger, Richard Myers, David Henry, Stephen Todd, David Atkinson, Colin Dickson, and Andy Longmore (Sept. 2014). "First on-sky SCAO validation of full LQG control with vibration mitigation on the CANARY pathfinder". In: *Optics Express* 22.19, p. 23565. ISSN: 10944087. DOI: 10.1364/OE.22.023565. URL: https://www.researchgate.net/publication/265863786_First_on-sky_SCAO_validation_of_full_LQG_control_with_vibration_mitigation_on_the_CANARY_pathfinder.

Soummer, Rémi and André Ferrari (2007). "The Strehl ratio in adaptive optics images: statistics and estimation". In: *The Astrophysical Journal* 663.1, p. L49.

Tatarski, V. I., R. A. Silverman, and Nicholas Chako (Jan. 1961). "Wave Propagation in a Turbulent Medium". In: *Physics Today* 14.12, pp. 46–51. ISSN: 0031-9228. DOI: 10.1063/1.3057286. URL: https://physicstoday.scitation.org/doi/abs/10.1063/1.3057286.

Taylor, G. I. (Feb. 1938). "The Spectrum of Turbulence". In: *Proceedings of the Royal Society of London. Series A - Mathematical and Physical Sciences* 164.919, pp. 476–490. ISSN: 0080-4630. DOI: 10.1098/rspa.1938.0032. URL: https://royalsocietypublishing.org/doi/10.1098/rspa.1938.0032.

Tesch, Jonathan, Tuan Truong, Rick Burruss, and Steve Gibson (2015). "On-sky demonstration of optimal control for adaptive optics at Palomar Observatory". In: *Opt. Lett.* 40.7, pp. 1575–1578.

Van Dam, Marcos A., David Le Mignant, and Bruce A. Macintosh (Oct. 2004). "Performance of the Keck Observatory adaptive-optics system". In: *Applied Optics* 43.29, pp. 5458–5467. ISSN: 15394522. DOI: 10.1364/AO.43.005458.

Van Helden, Albert (Mar. 1974). "The Telescope in the Seventeenth Century". In: *Isis* 65.1, pp. 38–58. ISSN: 0021-1753. DOI: 10.1086/351216.

Varela, A M, C Muñoz-Tuñón, and A G Gurtubai (2001). "Image Quality at the GTC Site". In: *Highlights of Spanish Astrophysics II*. Ed. by Jaime Zamorano, Javier Gorgas, and Jesús Gallego. Dordrecht: Springer Netherlands, pp. 301–304. ISBN: 978-94-017-1776-2.

Vernin, J and Casiana Munoz-Tunon (1992). "Optical seeing at La Palma Observatory. I - General guidelines and preliminary results at the Nordic Optical Telescope". In: *Astronomy and Astrophysics* 257, pp. 811–816.

Vidal, F., E. Gendron, M. Brangier, T. Morris, A. Basden, R. Myers, G. Rousset, Z. Hubert, F. Chemla, A. Longmore, T. Butterley, N. Dipper, C. Dunlop, D. Geng, D. Gratadour, D. Henry, P. Laporte, N. Looker, D. Perret, A. Sevin, G. Talbot, and E. Younger (2011). "Detailed analysis of the first MOAO results obtained by CANARY at the WHT". In: vol. 2. 2nd AO4ELT conference - Adaptative Optics for Extremely Large Telescopes.

Walter, Eric and Luc Pronzato (1997). *Identification of Parametric Models*. Ed. by MASSON.

Watson, A, J Acosta-Pulido, M Aguiar, L C Álvarez-Núñez, V Sánchez-Béjar, N Cardiel, O Chapa, S Cuevas, J J Díaz García, S Eikenberry, C Espejo, R Flores-Meza, J Fuentes-Fernández, J Fujarte, J Gallego, José Leonardo Garcés Medina, F Garzón López, P Hammersley, E Joven Álvarez, C Keiman, G Lara, J López, Carlos A Ortega, Sergio Pascual Ramírez, J Patrón Recio, A Prieto, Berenice Rodríguez, B Sánchez, and J Sánchez (2022). "FRIDA: diffraction-limited imaging and integral-field spectroscopy for the GTC". In: *Astronomical Telescopes + Instrumentation*. DOI: 10.1117/12.2630345.

Wizinowich, Peter L, D Scott Acton, Olivier Lai, J. Gathright, William Lupton, and Paul J Stomski (2000). "Performance of the W.M. Keck Observatory Natural Guide Star Adaptive Optic Facility: the first year at the telescope". In: *Astronomical Telescopes and Instrumentation*. DOI: 10.1117/12.390368.

Zernike, F. (1934). "Diffraction theory of the knife-edge test and its improved form, the phase-contrast method". In: *MNRAS* 94, p. 377 384.

Zidi, Amal, Henri-François Raynaud, Caroline Kulcsár, Fabrice Vidal, Eric Gendron, Yann Clénet, and Richard Davies (Aug. 2022). "The MICADO first light imager for the ELT: SCAO LQG control performance with windshake, vibrations, and mirror dynamics". In: *https://doi.org/10.1117/12.2629863*

12185, pp. 892–897. DOI: 10.1117/12.2629863. URL: https://www.spiedigitallibrary.org/conference-proceedings-of-spie/12185/121852P/The-MICADO-first-light-imager-for-the-ELT--SCAO/10.1117/12.2629863.full%20https://www.spiedigitallibrary.org/conference-proceedings-of-spie/12185/121852P/The-MICADO-first-light-.